Electrokinetic Transport Process in Nanopores Generated on Cell Membrane during Electroporation

by

Saeid Movahed

A thesis
presented to the University of Waterloo
in fulfillment of the
thesis requirement for the degree of
Doctor of Philosophy
in
Mechanical Engineering

Waterloo, Ontario, Canada, 2012

AUTHOR'S DECLARATION

I hereby declare that I am the sole author of this thesis. This is a true copy of the thesis, including any required final revisions, as accepted by my examiners.

I understand that my thesis may be made electronically available to the public.

Abstract

In this thesis, underlying concepts of transport phenomena through generated nanopores on a cell membrane during electroporation were studied. A comprehensive literature review was performed to find the pros and cons of the previous works and consequently extensive studies were accomplished to explain shortcomings of the former studies on this topic.

The membrane permeabilization of the single cell located in the microchannel was studied, and the effects of microchannel's wall and electrode size were investigated on cell electroporation. It was studied how the electrical (e.g., strength of the electric pulse) and geometrical parameters (e.g., microchannel height and electrode size) affect size, location, and number of created hydrophilic pores on the cell membrane.

Because of a transmembrane potential, the electrokinetic effects have decisive influence on the transport process through the created nanopores. A comprehensive study was performed to explain the electrokinetic transport through the nanochannels. Effects of surface electric charge and radius of the nanochannel on the electric potential, liquid flow, and ionic transport were investigated. Unlike microchannels, the electric potential field, ionic concentration field, and velocity field are strongly size-dependent in the nanochannels. They are also affected by the surface electric charge of the nanochannel. More counter ions than co-ions are transported through the nanochannel. The ionic concentration enrichment at the entrance and the exit of the nanochannel is completely evident from the simulation results. The study also shows that the fluid velocity in the nanochannel is higher when the surface electric charge is stronger, or the radius of the nanochannel is larger.

The obtained model of the electrokinetic effects in the nanochannels was utilized to examine the ionic mass transfer and the fluid flow through the generated hydrophilic nanopores of the cell membrane during electroporation. The results showed how the electric potential, velocity field, and ionic concentration vary with the size and angular position of the generated nanopores of the cell membrane. It was also shown that, in the presence of the electric pulse, the electrokinetic effects (the electroosmosis and the electrophoresis) had significant influences on the ionic mass transfer through the nanopores, while the effect of diffusion on the ionic mass flux was negligible in comparison with the electrokinetics. Increasing the radius of the nanopores intensified the effect of convection (electroosmosis) in comparison with the electrophoresis on the ionic flux.

Furthermore, the electrokinetic motion of the nanoparticle through the nanochannel was investigated to mimic inserting the nanoscale biological samples, such as QDots and DNAs, through the created

nanopores on the cell membrane. It was proved that, because of the large applied electric field over the nanochannel, the impact of the Brownian force was negligible in comparison with the electrophoretic and the hydrodynamic forces. It was demonstrated that increasing the bulk ionic concentration or the surface charge of the nanochannel will increase the electroosmotic flow, and hence affect the particle's motion. It was also shown that, unlike the microchannels with thin EDL, the change in the nanochannel size will change the EDL field and the ionic concentration field in the nanochannel, affecting the particle's motion. If the nanochannel size is fixed, a larger particle will move faster than a smaller particle under the same conditions.

Finally, it was examined how the nanoscale biological samples (nanoparticles) reach openings of the generated nanopores on the cell membrane during electroporation. It was examined what forces (electrophoresis, diffusion, and convection) brings the nanoparticles into the nanopores and how the size and the surface electric charge of the nanoparticle affect its transport to the opening of the nanopores.

Acknowledgements

I'd like to extend my gratitude to my supervisor Prof. Dongqing Li, for his support, patience and the lessons that he has taught me. I had a great PhD study under his supervision. His help and support was truly beyond the traditions of academic study.

I would also like to thank Prof. Sean Peterson, Prof. Stefan Idziak, Prof. Bae-Yuen Ha, and Prof. Aristides Docoslis for carefully reading my thesis and providing valuable comments.

I would like to thank my colleagues and fellow graduate students Dr. Xudong Wu, Hai Jiang, Xuan Weng, Fang Zhang, and Yasaman Daghighi. I enjoyed their kind support during my studies.

And last, but not the least, I'd like to thank my wonderful family, my parents Mr Masoud Movahed and Mrs. Nahid Mokhtarian, and my sister, Dr Elham Movahed, for the unwavering support they have consistently given to me during my life.

Dedication

To my family!

Table of Contents

List of Figures

List of Tables

Nomenclature

Chapter 3

$d_0 (= 2a)$: diameter of the cell
a : radius of the cell
t_m : cell membrane thickness
h_c : height of the microchannel
d : length of the electrode
ϕ_0 : electric pulse intensity
t_0 : electric pulse duration
s_i : intracellular conductivity
s_e : extracellular conductivity
s : Conductivity of the solution filling the pore
c_m : Specific membrane capacitance
g_1 : Surface conductance of the membrane
V_{rest} : rest potential
α : Creation rate coefficient
V_{ep} : Characteristic voltage of electroporation
N_0 : Equilibrium pore density at $V_m = 0$
r^* : Minimum radius of hydrophilic pores
r_m : Minimum energy radius at $V_m = 0$ pores
D : Diffusion coefficient for pore radius
T : Temperature
β : Steric repulsion energy
γ : Edge energy (Glaser, et al., 1988)
$F_{\max}$: Max electric force for $V_m = 1V$
r_h : Constant in Eq. (3.12.b) for advection velocity
r_t : Constant in Eq. (3.12.b) for advection velocity
q : Constant in Eq. (3.11) for pore creation rate
σ' : Tension of hydrocarbon-water interface
σ_0 : Tension of the bilayer without pores

Chapter 4

ε_T : relative permittivity
ε_0 : absolute permittivity
ρ : liquid density
σ_0 : surface electric charge

μ : dynamic viscosity
F : Faraday constant
a : nanochannel radius
L : nanochannel length
D_+ : diffusion coefficient of positive ion
D_- : diffusion coefficient of negative ion
μ_i : mobility of ion species *i*
T : temperature

Chapter 5

ε_T : relative permittivity
ε_0 : absolute permittivity
ρ : liquid density
ρ_s : surface electric charge density
T : temperature
R_g : universal gas constant
$C_{o,i}$: intercellular bulk ionic concentration of ion type i
$C_{o,e}$: extracellular bulk ionic concentration of ion type i
F : Faraday Constant
a : cell radius
t : cell thickness
R : radius of nanopore
R_0 : radius outside of nanopore
E_e : external electric field
D_i : diffusion coefficient of positive ion
μ_i : mobility of ion species *i*
TMP : Transmembrane Potential

Chapter 6

ε_T : relative permittivity
ε_0 : absolute permittivity
ρ : liquid density
σ_w : surface electric charge on the walls of nanochannel
σ_p : surface electric charge of nanoparticle
ϕ_1 : electric potential on the left
ϕ_2 : electric potential on the right
μ : dynamic viscosity
F : Faraday constant

k_B : Boltzmann constant
Rg : universal gas constant
R : nanochannel radius
a : nanoparticle side dimension
L : nanochannel length
D_+ : diffusion coefficient of positive ion
D_- : diffusion coefficient of negative ion
μ_i : mobility of ion species *i*
C_o : bulk ionic concentration
T : temperature
ς : Gaussian Random Number

Chapter 7

$d_0(=2a)$: diameter of the cell
a : radius of the cell
t_m : cell membrane thickness
h_c : height of the microchannel
d : length of the electrode
ϕ_0 : electric pulse intensity
t_0 : electric pulse duration
s_i : intracellular conductivity
s_e : extracellular conductivity
s : Conductivity of the solution filling the pore
c_m : Specific membrane capacitance
g_1 : Surface conductance of the membrane
V_{rest} : rest potential
α : Creation rate coefficient
V_{ep} : Characteristic voltage of electroporation
N_0 : Equilibrium pore density at $V_m = 0$
r^* : Minimum radius of hydrophilic pores
r_m : Minimum energy radius at $V_m = 0$ pores
D : Diffusion coefficient for pore radius
T : Temperature
β : Steric repulsion energy
γ : Edge energy
$F_{\max}$: Max electric force for $V_m = 1V$
r_h : Constant in Eq. (7.11.b) for advection velocity
r_t : Constant in Eq. (7.11.b) for advection velocity
q : Constant in Eq. (7.10) for pore creation rate

σ' : Tension of hydrocarbon-water interface

σ_0 : Tension of the bilayer without pores

F : Faraday constant

ε_T : relative permittivity

ε_0 : Vacuum permittivity

μ : Viscosity of medium

ρ : medium density

σ_s : surface electric charge of the nanochannel walls

σ_p : surface electric charge of nanoparticle

d_p : diameter of the nanoparticle

R_g : gas constant

$D(Na^+)$: diffusion coefficient of Na^+

$D(K^+)$: diffusion coefficient of K^+

$D(Cl^-)$: diffusion coefficient of Cl^-

μ_i : mobility of ion species type i

Chapter 1
Introduction

1.1 Overview

The main objective of this study is to investigate the underlying concepts of electrokinetic transport process in nanochannels and nanopores generated on cell membrane during electroporation performing in microfluidic lab-on-a-chip devices. Applying an electric field near the cell results in disturbance in its membrane structure and creating nanopores on it. This leads to a significant increase in the electrical conductivity and permeability of the cell membrane that usually refers as the electroporation or electropermeabilization (Neu, et al., 2009). To obtain the best cell viability and transfection rates and decrease the required samples, the microfluidic electroporation of the single cell is considered. During the electroporation, the nanoscale pores generate on the cell membrane. Because of transmembrane potential and surface electric charge of the cell membrane, the electrokinetic effects play important roles on cell transfection (performing electroporation to insert biological samples to the cells).

Traditional electroporation devices (macroscale devices) suffer from a number of problems: In addition to the insufficient understanding of its theoretical mechanism, the cell viability and electroporation efficiency are inadequate; some cells are distorted while others are unaffected. The cell viability is typically about 20~50%, and transfection rate for mammalian cell lines is less than 50% (Lee, et al., 2009). Because of the large size of these devices, excessive voltage must apply to the electrodes in order to generate the required electric field for electroporation. Special safety cautions are required to operate commercial electroporators at several hundred volts. The large distances between the electrodes in conjunction with the short duration electric pulses can also lead to a non-uniform and less stable electric field profile. Furthermore, the conventional electroporators usually have sensitive and complicated experimental processes. Aluminum based electrodes are widely used in commercial instruments that could be a source of Al^{3+} ions dissolved into the media, leading to unpredictable results in cells (Kim, et al., 2007). On the contrary, the microfluidic electroporation can provide spatial and temporal control of various electrical parameters. Many shortcomings of convectional electroporation such as variations in the local *pH*, electric field distortion, sample contamination, and the difficulties in transfection and maintaining the viability of desired cell types can be avoided in the microfluidic electroporation.

They are many advantages associate with the microfluidic electroporation (Lee, et al., 2009; Fox, et al., 2006). The required voltages in the microfluidic devices are much lower in comparison with the macroscopic systems. By shrinking the inter-electrode distance to a few tens of microns, it is possible to reduce the voltage requirement to a few volts (three orders of magnitude smaller than typical voltages required in a macroscopic apparatus). Consequently, the power consumption (P) becomes six orders of magnitude smaller ($P \propto V^2$) and heat generation is minimal. One of the challenging problems of the conventional electroporation systems is the heat generation. In microscale devices, the area-to-volume ratio is relatively large. This leads to the faster heat dissipation. The fast dissipation of the generated heat makes it possible to distinguish the heating effects and the electric field effects. The ability of performing the electroporation process in continuous flow is another advantage of the microfluidic electroporation devices. The required amounts of difficult-to-produce reagents, such as specific plasmids, are considerably small in comparison with the conventional electroporation. Microfluidic electroporation has the ability of *in situ* visualization of molecular uptake. One can have a real-time monitoring of intracellular response to the external electric pulses (using fluorescent probes for example). The ability to perform the single cell electroporation is a further advantage of the microfluidic electroporation. In the microfluidic electroporation, it is possible to trap single cells and perform transfection or determine intracellular content or other properties of the single cell, which is hardly feasible when using conventional equipment. One can have more symmetrical and uniform electric fields in the microfluidic electroporative devices. Cell handling and manipulation are also easier in the microfluidic electroporation. Last but not the least is the potential of the microfluidics electroporative devices for integration with other microfluidic components to form a multifunction lab-on-chip system for subcellular analysis, which would greatly facilitate large scales biochemical experimentation.

The cell electroporation and membrane permeabilization of the cells located in the microchannels has not been investigated yet. All the other studies on this topic consider the cells in an infinite domain which may not reflect the effects of microchannel walls and electrode size on the cell electroporation. Furthermore, there is not any comprehensive study on the electrokinetic effects in the nanoscale pores and channels. Because of the nanoscale dimensions of the generated pores, electric double layer has a signification overlapped and therefore conventional theories of the electrokinetics (such as Poisson-Boltzmann equation and Helmholtz-Smoluchowski theory of electroosmotic slip velocity) lose their credibility in such the nanoscale dimensions.

This thesis involves the theoretical studies on the cell electroporation and transfection in microfluidic devices. The membrane permeabilization of the single cell located in the microchannel is examined first. The effects of microchannel height, electrode size, and electric pulse and duration are investigated on the number and angular position of the created nanopores on the cell membrane. Next, the electrokinetic effects in the nanoscale channels and consequently created nanopores on the cell membrane are studied to model the flow field and ionic mass transfer through the created nanopores of the cell membrane. Then, the electrokinetic motion of the nanoparticle in the nanochannel is studied in order to mimic insertion of the QDots into the cells via the created nanopores of the cell membrane. Finally, the transport of the nanoparticle to the opening of the generated nanopore in cell membrane during electroporation is investigated.

1.2 Motivations

Quantum Dots (QDs) represent one newer form of technology that is now being exploited for the detection and tracking of dynamic cellular events in living systems (Algar, et al.; Algar, et al., 2009). It presents the feasibility of early detection of disease and also monitoring disease progression and therapeutic efficiency. In fact, the QDs are the bio-sensors for the detection and tracking of dynamic cellular events in living systems. Reversible electroporation technique can be utilized to insert these microscale bio-sensors into the cells. By exploiting the microfluidic lab-on-a-chip devices, the required reagents of the electroporation reduces significantly; in addition, the microfluidic devices are capable of performing the single cell electroporation and present the feasibility of online monitoring. Furthermore, microscale electroporation has the best cell viability and transfection rate compare with its counterparts (Lee, et al., 2009).

Current understandings on the theoretical aspects of the cell electroporation are too limited. There is no study on the membrane permeabilization of the cells located in the microchannels. The previous studies considered the cells in an infinite domain which may not reflect the influence of microchannel walls and microelectrode size and location on the cell membrane permeabilization. No studies also consider the effects of the electrokinetics on the flow field, ionic transport, and inserting the biological samples (QDots) through the nanopores of cell membrane into the cells.

The major motivation of this study is to expand the current understanding on the underlying concepts of the microfluidic cell electroporation.

1.3 Background

As it was indicated before, one of the most interesting applications of the microfluidic electroporation is cell transfection (inserting biological samples into the cell). The reversible cell electroporation and DNA electrotransfer trace its roots to 1982 (Neumann, et al., 1982). At the beginning of the millennium, the idea of using the microfluidic devices for the electroporation initiated. In a series of publications, Huang and Rubinsky presented their microfluidic electroporation device (Huang, et al., 2000; Huang, et al., 2001; Huang, et al., 2003). In fact, this is the first practical attempt to use microfluidic devices for the cell electroporation purpose. Figure 1.1 shows the schematic diagram and optical image of this work.

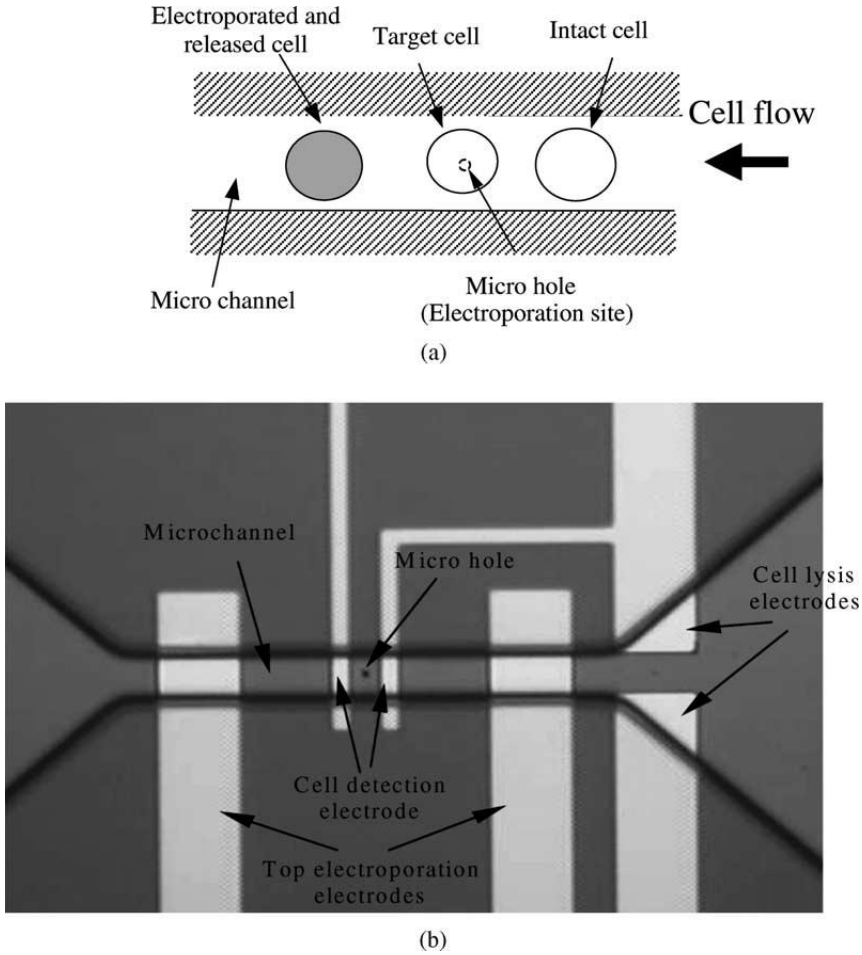

Figure 1-1 (a) Scheme of the first proposed flow-through micro-electroporation chip. (b) Optical image of the layout the first microfluidic electroporation device. Micro-hole, micro-channel and integrated electrodes are tagged in this picture (Huang, et al., 2003).

The electroporation system of Figure 1.1 contains one microchannel with an approximate width equal to 1.5 times of the cell diameter. In this way, the cells are forced to pass through the channels one by one and electroporated individually (single cell electroporation). There is a hole at the center of this channel. The purpose of the hole is to trap the cells and fixes them during the electroporation process. Three pairs of electrodes are used in this system. The function of one set of the electrodes at the entrance of the channel is to prevent the large cells from entering the channel. This was achieved by producing electrical repelling force against the large cells. Two 10 μm wide auxiliary microelectrodes were placed 10 μm away on both sides of the micro-hole for cell detection by impedance measurement. Two other electrodes were placed 100 μm apart on two sides of the micro-hole to generate the required electric field for performing the electroporation. The cells flew through the channels one by one, were trapped by the micro-hole and electroporated. By applying 10 V electric potential with 10 ms duration, this system is used to reversibly electroporate the Human prostate adenocarcinoma cells (ND-1 cell line). It was reported that the cell transfection efficiency of this system is 100%.

By recent advancements in the field of microfabrications (Ziaie, et al., 2004), much more studies conducted on microfluidics cell electroporation (Lee, et al., 2009; Movahed, et al., 2011; Fox, et al., 2006; Wang, et al., 2010). Most of the leading studies in this field have been reviewed in Chapter 2.

1.4 Objectives and Scopes

This thesis studies theoretical concepts of the microfluidic cell electroporation. Here, I investigate how different geometrical (e.g. microchannel size, electrode size, and nanoparticle size) and electrical parameters (e.g. surface electric charge, electric pulse intensity, and duration) affects the permeabilization of the cell membrane and transporting the nanoscale biological samples towards and into the generated nanopores on the cell membrane. In the future, the other researchers may use the results and finding of this study as a guideline to obtain the optimized design and improve the functionality of their proposed microfluidic cell electroporation design. Whit these into consideration, the scopes and objectives of this study can be classified as follows:

- To perform a comprehensive literature review on previous experimental and theoretical studies on the microfluidic cell electroporation.

- To get solid understanding on the governing theories of electroporation. They include theory of membrane permeabilization and the electrokinetic effects in the nanoscale dimensions.
- To study permeabilization of the single cell located in the microchannel.
- To develop an accurate and comprehensive model for the electrokinetic effects in the nanochannels and the nanopores.
- To model ionic mass transfer and cell uptake from the generated nanopores on the cell membrane and during electroporation.
- To study the electrokinetic motion of nanoparticles in the nanochannels.
- To investigate the nanoparticle transport to the opening of the nanopores generated on the cell membrane during the electroporation.

1.5 Overview of this thesis

This thesis consists of eight different chapters. The references are listed at the end of the thesis. Chapter 1, the current chapter, introduces the concepts and motivations of the microfluidic cell electroporation. The pioneer studies on this topic have been reviewed here. This chapter also includes the scopes and objectives of this study and also the overview of the whole dissertation.

Chapter 2 contains a critical review on the experimental and theoretical studies of the microfluidic cell electroporation. More than 100 papers are reviewed here. All the published theoretical models on the cell membrane permeabilization and the ionic mass transfer and the fluid flow through the generated nanopores of the cell membrane are studied. This chapter also reviews the previous experimental microfluidic set ups of the cell electroporation. Indeed, this chapter provides pros and cons of the previous studies on this topic and provides clues to the future trend of the microfluidic cell electroporation.

Chapter 3 contains the membrane permeabilization of the cells located in the microchannels. In this chapter, first a theory of membrane permeabilization is introduced. Then, for one specific case of study, electropermeabilization of the single cell located in the microchannel is investigated. A complete parametric study is performed, and the effects of microchannel height, electrode size, electric pulse intensity and duration on the density and size of the created nanopores are investigated.

Chapter 4 examines the electrokinetic transport through the nanochannels. Because of electric double layer overlapping in the nanochannels, the conventional theories of the electrokinetics such as the Poisson Boltzmann equation and the Helmholtz Smoluchowski slip velocity lose their credibility and cannot be used anymore. In this chapter, a highly coupled set of partial differential equations including the Navier Stokes equations, the Nernst Planck equation, and the continuity equations are solved to find the electric potential, the flow field, and the ionic concentration through the nanochannel. In this chapter, influences of the nanochannel height and surface electric charge on its walls are investigated on the electrokinetic transports.

In Chapter 5, the proposed model of Chapter 4 is utilized to examine the ionic mass transfer and the fluid flow through the generated nanopores on the cell membrane during the electroporation. The influences of angular position and cross sectional area of the created nanopores on the cell membrane are investigated. Furthermore, it is shown that in addition to the diffusion, the electrokinetics (electroosmosis and electrophoresis) play an important roles on the ionic mass transfer and fluid flow through the created nanopores.

In Chapter 6, the electrokinetic motion of a nanoparticle in the nanochannels is studied to mimic inserting biological samples into the cells through the nanopores on the cell membrane (electroporation). At each time step, the proposed model of Chapter 4 is utilized to find the flow field and the ionic mass transfer and consequently the inserted hydrodynamic (electroosmotic) and electrophoretic forces on the nanoparticle. Then, the Newton second law is utilized to obtain the velocity of the nanoparticle. It is shown that the effect of the Brownian force on the nanoparticle is negligible in comparison with the hydrodynamic (electroosmotic) and electrophoretic forces. A comprehensive parametric study is performed and the impacts of nanoparticle size, bulk ionic concentration, surface electric charge of the nanochannels, and nanochannel cross sectional area on the nanoparticle motion are investigated.

In Chapter 7, it is examined that how the nanoparticle reach the opening of the generated nanopores on the cell membrane. First the membrane permeabilization of the cell located in the microchannel is studied to find the radius of the generated nanopores and transmembrane potential in the vicinity of these generated nanopores. Then, the theory of electrokinetics in nanochannels is utilized to model the nanoparticle motion near the generated nanopores. It is shown that, unlike the hydrodynamic (electroosmotic) effect, the electrophoretic force tends to move the nanoparticle toward the opening

of the generated nanopores. It is also shown that more highly charged and smaller nanoparticles have better transport to the opening of the generated nanopores.

The concluding remarks are presented in Chapter 8. In this chapter, I explain the conclusions and contributions of this thesis. Furthermore, I propose some outlines for the future studies on this topic.

Chapter 2
Literature Review*

2.1 Introduction

In this chapter, the latest achievements of the microfluidic devices for the cell electroporation will be reviewed. Having a comprehensive understanding on the pro and con of the current experimental set-ups helps us to improve the functionality of the proposed design. However, before going through these experimental studies, it is worthy to have a look at some important analytical studies on the microfluidic cell electroporation. Although the current analytical studies are unclear regarding the exact mechanisms of ions and macromolecule exchange across the cell membrane, they present some interesting clues for future works.

2.2 Theoretical Studies

The underlying concept in many of these analytical studies is the "theory of cell membrane permeabilization" that will be explained in section 3.2. These studies can be categorized in three different groups:

- The studies investigated the effects of different parameters such as field strength, ionic concentration, pulse strength and duration on the cell membrane permeabilization.
- The studies conducted to evaluate the uptakes of fluid, ions, and macromolecules by the cell during the electroporation.
- The studies focused on optimizing and controlling of electric pulse during the cell electroporation.

In the following section, these categories are reviewed separately.

2.2.1 Studies investigated the effects of different parameters such as field strength, ionic concentration, pulse strength and duration on the cell membrane permeabilization.

Many studies investigated different parameters such as the field strength, the ionic concentration, the pulse strength and duration on the cell membrane permeabilization. In these studies, Laplace equation

* A version of this chapter has been published in the Microfluidic and Nanfluidic Journal as: "Saeid Movahed, Dongqing Li 'Microfluidics Cell Electroporation ', Microfluidics and Nanofluidics Journal, Springer, 2011, Vol. 10, No. 4, pp. : 703-734". A licence agreement of reprinting this article in the current dissertation has been presented in permission section (License Number: 3001440592254).

($\nabla^2\phi = 0$) was solved in order to find the electric potential inside (ϕ_i) and outside (ϕ_e) the cell. Equation (2.1) was suggested to find the current density across the cell membrane (DeBruin, et al., 1999). In this equation, the cell membrane is modeled as a parallel capacitor and resistance system. Transmembrane potential (V_m or TMP) is defined as: $V_m = \Phi_i - \Phi_e$. In this equation, I_{ion} is the ionic current, and I_{ep} is the current due to the electroporation.

$$-\hat{n}(\sigma_i \nabla \Phi_i) = -\hat{n} \bullet (\sigma_e \nabla \Phi_e) = C_m \frac{\partial V_m}{\partial t} + I_{ion} + I_{ep} \qquad (2.1)$$

Using this approach, in a series of papers DeBruin et al. studied the effect of the field strength, the rest potential, and the ionic concentration on the cell permeabilization (DeBruin, et al., 1999; DeBruin, et al., 1999). According to their results, TMP (the transmembrane potential) is symmetric about the equator with the same value at both poles of the cell. Larger shocks do not increase the maximum magnitude of TMP because more pores form to shunt the excess stimulus current across the membrane. In addition, the value of the rest potential does not affect induced transmembrane potential around the cell because the electroporation current is several orders of magnitude larger than the ionic current that supports the rest potential. Once the electric field is removed, the shock-induced discharges within 2s, but the pores persist in the membrane for several seconds. Complete resealing to pre-shock conditions requires approximately 20 s.

Bilska et al. modeled the electroporation in two geometries, a space-clamped membrane and a single cell, and investigated the effects of pulse duration, frequency, shape, and strength (Bilska, et al., 2000). The effectiveness of each shock is measured by the fractional pore area (FPA). The results indicate that FPA is sensitive to shock duration only in a very narrow range. In contrast, FPA is sensitive to shock strength and frequency of the pulse train, increasing linearly with shock strength and decreasing slowly with frequency. Their results indicate that varying the strength and frequency of a monophasic pulse train is the most effective way to control the creation of pores (Bilska, et al., 2000).

Mossop et al. investigated that how the intracellular field is altered by the electroporation (Mossop, et al., 2007). In their study, they showed that the intracellular current could vary several orders of magnitude whereas the maximum variations in the extracellular and total currents were less than 8% and 4%, respectively. A similar difference in the variations was also reported when comparing the electric fields near the center of the cell and across the permeabilized membrane,

respectively. According to their results, the electroporation also caused redirection of the extracellular electric field that was significant only within a small volume near the permeabilized regions, suggesting that the electric field can only facilitate passive cellular uptake of charged molecules near the pores. Within the cell, the field was directed radially from the permeabilized regions, which may be important for improving intracellular distribution of charged molecules.

Krassowska et al. presented a model of the electroporation in a spherical cell exposed to an electric field (Krassowska, et al., 2007). They investigated the pore density around the cell for one case of study. According to their results, the highest pore density occurs on the depolarized (the nearest point on the cell membrane near negative electrode) and hyperpolarized (the nearest point on the cell membrane near positive electrode) poles but the largest pores are on the border of the electroporated regions of the cell membrane. Despite their much smaller number, large pores comprise 95.3% of the total pore area and contribute 66% to the increased cell conductance. For stronger pulses, the pore area and the cell conductance increase, but these increases are due to the creation of the small pores; the number and size of the large pores do not increase (Krassowska, et al., 2007).

Talele and colleagues developed a numerical model for single and spherical cell electroporation (Talele, et al., 2010). They simulated spatial and temporal aspects of the transmembrane potential and pore radii as an effect of the applied electric field (Talele, et al., 2010). Based on their results, that the pore radii tend to be more normalized for AC fields. The relative difference in fractional pore area is reduced by the use of a 1 MHz sinusoidal applied electric field over a 100 kHz field.

These numerical and analytical studies on the cell electroporation have some underlying assumptions. First, they assumed the spherical cells. However, some studies indicated that in the presence of the applied electric field, the cells deform from spherical to elliptical shape (Teissie, et al., 2002). Second, they considered the cells in an infinite space. However, in the microfluidic electroporation, the cells are usually located in the microchannels or micro-chambers. The results of these studies may not reflect the boundary effects of the microfluidic based electroporative devices. Furthermore, the effects of cell expansion and rotation during the electroporation are not considered. More sophisticated analytical models are needed to investigate the effects of electro-deformation including swelling and rotation.

2.2.2 The studies conducted to evaluate the uptakes of fluid, ions, and macromolecules by the cell during the electroporation.

A few studies were conducted on the mass transfer and uptake rate into the cells during the electroporation. There are not any accurate models that consider the electrokinetic effects on the mass transfer through the nanopores in the cell membrane. Furthermore, most of the current studies are based on continuum hypothesis that may become invalid in the small dimensions of the nanopores. Zaharoff et al. used one dimensional mass transfer equation to compute the cellular uptake of macromolecules (Zaharoff, et al., 2008). This study utilized the analytical approach (will be explained in Section 3.2) to estimate the dimension of the generated pores due to the applied electric field in the cell membrane. They treated these pores as a channel to uptake the macromolecules to the cell. They considered only the effect of diffusion in this process and their analysis was based on the continuum hypothesis. However, they concluded that continuum assumption used in their mathematical modeling is improper for simulating the diffusion within the cell; convection is probably the dominant mechanism of transport for cellular uptake of uncharged macromolecules; in addition, the effect of the electrophoresis must be considered in the cellular uptake of highly charged molecules. Another important effect on cellular uptake is cell deformation that was ignored in this study.

Another study conducted by Granot and Colleagues (Granot, et al., 2008) numerically investigated the delivery of drugs into the tissue cells by the electroporation. This study was based on the following assumptions: the process of mass transfer happens in every cell in the tissue; the cells are infinitesimally small; and that the drug entering the cell can be modeled as a uniformly distributed reaction rate. They further assumed that the cells are uniformly packed in the tissue so that each spherical cell is contained in a cube whose edge is equal to 2r (r is the radius of the cell). They also considered only the effect of the diffusion. In this study, first they attributed to each cell at any location in the tissue a lumped value of permeability to drug which is proportional to the local value of the electrical field. After that, by only considering the diffusion as an uptake mechanism, the mass-transfer equation (Eq. 2.2) was solved to find the concentration distribution of drug in the tissue in the reversible electroporation. The reaction rate (R) can be computed as $R = J(A_p / V_0)$ where A_p is the pore cross-sectional area of the permeable cells in each point of the tissue, $V_0 = (2r)^3$ is the volume of cube surrounded the cell, J is flux per area that can be estimated by using the Fick's law: $J = -P.(c_{ex} - c_{in})$ where P is the permeability of the drug molecules through the membrane pores.

$$\frac{\partial c}{\partial t} - \nabla(D\nabla(c)) = R \qquad (2.2)$$

More recently, Li and Lin have conducted a two dimensional numerical on molecular uptake via the electroporation (Li, et al., 2011). Although their work is the most comprehensive study on this topic, they have not considered the effects of different parameters such as surface electric charge of the cell membrane and intercellular concentrations of Na^+, K^+, and Cl^- ions in their simulations. Because of EDL overlapping through the generated nanoscale pores on the cell membrane, these parameters have significant influences on the electric field and the ion transportation through the nanopores.

Because of the transmembrane potential, the electrokinetic effects most probably play a role in the cell uptake during the electroporation. So far the electrokinetic effects on transport processes in nanochannels have not been investigated adequately. The created nanopores in the cell membrane during the electroporation can be viewed as the nanochannels. Extensive researches are required to understand the electrokinetic transport of fluid, ions, and macromolecules through the nanochannels.

2.2.3 Studies focused on optimizing and controlling of electric pulse during the cell electroporation.

Effect of the electric pulse shape on the electroporation efficiency is important. Different pulse shapes can generate various effects on the cell (Fox, et al., 2006). Some studies investigated the effect of different pulse shapes (Sinusoidal, step, and triangular) on the transmembrane potential and the number of the pores. For example, Talele et al. showed that as long as a threshold of the transmembrane potential is maintained by the electric field, the pore density is increases. They also showed that the bipolar pulses leads to the asymmetrical pore density between the two cell polar regions (Talele, et al., 2010). In 2010, Miklavcic and Towhidi proposed an analytical model to predict the effects of arbitrarily shaped electroporation pulses on the cell membrane conductivity and on the molecular transport across the cell membrane (Miklavcic, et al., 2010). Knowing electrical and diffusive properties of the cells and the specific dye, their proposed model can be used to optimize of the electroporation protocol.

Other studies in this category used feedback control techniques in order to reduce the side effects of the electric pulse on the cell structure. Experimental studies showed that the feedback control improves the electroporation efficiency of the single cells (Cukjati, et al., 2007; Khine, et al., 2007).

The feedback control can ensure the safe and accurate transfection during the reversible electroporation by monitoring the radii of the pores and the time duration for which the pores remain open. So far some experimental studies have been reported on the feedback control of the single cell electroporation (Cukjati, et al., 2007; Khine, et al., 2007). The interest of performing analytical studies on the feedback control of the cell electroporation increases recently. Because of nonlinear behavior of the cell electroporation, many conventional controllers cannot be exploited. One of the first analytical studies on the closed loop control of the cell electroporation was conducted by Zhao et al (Zhao, et al., 2010). Using nonlinear control techniques, they regulate the input voltage in order to stabilize the generated pore radii around the desired value. However, their design control theory is based on some nonlinear mathematical analysis that may be hard to implement. Other user-friendly control techniques (for example fuzzy logic) can be utilized to control the electroporation process.

2.3 Experimental Studies

In the current study, by going through the current microfluidic devices and their applications, we have classified the microfluidic electroporation devices as follows:

- The microfluidic electroporative devices that are used to perform the cell lysis and release the subcellular contents.
- The microfluidic electroporative devices that are utilized for inserting external molecules (transfection) such as DNA and Q-dots (Ho, et al., 2010) into the cells.
- The microfluidic electroporation utilized in other processes such as electrofusion, metabolism monitoring, and localization of Kinases within cells.

In this section, we focus on the current mechanical structure, mechanism and performance of the microfluidic electroporation. The technical, biological, and electrical properties of these microfluidic devices are summarized in Tables 2.1-2.3.

Table 2-1 Technical property of Electroporative Devices

Ref.	Materials	Focusing Type	Typical Size	Electrode Material	Electrode Distance	Flow Type
(Lu, et al., 2005)	Pyrex 7740	Geometry Variation	30μm~130μm	Gold	30 ~130 μm	PDF
(Wang, et al., 2006-a)	PDMS	Geometry Variation	33μm ~213μm	Pt Wire	far (~7mm)	PDF
(Wang, et al., 2006)	PDMS	Geometry Variation	25 μm~219μm	Pt Wire	far (~10mm)	EKF
(Wang, et al., 2006-b)	PDMC	Geometry Variation	33μm ~213μm	-	far (7mm)	PDF
(Wang, et al., 2008)	PDMS	Geometry Variation	62.5μm~500μm	Pt Wire	far(4~5mm)	PDF
(Bao, et al., 2010)	PDMS	Geometry Variation	58μm~5mm	Pt Wire	far(12~25mm)	PDF
(Kim, et al., 2007)	PDMS	Salt Bridge	40μm~500μm	Ag/AgCl	far	PDF
(Ikeda, et al., 2007)	Pyrex 7740	Geometry Variation	50μm~100μm	Pt/Ti	50 μm	EKF
(Khine, et al., 2005)	PDMS	Cell Trapping-Negative Pressure	3.1μm	Ag/AgCl	far	PDF
(Valero, et al., 2008)	silicon-glass	Cell Trapping-Negative Pressure	4, 20, 50μm	Pt Wire	~17 μm	PDF
(Wang, et al., 2007)	PDMS/glass	elastomeric valve	200μm	N/S	far	N/S
(Fei, et al., 2007)	PMMA	Cell Trapping-Negative Pressure	500μm	Silver	far	EKF
(Suzuki, et al., 2007)	Glass	Cell Trapping-Negative Pressure	2μm	N/S	far	PDF
(Cao, et al., 2008)	Silicon	-	80μm	Ti/Gold	50~100μm	PDF
(Sedgwick, et al., 2008)	PDMS	Cell Trapping-Dielectrophoresis	100μm	Ti/Gold	10μm	PDF
(Khine, et al., 2007)	PDMS	Cell Trapping-Negative Pressure	N/S	Ag/AgCl	far	PDF
(Luo, et al., 2006)	PDMS	Microfluidic Droplet	30μm~300μm	Au	20μm	PDF
(Zhan, et al., 2009)	PDMS	Microfluidic Droplet	60μm~386μm	Gold	20μm	PDF
(Huang, et al., 2003)	Silicon/glass	Cell Trapping-Negative Pressure	30μm~500μm	Pt/Cr	10~100μm	PDF
(Shin, et al., 2004)	PDMS	No focusing	100μm~500μm	Pt	far (2cm)	PDF
(Vassanelli, et al., 2008)	silicon	No focusing	-	Gold	150~300μm	No Flow
(Lim, et al., 2009)	glass	No focusing	10 mm	ITO	10 mm	N/S
(Lee, et al., 2006)	Silicon	No Focusing	-	Pt, Ag/AgCl	near	No Flow
(Valley, et al., 2009-a)	Glass	By Light	255μm	Virtual	near	PDF
(Zhu, et al., 2010)	PDMS	Hydrodynamics	50 ~ 150 μm	Ag	far	PDF

PDE: Pressure Driven Flow, EK: Electrokinetic Flow, PMMA: Polymethylmethacrylate, ITO: indium tin oxide electrode

Table 2-2 Electroporated cell properties

Ref.	Purpose	Species	Cell Type	Cell Size	Moving or stationary cells	Single or Multi Cells
(Lu, et al., 2005)	lysis	Human	HT-29	10 µm	Moving	Single
(Wang, et al., 2006-a)	lysis / transfection	Hamster	CHO	10-16µm	Moving	Single
(Wang, et al., 2006)	lysis	Bacterial	E. coli	N/S	Moving	Multi
(Wang, et al., 2006-b)	swelling / lysis	Hamster	CHO	10-16µm	Moving	Single
(Wang, et al., 2008)	transfection	Hamster	CHO	10-16µm	Moving	Multi
(Bao, et al., 2010)	swelling / lysis	Mouse	RBC, WBC , M109, CTC	-	Moving	Multi
(Kim, et al., 2007)	transfection	Human	K569	-	Moving	Single
(Ikeda, et al., 2007)	cell lysis	Plant	Zucchini Protoplast Cells	40-85µm	Moving	Single
(Khine, et al., 2005)	transfection	Human	HeLa Cell	10µm	Stationary	Single
(Valero, et al., 2008)	transfection	Mouse, Human	C2C12 , MSCs	-	Stationary	Single
(Wang, et al., 2007)	transfection	Hamster	CHO	10-16µm	Stationary	Multi
(Fei, et al., 2007)	transfection	Mouse	NIH 3T3	-	Stationary	Multi
(Suzuki, et al., 2007)	transfection	Human	HeLa Cell	-	Stationary	Multi
(Cao, et al., 2008)	electrofusion	Human, Plant	HEK-293, CMP	-	Moving	Multi
(Sedgwick, et al., 2008)	cell lysis	Human	A431 squamous cell	-	Stationary	Single
(Khine, et al., 2007)	transfection	Human	HeLa Cell	-	Stationary	Single
(Luo, et al., 2006)	transfection	Plant	Yeast cells	-	Moving	Single
(Zhan, et al., 2009)	transfection	Hamster	CHO	-	Moving	Single
(Huang, et al., 2003)	transfection	Human	ND-1 cell line	-	Stationary	Single
(Shin, et al., 2004)	transfection	Human	SK-OV-3	10µm	Moving	Multi
(Vassanelli, et al., 2008)	transfection	Hamster	CHO	-	Stationary	Single
(Lim, et al., 2009)	lysis	-	FITC-BSA-laden vesicle	1~50µm	Stationary	Single
(Lee, et al., 2006)	transfection	-	vesicle	10µm	Stationary	Single
(Valley, et al., 2009-a)	transfection	Human	HeLa cells	10 µm	Stationary	Single
(Zhu, et al., 2010)	transfection	Yeast	-	-	Moving	Single

CHO: Chinese Hamster Ovary Cell, RBC: Read Blood Cells, WBC: White Blood Cells, CTC: Circulating Tumour Cells, K569: human chronic leukemia cell, NIH 3T3: mouse embryonic fibroblast cell line, HEK-293: Human embryonic kidney cells HEK-293, CMP: plant cucumber mesophyll protoplasts C2C12 : Mouse myoblastic cells, MSCs: Mesenchymal stem cell, ND-1 cell line: Human prostate adenocarcinoma cells

Table 2-3 Electrical properties of the different electroporation microdevices

Ref.	Purpose	Pulse Type	Electric Potential range	Pulse duration	Frequency	Generated electric Field (KV cm^{-1})
(Lu, et al., 2005)	cell lysis	AC	6, 8.5 V	-	5, 10 KHz	0.204 ~ 4.65
(Wang, et al., 2006-a)	cell lysis / transfection	DC	0~200 V	10~100 ms	-	Up to 1.2
(Wang, et al., 2006)	lysis	DC	0~930 V	Up to 45 s	-	Up to 2
(Wang, et al., 2006-b)	swelling /lysis	DC	-	Up to 150 ms	-	Up to 1.2
(Wang, et al., 2008)	transfection	DC	41~110V	0.2~20 ms	-	0.3~0.8
(Bao, et al., 2010)	swelling /lysis	DC	-	100~300ms	-	Up to 1.6
(Kim, et al., 2007)	transfection	DC	7~20V	0.8~8ms	-	0.6~1.8
(Ikeda, et al., 2007)	cell lysis	DC*	up to 30V	-	-	-
		AC*	up to 70V	-	Up to 1MHz	-
(Khine, et al., 2005)	transfection	DC	0.51±0.13V	6.5ms	-	-
(Valero, et al., 2008)	transfection	DC	2V	6ms	-	0.67
(Wang, et al., 2007)	transfection	DC	200~1000V	20~30ms	-	
(Fei, et al., 2007)	transfection	N/S	N/S	500 ms	1Hz	0.035
(Suzuki, et al., 2007)	transfection					
(Cao, et al., 2008)	electrofusion	DC		20~50μs	-	3.7
(Sedgwick, et al., 2008)	cell lysis	AC	Up to 20V	N/S	100kHz~1MHz	1
(Khine, et al., 2007)	transfection	DC	0~1V	5~60ms	-	N/S
(Luo, et al., 2006)	transfection	AC	18 V		1kHz	-
(Zhan, et al., 2009)	transfection	DC	5~9V	0.37~21.6ms	-	-
(Huang, et al., 2003)	transfection	DC	10V	100ms	-	-
(Shin, et al., 2004)	transfection	-	-	10ms		0.25~0.75
(Vassanelli, et al., 2008)	transfection	DC	0.9, 1.3, 1.7 V	5ms, 10ms	-	-
(Lim, et al., 2009)	cell lysis	AC	2~5V	N/S	20 Hz~ 1kHz	N/S
(Lee, et al., 2006)	transfection	DC	up to 2 V	Up to 1.5 S	-	-
(Zhu, et al., 2010)	transfection	DC	0.5~2.5V	2.2~ 11.7 ms	-	0.65~1.87kVcm^{-1}

*There are two sets of electrodes in the system. The DC voltage is applied at the outer electrodes to generate the electroosmotic flow while the AC voltage is applied at the inner electrodes for cell lysis

2.3.1 Microfluidic electroporation devices for cell lysis (irreversible electroporation)

Analysis of the intercellular contents is essential for many biological cell studies. In the microfluidic electroporation devices, the cell lysis usually accomplish in the microchannels and under a dynamic flow field. This may facilitate the removal of subcellular contents and cell debris. One of the leading studies that suggested using continuous flow in the microchannels with varying geometry for the electroporation carried out by Lu et al. (Lu, et al., 2005). Figure 2.1 shows the schematic diagram of this microfluidic electroporation system. This system contains vertical saw-tooth electrode on the two opposite sides of the channel wall. By using the saw-tooth shape electrode, the induced electric field could be intensified periodically along the channel. The duration of these electric pulses is tuned by the flow field velocity and geometry of the electrode-channel system. This system utilize thick electrode that last longer in the corroding environment. In spite of the planar electrodes, the vertical electrodes can generate a uniform electric field in the system. This study also suggested using AC electric field instead of DC in order to reduce bubble creation and pH changes in vicinity of the electrodes.

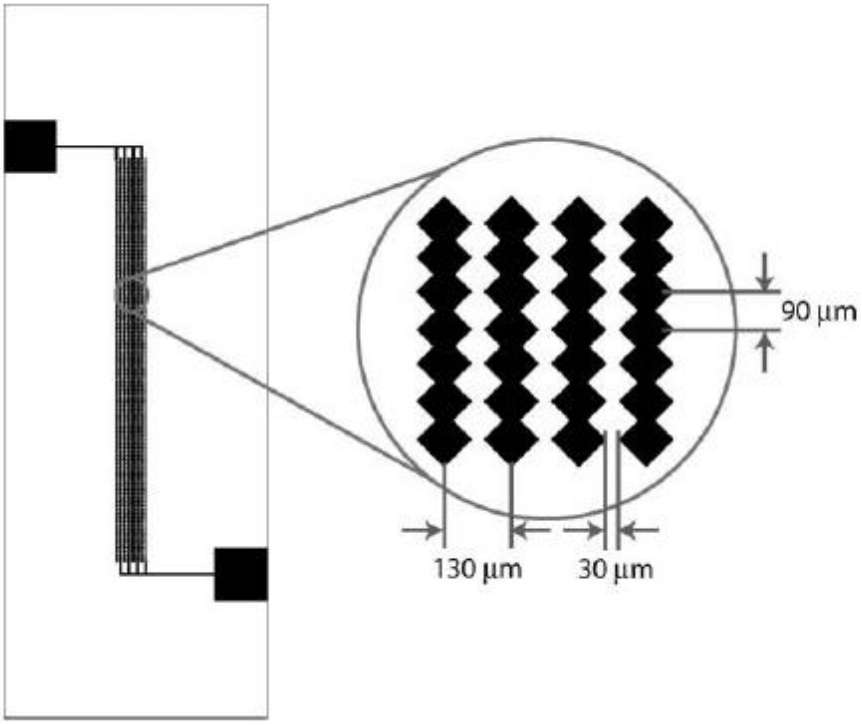

Figure 2-1 Schematic diagram and Dimensions of the electroporative device suggested by Lu et al (Lu, et al., 2005)

The more specific characteristics of the designed system and the electroporation mechanism proposed by Lu et al. (Lu, et al., 2005) have specified in Tables 2.1-2.3. Their results show that by applying a 6 V-AC electric field with 5 KHz frequency, 28% of cells are lysed completely while 81% of cells are partially lysed; their membrane did not disrupted completely and they just loss some parts of their organelles and Cytosolic material during the electroporation. In this system, the percentages of complete and partial cell lysis become 74% and 71% for a 8.5 V-AC electric field with 10 KHz frequency, respectively.

In 2006, Wang and colleagues proposed applying continuous DC voltage along the microchannel with variable cross-section for electric pulse generation (Wang, et al., 2006-a). Schematic diagram of this system has been show in Figure 2.2. The continuity of the electric current density leads to the stronger electric field in the narrower cross-sections of the channel. In this mechanism, the cell velocity and dimensions of the system can adjust the duration of the generated electric pulses. The

distinguished characteristic of this study is the direction of applied electric field. This is the first work that applies the electric field along the channel.

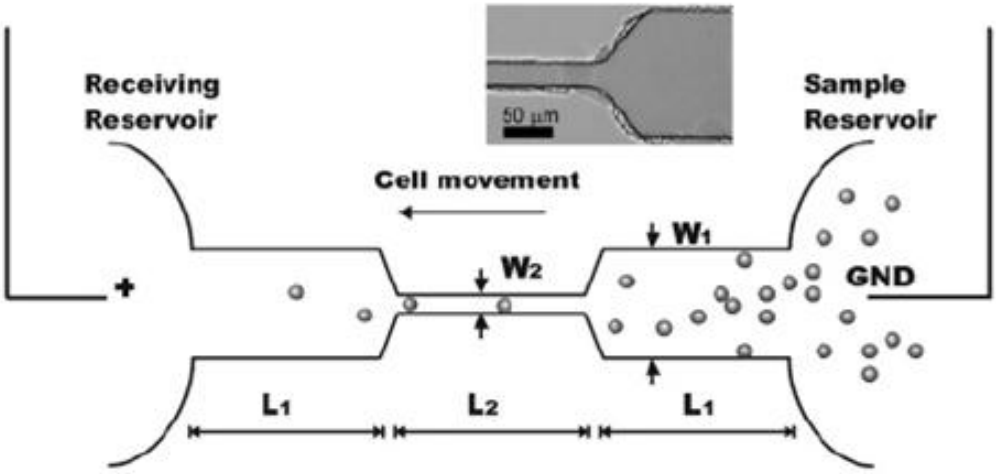

Figure 2-2 Schematic diagram of the electroporative device proposed by Wang et al. In the electroporative section, the cross-section area of the channels reduces in order to intensify the external electric field (Wang, et al., 2006-a).

The above mentioned mechanism proposed by Wang et al. (Wang, et al., 2006-a) has many advantages. Its auxiliary instruments are very simple. There is no need for pulse generator. It needs only a simple DC power supply and the pulse is generated by the geometric alteration. No microscale electrodes or subcellular structures needed. The low-cost and simple microfabrication procedure (such as soft-lithography) can be utilized to fabricate the chip. In addition, the narrow electroporative part of the channels allows performing the single-cell electroporation. This also presents the ability of on-line monitoring during the electroporation process. Above all, the presence of external electric field along the channel causes electrokinetic effects that can facilitate many pre- and post-processing requirements. For example, electroosmosis effect can generate the flow in the channels of the system, or electrophoresis force can be utilized to manipulate the cells in the system.

Using this system (figure 2.2), the electroporation carried out on Chinese hamster ovary (CHO) cells with diameters ranging from 10-16 μm. The results of this study include several parts. First, they

showed that the cells start expanding in the continuous electric field. In order to study the effect of electric field on the cell, they increased the electric field from 0 to 1200 V/cm. To study the internalization of dye SYTOX, they increased E (external electric field) while keep the pulse duration equal to 40ms. Their results showed that when E is below 400 V/cm, there is not any significant dye internalization or cell death. When E is higher than 400 V/cm, the cell electroporation is initiated. According to their findings, at E = 500 V/cm, about 56% of the cells are reversibly electroporated. In fact, the best efficiency of dye internalization takes place at E = 500 V/cm. Above this value, the rate of cell death is increased. At E = 800 V/cm almost all the cells are dead. This paper also includes studies on the effect of two main parameters affecting the cell viability in electroporation: the duration and the intensity of electric pulse. Based on their results, if E is less than 400 V/cm (the threshold of electroporation), the cell will be viable even for long duration pulses. For higher values of electric field, the cell viability is much more sensible to pulse duration. Their experimental results show that for E = 600 V/cm, almost all the intercellular contents will be depleted after 150 ms. The required time for complete cell lysis reduces to 60 ms for E = 1000 V/cm and 30 ms for E = 1200 V/cm. From the findings of this paper, one can concluded that for the cells with diameter ranging from 10 to 16 μm, if the applied electric field is between 0 to 400 V/cm, no electroporation will occur and almost all the cells will remain viable. Cell lysis starts at 600 V/cm. Cell internalization accomplishes at the applied electric fields between 400 V/cm to 600 V/cm. The best efficiency of the cell internalization will be happened at 500 V/cm and almost 56% of the cells remain viable after electroporation.

Using the mechanism proposed by Wang et al (Wang, et al., 2006-a), Bao and colleagues suggested conducting the selective intercellular release (Bao, et al., 2008). They showed that in general, Calcein was released at lower field intensities and shorter durations than did SykEGFP (72-kDa protein kinase, Syk, tagged by enhanced green fluorescent protein (EGFP) from chicken B cells). By tuning the electric pulse intensity and duration (which can be done easily by modifying the geometry and cell velocity), one specific intercellular contents can be released while the others remain in the cell.

Using their suggested electroporation microfluidic device (Wang, et al., 2006-a), Wang and colleagues could lysis one kind of bacterial cell, E-coli (Wang, et al., 2006). E-coli cell is much smaller than mammalian ones. Because the transmembrane potential linearly depends on the cell diameter, the E-coli cells required higher values of applied electric field for electroporation rather

than the mammalian cells. The results of this study show that the local electric field of 1000-1500 V/cm is required for nearly 100% cell death. In this range, the irreversible pores appear in the membrane of the cells that are sufficient for the cell lysis. They also showed that for the field strength higher than 2000 V/cm, the cell membrane completely disintegrated. The main difference between the mechanisms of this work and their previous work is the type of flow field. In this study, they suggested using electrokinetic effects to move the cells and generate flow field. By increasing the applied voltage to the system, on one hand the electric pulse is intensified, on the other hand the cell velocity increases and consequently the pulse durations is decreased (The pulse duration is calculated by the length of the electroporative section and the cell velocity). Therefore, there is only one degree of freedom in the system, which means that pulse magnitude and duration could not modify independently.

Figure 2.3 shows the schematic diagram of the electroporation device proposed by Ikea et al (Ikeda, et al., 2007). This system consists of two reservoirs that are connected by one flow channel. There is a pinched structure at the center of the channel. Two pairs of electrodes are used in this study. The outer electrodes locate at the end of channels (at reservoirs) and the inner electrodes situate at the center of the channels. The outer electrodes are used to generate the electroosmotic flow in the system while the function of the inner electrodes is to generate the required electric field for the electroporation. The pinched structure is used to capture the cells between two inner electrodes. Two different pinched structures were used in the system: triangular and trapezoidal. Because of point tips, the cells experiences much more electrical damage in the triangular structure than in the trapezoidal pinched structure.

In this study, the cell lysis was performed by both mechanical force (shear force) and electrical means. In their first step of the experiments, the triangular pinched structure was used. The voltage was only applied at the outer electrodes in order to generate the electroosmotic flow and drive the cells into the pinched structure. In this step, the cells were lysed by the shear force at the triangular pinched structure. Although their results show the effectiveness of this method, there are some limitations with this mechanism. Because the cell lysis is carried out by physical contact between the cells and the point tips of the pinched structure, the minimum cell diameter is restricted by the width of the triangular pinched structure. In this method, the flow field and cell movement are caused by the applied electric field. However, the applied potentials at the outer electrodes are restricted by the bubble generation and Joule heating. Because the outer electrodes is only used for flow generation

and does not have any contribution in the cell lysis, using other types of micro-pumps may be much more advantageous. In the second step, the voltage was applied at the both inner and outer electrodes.

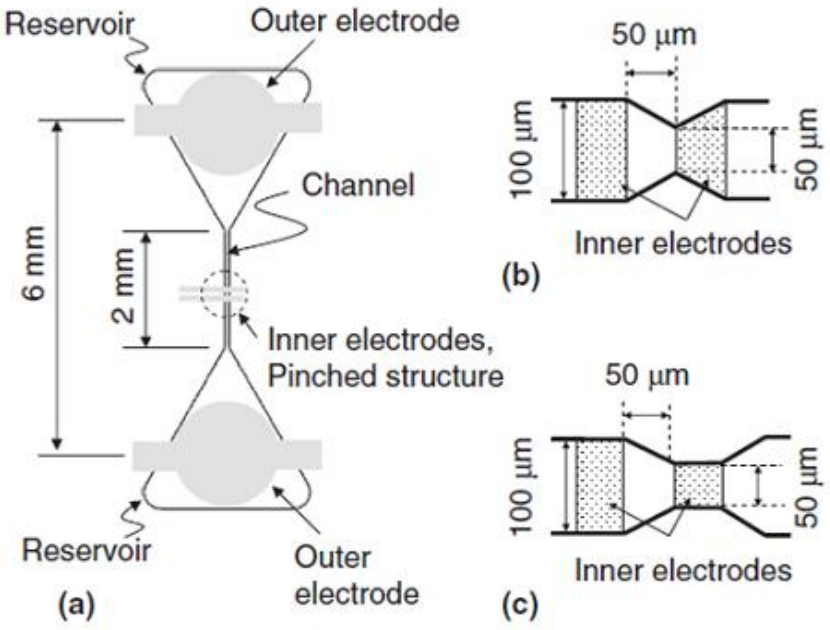

Figure 2-3 Channel structures of the microfluidic electroporation device proposed by IKEDA et al. for cell lysis (a) overview, (b) triangular pinched, and (c) trapezoidal pinched structure (Ikeda, et al., 2007).

The DC voltage at the outer electrodes causes the flow movement while the AC voltage applied at the inner electrodes resulted in the electrical cell lysis. In this step, both types of the pinched structure were utilized. The electrical parameters at the inner electrodes (applied voltage and frequency) were tuned in order to lysis the cells. The cell lysis was recorded at the frequencies of 5kHz to 1MHz. For one specific applied voltage, lower range of frequencies will result in the bubble generation while the cell can be lysed at the higher range of frequencies. They also experimentally showed that the larger cells will be electroporated at the lower ranges of applied voltages. This is because the transmembrane potential linearly depends on the cell diameter. It must consider that if the cell diameter is larger than the width of the pinched structure, the pinched type becomes important; in these cases, the physical contact can also play a role in the cell lysis. In the second method (when the voltage is applied at the inner electrodes) there is no restriction on the minimum cell diameter.

However, outer electrodes also does not have any influence on the cell lysis and should be replace by other types of micro-pumps in order to reduce the joule heating and bubble generation.

One of the first studies to use dielectrophoretic force for the cell trapping in the electroporation process was performed by Sedgwick and colleagues (Sedgwick, et al., 2008). Other studies have suggested trapping the cells in the fixed position during the cell transfection application by using negative pressure. The scheme of the system proposed by Sedgwick and colleagues is shown in Figure 2.4.

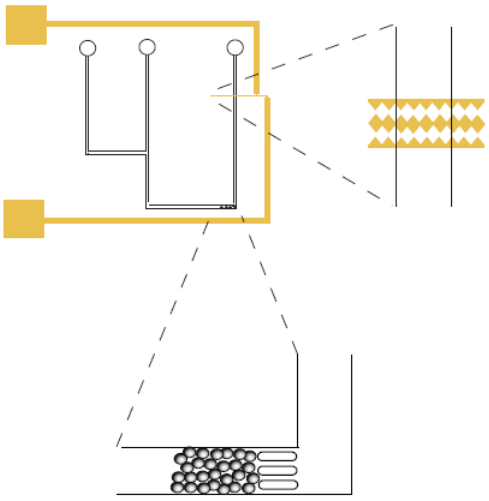

Figure 2-4 Schematic diagram of the electroporation microfluidic system proposed by Sedgwick and colleagues for cell lysis (Sedgwick, et al., 2008).

The system consists of two inlets and one outlet. One inlet is used for cell suspension and the other is used for buffer solution or microsphere injection. The microspheres are used for separation of subcellular contents. One saw-tooth gold microelectrode was positioned perpendicularly to the channel. The electrode exerts AC-voltage to generate dielectrophoretic force (for cell trapping) and to perform the cell lysis. The results show that 20 V-AC voltage with 1 MHz frequency can generate the required electrophoretic force to hold the cells against the flow field up to 30 mL/min and without performing cell lysis. Following the trapping step, the frequency was reduced to 100 kHz to perform the cell lysis. For one specific applied voltage, the cell will be trapped at a high frequency (for example 800 to 1000 kHz for 20 V). By decreasing the frequency, the dielectrophoretic force decreases while the cell lysis initiates (for example, at the applied voltage of 20 V and for the

frequency range between 200 to 80 kHz, both trapping and cell lysis take place simultaneously). By lowering the frequency, the dielectrophoretic force becomes weaker and can be neglected (For example at the applied voltage of 20 V and with 200 kHz frequency, the cells starts to lysis without trapping). At the very low range of frequencies and applied voltage, none of these effects will happen (for example, for the applied voltage below 13 V and for all ranges of frequencies). Their study recorded the cell expansion after trapping and before cell lysis. It was believed that this expansion is due to the osmotic pressure. In the post-processing step, the cell debris and subcellular contents are separated by using microspheres. Three obstacles were used in the channels to trap the microspheres. This section is used to separate the cell debris and its intercellular contents.

Another work that used the dielectrophoretic force to trap and fix the cells at the predefined positions was conducted by Lim et al. (Lim, et al., 2009). Figure 2.5 shows the schematic diagram of this system. There is an electrode at the lower wall of the channel that consists of sixteen 30 μm wide ITO (indium tin oxide) strips each having a thickness of 0.11 μm and separated by 120 μm bare glass. The upper wall is the uniform ITO-coated glass plate. Two types of electric field arrangement were applied to the system: normal (Figure 2.6) and co-planar (Figure 2.7). The distance between the upper and the lower walls are 10 millimeter. The FITC-BSA-laden vesicles are used to study the effectiveness of the proposed system for the cell lysis. The first step was to position the vesicles near the lower micro-pattern electrodes. To do this, the normal electric field arrangement (Figure 2.6) was utilized. The 2.0 Vrms AC voltage with the frequency range of 10 kHz~20kHz was applied in order to dielectrophoretically manipulate the vesicles and align them along the ITO electrode strips.

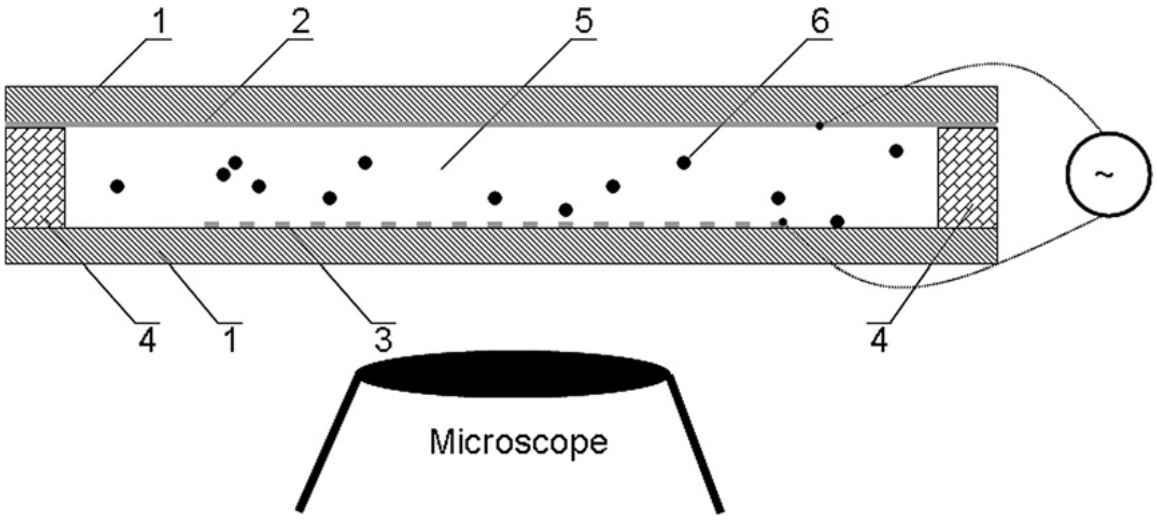

Figure 2-5 Schematic illustration of the microfluidic devices proposed by Lim et al for cell manipulation and electroporation The tagged sections are: (1) Glass slide. (2) Uniform ITO electrode coating. (3) Sixteen ITO microelectrode strips with 30 µm width and 120 µm inter-strip spacing. (4) One-millimeter thick polytetrafluoroethylene spacer. (5) Electrolyte solution. (6) Colloidal suspension (Lim, et al., 2009).

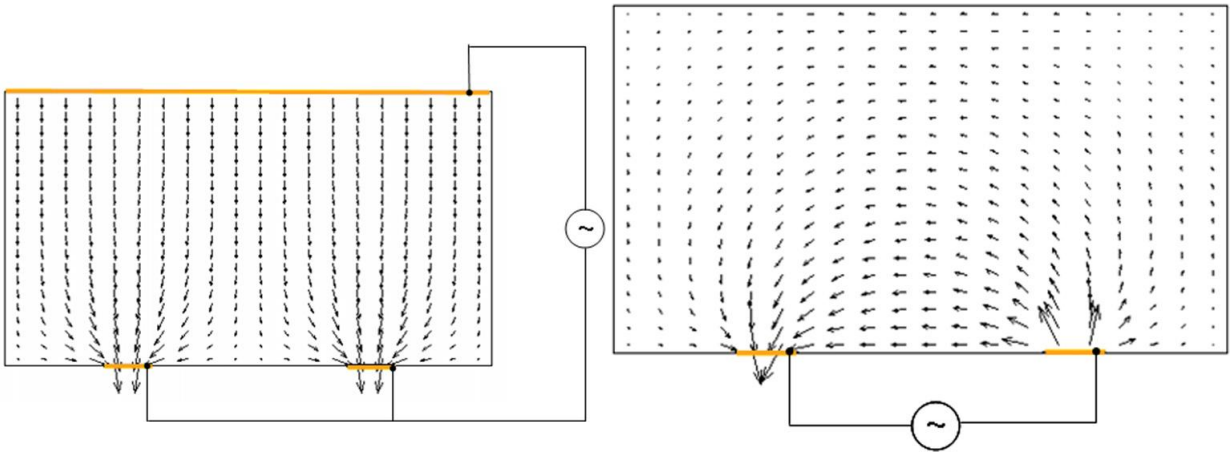

Figure 2-6 Normal (a) and Co-planar (b) field generator of the microfluidic electroporation devices depicted in figure 2.5 (Lim, et al., 2009)

For one specific applied voltage, the elevation of the trapped vesicles from the bottom surface was determined by the volume of the vesicle. After trapping the vesicles, the normal electric field (Figure 2.6(a)) was switched to the co-planar arrangement (Figure 2.6(b)) at 5 Vrms and 40 Hz to rapture the trapped vesicles.

The idea of using dielectrophoretic force to trap the cells during the cell lysis is beneficial. In this way, cells can be suspended and fixed in the flow field. During the cell lysis process, release of the intercellular contents is carried out with the flow to the desired position, while the cell debris can be trapped by the dielectrophoresis. In this way, the separation process can be carried out continuously.

Table 2-4 Electroporation and cell property of different transfection electroporation micro-devices

Ref.	Cell Type	Inserted molecule	Optimum State			Single or Multi Cell	Moving or Stationary
			Electrical Parameter	Transfected rate	Cell Viability		
(Wang, et al., 2006-a)	CHO	SYTOX Green	500 V	56%‡	-	Single	Moving
(Wang, et al., 2008)	CHO	SYTOX Green, PEGFP-C1	800Vcm^{-1} 1.1ms	80%	-	Multi	Moving
(Kim, et al., 2007)	K569	GFP*	7 V	20%	95%	Single	Moving
			20V	70%	50%		
(Khine, et al., 2005)	HeLa Cell	Trypan Blue	-	-	-	Single	Stationary
(Valero, et al., 2008)	C2C12 cells, MSCs	PI, EGFP, ERK1	-	> 75%	~100%	Single	Stationary
(Wang, et al., 2007)	CHO	DNA Dye SYTOX	279Vcm^{-1} 30ms	51%	70%	Multi	Stationary
(Fei, et al., 2007)	NIH 3T3	GFP and SEAP	35Vcm^{-1}	~40%	~90%	Multi	Stationary
(Suzuki, et al., 2007)	HeLa Cell	CFP-improtinβ	-	-	-	Multi	Stationary
(Khine, et al., 2007)	HeLa Cell	Calcein and Orange Green Dextran	-	-	-	Single	Stationary
(Luo, et al., 2006)	Yeast cells	Fluorescein	-	-	-	Single	Moving
(Zhan, et al., 2009)	CHO	EGFP	5.8V	11%	-	Single	Moving
			4.7V	-	68%		
			7.1V	-	14%		
(Huang, et al., 2003)	ND-1 cell line	YOYO-1, EGFP Green	-	100%	-	Single	Stationary
(Shin, et al., 2004)	SK-OV-3	PI dye, EGFP Green	-	-	-	Multi	Moving
(Vassanelli, et al., 2008)	CHO	LY	-	-	-	Single	Stationary
		TB	1.7V	100%	-		
		ODN	1.7V	100%	50%		
(Lee, et al., 2006)	Vesicle	-	1.7V	100%	-	Single	Stationary
(Valley, et al., 2009-a)	HeLa Cell	PI Dye†	1.5kVcm^{-1}	100%	100 %	Single	Stationary
(Zhu, et al., 2010)	Yeast cells		1.5V	70%	85%	Single	Moving

2.3.2 Microfluidic electroporation devices for cell transfection (reversible electroporation)

Cell transfection is the most important application of the microfluidic electroporation devices. Cell viability and transfection rate are the two most important indices that are usually used to compare the efficiency of these electroporation devices. The cells must remain viable after transfection, so the electroporation process must be reversible. In comparison with the cell lysis, the cell transfection usually takes place by lower applied electric field. Tables 2.1-2.3 show the technical, biological, and electrical properties of these microfluidic devices. Electroporation and cell properties of the different transfection micro-devices are summarized in Table 2.4. In the following sections, the reported experimental studies of microfluidic cell electroporation-transfection are reviewed in several groups.

2.3.2.1 Cell trapping based methods

One of the leading studies using a trapping section in electroporation in order to fix the cells in the predefined position was suggested by Khine and colleagues (Khine, et al., 2005). The manufacturing method of such a trapping section was proposed by Suzuki et al. (Suzuki, et al., 2007). Figure 2.7 depicts this electroporative system. At the center of the system, there is one circulation chamber that is connected to many microchannels in radial direction. The two main channels (wider channels) are used as the cell input and output. The other narrower microchannels are utilized as the trapping sections in order to fix the cells between the electrodes. The width of these trapping channels is 3.1 μm that is approximately one-third of the cell diameter. Using an external syringe connected to the trapping channels, 2 psi negative pressure is applied in order to trap the cells between the two electrodes hydrodynamically. One of the electrodes is connected to the main channel while the other is connected to the small channels (see Figure 2.7). In this system, the happening of the electroporation can be predicted by measuring the electrical parameters.

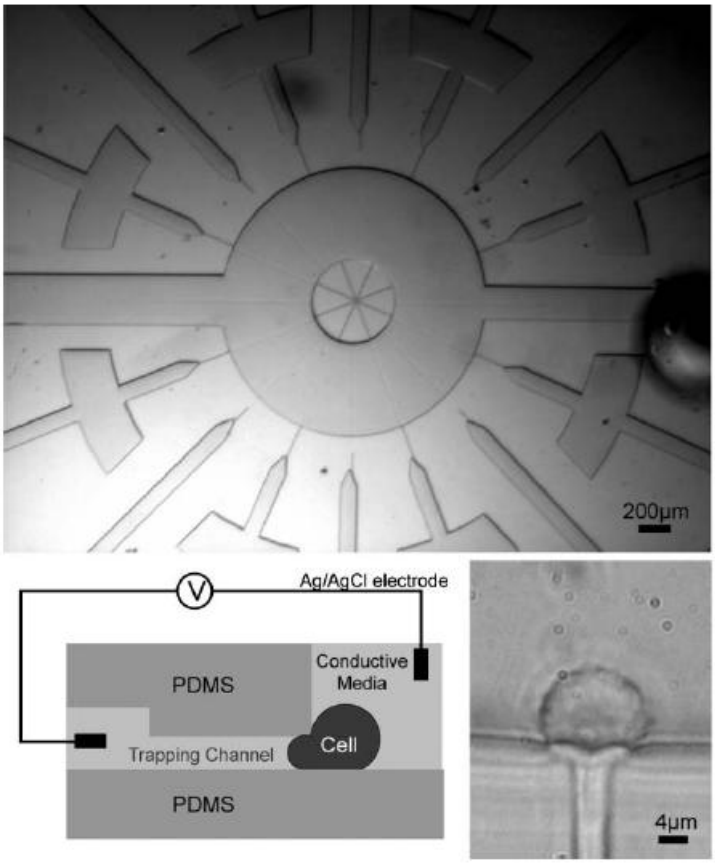

Figure 2-7 The image of the microfluidic cell transfection system proposed by Khine et al. The schematic diagram of the trapping section and the place of electrodes are shown. In this system, the negative pressure is induced to trap and fixe the cell (Khine, et al., 2005).

Figure 2.8 shows the electrical circuit of this system. The cell is modeled as the parallel combination of variable resistances and a capacitor. There is also R_{leak} in parallel with the cell which is because of the leakage around the cell. This parallel part is in series with the electrical resistance due to the microchannels and the electrodes. In this system, the trapped cell acts as a high resistance section which can be assumed as two in-series resistances due to the membrane inside and outside the trapping channel. Their images show that the cross section area of the membrane outside the trapping channel is 80 times bigger than the membrane inside the channels which means that the electrical resistance of inside membrane is 80 times bigger than the outside part (electrical resistance is inversely proportional to the surface area). This difference between the electrical resistances focus the

applied voltage over the inside membrane and generate the high electrical field required for electroporation in this part. According to the Ohmic law, voltage and electrical current in the system can be related by electrical resistance V = IR. Therefore, for constant voltage, changing in the electrical resistance can result in the electrical current variation. Disrupture in the membrane due to the electroporation can dramatically decrease the electrical resistance in the system which results in the sharp increase in the electrical current. Thus, by recording the electrical current, occurrence of the electroporation can be acknowledged. Using this method, the authors could reversibly electroporate the HeLa cells and the dye can be transfected to the cells by applying 0.76±0.095 V pulse with duration 6.5 ms.

The main issue that may affect the efficiency of the proposed method is the effects of cell deformation on the electroporation. In the paper, it is indicated that although for short pulses (50 ms) the membrane breakdown was dependent on tension in the membrane, at longer pulses (50–100 ms) the voltage required for the membrane breakdown was tension independent. By considering the pulse duration of this study (6.5 ms), further investigation must be pursued to study the effect of the generated shear tension on the membrane breakdown.

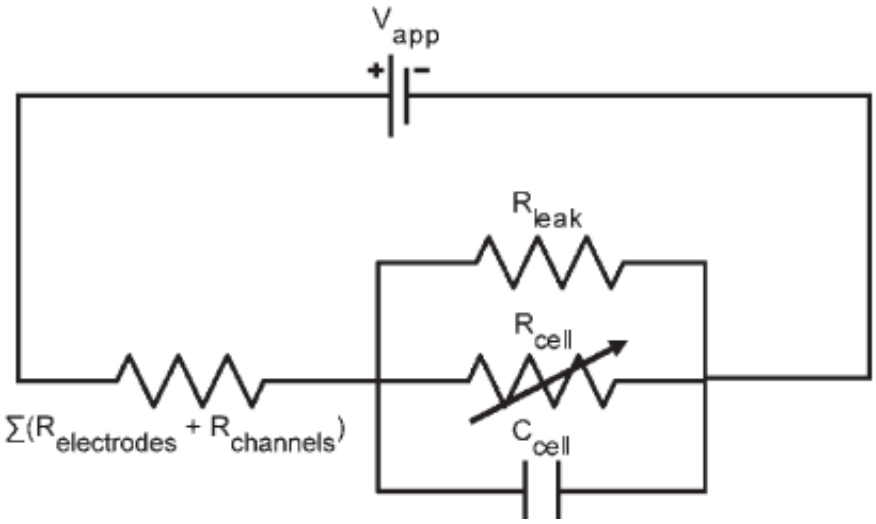

Figure 2-8 Electrical circuit model of the cell and chip in electroporation devices of figure 2.7 (Khine, et al., 2005)

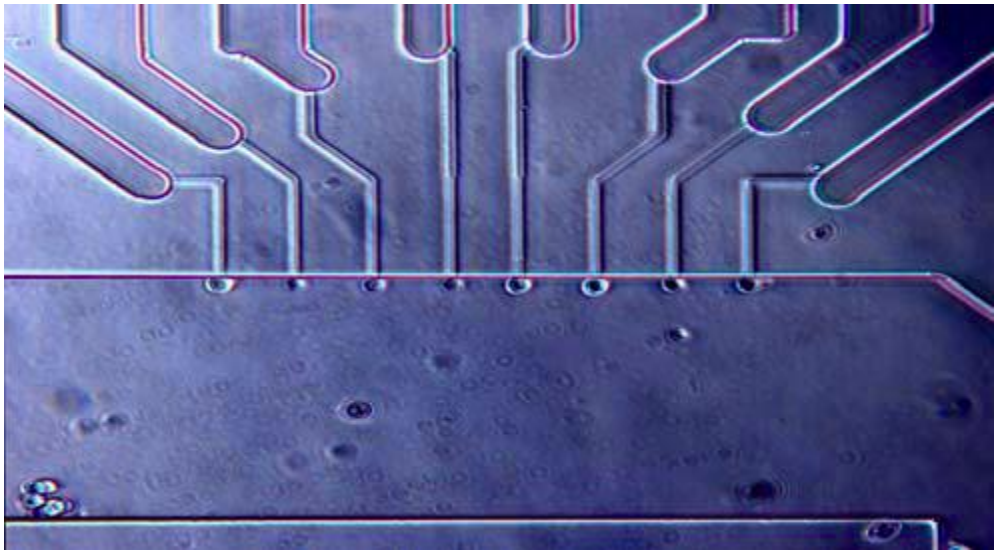

Figure 2-9 The layout of the mechanism suggested by Ionescu-Zanetti et. al. (Ionescu-Zanetti, et al., 2008)

Another study that used cell trapping to fix the cell in transfection process was performed by Ionescu-Zanetti et al (Ionescu-Zanetti, et al., 2008). Figure 2.9 shows the image of the system used in this study. They suggested using the electrophoresis effect in pre- and post-processing steps of the system proposed by Khine et al (Khine, et al., 2005) in order to decrease the required time of the process. The main idea of the system is shown in Figure 2.10. After trapping the cells, the electric field of 0 ~ 300mV is applied to the trapping channels in order to electrophoretically pre-concentrate the dye near the cell membrane (Figure 2.10.a). This electric field is considerably lower than the electroporation threshold (0.5 ~ 2V). After pre-concentrating, the cells can be electroporated by applied a large amplitude square wave (5 ~ 30 ms) while during the resealing period dyes can be loaded into the cells by electrophoresis mechanism and by applying the low electric field (for example 200 mV) in the system. By using this method, the required time for loading the dyes into the cell was reduced substantially. For example, Calcein could be transferred into the cell within 3 seconds, which took 16 s by diffusion alone. They also could load OGD into the cells within 40 s while this time is around 30 min without using electrophoresis effect.

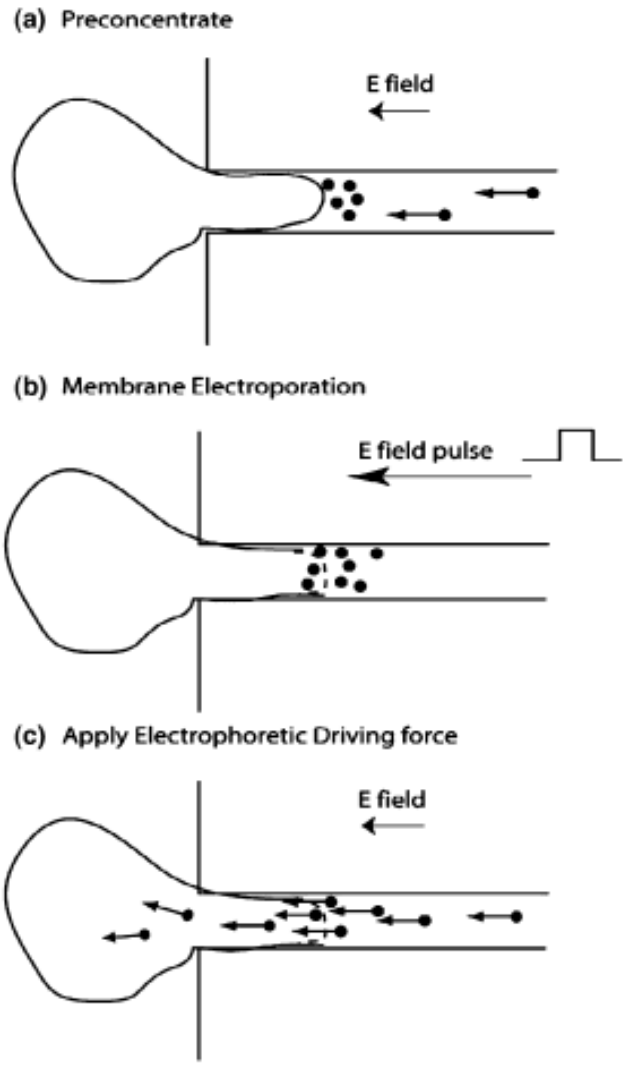

Figure 2-10 The schematic steps of the electrophoresis based electroporation device suggested by Ionescu-Zanetti *et. al.* (Ionescu-Zanetti, et al., 2008)

Using their proposed method (Khine, et al., 2005), Khine, et al designed an innovative feedback control system for reversibly electroporate the trapped cells (Khine, et al., 2007). This system is based on the measurement and monitoring the electrical resistance of the system. As discussed above, by performing the electroporation, the electrical resistance of the system is reduced substantially. In this study, by using the mechanism suggested by Cristian Ionescu-Zanetti (Ionescu-Zanetti, et al., 2008), the cell was trapped. They monitored the membrane resistance before, during, and after the electroporation to predict the electroporation happening and to monitor the membrane resealing after electroporation. In order to find the optimum electroporation condition, for various pulse durations

(5ms, 10ms, 30ms and 60ms), a voltage ranging from 0 V to 1 V was applied to the system with the increment of 0.1 V. As the electroporation happened, the sharp change in the electrical current appeared due to the reduction in the electrical resistance. By using this method, occurrence of the electroporation can be detected easily. The control program could stop the voltage increasing to avoid further disrupture in the cell membrane and significantly decrease the required resealing time for the membrane. After detecting the electroporation, a low-voltage (20 mV) was applied to the system in order to monitor the resealing kinetic of the cell. The resealing is complete when the electrical resistance recovers to its initial value. By using the feedback control suggested in this study, the resealing time can be reduced significantly; also, one specific cell can be reversibly electroporated repeatedly many times. Their results proved the fact that a shorter pulse width with higher intensity is required for electroporation. Shorter pulse width also results in the better membrane resealing. However, there is one problem associate with this method. Although by using this method the cell can reseal gently, it may not be enough time for dyes to transfect to the cell. To overcome this problem, the authors suggested using a pre-concentration method (Ionescu-Zanetti, et al., 2008).

Another innovative microfluidic device for transfection was proposed by Valero and coworkers (Valero, et al., 2008). Figure 2.11 shows the images of this system. As it can be seen, the system has two main parallel channels (with the width of 50µm and 20µm, respectively) that are connected to each other by nine channels (with the width of 4µm). These connecting channels serve as the trapping sections in order to fix the cells in the electroporative zone between the two electrodes.

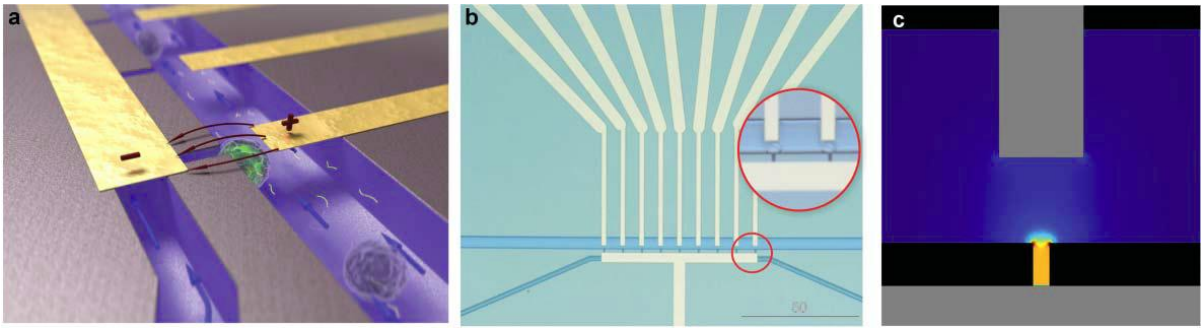

Figure 2-11 A single cell electroporation and gene transfection microfluidic device manufactured by Silicon and glass (a) 3D scheme of trapped cells; (b) Microfluidic chip picture, zoom-in on trapped single cells; (c) Electric field distribution at the trapping sites. Here, a voltage of 1 V yields electric field strength of 0.57 kV/cm (Valero, et al., 2008).

Each pairs of microelectrodes oriented at the opening of the trapping channels so that the electric field is focused on the trapped cells. The performance of each microelectrode is independent of the others. Hence, the cells that are not trapped or trapped at the neighbor channels may not be affected in the electroporation process of each individual cell. The cells and reagents flow through the upper main channel while the lower main channel is for producing the negative pressure in order to trap the cells at the opening of the connecting channels. The transfection process includes three main steps. First, the cell samples flowed along the upper channel, meanwhile the lower channel was creating a negative pressure (via a pump, 1-2 psi) to trap the cells at the opening of the trapping channels. After that, the pump was turned off and the DNAs were inserted into the upper channel in order to transfect to the cells. After 10 min incubating period, 1 V electric pulse with the duration of 6 ms was applied by the microelectrodes in order to generate the 0.67 kV/cm electric field to transfer the DNAs across the cell membrane. By using this method, they could perform transfection on the C2C12 and MSCs cells by applying a potential of 2 V for at least 6 ms. Their results show that the average transfection rate of their study is ~70% while they have a perfect cell viability (~100%).

2.3.2.2 Membrane Sandwich-based Microfluidic Electroporation

In a series of papers, Fei and colleagues proposed the membrane sandwich technique (MSE) for cell electroporation (Fei, et al., 2007; Fei, et al., 2010). This method suggested immobilizing and sandwich the cells between two polyethyleneterefthalate membranes (PET membrane) in order to improve the cell transfection and viability. Figure 2.12 shows the schematic of this system. The system consists of two crossing channels. One channel is located at the top and the other at the bottom of the system.

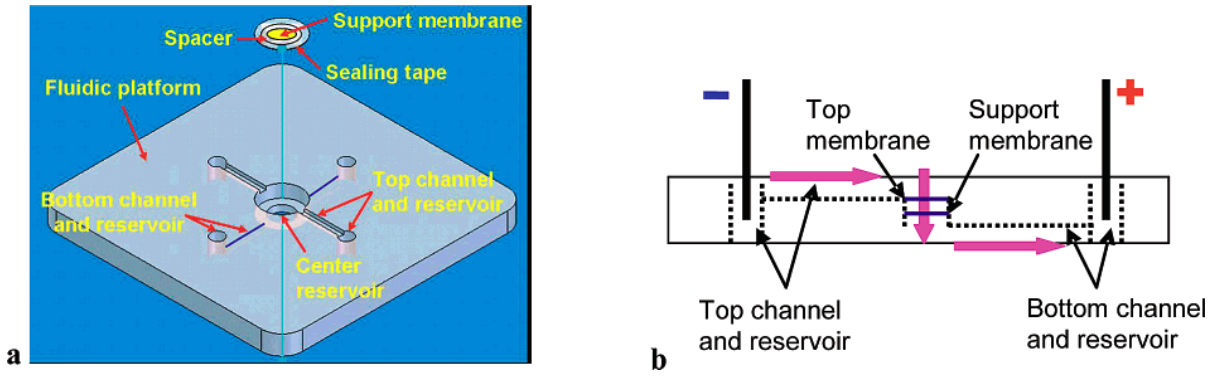

Figure 2-12 Schematic diagram of membrane sandwich electroporation (MSE) technique (Fei, et al., 2007)

One cuvette was placed at the intersection of the channels as an electroporation section. Figure 2.12-b shows the connection between the channels and the DNA migration path. The cells are sandwiched between the two membranes. A 3-mm-diameter PET membrane with an average pore size of 400 nm was used as the support for the cells. This membrane was fixed at the cuvette by a sealing tape. After that, the suspended cells (NIH 3T3) was loaded onto the supporting membrane and trapped on the supporting membrane by applying the 3 KPa vacuum pressure. Another 3-mm-diameter PET membrane with 3 µm pore sizes was added at the top of the system. The distance between the membranes is 10 µm. The electrodes located at the inlet and outlet reservoirs (see Figure 2.12-b). The DNA was loaded to the cathode reservoir. The electrodes have two tasks. First, 300 pulses with the duration of 5 ms and 100 Hz frequency were applied to generate the external electric field of 3.5 V/cm.

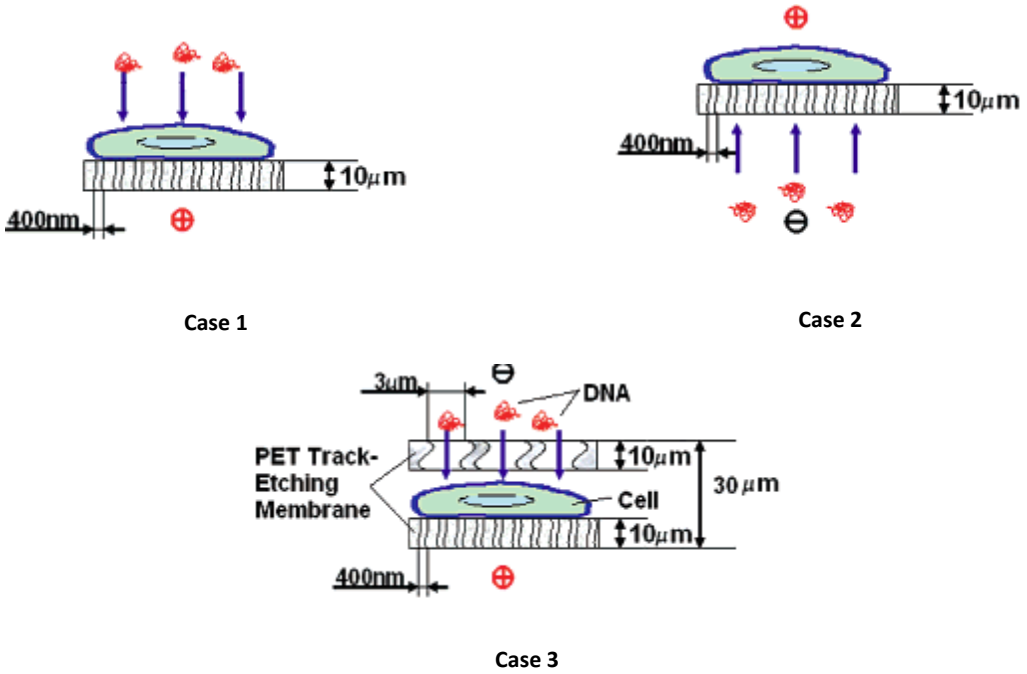

Figure 2-13 The orientation of cells and DNAs with respect to each other in three parts of the experiments accomplished by Fei et. al. (Fei, et al., 2007)

This external electric field caused electrophoresis force to move the DNAs from the cathode reservoir to the cell culture medium at the center of the system. After that, 5 pulses with 500 ms duration and 1 Hz frequency were applied to generate the 35 V/cm electric field to perform the electroporation. This system was utilized to transfect the plasmid GFP into the NIH 3T3. Two different experiments were performed and the results were compared with the conventional electroporation from the literature (see Figure 2.13).

The substantial improvement in the cell transfection was recorded compare to the conventional cell electroporation techniques. By using this method, the cell viability and transfected rates are 90% and 40%, respectively. In fact, the sandwich membranes prevent the diffusion of the DNA molecules from the membrane surface. After applying the external electric field, the membrane becomes negatively charged. This may repel the negative DNA molecules. The two negatively charged membranes trap the DNAs in the small volume near the cells and concentrate the DNAs near the cell membrane. This may result in the increase in the DNA transfection to the cell.

2.3.2.3 Polyelectrolytic Salt Bridges

Utilizing ionic bridge has been suggested in many microfluidics applications (Park, et al., 2009). Kim and collaborators suggested using ionic conductivity of polyelectrodytic gel electrodes for electric field concentration (Kim, et al., 2007) and cell electroporation. The microfluidic electroporator device was designed to work under a continuous low DC voltage (7~15 V). Figure 2.14 shows the schematic diagram of this mechanism. The two electrodes are placed in the hypertonic solution. A pair of pDADMAC plugs on both sides of the microchannel separates the cell suspension and the hypertonic solution. The pDADMAC plugs have a good ionic conductivity. The chip was designed to have low impedance so that a large portion of the potential difference is applied at the cell solution.

In this paper, the pDADMAC plugs and the hypertonic solution have the identical ionic conductivity (equal to 16 Sm-1) while the ionic conductivity of the cell media solution is 10 times more resistive. This difference leads to concentrate the electric field on the cells. By using this method, they could generate an electric field of 0.9 kV/cm over the microchannel with the input voltage of only 10 V. This value of the electric field is sufficient for performing electroporation of K562 human chronic leukemia cell.

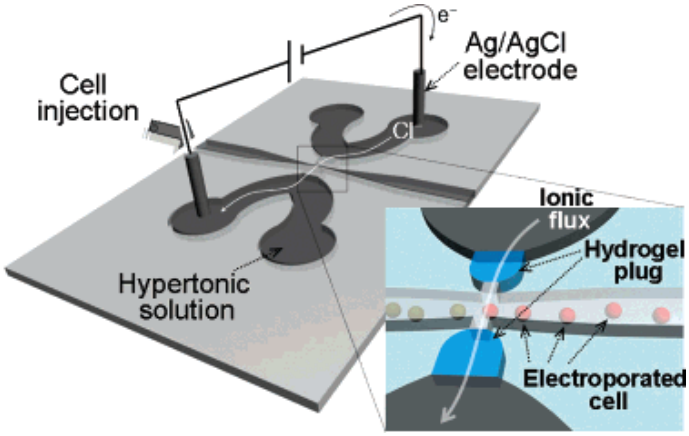

Figure 2-14 The schematic of the micro-electroporation chip that use ionic conductivity of polyelectrodytic gel electrodes for electric field concentration. Cells experience an electric field gradient by passing through the region between the salt bridges (Kim, et al., 2007).

In this study, the electroporation efficiency is defined as the number of live permeated cells divided by the number of live cells after electroporation. The viability is defined as the ratio of live cells to dead cells. For a constant cell velocity at 3.2 cm/s, they investigated the effects of input voltage on the electroporation efficiency and the cell viability. Their results show that increasing the input voltage from 7 to 20 volts results in increase of the efficiency from 20% to 70 %; however, it also brings about the cell membrane damage that decreases the cell viability from 95% to 50%. One important parameter in the cell electroporation is the pulse duration. This paper also includes some results of the effect of pulse duration on the electroporation. By increasing the cell velocity from 1 cm/s to 8 cm/s (which results in decreasing the pulse duration), the cell viability is increased from 70% to 95% while the electroporation efficiency dramatically decreases from 75% to 15% (Input voltage is constant and equal to 15 V).

The method of this study has some advantages: There is no bubble generation, heating shock, and chemical contamination associated with this method. The main reason for these positive points is that the electrodes are placed in the buffer solutions that are completely isolated from the electroporative section and the cells. However, there is one limitation associate with the method. The pDADMAC plug has the tendency to swell as it absorbs water. This plug expansion can be high enough to block the microchannel.

2.3.2.4 Using Mechanical Valve

Using mechanical valves in the microfluidic electroporation devices was presented by Wang et al (Wang, et al., 2007). The scheme of the experimental system of this study is shown in Figure 2.15. The system consists of fluidic channel (black one), control channel (gray one), DC power supply, solenoid valve, and control unit. There is a PDMS membrane between the fluidic and the control channels. Constant DC voltage is applied to the system by power supply. The valve is located in the vertical fluidic channel (channel 1), while the horizontal fluidic (channel 2) is used as the cell culture channel. If the electrical pulse with proper duration and intensity is applied in the fluidic channel, the electroporation can be performed on the cells in this channel. The electric pulse was generated by the control channel that turns on and off a DC electric field by physically connecting and separating the ionic buffer. The solenoid valve controls the operation of the control channel (gray one). The roll of the valve is to pressurize the PDMS membrane between the fluidic and control channels to block the fluidic channel 2, and hence the electrical current in fluidic channel 2. If the valve operates in a close-open-close sequence, the electrical pulse can be generated in the fluidic channel 2 to perform the electroporation.

Several parameters can affect the performance of this system: control channel width, actuation pressure (inserted by Solenoid valve), valve opening time, and applied constant DC voltage. The authors tested different values of these operating parameters and finally used the control channel with a width of 300 μm and applied 40 psi pressure for 30ms opening time. By using these parameters, they could reversibly electroporate the CHO (Chinese hamster ovary) cells and insert the SYTOX green into the cell. At optimum condition (electric field with 30 ms duration), the transfection rate and the cell viability are 51% and 70%, respectively.

This system is based on the insulating nature of the PDMS valve (membrane). It was indicated in the paper that long time contact between the PDMS and culture media can weaken the PDMS insulating property; therefore, they used a triangular structure between the fluidic channels 1 and 2 in order to completely separate the culture media (in fluidic channel 2) and the PDMS valve (fluidic channel 1).

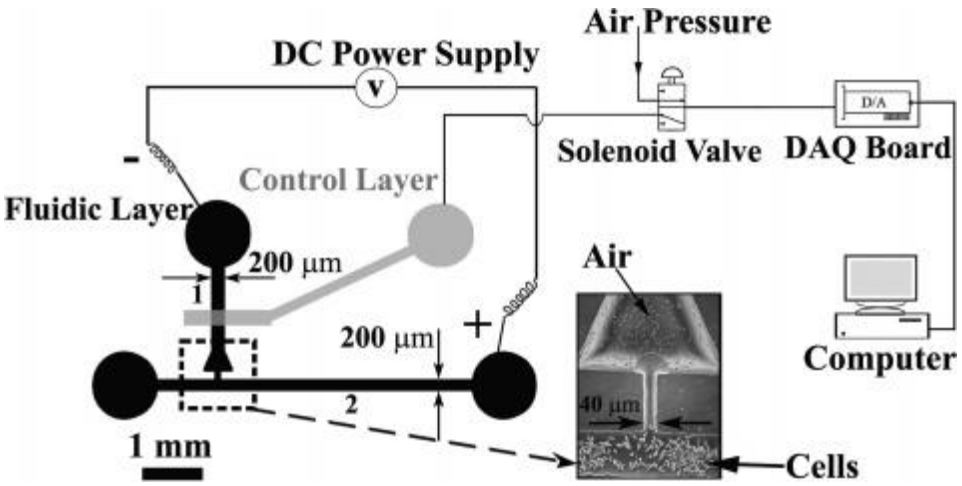

Figure 2-15 The schematic diagram of the electroporation microfluidic device that use mechanical valve for cell transfection (Wang, et al., 2007).

The main advantage of this device is its ability to electroporate the cells in the culture media and electroporate the adherent cells. The electroporation of the cells that adhere to the substance is desired because of the minimum defection to the cell culture. There are also some disadvantages of this method: First, the moving part and the limitation associate with it such as fatigue and vibration. In addition, this system is based on the insulating property of PDMS valve that can be weaken over time. Furthermore, the manufacturing process of this system seems not easy. Finally, the applied voltage to this system (200~1000 V) is considerably higher than the applied voltage (up to 100 times) in the other proposed electroporative systems. This high voltage can cause bubble generation, significant Joule heating effect, and also requires more safety measures.

2.3.2.5 Single cell electroporation microarray

Vassanelli and colleagueas (Vassanelli, et al., 2008) developed a new chip to conduct electroporation of single cells attached to the growing surface. Figure 2.16 shows the schematic of this chip. This chip has an array of 60 circular cell-size microelectrodes. The microelectrodes are connected to the external circuit by a metal line that is covered by a 200 nm layer of amorphous silicon nitride (Si3N4) to be insulated from the extracellular electrolyte. The electric potential can be applied to the cells via the circular gold layer at the ends of electrodes. The diameter of these free surfaces varies from 15μm to 50μm while the distance between microelectrodes was either 150μm or 300μm. The duration and the intensity of the applied voltage at each microelectrode can be controlled individually. In this way, each target cell can be directly electroporated in situ. There is no need for cell detachment and

harvesting that can be harmful to the cell structure. Instead, the pre-programmed control system activates the microelectrodes near the target cell to electroporate it. The time of electroporating each cell can also be different from the others. This may lead to the sequence electroporation of single cells. The cells may be electroporated many times while the different molecules are delivered to the cell.

By using this chip, the different molecules (LY, TB abd 24 nt ODN) were inserted into the Chinese hamster ovary cell by performing the reversible electroporation. The train of five 10 ms pulses was applied to the target cells. Below the applied voltage of 0.9 V, no uptake was recorded. Increase of the voltage from 0.9 V to 1.3 V leads to the improvement of the transfection of LY and TB. Above 1.3 V, ODN was also started to enter to the cell. At 1.7 V applied voltage, the uptake efficiency of ODN was about 70% while 100% efficiency was recorded for LY and TB.

In comparison with the other methods, there are many advantages associated with the proposed technique by Vassanelli et al. (Vassanelli, et al., 2008). First, the required voltage is relatively low. The transfection could be performed by applying only 0.9 V~ 1.7 V DC voltage. There is no need to detach and harvest the target cells. There is no restriction on the time for electroporating the cells in one specific culture medium. The cells can be electroporated independently from the others. The sequence electroporating of one specific cell could also be performed by this method. However, it was claimed in the article that this technique cannot be applied to the cells in a tissue.

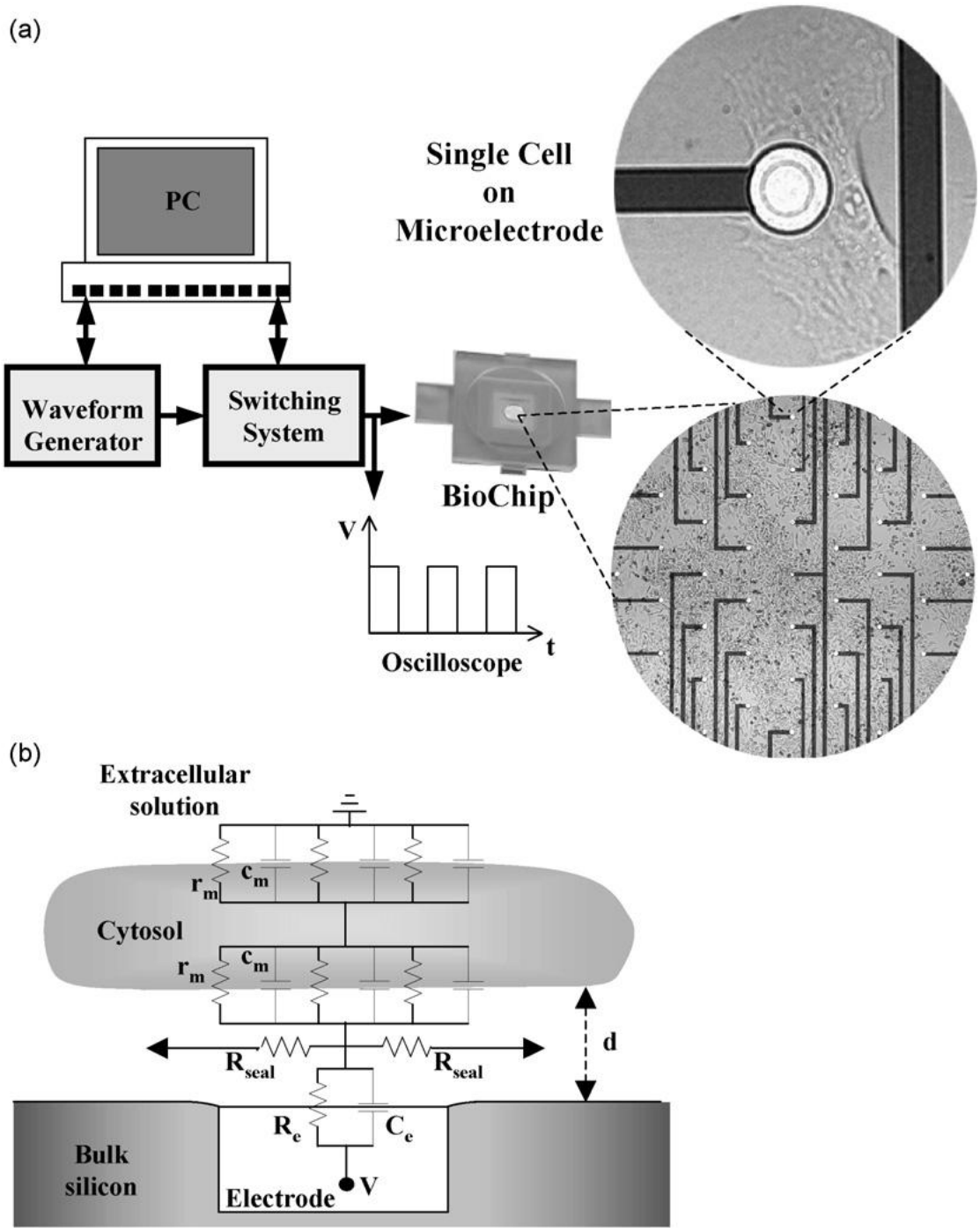

Figure 2-16 (a) Schematics of a BioChip device and its control system used microarray for single-cell electroporation. The control system driven by a personal computer. (b) Equivalent electrical model of the coupling between cell and chip (not to scale) (Vassanelli, et al., 2008).

2.3.2.6 Droplet Microfluidic Electroporation

The idea of using microfluidic droplet electroporative devices was first suggested by Luo et al. (Luo, et al., 2006). The device can electroporate the yeast cells encapsulated in the droplets. Following this study, Brouze and colleague presented a droplet-based microfluidic technology that shows the feasibility of high-throughput screening of single mammalian cells (Brouzes, et al., 2009). They could encapsulate the single cells and reagents in the independent aqueous micro-droplets and also manipulate and monitor the droplets. A critical study on the microfluidic droplet electroporation was conducted by Zhan et al (Zhan, et al., 2009). The schematic diagram of this electroporative device is shown in Figure 2.17. The chip has two inlets and one outlet. The inlets are connected to two reservoirs to supply non-conductive oil and the mixture of cells and ionic conductive buffer solution, respectively. First, the cells were encapsulated in the aqueous droplets flowing in the oil. In the downstream, the flow went through a pair of microelectrodes that apply a constant DC voltage to the system.

Because the oil is non-conductive, the cell experienced a transient electric pulse whose shape and duration depend on the velocity and dimensions of the droplet, electrical parameters of the system, distance between the electrodes, and location of the encapsulated cell in the droplet (see Figure 2.17). In this study, the velocity and dimensions of the droplets and also the distance between the electrodes are 1.38~8.86 m/min, 60~386 μm in the length, and ~ 20 μm, respectively. The main drawback of the droplet microfluidic electroporation is the effect of oil on cell viability. This study recorded 11% cell death due to the contact between the cells and the oil droplet. The percentage of viable cells dropped from 68% to 14% by increasing the applied voltage from 4.7 V to 7.1 V. By using this method, a plasmid vector coding EGFP could be transfected into CHO cells with the applied voltage of 5.8 V and the electroporation zone transit time of 1.8 ms.

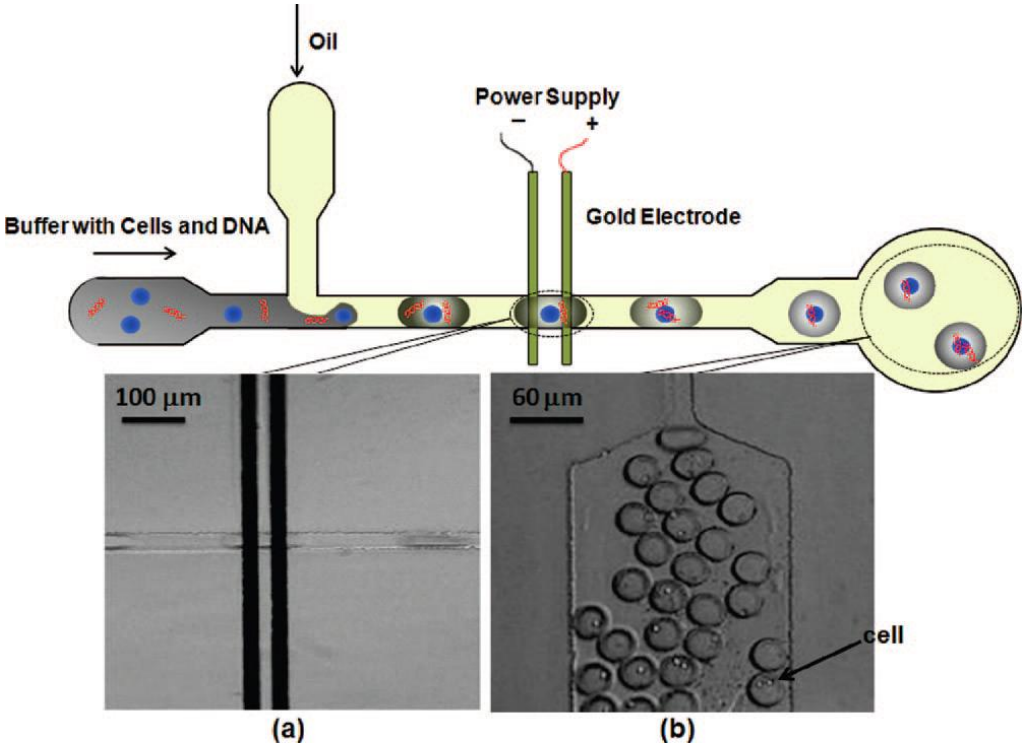

Figure 2-17 Schematic diagram of the droplet-based microfluidic electroporation. Parts (a) and (b) are the images of the droplets at different sections of the system. (a) The electroporation section that the droplets rapidly flow through the two microelectrodes on the substrate (each electrode was 25 µm wide, and the distance between the two electrodes was 20 µm). (b) Exit reservoir of the system where the droplets with encapsulated cells collected there after electroporation (Zhan, et al., 2009).

2.3.2.7 Optofluidic-based Microfluidic Electroporation Device

Recent studies proposed using optofluidic technology in biology (Brennan, et al., 2009) and cell study (Sott, et al., 2008; Lin, et al., 2009). In the series of papers, Valley et al. proposed using a photosensitive surface and patterned light to create virtual electrodes to manipulate and electroporate single cells (Valley, et al., 2009-a; Valley, et al., 2009-b). The main advantage of this method is the ability to perform in situ electroporation. Figure 2.18 schematically illustrates the device. It consists of two glass substrates coated with a layer of the transparent conductor indium tin oxide (ITO). The bottom substrate is coated with a photosensitive film (a-Si:H). A layer of lithographically patterned SU-8 defines the channel geometry and serves as the spacer between the top and bottom substrates. The space between the two substrates is filled with a solution containing the cells of interest. The two

ITO layers were used to apply an AC voltage to the system. In the absence of light, most of the electric field is concentrated across the highly resistive photoconductive layer. However, upon illumination, the resistance of the photoconductive layer (in the illuminated areas) decreases by many orders of magnitude due to creation of electron-hole pairs. This causes the majority of the electric field to be applied to the liquid layer wherever the device is illuminated. Therefore, if an object, such as a cell, is illuminated, the electric field will be concentrated on it. The optical power density required to operate the device is low (1 W/cm) that can be supplied by a standard projector. Therefore, the simplicity of the supporting equipment is another advantage of this method. They showed that 0.2 kV/cm AC electric field with 100 kHz frequency could produce the required dielectrophoretic force to manipulate and trap the HeLa cells in the predefined positions. By intensifying the electric field to 1.5 kV/cm, the cells could be reversibly electroporated. Their results show the high efficiency of the proposed method, the cells could be electroporated individually while the surrounding cells remain intact. Therefore, the single cell electroporation can be performed with very good efficiency.

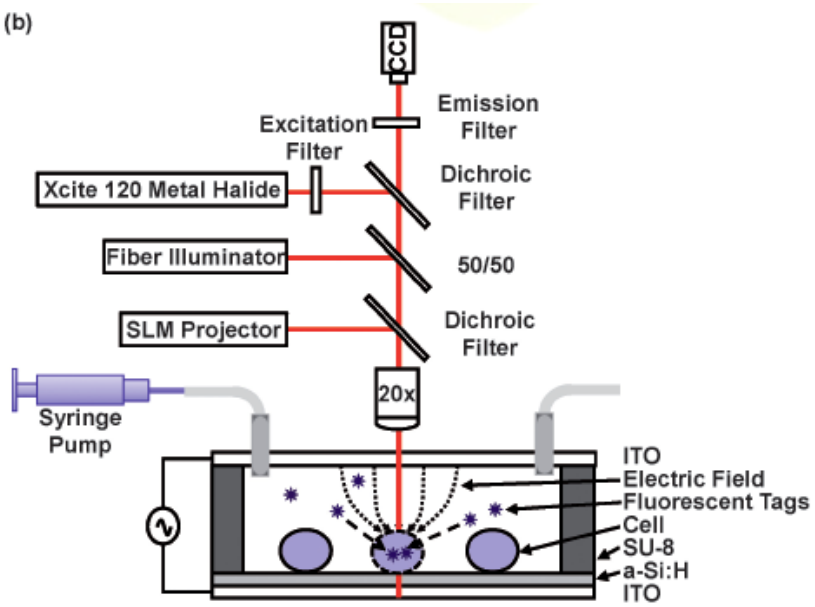

Figure 2-18 Cross section of the Optofluidic-based microfluidic electroporation Device. Experimental setup and mechanism of the light-induced electroporation system are demonstrated. The electric field concentrates across the illuminated cells by creating the virtual electrodes near the cell membrane (Valley, et al., 2009-a).

2.3.2.8 Cell Transfection in Continuous Flow in Microchannels

Wang et al used the electroporation device reported in their previous studies (Wang, et al., 2006; Wang, et al., 2006-a; Wang, et al., 2006-b; Wang, et al., 2008) to insert the SYTOX green dye and pEGFD-C1 protein into the Chinese hamster ovary cell (see Figure 2.2) (Wang, et al., 2008). The constant voltage was applied along the channels while electric pulses were generated by the geometric variation of the microchannel. Their results show that the percentage of viable cells is increased up to the field intensity of 500-600 V/cm. For higher field intensities, the pulse duration must be lower than 6 ms in order that the cells are viable. According to their results, if the electrical parameters are tuned properly in the system, increasing the number of narrow sections (and hence the number of pulse and pulse duration) in the microchannel improves transfection efficiency (see Figure 2.19). For example, the device with five 700 V/cm pulses and the durations of 0.22 ms has the transfection efficiency of 21.2 %; while this efficiency is 14.4% for the device with one 1.1 ms pulse.

In another their study, they showed that the cells started "growing" immediately when electroporation began (Wang, et al., 2006-b). It may be caused by the difference between the permeability of the ions and larger-molecules (macro- molecules) inside the cell. In this study, the mechanism suggested in their previous studies (Wang, et al., 2006-a) was used to study the cell swelling and the cell rapture. For the first several hundred mili-seconds, the cells were exposed to the electric field of 200-500 V/cm.

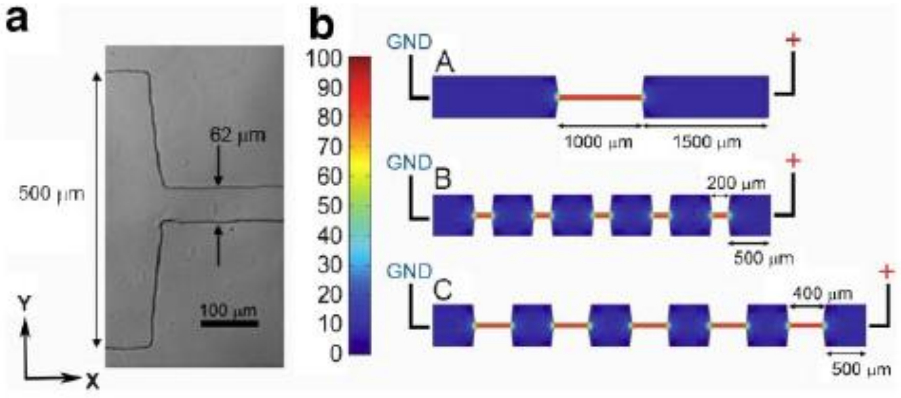

Figure 2-19 The field intensity in electroporation microfluidic device that utilize cross sectional geometric variation to generate electric pulse (Wang, et al., 2008)

They used three different buffer solutions (with 8 mM Na2HPO4, 2 mM KH2PO4, sacrose of various concentrations (hypotonic: 125 mM, isotonic: 250 mM and hypertonic: 375 mM), and pH value of 7.4). In these solutions, the increase in the cell volume was observed and the swelling rate and the rapture of cell membrane in the real time at single cell level were recorded.

For external electric field of 400 V/cm, Figure 2.20 shows the swelling of one CHO cell at different points of electroporation sections of the device and at different time. The cell velocity is 0.1~1 mm/s and the buffer solution is isotonic. This figure shows the cell growth in the presence of electric field. Their results show that the swelling and the membrane rapture occurs more rapidly in hyper- and hypotonic buffers than in isotonic buffer. For example, for the field intensity of 400 V/cm and isotonic buffer solution, there is 128% increase in the average percentile of the cell diameter after 300 ms; while this value is 149% and 145% in the hypotonic and hypertonic buffer solutions, respectively. The results show that the swelling rate is more considerable in hypotonic than hypertonic solution. They assumed that the swelling is because of water influx into the cells when the nanopores are open. Based on this assumption, they concluded that the nanopore density and size are higher in hyper- and hypotonic solutions. Therefore, hyper- and hypotonic buffer could contribute to the increased delivery of biomolecules into the cells. However, there is another theory for the swelling modeling rather than the water influx that will be explained later.

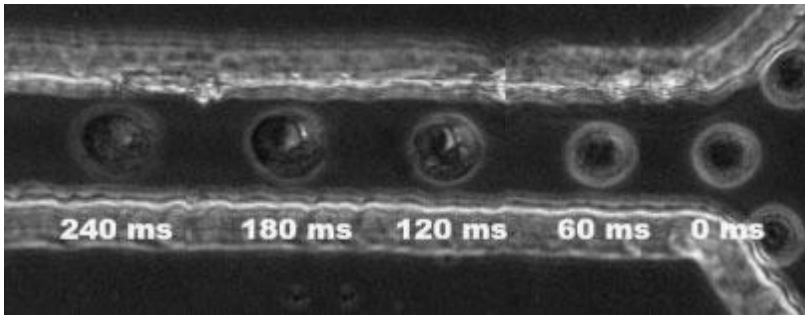

Figure 2-20the time-sequence images of the same CHO cell flowing in the isotonic buffer (10mM phosphate and 250mMsucrose; E2=400 V/cm). The images were captured at a rate of 16 Hz. The velocity of the cell was in the range of 0.1–1 mm/s (Wang, et al., 2006-b).

Using the proposed techniques by Wang et al (Wang, et al., 2006-a), Geng et al delivered genes into CHO cells at high flow rates (up to ~ 20 mL/min). With the optimal design, ~75% of the viable CHO cells were transfected after the procedure (Geng, et al., 2010; Schaper, et al., 2007). Bao et al utilized the electroporation microfluidic device proposed by Wang et al (Wang, et al., 2006-a) to electroporate blood cells (Bao, et al., 2010). These cells are circulating tumour cells (CTC), red blood cells (RBC), and white blood cells (WBC). CTC refers to the cells that detached from the primary tumour. They are circulating in the blood stream and may settle down at a secondary site and from metastases. Their results show that there are significant differences in the threshold electric field for the irreversible electroporation of these cells. For example with the pulse duration of 100~300 ms, the irreversible electroporation was occurred at 300~ 400 V/cm, 400~ 500 V/cm and 1100~ 1200 V/cm for M109 tumour cells, white blood cell and red blood cell, respectively. These differences could lead to the selective electroporation in the stream of blood cells. The difference between the cell diameters is the reason of these different threshold values. For the identical external electric field, the cells with the bigger radius have the higher transmembrane potential and are easier to be electroporated at lower external electrical field.

This paper of Bao and colleagues (Bao, et al., 2010) also includes some interesting results on the swelling of cells during the electroporation. Using the coherent anti-Stokes Raman scattering (CARS) microscope and fluorescence microscopy tools, they could observe the subcellular changes during the swelling. Their results show that the major part of the swelling is due to nucleous expansion. According to their results, the nucleus of the cell starts expanding upon applying the external electric field; if the applied electric field is removed, the nucleus will shrink. Under 400 V/cm applied electric field, Figure 2.21 shows their captured images in different times.

For 400 V/cm external electric field, they also have depicted the separate rates of the nucleus and cytoplasm expansion versus time (see Figure 2.22). This diagram shows that the cytoplasm approximately remains unchanged during the electroporation. According to their findings, they suggested one of two possible mechanisms (that are potentially mutually exclusive) to be responsible for the cell expansion during electroporation. However, they could not conclude that which one of these two theories is true. First, the expansion is due to solution influx into cells, as suggested in previous studies. However, the influx solution preferably locates in the nucleus (instead of the cytoplasm) after entering through the membrane. Second, the solution influx only accounts for a

minor contribution to the expansion. Cells expand mostly due to the nucleus expansion when electroporated.

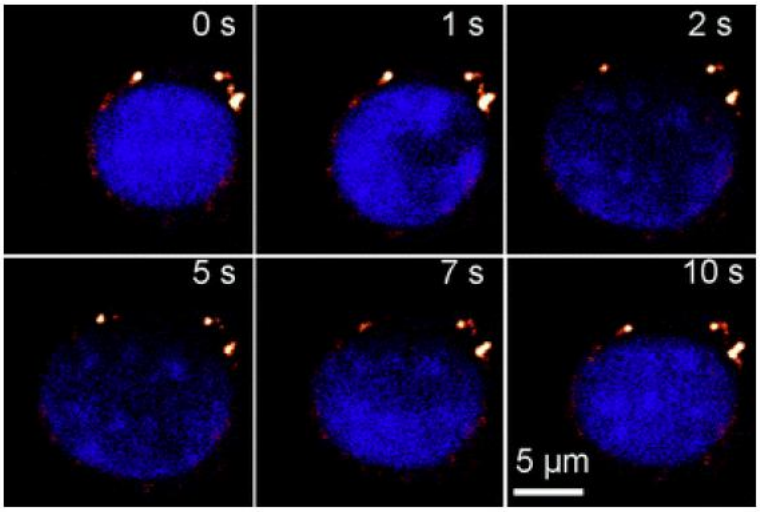

Figure 2-21 Nucleus expansion in a M109 cell. The CARS signal and TPEF were utilized to detect the Lipid rich structures (red) and Hoechst 33 342-stained nucleus (blue), respectively. The electric field of 400 V/cm was applied during 0–5 s and removed afterwards (5–10 s) (Bao, et al., 2010).

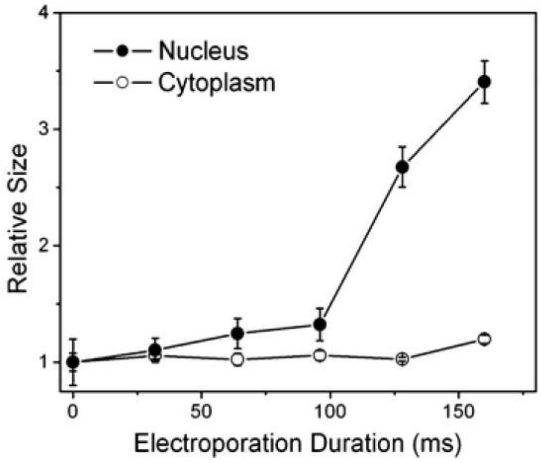

Figure 2-22 The relative increase in the size of cytoplasmic and nucleic areas during the swelling. The original size at time 0 is designated as 1 (Bao, et al., 2010).

Zhou et al studied single the cell electroporation in continuous flow field (Zhu, et al., 2010). Figure 2.23 depicts the schematic diagram of the system. The cellular suspension was injected to the sample channel from its inlet. The KCl solution meanwhile was injected from the channels on both sides. They were driven by the computer programmed syringe pumps. In the confluent channel of two fluids, the cellular suspension flow was squeezed into a thin laminar layer by the KCl solution flows. A constant DC voltage was applied onto two chlorinated Ag wires punched in the inlets of the KCl channels, to produce a large potential drop on the cellular flow of the central layer. According to Ohm's law, as the conductivity of the KCl solution is much higher than that of the cellular suspension solution, major voltage drop will occur over the central layer of the flow.

Because the size of the cellular flow could be changed by varying the speed ratio of the flows, the width of the central layer could be very small (<20 μm as the velocity ratio k = 2). Therefore, a low voltage supply (e.g. around 1.5 V) could generate a high electric field on the narrow cellular layer to accomplish electroporation with a limited pulse duration. At the optimum operating condition, they could successfully transfect the Yeast cells by only applying 1.5 V to the system. In this optimum condition, the cells have 70% viability while the transfection rate is around 85%.

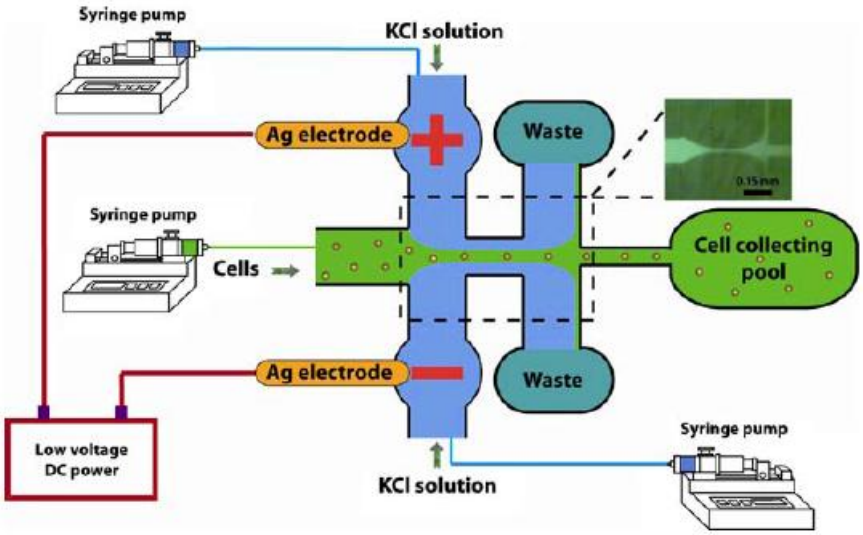

Figure 2-23 Schematic of the electroporation chip used hydrodynamic focusing during the electroporation process. By going through the focusing region, cells experience a local electric charge of high density. The figure located at the upper-right corner shows the fluorescence images captured during the experiment (Zhu, et al., 2010).

2.3.3 Microfluidic electroporation in other processes

Many other studies utilized cell electroporation for other applications such as electrofusion (Cao, et al., 2008; Schaper, et al., 2007), metabolism monitoring (Cheng, et al., 2010), localization of Kinases within cells (Wang, et al., 2008), inactivation of Lactobacillus plantarum by pulsed electric fields in a microfluidic reactor (Fox, et al., 2008) gene therapy (Valero, et al., 2008; Fei, et al., 2007; Li, 2008-b), electrochemotherapy (Gothelf, et al., 2003), electrogenetransfection (Valero, et al., 2008), electrofusion (Cao, et al., 2008; Janina, et al., 2007), and transdermal drug delivery (Herwadkar, et al., In Press, Corrected Proof). Electrofusion is the method to create hybrid cells by utilizing high-voltage electrical pulses. It consists of three main steps: cell alignment, electroporation and, fusion. A key step in electrofusion is the electroporation of the cells that are desired to be attached to each other. One of the microfluidic systems that is utilized for electrofusion was developed by Cao (Cao, et al., 2008). Figure 2.24 schematically shows the system. There are up to 2376 microelectrodes located on the chip. The electrodes were placed on both sides of channels. The microchip consists of six micro-chambers with the serpentile microchannels. The depth and width of the channels are 20 and 80 μm, respectively. The distance between the microelectrode pairs on both sides of the microchannels varies from 50 to 100 μm with the increment of 10 μm in each micro-chamber. In this way, one can also have a better control on the electric field applied to each cell. By using this system, two kinds of cells have been electroporated for electrofusion (animal HEK-293 cells and plant cucumber mesphy II protoplants). The applied electrical pulse for electroporation is 3~7 kV/cm with 20~50 μs duration. Considering the distance between the microelectrode pairs (50 to 100 μm), approximately 20 to 50 V voltage needs to be applied. Although this is not so high in comparison with the other electroporative micro-devices (see Table 2.1), Joule heating effect and bubble generation may occur and must be considered carefully.

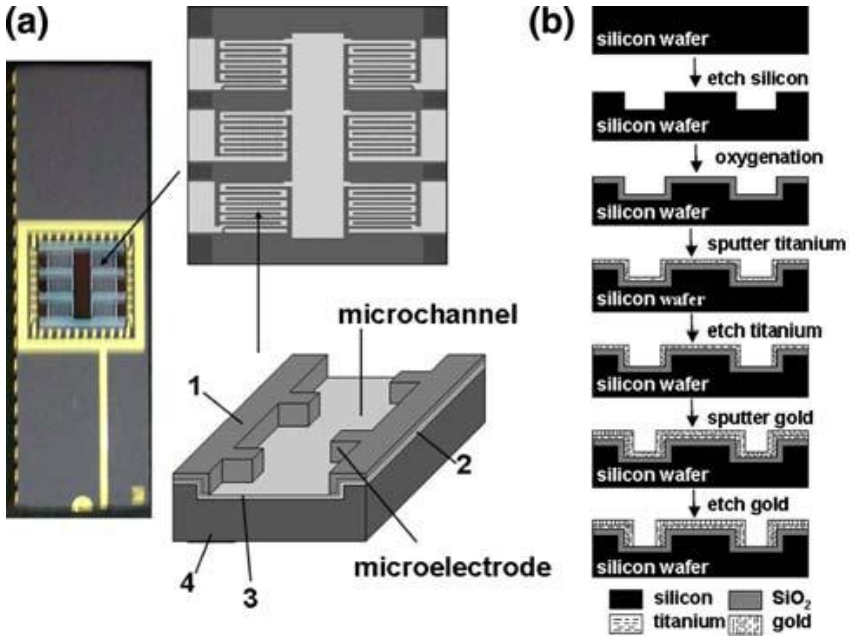

Figure 2-24 The schematic diagram and manufacturing process of the Cell-fusion chip. Part (a) shows the layout of a cell-fusion microchip, microchannels, microelectrodes on the chip, and the 3D schematic diagram of the system. Part (b) demonstrates the manufacturing process of the system. The tagged areas are: 1 = Au, 2 = Ti, 3 = SiO2, 4 = Si (Cao, et al., 2008).

Chapter 3
Membrane Permeabilization*

3.1 Introduction

Presence of an external electric field near the cell membrane may have different effects ranging from manipulating the cell (Gimsa, 2001; Kang, et al., 2009) to altering the cell membrane structure (Wong, et al., 2005; Movahed, et al., 2011). When the cell membrane is in contact with aqueous solutions, ionization of the surface molecules or adsorption of the ions from the liquid solution causes electric charge on the cell membrane. Electroporation is one of the most interesting influences of the electric field on the cell membrane. Applying an electric pulse near the cell alters the electric potential difference on both sides of the cell membrane; this difference is usually named as the transmembrane potential (TMP). When the applied electric field is larger than a critical TMP value, the cell membrane structure will be disturbed significantly and nanopores are created in the cell membrane. This leads to a significant increase in the electrical conductivity and permeability of the cell that refers as an electroporation or electropermeabilization (Neu, et al., 2009; Weaver, 1995). Electroporation has many applications in the cell biomedical treatment such as gene therapy (Valero, et al., 2008; Fei, et al., 2007; Li, 2008-b), electrochemotherapy (Gothelf, et al., 2003), electrogenetransfection (Valero, et al., 2008), electrofusion (Cao, et al., 2008; Janina, et al., 2007), transdermal drug delivery (Herwadkar, et al., In Press, Corrected Proof), cell lysis (Yen-Heng, et al., 2009), and cell transfection (Wang, et al., 2009). In many of these applications, the cells should remain viable after the electroporation. Thus, the electric pulse duration and intensity should be controlled precisely in order to not cause permanent effects on the cell structure or kill the cells.

Many experimental studies on the cell electroporation have been conducted. These experimental studies have been reviewed in Chapter 2. So far, theoretical studies on the cell electroporation have lagged the experimental ones though they are completely essential to boost the current understanding of the mechanism of the cell electroporation, reducing the side-effects of the external electric field on the cell structure, and increase of the electroporation efficiency. It should be pointed out that all the

* A version of this chapter is under review in the Journal of Membrane Biology as: "Saeid Movahed, Dongqing Li 'A Theoretical Study of Single-Cell Electroporation in a Microchannel', Journal of Membrane Biology, Online first: 5 November 2012". The licence agreement of reprinting this article in the current dissertation has been presented in Permissions section (License Number: 3033881359908).

reported studies on the cell membrane permeabilization (creating the nanopores on the cell membrane due to applied electric field) considered the cells in an infinitely large medium. In microfluidic devices, the cells are usually located in the microchannels or micro-chambers. The results of the current published studies may not reflect the boundary effects of microfluidic based electroporative devices. Moreover, the size and position of electroporative electrodes may have significant influences on the membrane permeabilization. In this chapter, the membrane permeabilization of a single cell located in a straight microchannel is investigated. In this study, the pulse shape is chosen as a square wave which is widely used in the microfluidic devices (Wang, et al., 2006; Wang, et al., 2006-a; Wang, et al., 2006-b; Wang, et al., 2008; Ionescu-Zanetti, et al., 2008; Khine, et al., 2005; Vassanelli, et al., 2008). This electric pulse shape can be easily generated by contracting the cross sectional area of the microchannels or using a high voltage pulse generator. We will study the effects of the microchannel height, the electrode dimensions, and pulse intensity and duration on the distribution and radius of the created nanopores on the cell membrane. The rest of this chapter is organized as follows: The following section explains the theory of membrane permeabilization. The model considered in the current study will be explained next. Section 3.4 describes the numerical approach of the current study. The results and discussions will be provided in section 3.5, before the concluding remarks.

3.2 Membrane Permeabilization

The theory of the generation and the development of the pores on the cell membrane due to the applied electric field can be found in a number of papers (Weaver, et al., 1996; Krassowska, et al., 2009; Krassowska, et al., 2007; Escoffre, et al., 2009). This theory is based on the energy minimum principle and is valid for the uniformly polarized membrane. Many other studies utilized this approach to investigate the effect of different parameters on the cell electroporation such as field strength and rest potential (DeBruin, et al., 1999), ionic concentration (DeBruin, et al., 1999), duration and frequency of electrical shock (Bilska, et al., 2000), electroporation of circular cells (Shil, et al., 2008; Talele, et al., 2010), cellular uptake of macro-molecules (Zaharoff, et al., 2008), and feedback control of generated pore radii (Cukjati, et al., 2007). Many of these studies have been reviewed in Chapter 2.

According to this theory, there are two kinds of pores in the cell membrane: hydrophobic and hydrophilic (see Figure 3.1). The hydrophobic pores are simply gaps in the lipid bi-layer of the

membrane that are formed because of the thermal fluctuation. The hydrophilic or inverted pores have their walls lined with the water-attracting heads of lipid molecules. The hydrophilic pores allow the passage of water-soluble substances, such as ions, and thus they conduct electric current while the hydrophobic pores do not.

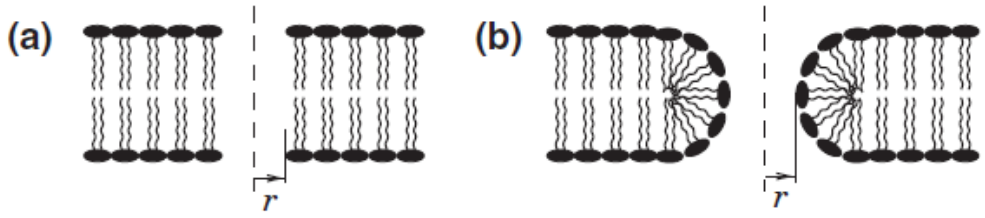

Figure 3-1 The structure of (a) hydrophobic and (b) hydrophilic pores created in cell membrane.

The pore energy is the required energy to introduce a single pore with radius r to the cell membrane while the other pores are fixed. This energy consists of two parts: $E(r)$ for hydrophilic pores and $U(r)$ for hydrophobic pores. The hydrophobic pore energy can be calculated as (Krassowska, et al., 2009):

$$U(r) \approx E_*(\frac{r}{r_*})^2 - \frac{1}{2h}(\varepsilon_W - \varepsilon_m)V_m^2 \pi r^2 \tag{3.1}$$

where radius r_* and energy E_* are the threshold radius between the hydrophobic and the hydrophilic pores and the threshold pore energy at r_*, respectively. The pores with $r < r_*$ are hydrophobic, and the pores with $r > r_*$ are hydrophilic. h is the membrane thickness, and ε_w and ε_m are permittivity of water and membrane, respectively.

The first term in $U(r)$ represents the energy cost for creating a cylindrical gap of radius r in the membrane and the second term is the effect of the transmembrane potential, V_m, that decreases the energy of the membrane by affecting the capacitive energy stored in the membrane. The hydrophilic energy, $E(r)$, can be calculated by (Krassowska, et al., 2009):

$$E(r) \approx \beta(\frac{r_*}{r})^4 + 2\pi\gamma r - \sigma\pi r^2 - \int_{r_*}^{r} F(r', V_m)dr' \tag{3.2}$$

where β and γ are constants, σ is the membrane tension, and F is the electric force. In equation (3.2), the first term represents the electrostatic repulsive force between the lipid heads forming the walls of the pores. Second term is the energy required to bend the bi-layer to form the pore perimeter. The third term represents the decrease in the energy due to the effect of the membrane tension; and the forth term is due to the effect of the transmembrane potential V_m that is derived by evaluating the mechanical work required to deform a dielectric body in an ionic solution with steady-state electric current. $F(r,V_m)$ can be calculated by the following equation (Krassowska, et al., 2007). In this equation, $F_{\max}$ and r_h are constants.

$$F(r,V_m) = \frac{F_{\max}}{1 + r_h/(r + r_h)} V_m^2 \tag{3.3}$$

The creation of the pores is believed to be two steps. The pores are initially created as the hydrophobic pores with radii between r and $(r + dr)$ at the following rate (per unit area of the membrane) (Krassowska, et al., 2009):

$$\nu_c h \frac{\partial}{\partial r}\left(\frac{U}{kT}\right) e^{-U/kT} dr \tag{3.4}$$

where ν_c is the fluctuation rate of the bi-layer per unit volume, k is Boltzmann's constant, and T is absolute temperature.

The pores are initially hydrophobic ($r < r_*$) (r_* is the threshold radius between the hydrophobic and hydrophilic pores). At $r = r_*$ pores instantaneously changes their configuration (from hydrophilic to hydrophobic) to minimize their energy. The pores with $r > r_*$ are hydrophilic.

As the hydrophobic pores are created, they started to expand or shrink due to two different mechanisms: advection and diffusion. Advection is the definite time rate of change of the pore radius, leading to the decreasing of the bi-layer energy; and diffusion refers to the random increases and decreases of the pore radius induced by thermal fluctuation. However, between these two mechanisms, advection is dominant by far. The hydrophilic pore of radius *r* is assumed to evolve with advection velocity u (Krassowska, et al., 2009):

$$u = \frac{dr}{dt} = -\frac{D}{kT}\frac{\partial E}{\partial r} \tag{3.5}$$

In the above equation, E is the hydrophilic pore energy and D is the diffusion coefficient associated with random fluctuation of pore radius.

In order to consider the effect of interfacial energy on the pore generation, constant membrane tension in equation (3.2) can be replace by the effective membrane tension (Krassowska, et al., 2009) :

$$\sigma_{eff}(A_p) = 2\sigma' - \frac{2\sigma' - \sigma_0}{(1-(A_p/A))^2} \tag{3.6}$$

In this equation, σ' is the interfacial energy per area of the hydrocarbon–water interface, σ_0 is the surface tension of the membrane without the pores, A_p is the total area of the pores, and A is the area of the lipid bi-layer. Therefore, the advection velocity in equation (3.5) can be approximated as (Krassowska, et al., 2009):

$$u(r, V_m, A_p) = \frac{D}{kT}\{4\beta(\frac{r_*}{r})^4\frac{1}{r} - 2\pi\gamma + 2\pi\sigma_{eff}(A_p)r + F(r, V_m)\}, \quad \text{in } r \geq r_* \tag{3.7}$$

As indicated above, the pores are created in order to minimize the energy. E has two local minima at $r = r_m \approx 1\,nm$ and at $r = r_s \geq r_m$. It means that the pores divided themselves into two different groups, small pores ($r = r_m$) and large pores ($r = r_s$). By removing the external electric field, the transmembrane potential becomes zero; consequently, all the pores shrink to r_m . After that, the pores can reseal by first converting to the hydrophobic configuration and then being destroyed by lipid fluctuations.

Considering the above procedure, the electroporation process can be categorized into five different steps: induction, expansion, stabilization, resealing, and memory. Through the induction step, the transmembrane potential increases until it reaches its critical value. This step is usually takes less than one microsecond. As long as the threshold value of TMP maintains, the number and radius of the created nanopores increases continuously, this step is usually called expansion. The shape and the duration of the electric pulses determine the time span of this step that is usually in the range of microseconds to milliseconds. When decreasing the external electric field to its subcritical value, as

long as the nanopores are exit, most cell membranes have a much more normal state that is called stabilization. By removing the external electric field, the cell membrane runs into the resealing process that usually spans from second to minutes. After this step, some more resilient changes are usually remains in the cell membrane that takes from minutes to hours. This phase is usually called as memory (Wang, et al., 2010).

By considering the physics of pore creation, evolution and resealing, the following advection-diffusion partial differential equation (PDE) can be obtained for the pore density distribution, $n(r,t)$ (Krassowska, et al., 2009):

$$\frac{\partial \mathrm{n}}{\partial \mathrm{t}} = D\frac{\partial^2 n}{\partial r^2} - \frac{\partial}{\partial r}(u\,n) + \upsilon_c h \frac{\partial}{\partial r}\left(\frac{U}{kT}\right)e^{-U/kT} - \upsilon_d \eta H(r_* - r) \tag{3.8}$$

The four terms on the right-hand side in equation (3.8) represent the four mechanisms that causes change in $n(r,t)$:

$D\frac{\partial^2 n}{\partial r^2}$: the diffusion term describes random fluctuation of pore radii caused by thermal energy

$-\frac{\partial}{\partial r}(u\,n)$: the advection term describes the changes in pore radii that are driven by minimization of the energy of the bi-layer; u is the drift velocity. For hydrophilic pores, E is replaced by U in equation (3.5).

$\upsilon_c h \frac{\partial}{\partial r}\left(\frac{U}{kT}\right)e^{-U/kT}$: creation rate of pores (equation (3.4)).

$-\upsilon_d \eta H(r_* - r)$: the destruction term describes disappearance of pores; since only the hydrophobic pores can be destroyed by lipid fluctuation, this term contains the Heaviside step function $H(r)$.

Because of the exponential dependence of the creation rate on the pore energy and the existence of disparate spatial and temporal scales, the numerical solution of PDE (3.8) requires very small discretization steps. To avoid the large computational cost associated with the numerical solution of PDE (3.8), this equation is asymptotically reduced to a following system of ODE (Neu, et al., 1999):

$$\frac{dN}{dt} = \alpha e^{(V_m / V_{ep})^2} (1 - \frac{N}{N_{eq}(V_m)}) \tag{3.9}$$

where $N(t)$, the density of pores, defines as:

$$N(t) = \int_{r_*}^{\infty} n(r,t)dr \tag{3.10}$$

N_{eq} is the equilibrium pore density for the given transmembrane voltage, V_m:

$$N_{eq}(V_m) = N_0 e^{q(V_m / V_{ep})^2} \tag{3.11}$$

For the membrane with k pores, the rate of change of their radii, r_j , can be determined by the following set of equations:

$$\frac{dr_j}{dt} = U(r_j, V_m, \sigma_{eff}), \quad j = 1, 2, ..., k \tag{3.12.a}$$

$$U(r, V_m, A_p) = \frac{D}{kT}\{4\beta(\frac{r_*}{r})^4 \frac{1}{r} - 2\pi\gamma + 2\pi\sigma_{eff} r + \frac{{V_m}^2 F_{\max}}{1 + r_h/(r + r_t)}\}, \quad \text{in } r \geq r_* \tag{3.12.b}$$

In equations (3.9)-(3.12), N_0, q, α and V_{ep} are constants.

The above-reviewed theory is the most widespread analytical approach to study the effect of electric field on the pore creation in the cell membrane. Many studies utilized this theory to investigate different aspects of the cell electroporation. Although the above theoretical model can address many aspects of the cell electroporation, there are some shortcomings associated with it:

- First, this model cannot explain the mechanism of resealing the pores with radius $r \geq r_m$.
- The effect of changing volume of the cell is not considered in the above analysis. Many studies show that in the presence of the external electric field, the cells started to deform from circular to elliptical shape (Teissie, et al., 2002), and to expand (Wang, et al., 2006-b) or rotate (Gimsa, 2001). For example, previous experimental studies show that in the presence of external electric field, the cell can expand up to 300% of its original volume (Wang, et al., 2006-b).

3.3 Model Description

Figure 3.2 shows the schematic diagram of the system in the current study. The spherical cell of radius a (diameter d_0) immersed in the microchannel of height h_c is considered. The microchannel is filled with a conductive medium (an aqueous solution). The thickness of the cell membrane is

assumed to be h. The required electric pulse for electroporation (ϕ_0) is applied to the cell via the two electrodes on the side walls of the microchannel. Five points are defined on cell membrane: *D* and *H* are the depolarized (*DP*) and hyperpolarized (*HP*) poles, *E* indicates the equator line, D_b and H_b define the border between the electroporated and the non-electroporated regions on the membrane. The values of these parameters used in the current study are listed in Table 3.1.

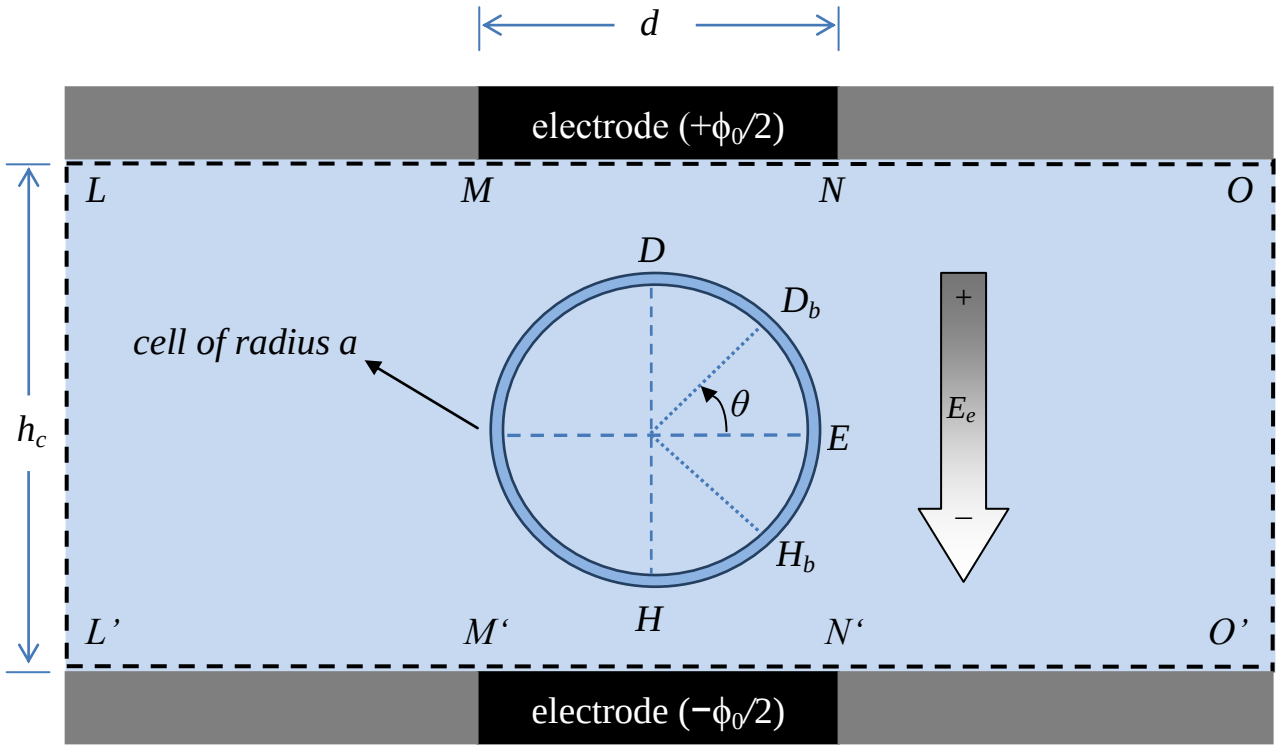

Figure 3-2 The schematic diagram of the assumed system of the current study. A cell of radius a is assumed in the microchannel of height h_c. The microchannel is filled with the conductive medium. The required voltage of the electroporation (ϕ_0) is applied via the two electrodes of length d located on the wall of the microchannel

In this study, we aim to investigate the creation of the hydrophilic nanopores in the presence of the applied electric field. When the transmembrane potential reach the values of $0.5 \sim 1V$, the hydrophilic nanopores will be created with the initial radius of r^*. In fact, r^* is the threshold radius that the hydrophobic nanopores convert to the hydrophilic ones. In the current study, we applied the

asymptotic ODE model (Neu, et al., 1999), (Eqns. (3.9)-(3.12)), to the system shown in Figure 3.2, i.e., to investigate the cell membrane permeabilization in the microchannel and study the effects of various boundary conditions, including the microchannel dimensions, the location and the size of the electrodes, on the cell membrane permeabilization.

Table 3-1The values for constants and parameters used in the simulations

Parameter	value (unit)	Definition
$d_0 (= 2a)$	$15\,(\mu m)$	diameter of the cell
t_m	$5\,(nm)$	cell membrane thickness (Glaser, et al., 1988)
h_c	$30\,(\mu m)$	height of the microchannel
d	$20\,(\mu m)$	length of the electrode
ϕ_0	$1.7\,(V)$	electric pulse intensity
t_0	$10\,(\mu s)$	electric pulse duration
s_i	$0.455\,(S\,m^{-1})$	intracellular conductivity (Hibino, et al., 1993)
s_e	$5\,(S\,m^{-1})$	extracellular conductivity (Hibino, et al., 1993)
s	$2\,(S\,m^{-1})$	Conductivity of the solution filling the pore (Smith, et al., 2004)
c_m	$0.0095\,(F\,m^{-2})$	Specific membrane capacitance (Hibino, et al., 1993)
g_1	$2\,(S\,m^{-2})$	Surface conductance of the membrane (Hibino, et al., 1993)
V_{rest}	$-80\,(mV)$	rest potential (Chambers, et al., 1979)
α	$1\times10^{9}\,(m^{-2}s^{-1})$	Creation rate coefficient (DeBruin, et al., 1999)
V_{ep}	$0.258\,(V)$	Characteristic voltage of electroporation (DeBruin, et al., 1999)
N_0	$1\times10^{9}\,(m^{-2})$	Equilibrium pore density at $V_m = 0$ (DeBruin, et al., 1999)
r^*	$0.51\,(nm)$	Minimum radius of hydrophilic pores (Glaser, et al., 1988)
r_m	$0.8\,(nm)$	Minimum energy radius at $V_m = 0$ pores (Glaser, et al., 1988)
D	$5\times10^{-14}\,(m^2\,s^{-1})$	Diffusion coefficient for pore radius (Freeman, et al., 1994)
T	$300\,(.K)$	Temperature
β	$1.4\times10^{-19}(J)$	Steric repulsion energy (Neu, et al., 1999)
γ	$1.8\times10^{-11}(J\,m^{-1})$	Edge energy (Glaser, et al., 1988)
$F_{\max}$	$0.7\times10^{-9}(N\,V^{-2})$	Max electric force for $V_m = 1V$ (Neu, et al., 2003)
r_h	$0.97\times10^{-9}(m)$	Constant in Eq. (3.12.b) for advection velocity (Neu, et al., 2003)
r_t	$0.31\times10^{-9}(m)$	Constant in Eq. (3.12.b) for advection velocity (Neu, et al., 2003)
q	$(r_m/r^*)^2$	Constant in Eq. (3.11) for pore creation rate (DeBruin, et al., 1999)
σ'	$2\times10^{-2}(J\,m^{-2})$	Tension of hydrocarbon-water interface (Israelachvili, 1992)
σ_0	$1\times10^{-6}(J\,m^{-2})$	Tension of the bilayer without pores (Hénon, et al., 1999)

3.3.1 Electric Field:

Laplace equation should be solved to find the electric potential inside (ϕ_i) and outside (ϕ_e) the cell.

$$\nabla^2 \phi_{i,e} = 0 \tag{3.13}$$

The required voltage of electroporation (ϕ_0) is applied via the embedded electrodes on the two sides of the cells. Thus, the electrical boundary condition on boundaries *MN* and *M'N'* is assumed as:

$$\phi_{e,MN} = \phi_0/2 \tag{3.14.a}$$

$$\phi_{e,M'N'} = -\phi_0/2 \tag{3.14.b}$$

The walls of the microchannels are electrically insulated. There is also no current flow at the two ends of the microchannel. Therefore, the assumed electrical condition on boundaries *LM*, *NO*, *OO'*, *O'N'*, *M'L'*, and *L'L* is:

$$\hat{n} \bullet \vec{J} = 0 \tag{3.15}$$

The electric current density should be continuous across the cell membrane:

$$-\hat{n} \bullet (s_i \nabla \phi_i) = -\hat{n} \bullet (s_e \nabla \phi_e) = c_m \frac{\partial V_m}{\partial t} + g_1 (V_m - V_{rest}) + I_p \tag{3.16}$$

In this equation $\hat{n}$ is the local outward unit vector normal to the surface of cell membrane, ∇ is the Nabla symbol, s_i and s_e are the intracellular and extracellular conductivities; V_m and V_{rest} are the transmembrane potential (TMP) and rest potential. g_1 and c_m are the surface conductance and capacitance of the membrane, in that order.

The transmembrane potential (V_m) is defined as:

$$V_m = \phi_i(t, a, \theta) - \phi_e(t, a, \theta) \tag{3.17}$$

3.3.2 Number of nanopores:

As it was explained in section 3.2, the rate of creation of the nanopores can be found by solving Eqns. (3.9-3.11):

$$\frac{dN(t)}{dt} = \alpha e^{(V_m / V_{ep})^2} (1 - \frac{N(t)}{N_{eq}(V_m)}) \tag{3.9}$$

where $N(t)$ is the density of pores define as:

$$N(t) = \int_{r_*}^{\infty} n(r,t) dr \tag{3.10}$$

N_{eq} is the equilibrium pore density for the given transmembrane voltage, V_m :

$$N_{eq}(V_m) = N_0 e^{q(V_m / V_{ep})^2} \tag{3.11}$$

In the above Equations, α , V_{ep}, q , and N_0 are the constants that can be found in table 3.1.

3.3.3 Radius of nanopores:

Based on the asymptotic model of the cell membrane permeabilization (Section 3.2), the nanopores are initially created with a radius of r^*. By increasing the applied electric field, the nanopores start to develop in order to minimize the energy of the cell membrane. For the membrane with n nanopores, the rate of change of their radii, r_j , can be determined by the following set of equations (see section 3.2):

$$\frac{dr_j}{dt} = U(r_j, V_m, \sigma_{eff}), \quad j = 1, 2, ..., n \tag{3.12}$$

$$U(r, V_m, A_p) = \frac{D}{kT} \{4\beta (\frac{r_*}{r})^4 \frac{1}{r} - 2\pi\gamma + 2\pi\sigma_{eff} r + \frac{V_m{}^2 F_{\max}}{1 + r_h / (r + r_t)}\}, \quad \text{in } r \geq r_* \tag{3.18}$$

The constants of the above equations have been defined in table 3.1. σ_{eff} is the effective tension of the membrane. As it was indicated in Section 3.2, if A is the surface area of the cell membrane and A_p is the area of the created nanopores ($A_p = \sum_{i=1}^{n} \pi r_i^2$), σ_{eff} can be computed as:

$$\sigma_{eff}(A_p) = 2\sigma' - \frac{2\sigma' - \sigma_0}{(1 - (A_p / A))^2} \tag{3.7}$$

3.4 Numerical Simulation

In this study, the above mentioned equations were solved numerically to find the electric potential in the domain and investigate the creation of the nanopores on the cell membrane. "Comsol 3.5a with MATLAB" commercial package was used in the numerical simulations. The cell membrane has been discretized with a discretization step of $\Delta\theta = \pi/60$. In order to discretize the solution domain, the un-structured meshes were applied. The solution domain is broken into small meshes to allow that the meshes fully cover the solution domain without overlapping.

Before applying the electric pulse, transmembrane potential is equal to the rest potential ($V_m = V_{rest}$). At each time step, first Eqns. (3.13–3.17) were solved by Finite Element Method to find the electric potential in the domain. After the electric potential was obtained, Eqns. (3.7, 3.9-3.12, and 3.18) were then solved to find the location, number, and radius of the created nanopores on the cell membrane. The Runge-Kutta method was utilized to solve ODE equations 3.9 and 3.12. This system of equations were solved with a time-step of $\tau_c/32$, in which τ_c is the time constant of the cellular polarization (Hibino, et al., 1993):

$$\tau_c = aC_m\left(\frac{1}{s_i} + \frac{1}{s_e}\right) = 2.4\mu s \tag{3.19}$$

3.5 Results and Discussion

The quantitative information used in the simulations is provided in Table 3.1. The cell of diameter a $(15um)$ is considered in the microchannel of height h_c $(25um, 30um, \text{and } 35um)$. The necessary electric field $(1 \sim 3V)$ is applied by the two electrodes of width d $(5 \sim 20um)$ located on the walls of the microchannel. The electric pulse span is in the order of micro-seconds (μs). In this section, we aim to study the influence of the electric pulse intensity (ϕ_0) and the duration (t_0), the electrode size (d), and the microchannel height (h) on the electro-permeabilization of the cell.

The pulse shape in this study was chosen as a square wave and can mathematically express as $V = \phi_0 \times u(t - t_0)$. Here, $u(t - t_0)$ is the step unit function that is equal to one for $0 \le t \le t_0$ and is zero for $t > t_0$ (Figure 3.3). The obtained results show that the nanopores' radius and density are symmetric along the equator (see Figure 3.2). The transmembrane potential has the same magnitude

with the opposite sign on the two sides of the cell membrane ($0^\circ \le \theta \le 180^\circ$ and $180^\circ \le \theta \le 360^\circ$). Therefore, in the present study, only the permeabilization of the back side of the cell membrane has been illustrated ($180^\circ \le \theta \le 360^\circ$).

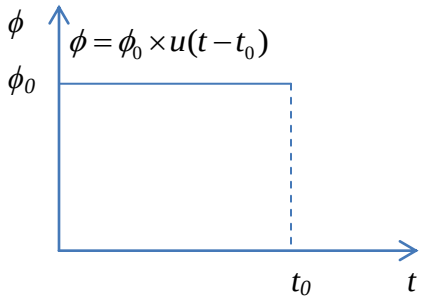

Figure 3-3The Schematic diagram of the applied electric pulse

3.5.1 Time Evaluation:

For one specific case of study ($h_c = 30\,um, a = 15\,um, \phi_0 = 3V,$ and $d = 20\,um$), Figure 3.4 depicts the TMP and the radius of the generated nanopores on the back side of the cell membrane. Once the nanopores are generated, the TMP reduces. The TMP has a sharper reduction at the poles ($\theta = 90^\circ$ and 270°). At the beginning ($t \le 2\mu s$), the biggest nanopores are created at DP and HP poles. As the nanopores are created, TMP decreases, also the angular positions of the highest TMP and the biggest nanopores move toward the equator (E). For this case of study, Figure 3.5 depicts the density of the created nanopores (N). This figure shows that the number of the generated nanopores reach its maximum value very fast ($1 \sim 2\,\mu s$). From the results shown in Figure 3.4 and Figure 3.5, once the nanopores are created, their number and location may not be influenced by the electric pulse anymore; the electroporated area also remains unchanged. Further presence of the electric pulse results in developing the size of the generated nanopores. Here, the energy level of the cell membrane increases in the presence of the electric pulse. According to the theory of membrane permeabilization, the created nanopores consume the absorbed energy in order to keep growing and thus results in reduction in the TMP. The numerical results of this study also agree with this fact (see Figures 3.4and 3.5).

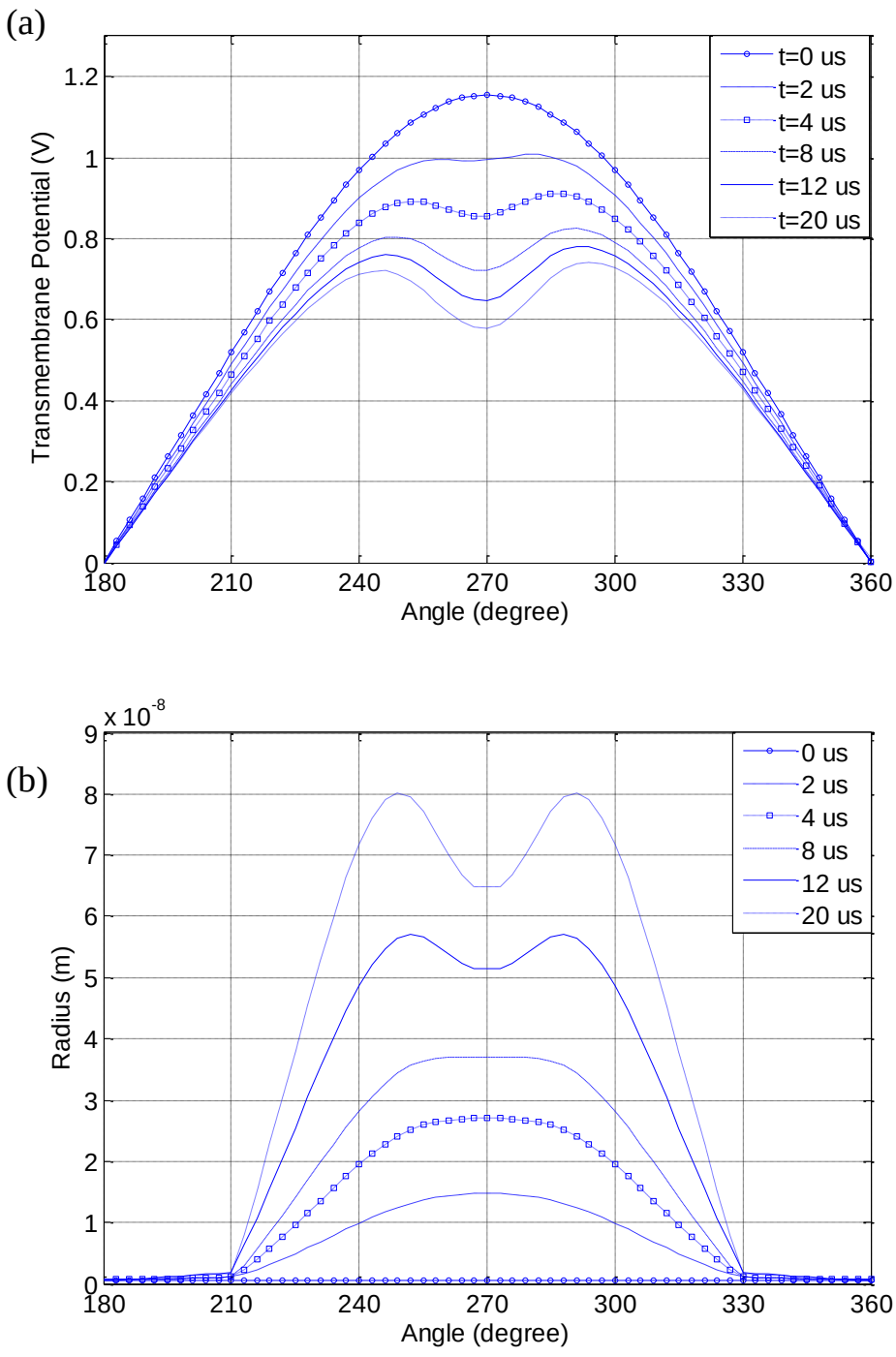

Figure 3-4 Time evaluation of the membrane permeabilization of the cell located in microchannel. ($h_c = 30\,um, a = 15\,um, \phi_0 = 3V$, and $d = 20\,um$). (a) Transmembrane potential and (b) radius of the created nanopores.

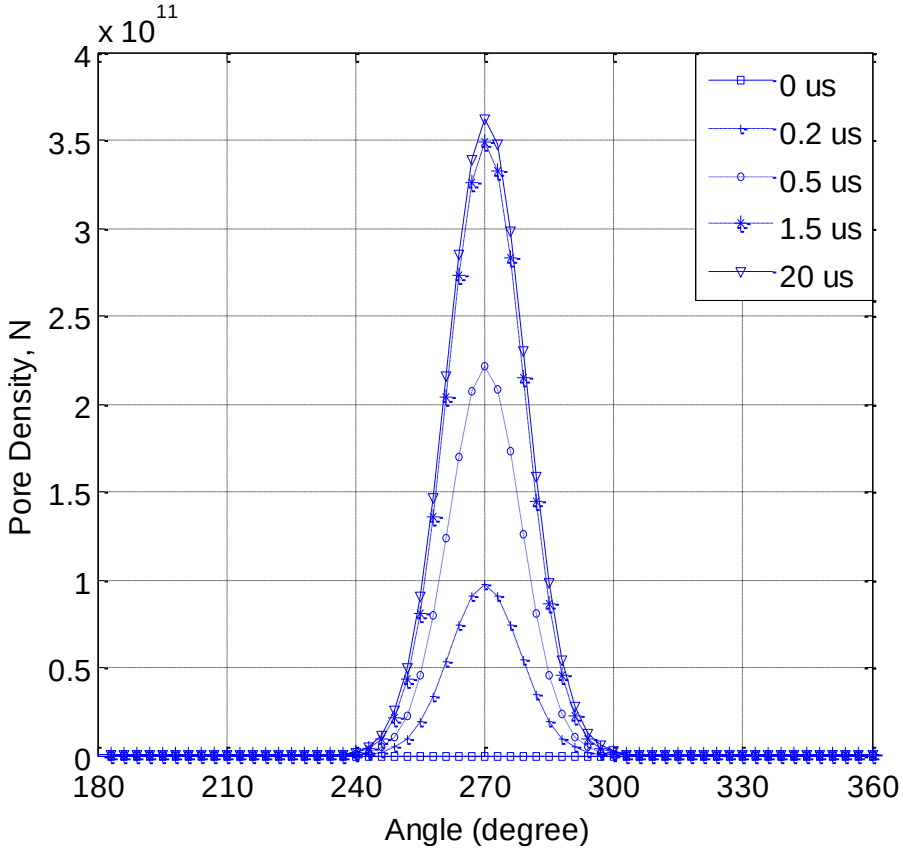

Figure 3-5 Time evaluation of the density of the created nanopores on the membrane of the cell located in the microchannel ($h_c = 30\,um, a = 15\,um, \phi_0 = 3V,$ and $d = 20\,um$ **).**

3.5.2 Electrode Size:

Figure 3.6 illustrates the effect of electrode size (d) on the transmembrane potential, before the nanopores are created on the cell membrane. A parameter x is defined as the ratio of the electrode width (d) to the cell diameter (d_0) i.e. $x = d/d_0$.

For the cells located in an infinite domain and exposed to a uniform electric field of E_e, if the nanopores are not created, the transmembrane potential is given by the Schwan equation (Pauly, 1959):

$$V_m = 1.5 E_e a \cos(\theta) \tag{3.20}$$

The Schwan equation shows that in an infinite domain, if the nanopores are not created on the cell membrane, TMP has a sinusoidal distribution. For the cell located in the microchannel as shown in Figure 3.2, the numerical simulation in this study also shows that TMP has sinusoidal profile around the cell membrane when $x > 1$. However, as the ratio of the electrodes width to the diameter of the cell decreases, the following occurs (see Figure 3.6): (1) the local TMP value reduces, (2) TMP values decrease sharply from poles of the cell membrane ($\theta = 90^{\circ}$ and 270°) to the equator ($\theta = 0^{\circ}$ and 180°). If the applied voltage is kept constant, decreasing the height of the microchannel (the distance between the two electrodes) produces stronger electric field; consequently, the local TMP will be increased and the nanopores are created with the smaller applied voltage via the electrodes.

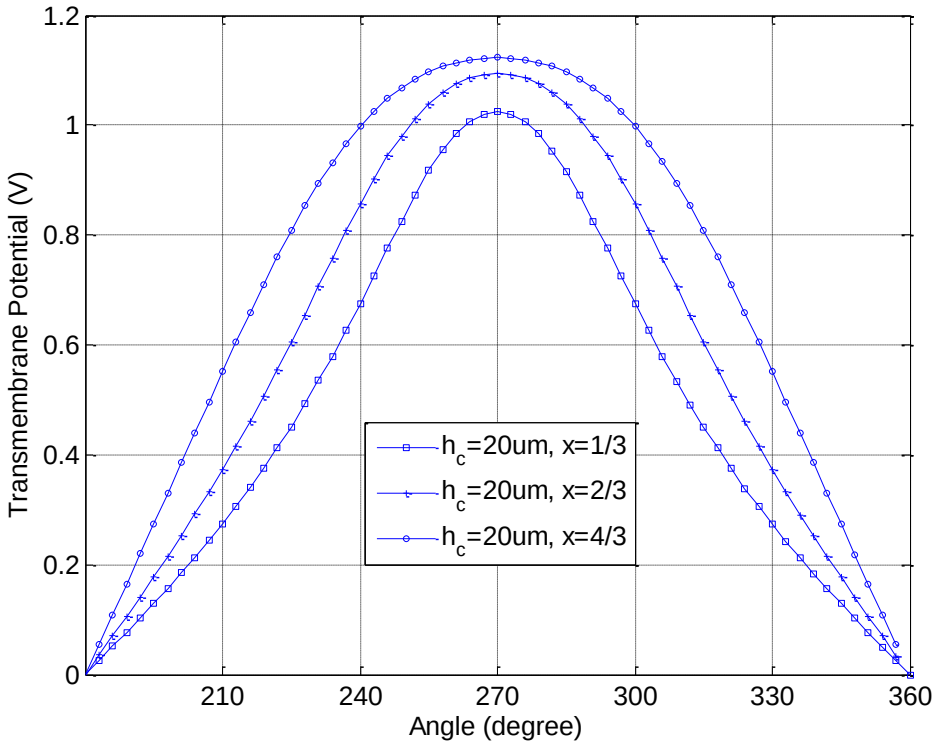

Figure 3-6 This figure illustrates the effect of size of electrodes on Transmembrane potential before the nanopores are created. In this figure, the parameter is defined as the ratio of electrodes width (d) to the cell diameter (d_0) i.e., $x = d/d_0$ ($a = 15\,um, \phi_0 = 2.3V$).

Figure 3.6 also depicts the effect of the electrode size on the initial TMP; here, the nanopores have not been created yet. Larger values of the initial TMP will produce more nanopores on the cell membrane. The TMP tends to decrease less sharply for the higher values of x. Therefore, increasing the width of the electrodes enhances the local TMP on the cell membrane. Hence, if we aim to increase the created nanopores on the cell membrane, the width of the electrode should be larger than the cell diameter (useful in transfection applications). Thus, in order to maximize the efficiency of the cell transfection (reversibly electroporate the cell to insert biological samples into the cell), the width of the electrode should be bigger that the cell diameter. If the interest is to electroporate only specific part of the cell (for example in electrofusion), x may be smaller than 1.

3.5.3 Microchannel height and Pulse intensity:

Figures 3.7 and 3.8 illustrate the effects of microchannel height (h_c) and pulse intensity (ϕ_0) on the permeabilization of the cell membrane. In these figures, the microchannel heights are $25\ \mu m$, $30\ \mu m$, and $35\ \mu m$. The applied electric pulse intensities are $1V, 1.5V, 2V,$ and $2.3\ V$. The pulse span is kept constant ($t_0 = 10\ \mu s$).

As it can be seen from these figures, both the electric pulse intensity and the microchannel height have great influences on the radius and the density of the created nanopores. For the same size microchannels, intensifying the electric pulse increases both the density and the radius of the created nanopores. As an example, Figures (3.7a) and (3.8a) shows that for $h_c = 25\ \mu m$, when the applied electric pulse is $\phi_0 = 1V$, the generated nanopores size is minimum. By increasing the applied electric pulse from $1V$ to $2V$, the maximum radius of the nanopores reach $\sim 45\ nm$. If the applied electric pulse is enhanced to $2.3V$, the maximum radius of the nanopores reach $\sim 65\ nm$. These maximum size nanopores are mainly located around the poles ($\theta = 270^o$) (Figure 3.8). Intensifying the electric pulse also expands the electroporated area of the cell membrane. For example, consider the case of a microchannel height $25\ \mu m$ (Figure 3.7a and Figure 3.8a). When the applied voltage is $1V$, no significant nanopores are created on the cell membrane. However, when the applied voltage increases to $1.5V$ and $2V$, the angular area with significant number of the electroporated nanopores covers approximately $230^o \le \theta \le 310^o$ and $215^o \le \theta \le 325^o$, respectively (see Figure 3.8a).

(a)

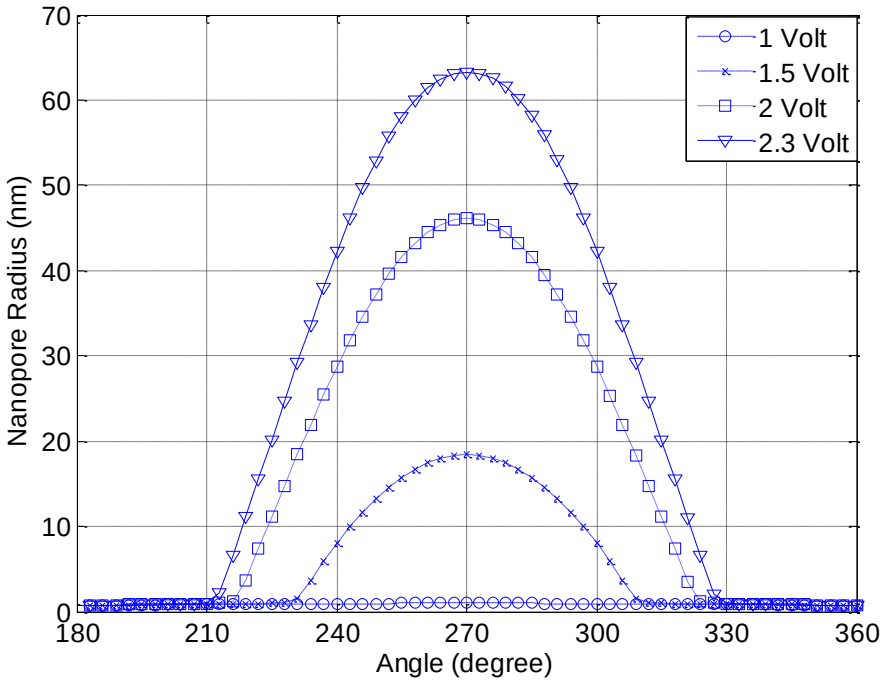
1 Volt
1.5 Volt
2 Volt
2.3 Volt
Nanopore Radius (nm)
Angle (degree)
0
10
20
30
40
50
60
70
180
210
240
270
300
330
360

(b)

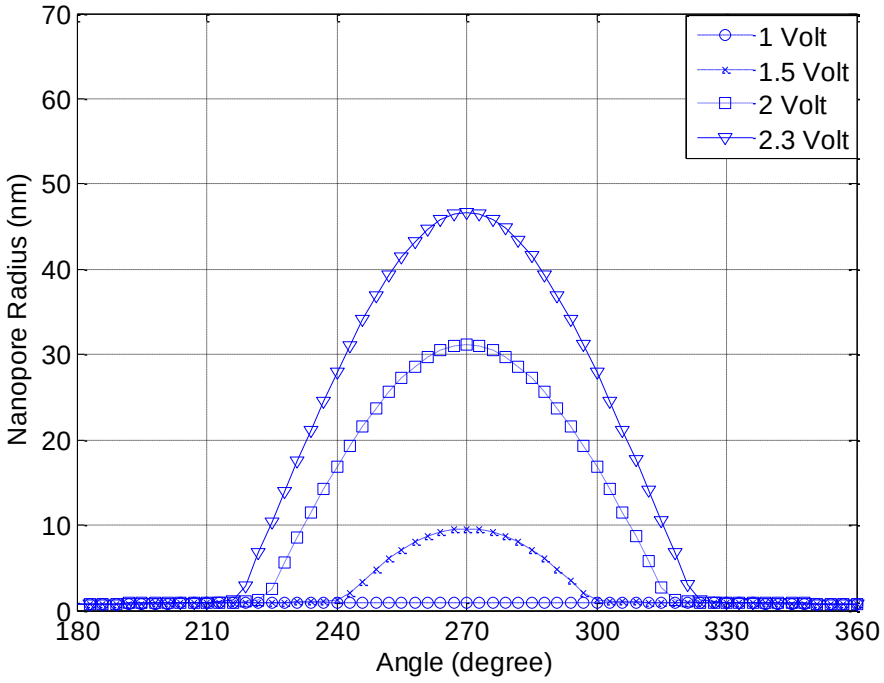
1 Volt
1.5 Volt
2 Volt
2.3 Volt
Nanopore Radius (nm)
Angle (degree)
0
10
20
30
40
50
60
70
180
210
240
270
300
330
360

(c)

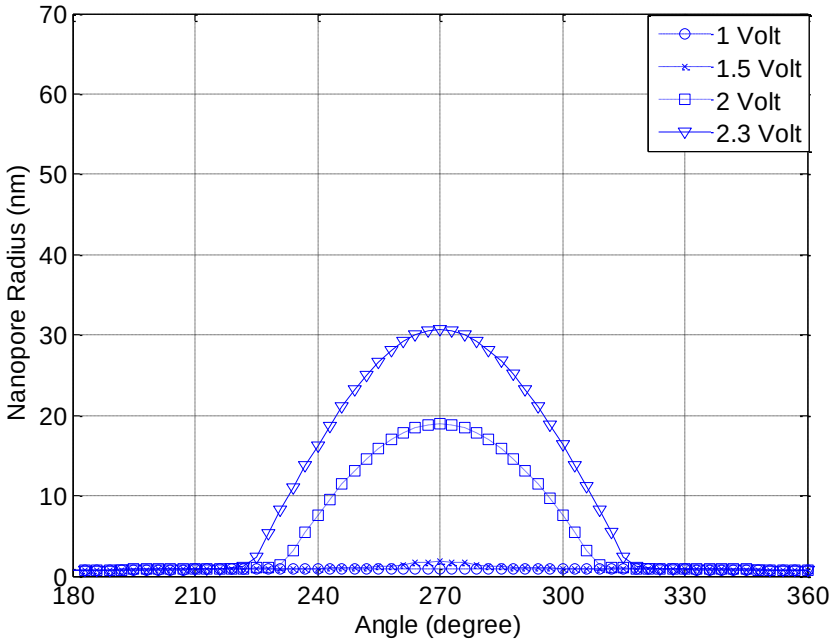

Figure 3-7 Effect of pulse intensity on the radius of the created nanopores on the cell of diameter 15 um. The height of the microchannel is $25\ \mu m$ **(a),** $30\ \mu m$ **(b), and** $35\ \mu m$ **(c).**

(a)

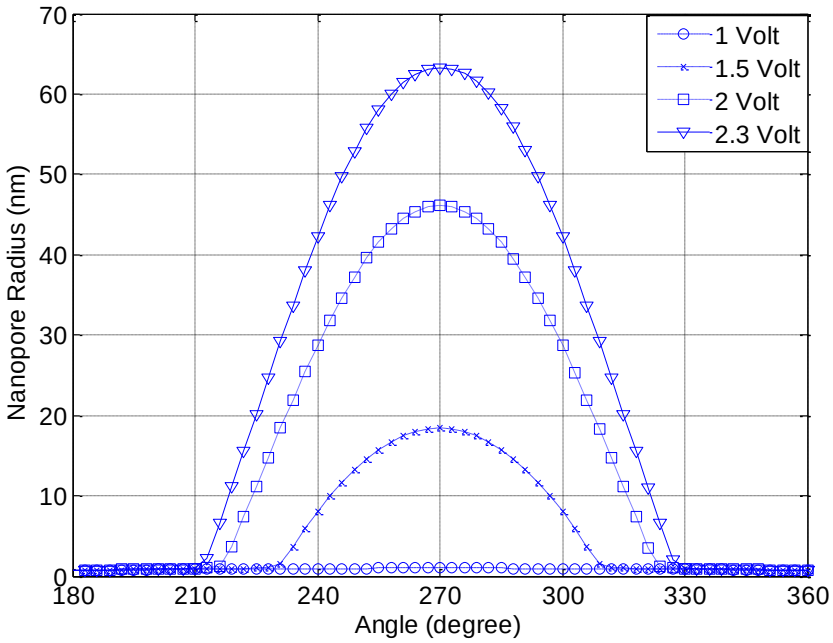

(b)

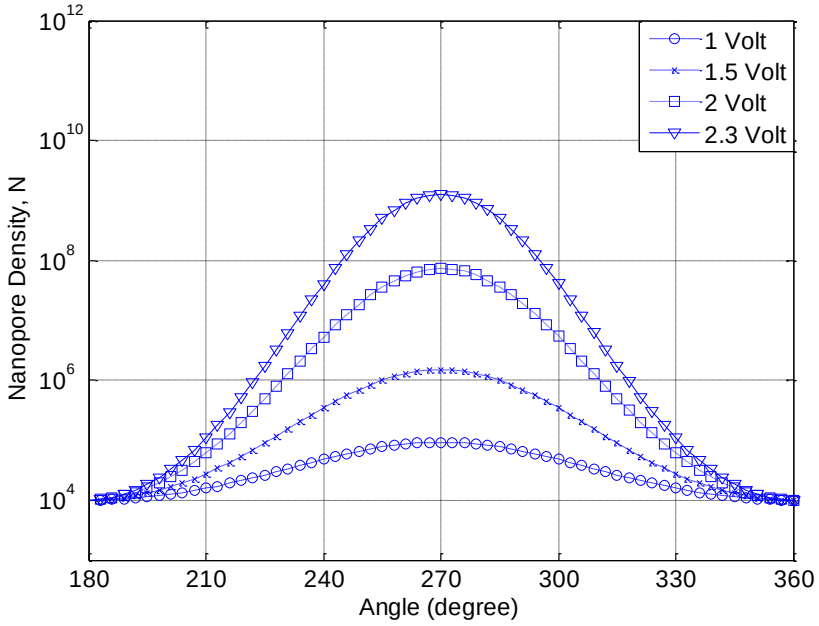

(c)

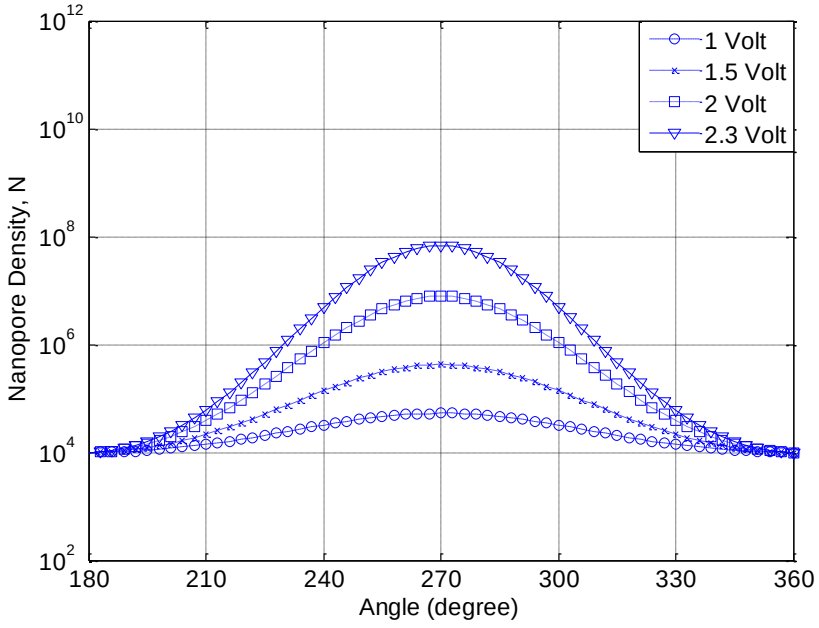

Figure 3-8 Effect of pulse intensity on density of created nanopores on cell of diameter 15 um. Assumed heights of microchannels are $25\,um$ **(a),** $30\,um$ **(b), and** $35\,um$ **(c).**

3.6 Conclusion:

In this chapter, the membrane permeabilization of the single cell in the microchannel was investigated. The previous studies on the cell electroporation consider the cells in an infinite domain which does not reflect the finite boundary effects of microchannel walls on the membrane permeabilization process. In the study presented in this chapter, we found that the size of the microchannels and the electrodes as well as the position of the electrodes in the microchannels have great influences on the cell electroporation. Following conclusions have been obtained:

- In the microfluidic electroporative devices, the membrane permeabilization can be performed with very low-intensity electric pulses ($1 \sim 3V$).
- If the electric pulse intensity and duration and also the electrode dimension keep constant, expanding the microchannel height reduces the number and radius of the large nanopores; the electroporated area of the cell membrane is also decreased.
- Increasing the electric pulse intensity intensifies the size and the number of the created nanopores and also increases the electroporated area on the cell membrane.
- Transmembrane potential becomes less widely spread for the electrodes with a width larger than the cell diameter. The TMP profile is sinusoidal in the non-electroporated area.
- If the width of the electrodes is smaller than the cell diameter, the local transmembrane potential decreases everywhere and sharply in the area from the poles (the nearest points of the cell membrane to the electrodes) to the equator.
- The number of the created nanopores reaches its maximum value extremely fast; further presence of the electric pulse may not influence the number and the location of the created nanopores anymore. It only develops the generated nanopores.
- The most nanopores are created around the poles.

Chapter 4
Electrokinetic Transport through Nanochannels*

4.1 Introduction

In many microfluidic instruments, the electrokinetic effects are exploited to perform various applications ranging from biological process such as cell culture (Movahed, et al., 2010) to cooling microelectronic devices (Wang, et al., 2009). Extensive studies have been conducted on the electrokinetic transport phenomena in the microscale channels (Li, 2004; Li, 2008). Sophisticated theories have been proposed to model the electrokinetic effects in the microchannels. Usually Poisson-Boltzmann equation is used to find the electric potential in the microchannels; Helmholtz–Smoluchowski theorem is commonly utilized to model the electroosmotic flow through the microchannels. With the advancement of nano-fabrication technology (Cho, et al., 2010), more and more attention has been paid to transport phenomena in devices involving nanochannels (Garcia, et al., 2005; Lee, et al., 2010; Joseph, et al., 2006). By reducing the dimensions of the channels to the submicron and nano-scales, these theories may not be applicable anymore. Mostly, this is because the ion distribution in the nanochannel cannot be described by Boltzmann distribution, and hence the electric field generated by the nanochannel's surface charge does not obey the Poisson-Boltzmann equation. The current understanding of the electrokinetic effects in the nanochannels is very limited.

In modeling the electrokinetic flow in the microchannels, the Boltzmann distribution is one of the fundamental equations. The Boltzmann distribution requires a semi-infinite large liquid phase, the equal number of co-ions and the counter-ions in positions sufficiently far away from the charged surface, and no significantly overlapped electric double layer fields. However, all these key assumptions are not valid for the smaller nanochannels. For example, the concentrations of co- and counter ions are not equal in the nanochannels (Zangle, et al., 2010). Since the Boltzmann distribution is not valid, the Poisson-Boltzmann equation cannot be used to describe the electric field in the small nanochannels. Furthermore, there is an essential difference in defining the electrical boundary condition between the microchannels and the nanochannels. In the microchannels, the Poisson-Boltzmann equation can be utilized to obtain a relationship between the surface electric

* A version of this Chapter has been published in Electrophoresis Journal as: "Saeid Movahed, Dongqing Li 'Electrokinetic Transport through Nanochannels', Electrophoresis Journal, Wiley, 2011, Vol. 32, No. 11, pp.: 1259-1267". The licence agreement of reprinting this article in the current dissertation has been presented in Permissions section (License Number: 2936541284804).

charge and the surface electric potential, approximately the zeta potential. That is, fixing the surface electric charge is equivalent to fix the zeta potential (Li, 2004). Therefore, a constant zeta potential is usually used as the boundary condition to solve for the electric double layer field in the microchannels. However, in the small nanochannels, because the Poisson-Boltzmann equation is not valid, the surface electric charge, via the use of the Poisson equation, can relate only to the electric potential gradient at the charge surface, not the zeta potential.

Thus, the zeta potential cannot be used as the boundary condition for the electric field in the small nanochannels. Instead, the surface electric charge should be utilized as the electrical boundary condition at the walls of the nanochannels. By considering these facts, the conventional theories of the electrokinetic flow are no longer valid in the nanochannels.

Some studies have been conducted to model and simulate the electrokinetic effects in the nano-scale channels. Several of them are based on the Poisson-Boltzmann equation (Behrens, et al., 1999; Petsev, et al., 2006; Rice, et al., 1965; Wan, 1997). The Boltzmann distribution is derived under the following boundary conditions: At positions infinitely far away from the charged solid surface, 1- the electric potential is zero, and 2- the bulk solution is electrically neutral or has zero net charge. However, in the nanochannel with significantly overlapped electric double layers, the above conditions do not exist. Therefore, the Boltzmann equation and hence the Poisson-Boltzmann equation are no longer valid in nano-scale channels. A widespread numerical technique used to model the electrokinetic effects in the nanochannels is molecular dynamics simulation (Qiao, et al., 2003; Qiao, et al., 2002; Qiao, et al., 2005). Using this method, Qiao and Aluru modeled ion distribution and velocity profiles for the electroosmotic flow in the nanochannel (Qiao, et al., 2003). They proposed electrochemical potential correction term to modify Poisson–Boltzmann equation and predict the ion distribution with good accuracy; however, they considered only the presence of the counter-ions in their simulations. By using this technique, they also studied the transient response of the electroosmotic flow in the nanochannels (Qiao, et al., 2002). However, it must mention that molecular dynamics technique needs huge computational effort and may not be practical for larger computational domains. In 2000, Freund studied the electroosmotic flow in the nano-scale channels (Freund, 2000). In this study, the author only considered the effects of counter-ion on liquid flow; they also utilized the Poisson-Boltzmann equation to find the ionic distribution and the electric potential. Some studies have been conducted to investigated EDL overlapping for simple cases of long and slit nanochannels (Baldessari, 2008; Baldessari, 2008; Pennathur, et al., 2005; Pennathur, et

al., 2005); however, the results of these studies cannot be used for the nanochannels with sharp changes in geometry such as microchannel-nanochannel connection or three-dimensional nanochannels.

Several new studies utilized the Poisson-Nernst-Plank equations to model the electrokinetics in the nano-scale channels. These studies are usually based on two dimensional modeling or did not consider the effect of convection on ion mass transfer. For example, *Choi* and *Kim* used a two-dimensional model to investigate the electrokinetic effects in the slit nanochannel (Choi, et al., 2009). In 2008, Cheng investigated the electrokinetic ion transport in a one-dimensional slit nanochannel (Cheng, 2008). However, this study did not present any results for the flow (velocity) field. The more accurate study on the electrokinetic effects in the nano-scale channels was performed by Vlassiouk et al. (Vlassiouk, et al., 2008). However, in that study, the authors did not consider the effect of the electroosmosis on the ion transfer; therefore, the Poisson-Nernst-Plank and the Navier-Stokes equations became decoupled. In this way, it dramatically decreased the difficulties associated with the numerical simulations. At the end of mentioned article, the authors showed that their approximation (neglecting the effect of the electroosmosis on the ion mass transfer) can contribute 20% to the total current (the ion mass transfer). In addition, at the exit of the nanochannel to the microchannel, they could not model concentration polarization effect that was experimentally shown in the other studies (Zangle, et al., 2010; Kim, et al., 2007).

It is highly desirable to study the electrokinetic effects in three-dimensional nano-scale channels in order to improve the current understanding in this field. For the small nanochannels, the Poisson-Nernst-Plank equations along with the modified Navier-Stokes equation and the continuity equation must be solved in order to find the ionic mass transfer, the electric field, and the velocity field. These governing equations are highly coupled and the results are affected by all these equations and the corresponding boundary conditions. This chapter considers one circular cross-section and three-dimensional nanochannel connected to two reservoirs at the ends. The Poisson-Nernst Plank, the Navier-Stokes, and the continuity equations are solved simultaneously to calculate the electric potential, the ionic concentration, and the fluid flow in the nanochannel. The remaining of this chapter is organized as follow: Section 4.2 presents the mathematical model of the electrokinetic effects in the nanochannels. Section 4.3 explains the details of numerical method. The results are described and discussed in Section 4.4 and the concluding remarks are provided at the end of the chapter.

4.2 Mathematical Modeling

Figure 4.1 depicts the nanochannel system of this study. A nanochannel with circular cross sectional area of radius a and length L connects two reservoirs. The nanochannel and the reservoirs are filled with an aqueous solution ($NaCl$). Contact between the aqueous solution and the wall of the nanochannel brings about the surface electric charge on the wall. Application of electric potential at the two ends of the nanochannel causes liquid flow and the ionic mass transfer through the nanochannel (the electrokinetic effects).

In the nanochannels, the electric double layer thickness cannot be ignored in comparison with the channel dimensions. For the smaller nanochannels, the electric double layer fields may overlap significantly. Unlike a bulk solution, the electric double layer has substantially different numbers of co-ions and counter-ions. Therefore, the ionic concentration of the co-ions and the counter ions are not the same through the smaller nanochannels. This may cause concentration polarization at a connection of the nanochannel to the reservoirs (Zangle, et al., 2010).

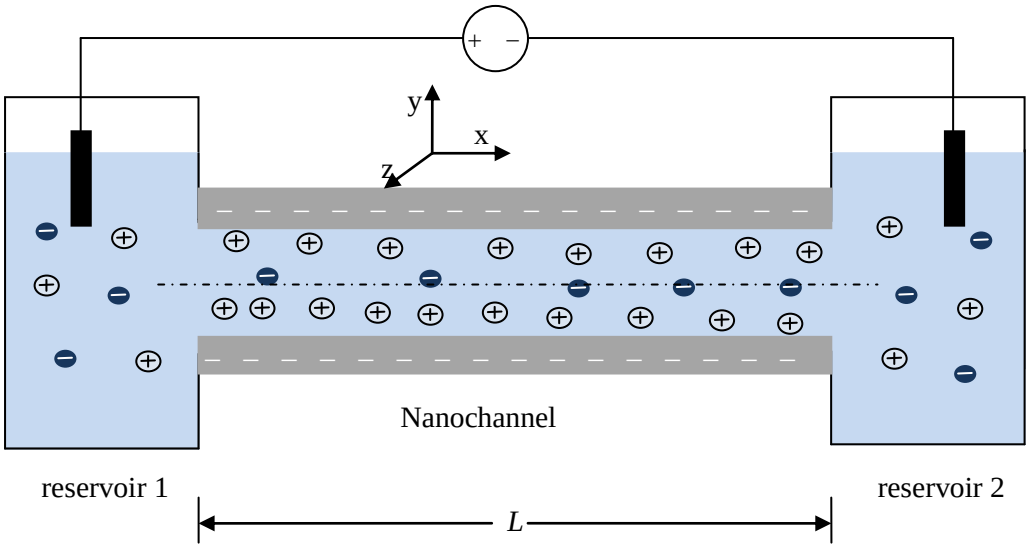

Figure 4-1 Schematic diagram of the assumed system of this study. Two reservoirs are connected to each other by a circular nanochannel of length *L* and radius *R*. Two electrodes located in the reservoirs apply electric potential to the ends of the nanochannel.

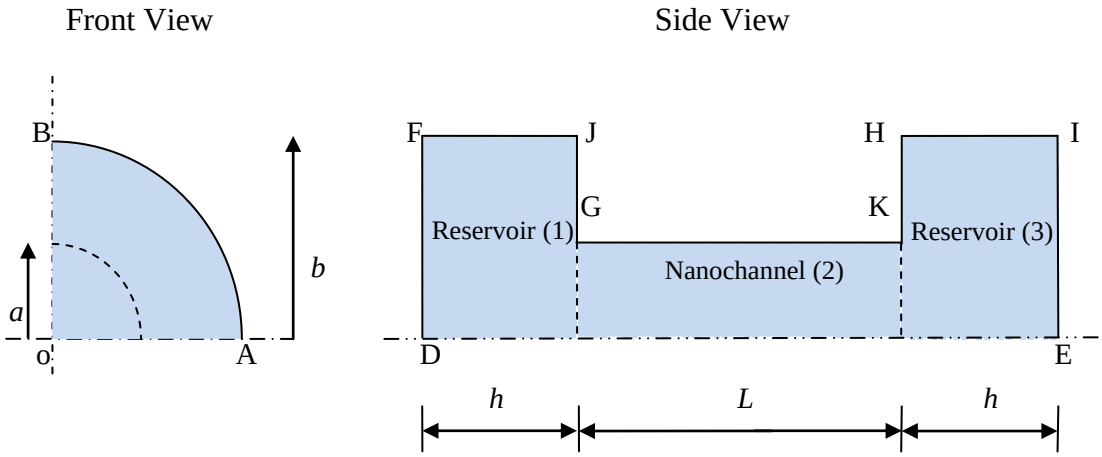

Figure 4-2 This figure depicts the computational domain of the present study. Taking the advantage of symmetric boundary conditions, only a quarter of the domain is simulated.

In the governing equations presented in the following sections, ϕ is the electric potential, E is the electric field, c_i is the concentration of ion species i, and also p and $\vec{u}$ are the pressure and the velocity vector, respectively. The constants include permittivity ($\varepsilon_0\varepsilon_r$), medium density ($\rho$), Faraday number ($F$), fluid viscosity ($\eta$) and valance number ($z_i$), diffusion coefficient (D_i), and mobility (μ_i) of ion species i. The values of these constants and parameters are listed in Table 4.1.

4.2.1 Electric Field

The electric field in the computation domain can be described as follows. In such a nano-scale channel, the Poisson equation must be solved in order to find the electric potential. As seen from Eq. (4.1), the Poisson equation is a function of the local ionic concentrations. The electric field is the gradient of the electric potential (Eq. (4.2)).

$$-\nabla(\varepsilon_0\varepsilon_r\nabla\phi) = F\sum_i z_i c_i \tag{4.1}$$

$$E = -\nabla\phi \tag{4.2}$$

The surface electric charge is utilized as one boundary condition. In the present study, the following equations are applied at the boundaries *GK* (the nanochannel wall), *JG*, and *KH* to set the electrical boundary condition:

$$\vec{D} = \varepsilon\varepsilon_0\vec{E} \tag{4.3}$$

$$\vec{n}\bullet\vec{D}(r) = \sigma_0 \tag{4.4}$$

The electric potential at boundaries *FD* and *IE* (the reservoirs) is set as follow:

$$\phi = \phi_0 \tag{4.5}$$

The symmetric condition is applied at boundaries *OA*, *OB*, and *DE*. The zero charge condition is employed at the other boundaries (*FJ* and *HI*). Following equation is used for these two types of boundary conditions (symmetric and zero charge):

$$n\bullet D = 0 \tag{4.6}$$

4.2.2 Ionic Concentration Field

Equation (4.7), the Nernst-Plank equation, is used to describe the mass transfer in the computation domain.

$$\nabla\bullet(\vec{u}c_i) - \nabla\bullet(D_i\vec{\nabla}c_i) - \nabla\bullet(z_i\mu_i c_i\nabla\phi) = 0 \tag{4.7}$$

In this equation, first term is the effect of the electroosmosis on the ionic mass transfer. The second and the third terms present the influences of diffusion and the electrophoresis on the ionic mass transfer, respectively. The Nernst-Plank equation is the general form of Boltzmann distribution. By neglecting the effect of convection ($\nabla\bullet(\vec{u}c_i)$) on ionic mass transfer, the Nernst-Plank equation is simplified to Boltzmann equation. However, it will be shown in Chapter 5 that the influence of convection on the ionic mass transfer through the nanopores is not negligible compare with electrophoresis. Increase of the size of nanochannels is also intensified the impact of convection on ionic mass transfer. Thus, Boltzmann distribution, and consequently Poisson-Boltzmann equation, may not be applicable in the nanochannels.

At boundaries *FD* and *IE* (see Figure 4.2), a constant bulk ionic concentration c_0 is utilized (Eq. 4.8).

$$c = c_0 \tag{4.8}$$

The walls of the nanochannel (*GK*) and the reservoirs (*JG* and *KH*) are assumed to be impermeable for mass transfer. Symmetric boundary conditions are implemented at boundaries *OA*,

OB, *FJ*, *HI*, and *DE*. The following set of equations is employed for these two kinds of boundary conditions (impermeable and symmetric):

$$n \bullet \vec{N} = 0 \tag{4.9}$$

$$\vec{N} = -D_i \nabla c_i - z_i \mu_i c_i \nabla \phi + c_i \vec{u} \tag{4.10}$$

4.2.3 The flow field

Modified Navier-Stokes equations (Eq. 4.11) along with the continuity equation (Eq. 4.12) are solved in order to find the flow field in the system. At boundaries *FD* and *IE* we assumed the open boundary condition (Eq. 4.13). This type of boundary condition is usually used when the boundaries are connected to a large reservoir. The flow can either enter or exit from these boundaries. At the walls of the nanochannel (*GK*) and reservoirs (*JG* and *HK*) the no-slip boundary condition is assumed (Eq. 4.14). We also utilized the symmetric boundary condition (Eqns. 4.15 and 4.16) for boundaries *OA*, *OB*, *DE*, *FJ* and *HI*.

$$\rho((\vec{u} \bullet \nabla)\vec{u}) = -\nabla p + \eta \nabla^2 \vec{u} - (\sum\nolimits_i z_i F c_i) \nabla \phi \tag{4.11}$$

$$\nabla \bullet \vec{u} = 0 \tag{4.12}$$

$$\nabla \vec{u} = 0, \quad p = 0 \tag{4.13}$$

$$\vec{u} = 0 \tag{4.14}$$

$$n \bullet \vec{u} = 0 \tag{4.15}$$

$$t \bullet [-pI + \eta(\nabla u + (\nabla u)^T)] = 0 \tag{4.16}$$

4.3 Numerical Simulation

All the above-mentioned, highly-coupled equations were solved simultaneously with the corresponding boundary conditions, as described in the last section. The numerical simulation was conducted by using COMSOL Multiphysics 3.5a; we employ a mesh independent structure to make sure that the results are unique and will not change if any other grid distribution was applied. In order to discretize the solution domain, the structured meshes were applied. The solution domain is broken into small meshes to allow that the meshes fully cover the solution domain without overlapping. In order to find reliable results, which are grid independent, we examined the effect of different number of grids. Finally, we found the number of grids with which the numerical results will not change if we further increase the number of grids.

The transient period of the electroosmotic flow and the ionic mass transfer in the nano-scale channels is very small (usually on the order of μs or smaller) and is negligible. Therefore, we solved the Navier-Stokes and the Nernst-Plank equations in the steady state flow field. In order to verify the accuracy and correctness of our numerical approach, the governing equations were solved in the cross section of a slit nanochannel and the results were compared with the published result of Cheng (Cheng, 2008). As an example, Figure 4.3 depicts the electric potential obtained by the two different studies; the excellent agreement verifies our numerical method. This figure also shows the electric potential distribution predicted by the Poisson-Boltzmann equation. It is clear that there is a considerable difference between the results of the Poisson-Boltzmann model and the Poisson-Nernst-Plank and the Navier-Stokes equations. This is because in the nanochannel, there is significant EDL overlapping and hence the Poisson-Boltzmann equation is not valid.

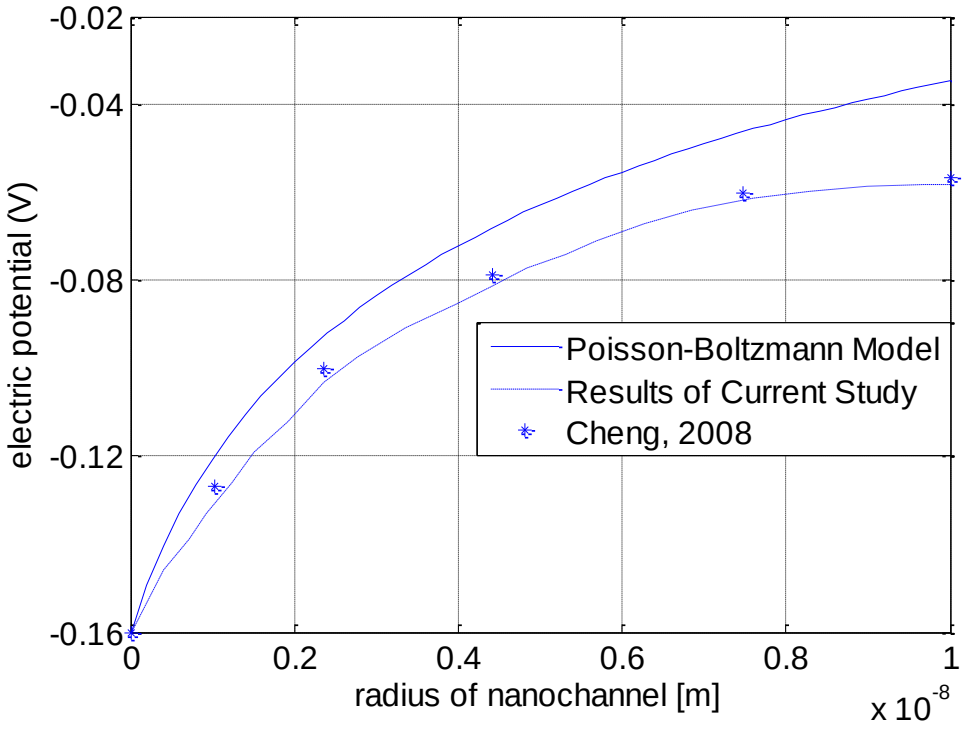

Figure 4-3 For one specific case of study (*KCl* aqueous solution in slit nanochannel, $C_0 = 1mM$, $h = 20nm$ and $\sigma_0 = -0.05 C/m^2$), this figure compares obtained electric potential from our numerical approach with published result by Cheng (Cheng, 2008) and PB model. In PB modeling, the ζ-potential is assumed to be equal to the numerical result of current study (–0.16 V).

Table 4-1The values for constants and parameters used in the simulations

Parameter	value/range	Unit
ε_T *(relative permittivity)*	80	-
ε_0 *(absolute permittivity)*	8.85×10^{-12}	*F/m*
ρ *(liquid density)*	1000	Kg/m^3
σ_0 *(surface electric charge)*	$-0.0001 \sim -0.001$	C/m^2
μ *(dynamic viscosity)*	1×10^{-3}	*Pa·s*
F(Faraday constant)	96485.3415	$A\bullet s/mol$
a (nanochannel radius)	$5 \sim 15$	*nm*
L (nanochannel length)	140	*nm*
D_+ *(diffusion coefficient of positive ion)*	1.28×10^{-9}	m^2/s
D_- *(diffusion coefficient of negative ion)*	1.77×10^{-9}	m^2/s
μ_i *(mobility of ion species i)*	$D_i/(R_g \bullet T)$	-
T (temperature)	300	*.K*

4.4 Results and Discussion

Table 4.1 summarizes the quantitative information used in our simulations. We consider *NaCl* aqueous solution. The characteristic parameters of Na^+ and Cl^- ions such as electrophoretic mobility and diffusion coefficient, can be found elsewhere (Li, 2004; Koneshan, et al., 1998). In the simulations, we assumed the nanochannels with three different radii (10 *nm*, *1*5 *nm*, and 20 *nm*). The electric potential at boundaries *FD* and *IE* (the two reservoirs) are 0 and –2 V, respectively. The bulk ionic concentration of the positive and negative ions at boundaries *FD* and *IE* is 1×10^{-3} mol/m^3. Three different values of –0.0001 C/m^2, –0.0005 C/m^2, *and* –0.001 C/m^2 are assumed for the surface electric charge.

4.4.1 Electric Potential

For different values of nanochannel radius and surface charge, Figure 4.4 depicts the variation of the electric potential along the centerline of the channel. Zones 1, 2 and, 3 represent reservoir 1, nanochannel, and reservoir 2, respectively. Figure 4.4a illustrates the effect of the radius on the electric potential drop. For a given value of surface electric charge ($-0.0005\,C/m^2$), the average slope of the potential curve decreases with the increase of the nanochannel`s cross section area.

(a)

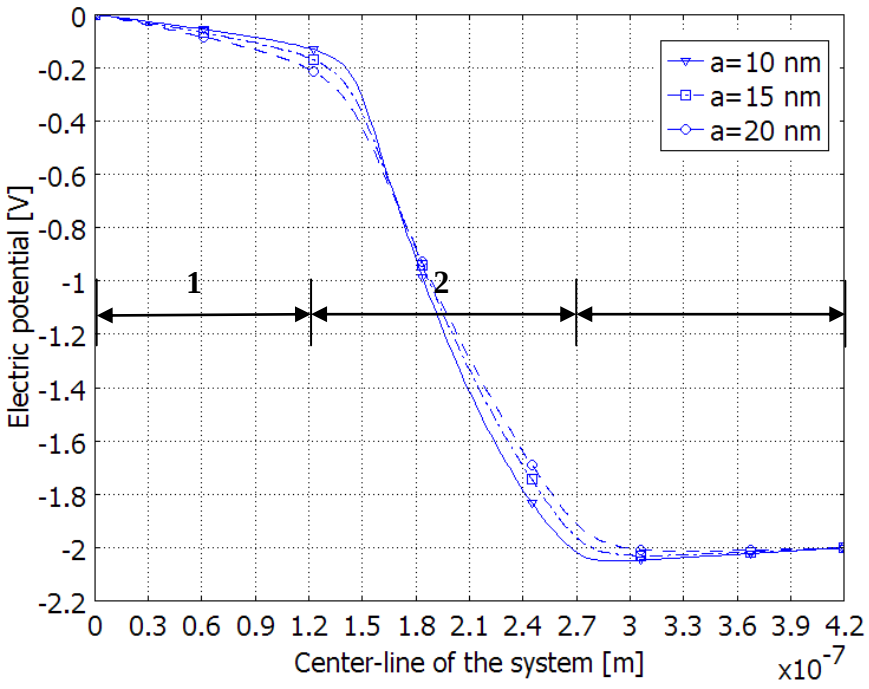

(b)

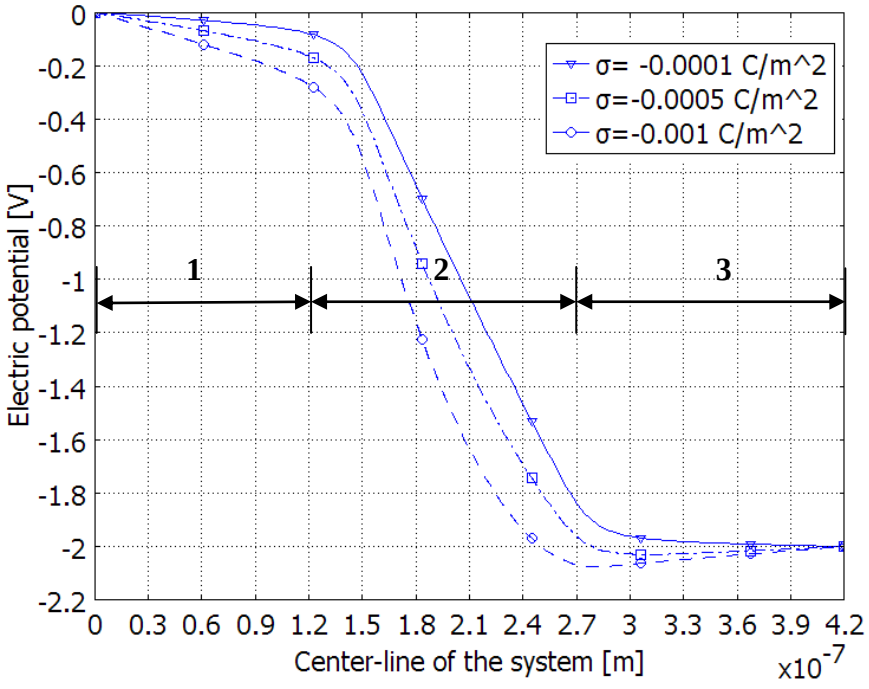

Figure 4-4 Electric potential along the center-line of the reservoir 1 (zone 1), nanochannel (zone 2), and reservoir 2 (zone 3). Figures (a) and (b) illustrate the effects of channel radius and surface electric charge on the electric potential, respectively.

Figure 4.4b illustrates the influences of the surface electric charge on the applied electric potential distribution along the centerline of the nanochannel. This figure shows that, for the given channel radius, increasing the value of the surface electric charge causes sharper decrease in the electric potential along the nanochannel. It should be pointed out that, in the microchannels, the applied.

Figure 4.5 shows the electric potential distribution in the cross section of the nanochannel at the middle of the nanochannel, position $x = 210nm$ (in the length of the nanochannel). From figure 4.5a, one can conclude that for the same value of the surface electric charge, the electric potential has different values when the radius of the nanochannel changes; for example, it has a smaller absolute value in a larger channel. It is also evident from this figure that the electric potential distribution in the channel`s cross-section is essentially a horizontal line in the smaller nanochannels, while slightly curved in larger channels. Figure 4.5b exemplifies that for the lower values of surface electric charge, the electric potential has a lower absolute value and tends to be a constant value in the cross section of the channel. For a larger surface charge, the electric potential is higher and tends to have a minimum absolute value in the central of the channel.

The dependence of the electric potential in the channel cross-section on the radius of the channel is one of the unique characteristics of the electrokinetic phenomena in the nanochannels. In the conventional electrokinetic theory, the surface electric charge and the surface electric potential can be related by using the Poisson-Boltzmann equation via the following equation (Li, 2004):

$$\sigma_0 = \frac{4n_\infty ze}{k}\sinh(\frac{ze\varphi_0}{2k_bT}) \tag{18}$$

Therefore, in the microchannels, once the surface charge is specified, the surface electric potential is a fixed value. The maximum value of the electrical potential in the channel's cross section is fixed, and will not change with the channel's radius. Clearly, this is not the case in the small nanochannels, as shown in Figure 4.5a.

(a)

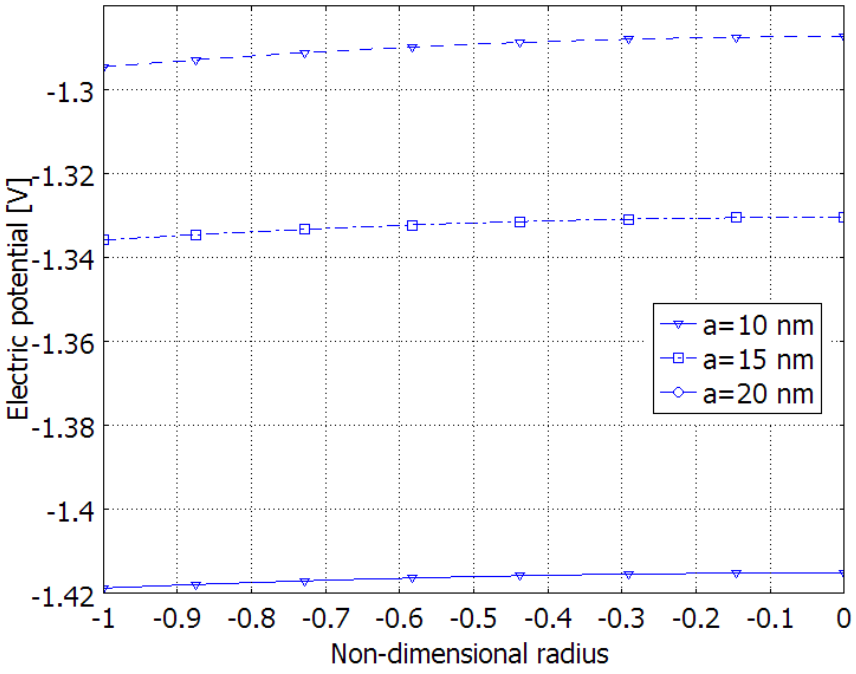

(b)

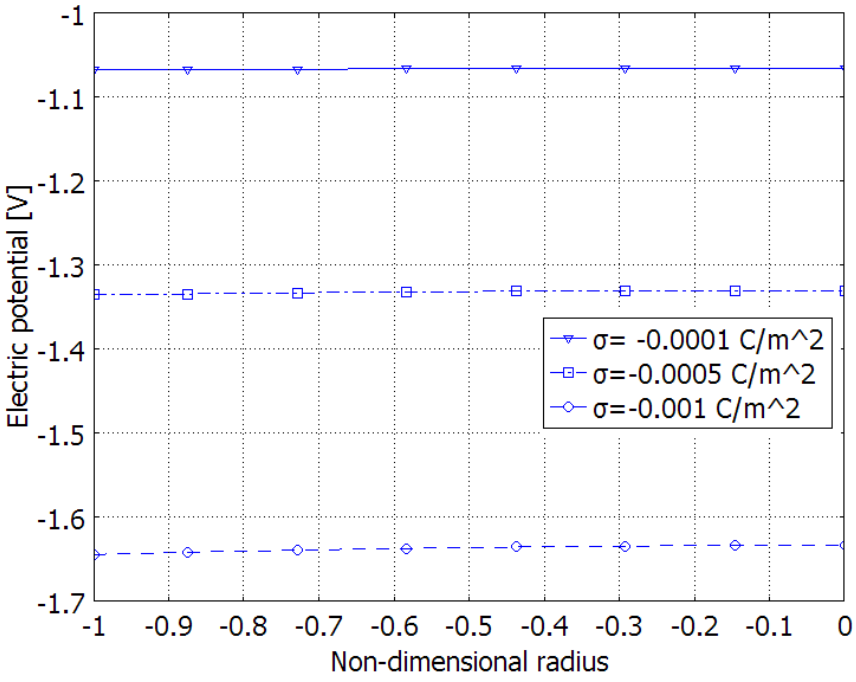

Figure 4-5 Electric potential at the cross section of the nanochannel. Figure 5 (a) and 5 (b) illustrate the effects of channel radius and surface electric charge on the electric potential, respectively.

4.4.2 Ionic Mass Transfer

One of the main differences of the electrokinetic flow through the micro- and nanochannels is concentrations of the positive and negative ions. As it was explained before, the concentrations of the co-ions and the counter-ions are substantially different in the EDL. In the smaller nanochannels, the EDL fields are significantly overlapped. Therefore, the co-ions and the counter-ions do not have the same concentration in the nanochannels. All parameters affecting the electric double layer in the nanochannel influences the concentrations of the positive and negative ions. As an example, consider negatively charged walls of the nanochannels. With the flow, the ions transported through the nanochannel are mostly positive ions (counter ions). Increasing the value of the surface electric charge intensifies the negative electric potential in the channel (see Figures 4.4b and 4.5b), therefore, increases the difference between the transported positive and negative ions through the nanochannel. Alternatively, by decreasing the radius of the nanochannel, the ratio of the electric double layer thickness to the nanochannel cross sectional area increases; consequently, the electric double layer plays much more important roles in the nanochannel. The stronger the EDL field, the higher concentration of the counter-ions in the nanochannel. Consequently, there is a larger difference between the transported counter-ions and the co-ions through the smaller nanochannel. Figure 4.6 presents the concentrations of the positive and the negative ions at the centerline of the system. Figure 4.7 shows the concentration of the positive ions (counter ions) at the cross section of the nanochannel (x=210 *nm*). From these figures, it is clear that decreasing the radius or increasing the surface electric charge results in a larger (smaller) concentration of the positive (negative) ions in the nanochannel. This figure shows that the concentrations of the positive ions (counter-ions) at the exit of the nanochannel increases substantially. This is because of ion polarization and enrichment of the counter ions, and the phenomena was observed in a previous experimental study (Zangle, et al., 2010). Zangle et al. (Zangle, et al., 2010) showed experimentally the ion polarization and enrichment effect at the intersection of the microchannel and the nanochannel. There is a good qualitative agreement between our numerical simulation results and their experimental and numerical results.

(a)

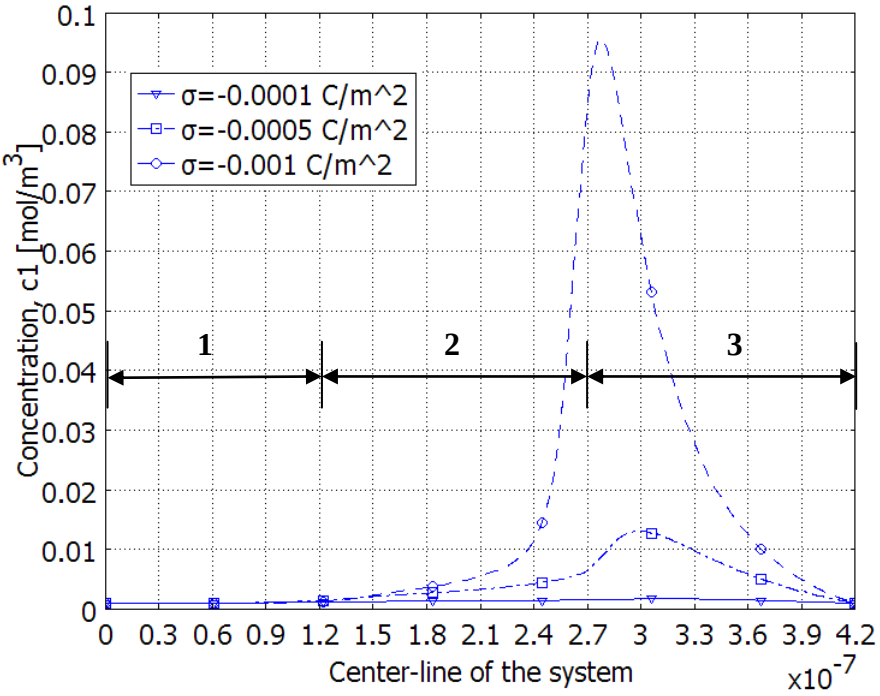
σ=-0.0001 C/m^2
σ=-0.0005 C/m^2
σ=-0.001 C/m^2
Concentration, c1 [mol/m^3]
Center-line of the system
x10^-7
1
2
3

(b)

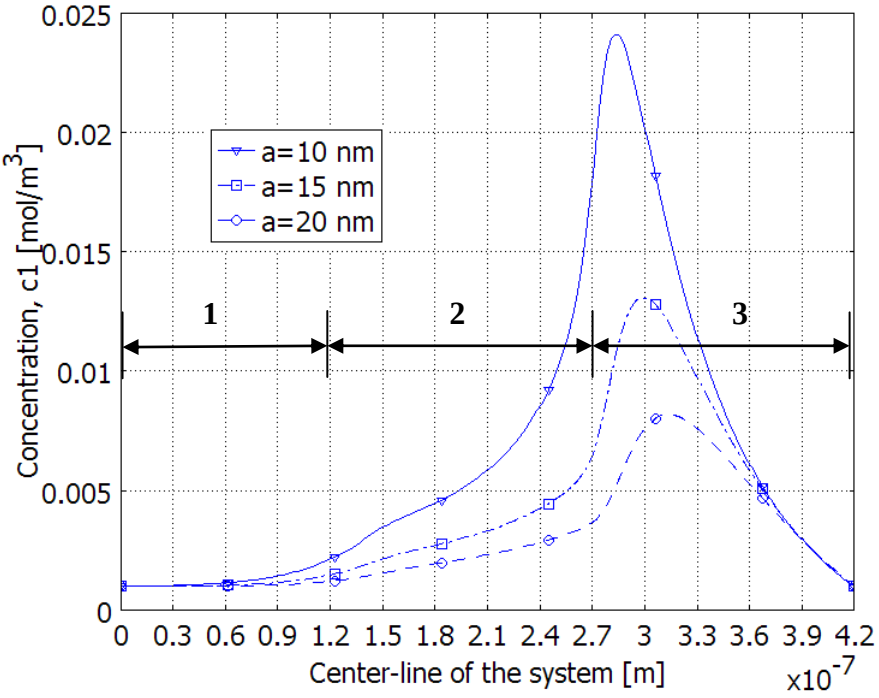
a=10 nm
a=15 nm
a=20 nm
Concentration, c1 [mol/m^3]
Center-line of the system [m]
x10^-7
1
2
3

(c)

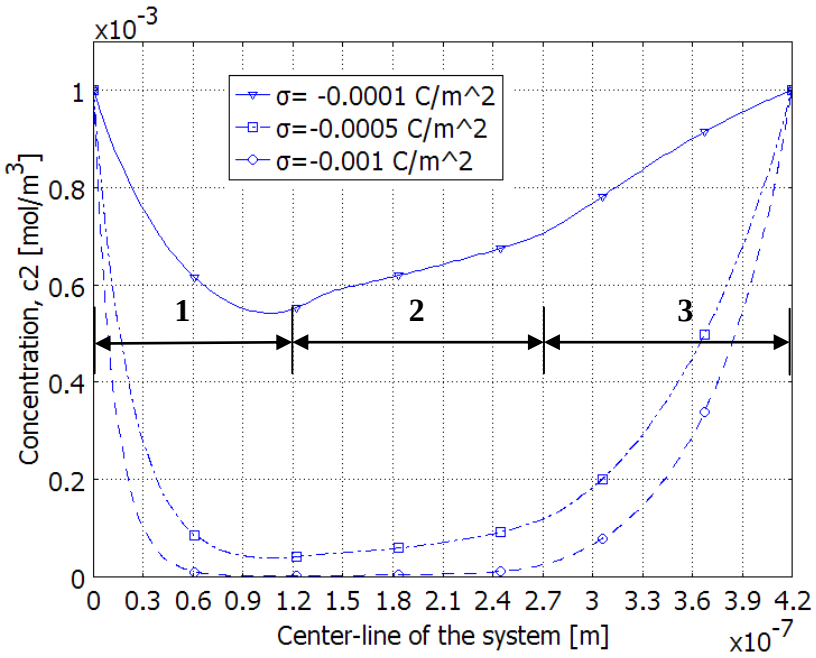

(d)

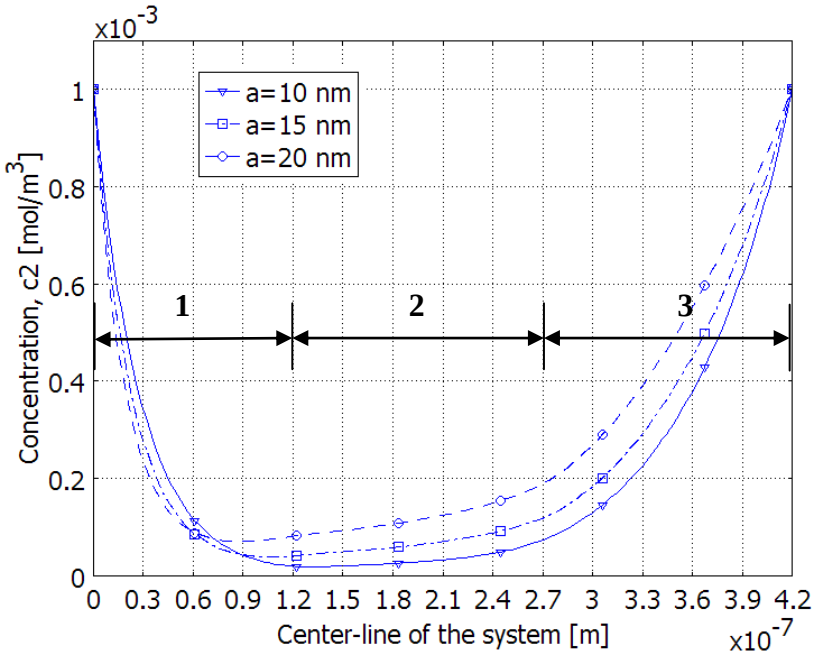

Figure 4-6 The concentrations of positive and negative ions at the centerline of the reservoir 1 (zone 1), nanochannel (zone 2), and reservoir 2 (zone 3). The effects of surface electric charge (a and c) and radius (b and d) on positive and negative ionic concentrations at the centerline of the system are shown from these figures.

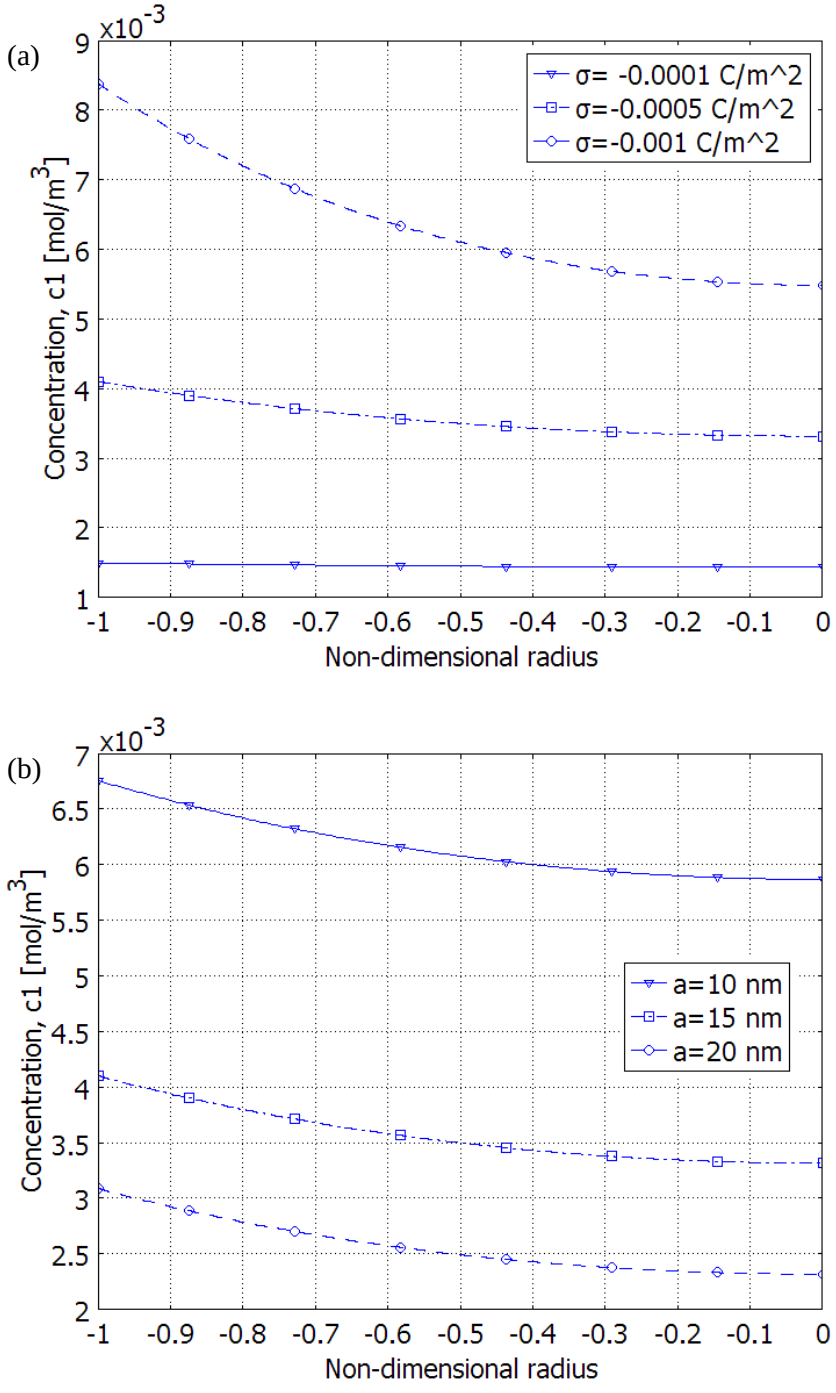

Figure 4-7 Distribution of positive ion (counter ion) at the cross section of the nanochannels (*x*=210 *nm*). The effects of surface electric charge (a) and radius (b) on the ionic concentration are clearly seen from these figures.

4.4.3 Flow Field

Figures 4.8 and 4.9 depict the velocity field at the centerline and the cross section of the nanochannels, respectively. Zones 1, 2, and 3 represent reservoir 1, nanochannel, and reservoir 2, respectively.

Figure 4.8a illustrates the impact of the radius of the nanochannel (cross-sectional area) on the flow field. From this figure, it is clear that by increasing the radius of the nanochannel (cross-sectional area), the velocity is also increased (while the surface electric charge, the applied voltage and, the nanochannel length are kept constant). For the smaller nanochannels, due to the ionic polarization of the nanochannel and the positive ion concentration enrichment at the exit of the nanochannel, a local electric potential minimum exists near the nanochannel exit. This creates a local electroosmotic flow in the opposite direction and consequently reduces the net flow in the applied electric field direction. As the radius of the nanochannel increases, the local electric potential minimum is smaller; correspondingly, the net electrokinetic flow velocity is higher. The effect of the surface electric charge on the fluid flow is showed in Figure 4.8b. For the fixed nanochannel dimensions (length and radius) and a fixed applied voltage difference, increasing the value of the surface electric charge increases the velocity through the nanochannel. This may be understood as the net charge density in the nanochannel is increased with the increase of the surface charge. These conclusions are also obvious from Figure 4.9. This figure shows the velocity field at the cross section of the nanochannel. Figure 4.9a shows that increasing the surface electric charge results in increasing the velocity field through the nanochannel. From Figure 4.9b, one can see that increasing the radius of the nanochannel (cross-sectional area) also raises the velocity in the system.

(a)

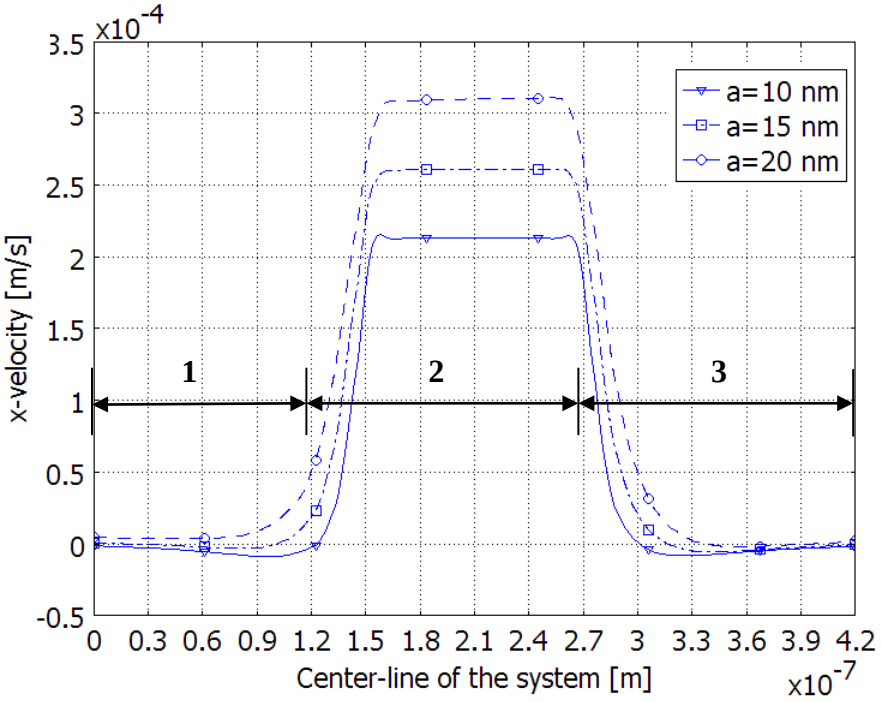

(b)

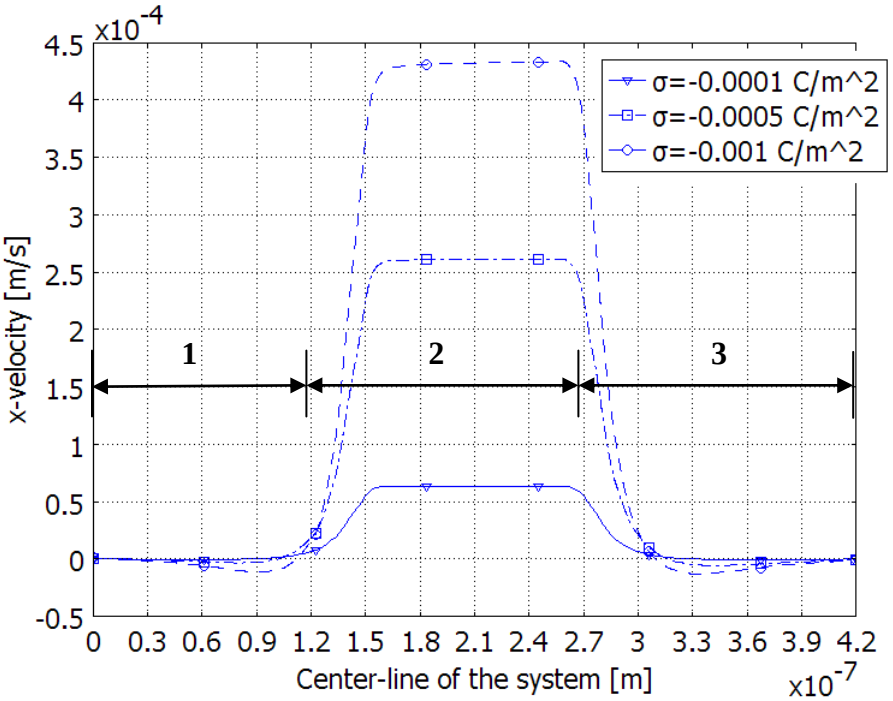

Figure 4-8 The velocity field at the centerline of the reservoir 1 (zone 1), nanochannel (zone 2), and reservoir 2 (zone 3). The effects of radius (a) and surface electric charge (b) on the velocity at the centerline of the system are clearly seen from these figures.

(a)

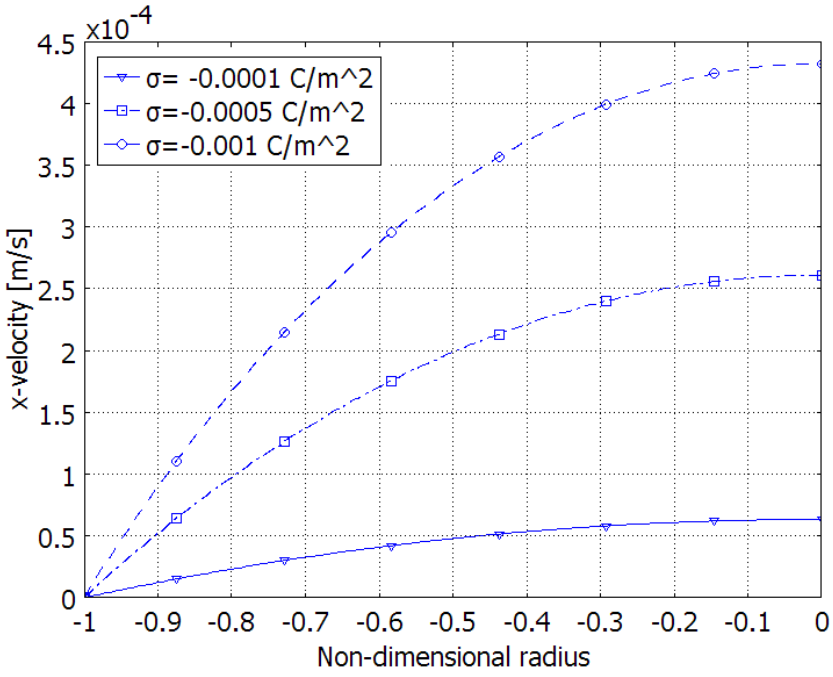

(b)

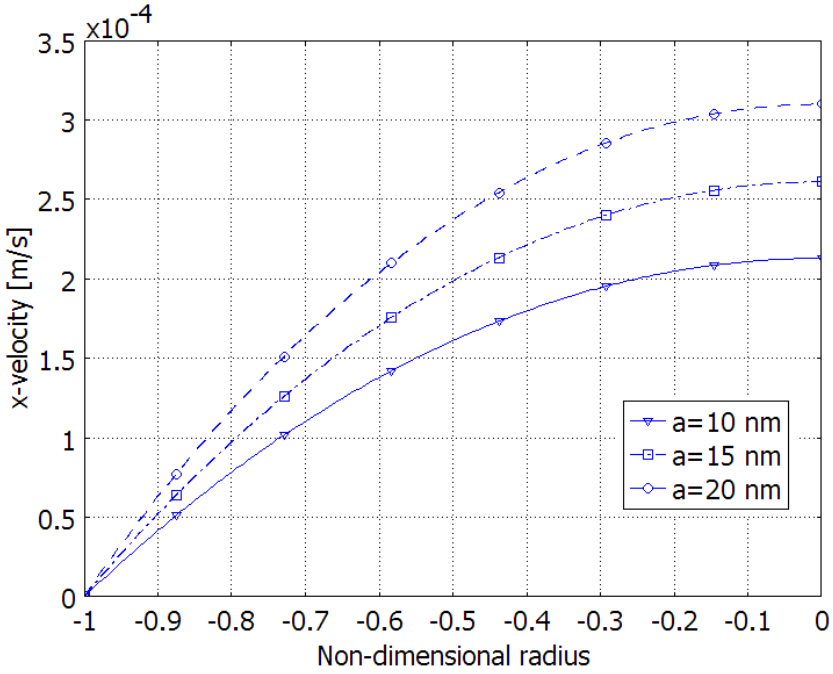

Figure 4-9 The velocity field at the cross-section of the nanochannel. This figure shows the effects of surface electric charge (a) and radius (b) on the velocity.

4.5 Concluding Remarks

Conventional electrokinetic theories, based on the Boltzmann distribution and the Poisson-Boltzmann equation, are not valid in the small nanochannels. A more general model employing the Poisson-Nernst-Plank equation coupled with the modified Navier-Stokes equation is used in this study to examine the electric potential, the ionic concentration, and the velocity field in the nanochannels. Unlike in the microchannels, the electric potential, the ionic concentration, and the liquid flow are strongly dependent on the nanochannel's cross section area (diameter), while the surface charge of the nanochannel wall is fixed. Higher values of the surface electric charge or the smaller nanochannels results in a significantly larger difference between the counter-ions and the co-ions in the nanochannel. The velocity of the electrokinetic flow in the nanochannel is larger for the higher surface electric charge and the bigger nanochannels.

Chapter 5
Electrokinetic Transport through the Nanopores in Cell Membrane during Electroporation*

5.1 Introduction

The underlying concepts of the membrane permeabilization and the cell electroporation have been introduced in Chapter 3. As it was indicated before, one of the most important applications of the cell electroporation is cell transfection: nanopores created in the cell membrane are used as a pathway to insert biological molecules into the cell. Although the cell electroporation was reported in early 70's (Neumann, et al., 1972), the first successful reversible electroporation and DNA electrotransfer can trace its roots back to thirty years ago, in 1982 (Neumann, et al., 1982). Nowadays, the microscale cell electroporation has been demonstrated to have the best cell viability and transfection efficiency among all recognized gene transfection methods (Lee, et al., 2009). More and more experimental studies on the microfluidic cell electroporation have been reported in recent years (Movahed, et al., 2011; Lee, et al., 2009; Wei, et al., 2011; Wang, et al., 2009; Zhan, et al., 2009; Fox, et al., 2006; Wang, et al., 2010).

As it was explained before, presence of applied electric field near the cell membrane causes the extra transmembrane potential, TMP (U_m), across the cellular membrane. If there is not any hydrophilic nanopore on the cell membrane, the TMP is linearly proportional to the cell radius and the external electric field (E_e). For the spherical cells surrounded by sufficiently high conductive media, the steady state TMP can be evaluated as $U_m = 1.5E_e a\cos(\theta)$, where E_e is the external electric field, a is the cell radius, and θ is the polar angle measured with respect to the direction of the external field E_e, see Figure 5.1. This equation is usually stated as the Schwan equation (Pauly, 1959). If the medium is not highly conductive, the constant of the Schwan equation should be less than 1.5. Excessive theoretical studies have been done to investigate the transient response of the Schwan equation (Kotnik, et al., 1998), also the effects of different parameters such as alternating the

* A version of this Chapter has been published in Journal of Colloid and Interface Science as: "Saeid Movahed, Dongqing Li, 'Electrokinetic Transport through the Nanopores in Cell Membrane during Electroporation' Journal of Colloid and Interface Sciences, Elsevier, 2012, Vol. 369, Issue 1, pp.: 442-452". The licence agreement of reprinting this article in the current dissertation has been presented in Permissions section (License Number: 3001440988704).

electric fields, the conductivity of the media, and the shape of the cell on the induced transmembrane potential (Marszalek, et al., 1990; Grosse, et al., 1992; Kotnik, et al., 1997; Kotnik, et al., 2000; Pucihar, et al., 2009). The sinusoidal dependency of TMP to the angular position on the cell membrane is proved experimentally (Gross, et al., 1986; Hibino, et al., 1991; Hibino, et al., 1993). TMP causes random hydrophobic pores in the cell membrane. These pores grow under the stress from TMP and become hydrophilic at the threshold value of $U_m = 0.5 \sim 1V$ (Fox, et al., 2006). Upon creating the first hydrophilic nanopore, the TMP remains constant in the vicinity of the created pores and further increase of the external electric field will no longer have any effects on the TMP. In this stage, further increase in the electric field has two effects: first, increasing the electroporated area (the area with hydrophilic nanopores) on the cell membrane; second, increasing the radius of the created nanopores (Escoffre, et al., 2007). Under the controlled condition (restricted pulse duration and intensity), these nanopores are reversible and can act as a pathway for either inserting hydrophilic molecules such as membrane-impermeant molecules (Wang, et al., 2008), gene (Fei, et al., 2007), and DNA plasmid (Kim, et al., 2007) to the cell or releasing internal contents of the cell (Bao, et al., 2008; Agarwal, et al., 2009). By removing the electric pulse, the hydrophilic nanopores are present on the cell membrane from seconds to minutes (Movahed, et al., 2011).

Many studies have been done on the creation of the nanopores. These studies have been reviewed extensively in Chapter 2. It was explained in section 2.2.2 that, because of the presence of the transmembrane potential, the electrokinetic effects may have considerable influence on the ion insertion and flow uptake of the cell. However, the current studies on the cell uptake do not consider the electrokinetic effects on the process.

Here, it should be pointed out that the influence of the electrokinetics is present until the end of the electric pulse. As it was indicated before, by removing the electric pulse, the hydrophilic nanopores are still present on the cell membrane from seconds to several minutes. In this stage, diffusion may play the decisive role on ion insertion. Nevertheless, the effect of the electrokinetics is not negligible on the cell transfection. Because the nanometer dimensions of the created pores, the conventional electrokinetic theories such as Helmholtz Smoluchowski model are not applicable. In these small nanochannels, the electric field generated by the surface charge and the ionic distribution no longer obeys the Poisson-Boltzmann model (Li, 2004; Li, 2008). However, previous experimental studies show that the continuum assumption for liquid flow of aqueous solution is valid in the channels as small as 4nm (Zheng, et al., 2003).

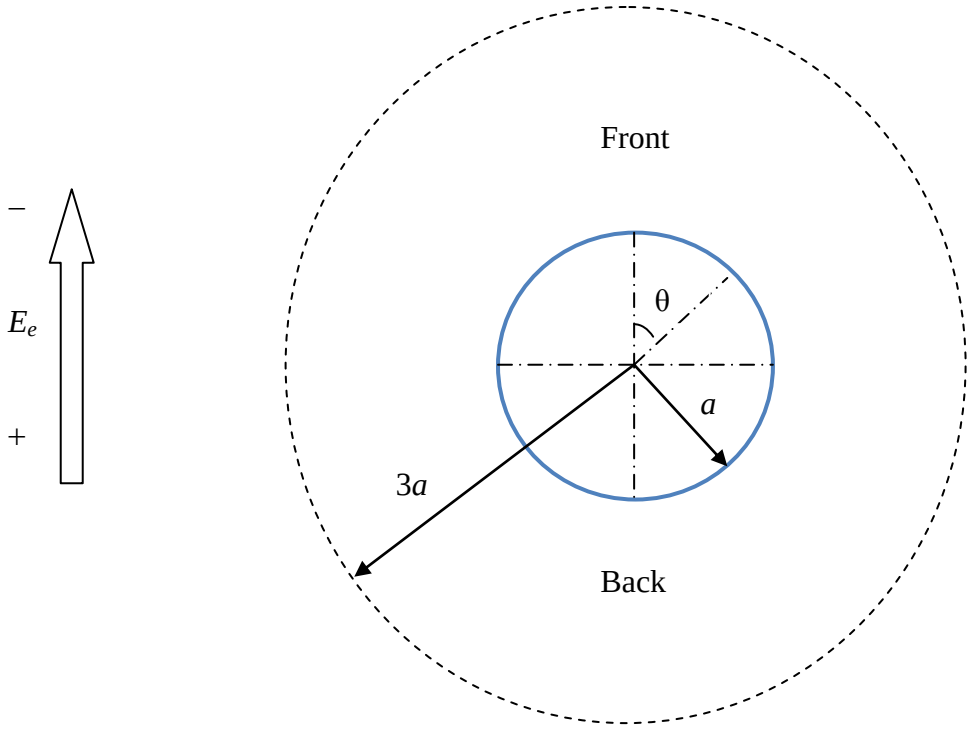

Figure 5-1 The schematic diagram of the circular cell exposed to the external electric field. The arrow indicates the direction of external electric field (E_e) and θ is the polar angle determines the location of nanopore on cell membrane. Radius of the cell is *a*. To find the electric potential around the cell, it is assumed that the cell is immersed in a spherical shell of extracellular fluid of thickness 2*a*.

In chapter 4, we studied the electric potential, the ion distribution, and the flow field in the nanochannels by solving the set of highly coupled partial differential equations including the Poisson equation, the Nernst-Planck equation, the modified Navier-Stokes equations, and the continuity equation. We have shown that unlike microchannels, the electric potential, the ionic concentration, and the velocity fields of the electroosmotic flow are strongly size-dependent in the nanochannels. In the present chapter, the ionic transfer and the flow uptake to the cell through the nanopores are investigated during the presence of the electric pulse. First, the mathematical model of the electrokinetic mass and momentum transfers in the nanopores is presented. Then, the numerical

method utilized in the present study is introduced. Finally, the effects of different parameters such as the location of the nanopores in the cell membrane, and the nanopore size on the ionic mass transfer and the liquid flow in the nanopores are examined. The effects of the electroosmosis, the electrophoresis, and the diffusion on the ionic mass transfer through the created nanopores are compared.

5.2 Mathematical Modeling

The appearance of external electric field in a vicinity of cell surface can create hydrophilic nanopores in the cell membrane. These nanopores can serve as a pathway for ions and fluid transport. The flow and the ion transfer in such a nanoscale channel can be analyzed by a combination of equations governing the nanopore creation, the electrostatics, the mass transfer, and the momentum transfer. In the present study, we examine the mass and momentum transfer in one nanopore. Figure 5.2 depicts the computational domain. The pore is circular, and the length of the pore is equal to the cell membrane thickness. Taking advantages of symmetric boundary conditions, only a quarter of the domain is simulated. "Inside" and "outside" domains are considered in order to study the effects of interior and exterior of the cell on ionic mass transfer and the fluid flow through the nanopore.

As explained before, after the creation of the first hydrophilic nanopore, the transmembrane potential (TMP) around the electroporated area becomes constant and further increasing of the external electric field does not increase the TMP.

5.2.1 Electric Field around the Cell Membrane

In the present study, the same parameters (cell type, size, computational domain, and external electric field) as those in DeBruin's works (DeBruin, et al., 1999; DeBruin, et al., 1999) were used. A spherical cell of radius a suspended in a circular conductive medium of radius $3a$ and exposed to the electric field of strength E_e is considered. The intercellular and extracellular potential ϕ_i and ϕ_e can be calculated by solving Laplace equation ($\nabla^2\phi = 0$). The transmembrane potential (TMP) is applied at the cell membrane to relate the intercellular and the extracellular electric potentials. The transmembrane potential is the difference of intercellular and extracellular potentials at both sides of the cell membrane. At the non-electroporated areas, transmembrane potential (U_m) can be calculated by (DeBruin, et al., 1999; DeBruin, et al., 1999):

$$U_m = \phi_i(t,a,\theta) - \phi_e(t,a,\theta) = 1.5E_e a\cos(\theta) \tag{5.1}$$

As explained before, after the creation of the first hydrophilic nanopore, the TMP becomes constant and further increasing of the external electric field does not amplify the TMP. The transmembrane potential at the front and backside of the cell are assumed to be $+1V$ and $-1V$, respectively. As explained before, the same parameters as that used in DeBruin's work have been adopted in the present study (DeBruin, et al., 1999; DeBruin, et al., 1999); and the critical value of TMP has been assumed to be $1V$. However, the possible values for critical TMP are different from cell to cell and TMP threshold can be as low as 250 mV. Further information about the possible values of TMP can be found in Refs. (Teissie, et al., 1993; Kakorin, et al., 2003; Towhidi, et al., 2008). According to the results of DeBruin's works, if the applied external electric field is $40kV/m$, the electroporated areas are approximately between $-45° \le \theta \le 45°$ and $-135° \le \theta \le 135°$.

In order to consider the effect of applied external electric field (E_e), the following boundary condition is applied at $r = 3a$:

$$\phi = -E_e r\cos(\theta) \tag{5.2}$$

The results of this section are utilized to define the proper electrical boundary condition near the entrance and the exit of nanopores (more explanations are given below).

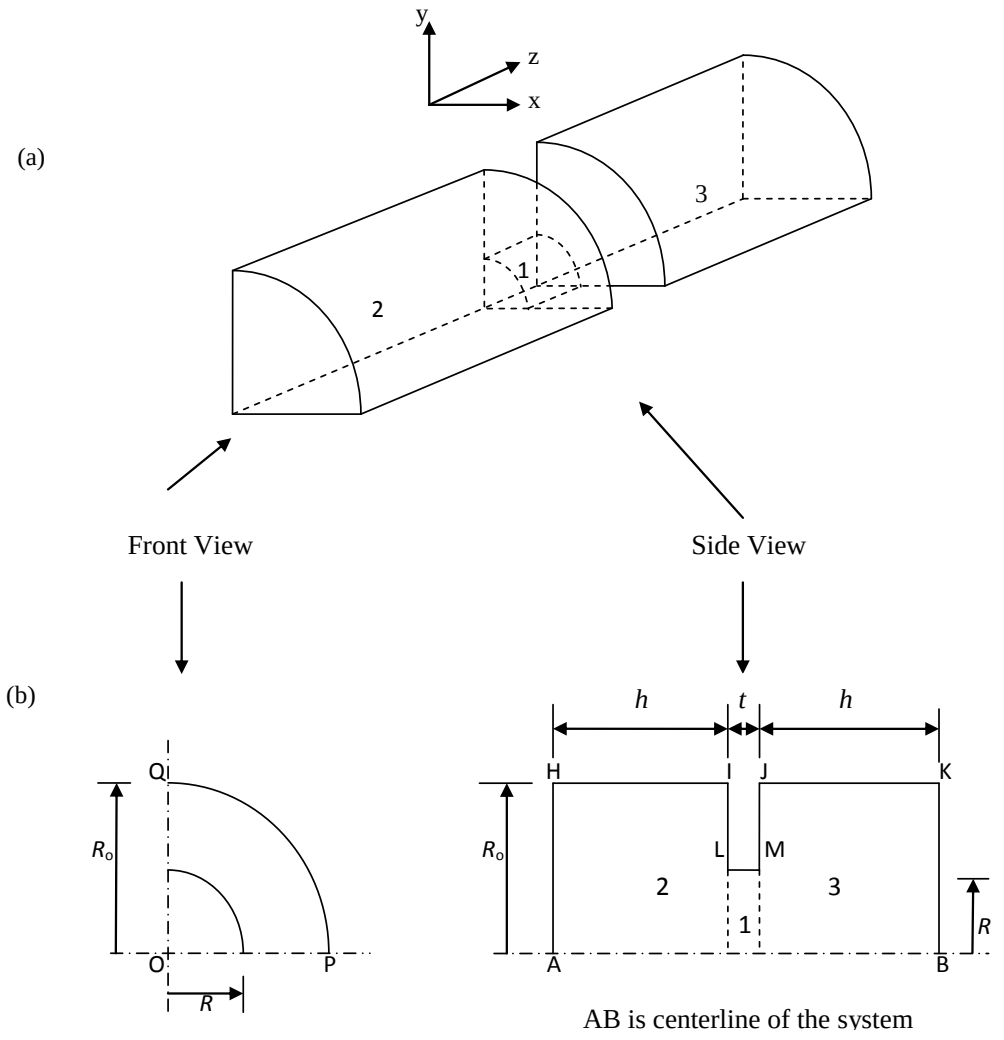

Figure 5-2 Schematic diagram of the computational domain. Parts (a) and (b) are 3-D and side-view illustrations of computational domain. Arrows show the view of each figures of part (b). With the advantages of symmetric boundary conditions, only one quarter of physical domain is simulated. The pore is circular with a radius R. The length of the pore is equal to the cell membrane thickness (t). h **is assumed to be ten times of the membrane thickness (** $h = 10t$ **). In order to consider the effects of interior and exterior of the cell on flow field and ionic mass transfer through the nanopore, "inside" and "outside" sections are considered. The radius at these parts is** R_o **.**

5.2.2 Electric Field through the Nanopores

The electric field in the computation domain can be described as follows. In the created nanopores, the electric double layer (EDL) thickness is not negligible in comparison with the nanochannel dimensions. Concentrations of co-ions and counter-ions are substantially different in the EDL. In the smaller nanochannels, the EDL fields are significantly overlapped. Therefore, the co-ions and the counter-ions do not have the same concentration in the nanochannels. In such nanoscale channels, the electric field no longer obey the Poisson-Boltzmann model which is derived under the assumption of an infinitely large liquid and by using the boundary condition of zero net charge at positions of infinitely far away from the charge solid surface. Because these conditions are no longer valid inside the small nanochannel, the Poisson equation ($\nabla\bullet(-\varepsilon_0\varepsilon_r\vec{\nabla}\phi)=F\sum_i z_i c_i$) must be solved in order to find the electric potential distribution in the nanochannel. This equation is a function of the local ionic concentrations. The electric field is the gradient of electric potential ($\vec{E}=-\vec{\nabla}\phi$). The electric field through the nanopores is influenced by the nanopores dimension, the ionic concentrations, and the surface charged of the nanopores. Here, z_i and c_i are the valence and concentrations of ion type i, ϕ is the electric potential, $\vec{E}$ is the electric field, ε_0 and ε_r are the absolute and the relative permeability, and F is Faraday constant.

As explained in the introduction, once the nanopores are created, the TMP no longer depends on the externally applied electric field and becomes constant and equal to the threshold value ($1V$). At the front of the cell, this threshold value is assumed to be $1V$, while at the back of the cell, the threshold TMP is set to $-1V$. TMP is the potential difference along the nanopore length direction. Inside the cell membrane, the electric potential is equal to rest potential ($\phi_{rest}=-80\,mV$); so, in the computational model the electric potential at boundaries *IL* and *MJ* become:

$$\phi_{MJ}=\phi_{rest} \tag{5.3.a}$$

$$\phi_{IL}=-U_m+\phi_{rest} \tag{5.3.b}$$

Here, it should again be mentioned that upon removing the electric pulse, TMP becomes zero and the electrokinetic effects vanish through the nanopores. However, at this stage the hydrophilic nanopores are still present on the cell membrane, and the diffusion may be the main means of the ion transportation through the nanopores.

The wall of the nanopore has electrostatic charge. In the conventional theory of the electrokinetics, the surface electric charge and the surface electric potential can be related by using the Poisson-Boltzmann equation (Li, 2004). However, in the small nanochannels, this equation is not valid anymore and the surface electric charge must be utilized directly in order to set the electrical boundary condition at the walls of the nanopores. If the constant surface electric charge density (ρ_s) is considered at the walls of the nanopore, following relations can be used to set the electrical boundary conditions at the walls of the nanopores (boundary *LM*):

$$D = \varepsilon\varepsilon_0 E \tag{5.4.a}$$

$$n\bullet D = -\rho_s \tag{5.4.b}$$

At boundary *AH* and *KB*, proper electric potentials (ϕ_1 and ϕ_2) should be applied in order to consider the effects of the external electric field (E_e) on the electrokinetic effects in the nanopore. These electric potentials are obtained from the results of the model described in section (5.2.1).

$$\phi_{AH} = \phi_1 \tag{5.5.a}$$

$$\phi_{KB} = \phi_2 \tag{5.5.b}$$

The symmetric condition is applied at boundaries *OP*, *OQ*, and *AB*. There is no surface electric charge at boundaries *HI* and *JK*. Following mathematical equations are used to model these two kinds of boundary conditions (symmetric and no surface electric charge):

$$n\bullet D = 0 \tag{5.6}$$

5.2.3 Ionic Concentration Field

The Nernst-Planck equation (Eq. (5.7)) is used to describe the mass transfer in the computation domain.

$$\nabla\bullet(\vec{u}c_i) - \nabla\bullet(D_i\vec{\nabla}c_i) - \nabla\bullet(z_i\mu_i c_i\nabla\phi) = 0 \tag{5.7}$$

In this equation, the first term is the effect of the electroosmosis (convection) on the ionic mass transfer. The second and the third terms present the influences of the diffusion and the electrophoresis on the ionic mass transfer, respectively.

The Nernst-Plank equation is the general form of Boltzmann distribution. By neglecting the effect of convection ($\nabla\bullet(\vec{u}c_i)$) on ionic mass transfer, the Nernst-Plank equation is simplified to Boltzmann equation. However, the results of this chapter show that the influence of convection on the ionic mass

transfer through the nanopores is not negligible compare with electrophoresis. Increase of the size of the nanochannels is also intensified the impact of convection on ionic mass transfer. Thus, Boltzmann distribution, and consequently Poisson-Boltzmann equation, may not be applicable in the nanochannels.

At boundaries *AH* and *KB*, constant bulk ionic concentration c_i is utilized (Eq. (5.8)). Here, subscripts i and e indicate the inside and the outside of the cell.

$$c = c_{0,i} \tag{5.8.a}$$

$$c = c_{0,e} \tag{5.8.b}$$

The walls of the nanopore (*LM*) and the cell membrane surface (*IL* and *MJ*) are assumed to be impermeable for mass transfer. The symmetric boundary conditions are implemented at other boundaries (*OP*, *OQ*, *AB*, *HI*, and *JK*). The following set of equations is usually employed for these two kinds of boundary conditions (impermeable and symmetric):

$$n \bullet N_i = 0 \tag{5.9}$$

$$N_i = -D_i \nabla c_i - z_i \mu_i c_i \nabla \phi + c_i \vec{u} \tag{5.10}$$

5.2.4 The Flow Field

Modified Navier-Stokes equations (Eq. (5.12)) along with the continuity equation (Eq. (5.11)) should be solved in order to find the flow field in the system. Boundaries *AH* and *KB* are assumed as the open boundary (Eq. (5.13)). This type of boundary condition is usually used when the boundaries are connected to a large reservoir (for example, comparing the volume of the nanopore with the interior of the cell). The flow can either enter or exit from these boundaries. At the wall of the nanopore (*LM*) and the surface of the cell (*IL* and *MJ*), no-slip boundary condition is assumed (Eq. (5.14)). We also utilized the symmetric boundary condition (Eqns. (5.15) and (5.16)) for other boundaries (*OQ*, *OP*, *AB*, *HI*, and *JK*).

$$\nabla \bullet \vec{u} = 0 \tag{5.11}$$

$$\rho\left(\frac{\partial \vec{u}}{\partial t} + (\vec{u} \bullet \nabla)\vec{u}\right) = -\nabla p + \eta \nabla^2 \vec{u} - \left(\sum_i z_i F c_i\right) \nabla \phi \tag{5.12}$$

$$\nabla \vec{u} = 0\,, \quad p = 0 \tag{5.13}$$

$$\vec{u} = 0 \tag{5.14}$$

$$n \bullet \vec{u} = 0 \tag{5.15}$$

$$t \bullet [-pI + \eta(\nabla u + (\nabla u)^T)] = 0 \tag{5.16}$$

In Eqs. (5.1) - (5.16), ϕ is the electrostatic potential and c_i is the concentration of ion species i; p and $\vec{u}$ are the pressure and the velocity vector, respectively. The constants include permittivity ($\varepsilon_0 \varepsilon_r$), medium density ($\rho$), Faraday number ($F$), fluid viscosity ($\eta$), valance number ($z_i$), diffusion coefficient (D_i), and mobility (μ_i) of ion species i.

5.3 Numerical Simulation

The details of the numerical solution of the governing equations have been explained in section 4.3. In this study, the interior of the cell can be considered as a big reservoir for the nanopores. The electroporation time span is not sufficiently long to change the ionic concentration inside the cell and far from the exit of the nanopores. Thus, in the computational domain, the parameter h is assumed to be sufficiently long ($h = 10 \times t$) and the boundary *KB* is located far from the exit of the nanochannel. Therefore, assuming constant bulk ionic concentrations for this boundary is reasonable, and the steady state Navier-Stokes and Poisson-Nernst-Planck equations are solved for the system in this study.

5.4 Results and Discussion

Table 5.1 summarizes the quantitative information used in the simulations. We consider a mammalian cell with radius 50 μm and the membrane thickness of 5nm (DeBruin, et al., 1999); the liquid is a mixture of $NaCl$ and KCl aqueous solutions. Cell electroporation is usually conducted in vitro. We can modify the extracellular ionic concentrations to appropriate values; however, the assumed ions (Na^+, K^+, and Cl^-) have predefined concentrations inside the cell. In the simulations, we consider the typical intercellular concentrations of these ions, see Table 5.1. The characteristic parameters of Na^+, K^+, and Cl^- ions such as the electrophoretic mobility, and the cell characteristics such as the radius, the membrane thickness, the rest potential, and the surface electric charge can be found elsewhere (Li, 2004; Taheri-Araghi, 2010; Lodish, et al., 2003; Koneshan, et al., 1998; Weaver, et al., 1996; Catacuzzeno, et al., 2008).

In the following four sections, the numerical simulation results of the electric potential, the ionic concentration, the ionic flux, and the velocity field through the nanopore created on the cell

membrane will be discussed. In the simulations, we assume the nanopores with three different values of radius (5 nm, 8 nm, and 10 nm) located in the front and the back of the cell (relative to the external electric field direction). The radius of the inside and the outside zones (see Figure 5.2) is assumed as 50 nm. Because the nanopores are created on the cell membrane, the TMP is fixed and equal to the threshold value (as explained before). In the present study, for the nanopores located at the front and the back of the cell, this threshold values are assumed to be $+1V$ and $-1V$, respectively.

Table 5-1 The values of the constants and parameters used in the simulations

Parameter	value/range	Unit
ε_T *(relative permittivity)*	80	-
ε_0 *(absolute permittivity)*	8.85×10^{-12}	F/m
ρ *(liquid density)*	1000	Kg/m^3
ρ_s *(surface electric charge density)*	–0.0001	C/m^2
T (temperature)	300	K
R_g *(universal gas constant)*	8.314	$J/mol.K$
$C_{o,i}(Na^+)$ (Lodish, et al., 2003)	*12*	mM
$C_{o,i}(K^+)$ (Lodish, et al., 2003)	*139*	mM
$C_{o,i}\ (Cl^-)$(Lodish, et al., 2003)	*4*	mM
$C_{o,e}(Na^+)$	*50*	mM
$C_{o,e}(K^+)$	*50*	mM
$C_{o,e}(Cl^-)$	*100*	mM
F(Faraday Constant)	*96 485.3415*	$A\bullet s/mol$
a (cell radius) (DeBruin, et al., 1999)	*50*	μm
t (cell thickness) (DeBruin, et al., 1999)	*5*	nm
R(radius of nanopore)	*5, 8, and 10*	nm
R_o *(radius outside of nanopore)*	*50*	nm
E_e *(external electric field)*	*40*	kV/m
$D\ (Na^+)$ (Koneshan, et al., 1998)	1.28×10^{-9}	m^2/s
$D\ (K^+)$(Koneshan, et al., 1998)	1.83×10^{-9}	m^2/s
$D\ (Cl^-)$(Koneshan, et al., 1998)	1.77×10^{-9}	m^2/s
μ_i	$D_i/(R_g\bullet T)$	-
TMP(front of the cell) When nanopore is formed	1	V
TMP(back of the cell) When nanopore is formed	–1	V

5.4.1 Electric Potential through the nanopores

Figure 5.3 show the electric potential distribution in the computational domain and along the center line of the nanopores (line *AB*). Here, a = 5nm, $\sigma_0 = -0.0001\,C/m^2$ and the nanopore is located at the back side of the cell (TMP= 1 *V*). In Figure 5.3, zones 1, 2, and 3 represent "outside the cell", "nanopore", and "inside the cell", respectively. In order to consider the effects of the external electric field (E_e) on the flow field and the ionic concentrations through the nanopores, the electric potentials at x=0 nm (boundary *AH*) and x= 105 nm (boundary *KB*) are determined by solving equations (5.1) ~ (5.4). Table 5.3 presents the quantitative values of these electric potentials.

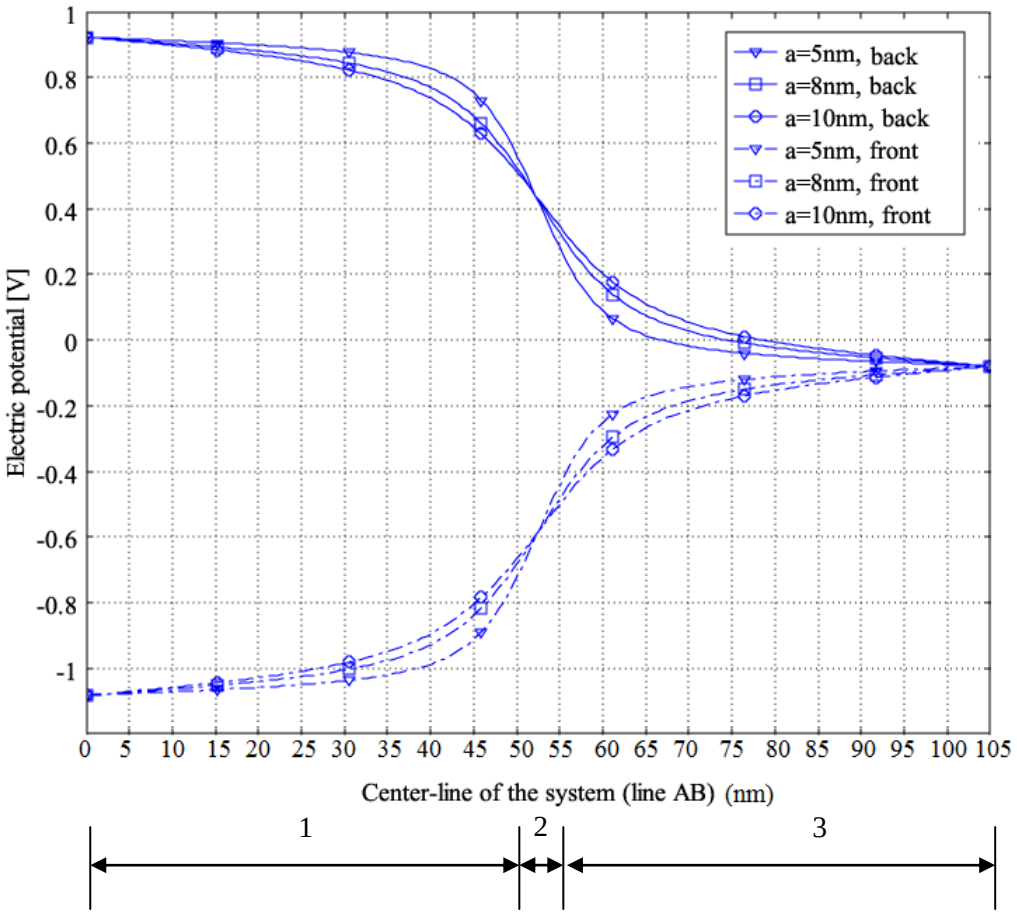

Figure 5-3 The electric potential distribution in the nanopores along the centerline of the nanopores. Zones 1, 2, and 3 represents outside the cell, nanopore, and inside the cell, respectively. The radius of the nanopore is 5 nm, $\sigma_0 = -0.0001\,C/m^2$, and the nanopore is located at the back side of the cell (TMP= –1 V).

The electric potential has sharp variation in zone 2 (through the cell membrane); this generates a considerably high electric field through the nanopores. Because of the difference in ionic concentrations of positive and negative ions, electric potential does not vary linearly in the nanopores. The substantially high electric field through the nanopores intensifies the impacts of electrokinetics on liquid flow and ionic mass transfer. This will be explained in the following sections.

5.4.2 Flow Field

Figure 5.4 depicts the velocity vectors of the flow field in the system. Here, the figure is captured from side-view (see Figure 5.2), $\sigma_0 = -0.0001\, C/m^2$, radius of the nanopores are 5 nm and 10 nm, and the nanopores are located at the backside of the cell membrane.

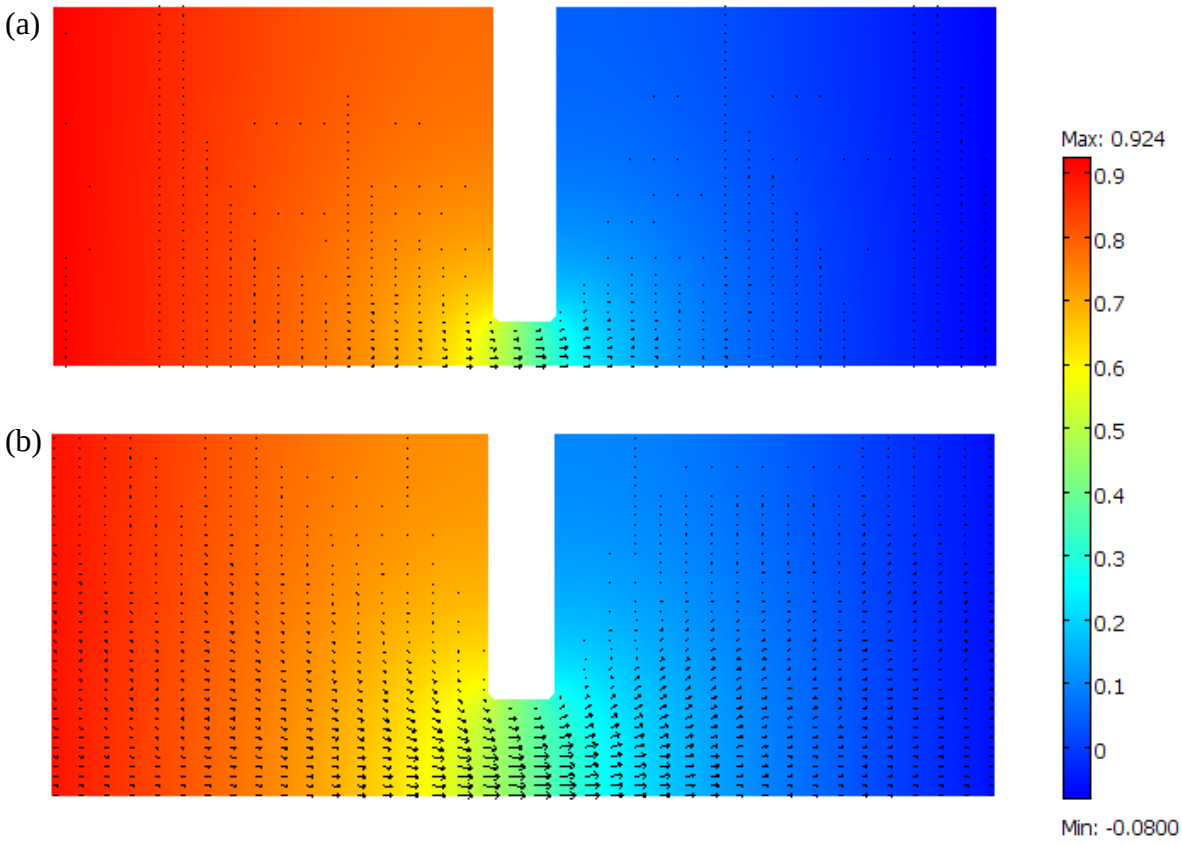

Figure 5-4 The side view of the velocity field and the electric field in the computation domain. The vectors represent the flow field, the color bar shows the scale for the electric potential. The radius of the nanopores are 5 nm (a) and 10 nm (b), respectively. $\sigma_0 = -0.0001\, C/m^2$, and the nanopores are located at the backside of the cell membrane.

Figure 5.5 shows the effects of the nanopores dimension and angular orientation on the velocity field. Tables 5.2 and 5.3 also present the quantitative values of the average velocity. In these figures and tables, the velocity field in the axial direction of the nanopores (x-direction) is averaged over the cross section of the nanopore. Positive (negative) sign of the averaged velocities means that the velocity field is from the outside (inside) to the inside (outside) of the cell membrane. Figure 5.6 shows that on each side of the cell, the angular orientation of the nanopores has small influence on the flow field. This can be explained as the TMP on the electroporated areas has the fixed values; only the electric potential at boundary *AH* slightly changes by angular orientation. The values of these electric potentials are presented in Table 5.3.

Figure 5.5 also shows that by increasing the dimensions of the nanopores, the average velocity in x-direction is also increased. To simplify the analysis of the velocity field in the nanopores, let us consider a one-dimensional slit nanochannel of height h. In the Appendix B of this manuscript, it has been shown that the averaged electroosmotic velocity at the center of such the slit nanochannel can be approximated as:

$$U_{EOF} = h^2 \times \overline{FE_x(z_i c_i)} \tag{5.17}$$

In this equation, z_i and c_i are the valance and the concentration of ions type - i , respectively. F is Faraday constant, E_e is external electric field, and h is the height of the nanochannel. As shown in Eq. (5.17), in addition to the applied electric field, the averaged electroosmotic velocity in the nanochannels is a function of the ionic concentrations of the co-ions and the counter-ions ($z_i c_i = c_{Na^+} + c_{k^+} - c_{cl^-}$) and the height of the nanochannel (h). By increasing the height of the nanochannel, the averaged axial velocity should also increase. The obtained numerical results also show this effect. Figure 5.6b (and also the results of Table 5.2) shows that by increasing the radius of the nanopores, the averaged axial velocity is also increased.

Table 5-2 Effects of nanopore radius on averaged velocity

	Radius (nm)	u (m/s)	Na^+ (mol/m^3)	K^+ (mol/m^3)	Cl^- (mol/m^3)
Front	5	-0.001693	0.054176	0.466591	1.266189
	8	-0.131462	0.180661	1.483154	2.06E+00
	10	-0.224252	0.242076	1.891859	2.632984
Back	5	0.178161	0.637799	0.529499	0.017929
	8	0.573485	1.033349	0.745952	0.059999
	10	0.971606	1.331049	0.831815	0.080416

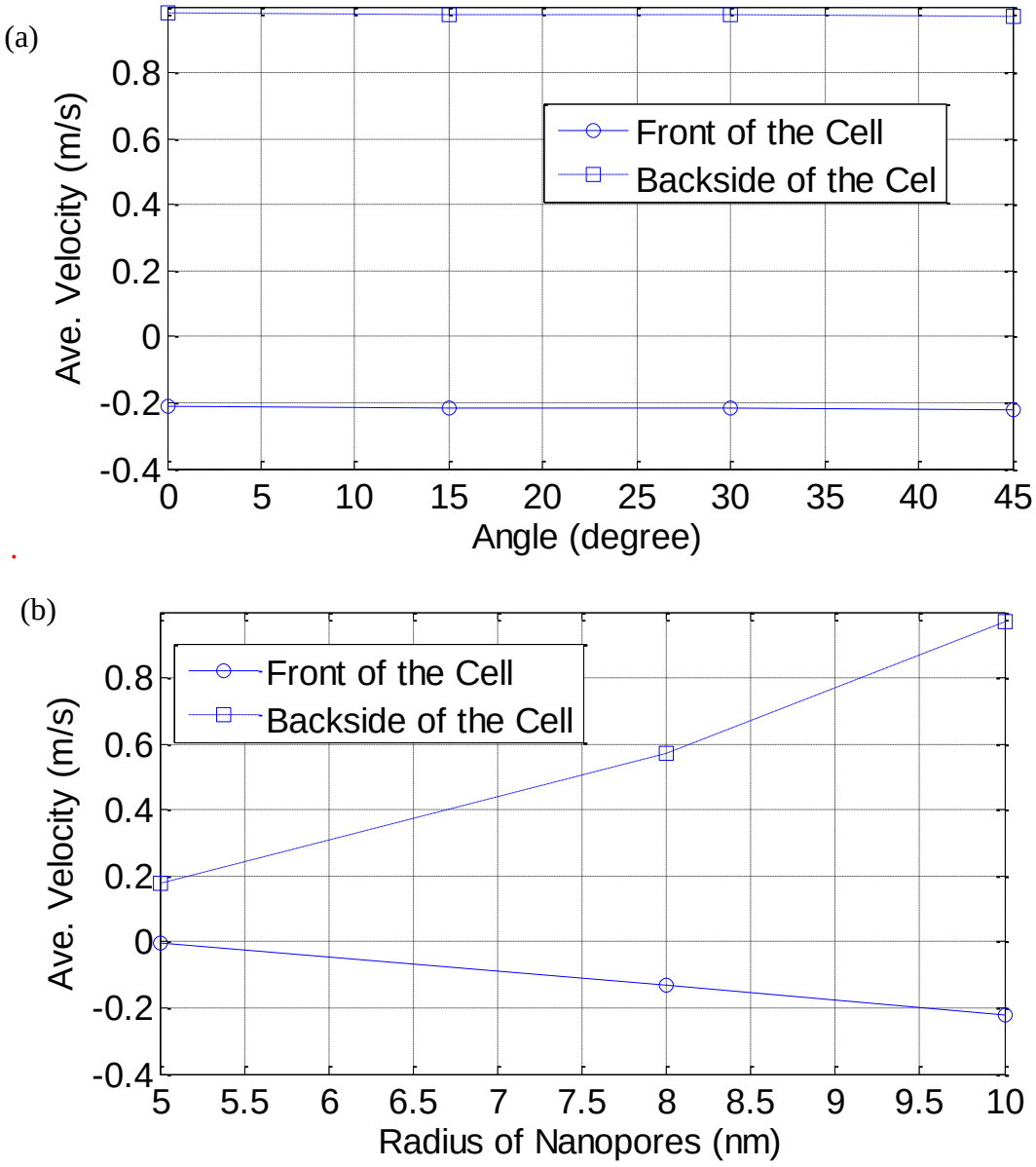

Figure 5-5 Averaged velocities at the cross section of the nanopores. In parts (a) and (b), radius and angle are 10 nm and 45˚, respectively. Here, angle is defined as θ and (π-θ) in front and backside of the cell membrane, correspondingly. It is clear that on each side of the cell, angular orientation of the nanopores on cell membrane has negligible effects on the flow field (5-5.a). Increasing the nanopore radius will result in escalation in averaged velocity (5-5.b).

Table 5-3 Effects of angular orientation of nanopores on flow field and ionic concentrations. Angle is defined as θ and (π-θ) in front and backside of the cell membrane, respectively. (r=10nm)

	Angle(degree)	ϕ_1 (V) *	ϕ_2 (V)**	u (m/s)	Na^+ (mol/m^3)	K^+ (mol/m^3)	Cl^- (mol/m^3)
Front	0	-1.0835	-0.08	-0.21286	0.242095	1.892151	2.673728
	15	-1.08335	-0.08	-0.21438	0.242091	1.892117	2.669082
	30	-1.0829	-0.08	-0.21828	0.242087	1.891946	2.657606
	45	-1.0826	-0.08	-0.22425	0.242076	1.891859	2.632984
Back	0	0.9237	-0.08	0.979437	1.344391	0.839993	0.080418
	15	0.9235	-0.08	0.977901	1.341965	0.838466	0.080408
	30	0.9231	-0.08	0.977901	1.341965	0.838466	0.080408
	45	0.92275	-0.08	0.971606	1.331049	0.831815	0.080416

* Electric potential at boundary *AH*

** Electric potential at boundary *KB*

The other parameters that affect the velocity field are the ionic concentrations of the positive and the negative ions ($c_{Na^+} + c_{k^+} - c_{cl^-}$). As it can be seen from the results of Tables 5.2 and 5.3, ($c_{Na^+} + c_{k^+} - c_{cl^-}$) has greater absolute values in the nanopores located at the backside rather than the front of the cell. This is why the absolute values of average velocity in the nanopores at the back of the cell are larger than the nanopores in the front of the cell.

5.4.3 Ionic Mass Transfer

Unlike the microchannels, the concentrations of the positive and the negative ions are not the same in the smaller nanochannels due to the overlapped EDL effect. The positive ions migrate in the direction of the electric field (e.g., from the positive to the negative electrodes). Negative ions migrate in the opposite direction of the electric field. For simplicity, in the Appendix B, it is shown that the ratio of the electroosmosis and the electrophoresis effects on the ionic flux through the slit nanochannels can be approximately estimated by the following equation.

$$\frac{\vec{N}_{eo}}{\vec{N}_{ep}} = \frac{\vec{u}}{z_i \mu_{m,i} F \vec{\nabla} \phi} \tag{5.18}$$

Clearly, in addition to the parameters in the numerator of Eq. (5.18), all parameters influencing the velocity will alter the ratio of the convective (electroosmotic) versus the electrophoretic mass transfer rates. Because of the strong electric field through the created nanopores during the electroporation

($\sim 2\times10^{7}\ V/m$), the electrokinetics (the electroosmosis and the electrophoresis) must have great influences on the ionic mass transfer rate. The diffusive mass transfer rate is negligible in comparison with the electrokinetic ones. In the present study, in order to compare the effects of the electroosmotic, the electrophoretic, and the diffusive mass transfer rates, we normalized their absolute values and studied the effects of the nanopore radius and its angular orientation on normalized convective, electrophoretic, and diffusive mass transfer rates. These normalized mass transfer rates are defined as:

Normalized electrophoretic mass transfer rate: $$\frac{\left|z_i\mu_{m,i}Fc_i\vec{\nabla}\phi\right|}{\left|c_i\vec{u}\right|+\left|D_i\vec{\nabla}c_i\right|+\left|z_i\mu_{m,i}Fc_i\vec{\nabla}\phi\right|}$$

Normalized diffusive mass transfer rate: $$\frac{\left|D_i\vec{\nabla}c_i\right|}{\left|c_i\vec{u}\right|+\left|D_i\vec{\nabla}c_i\right|+\left|z_i\mu_{m,i}Fc_i\vec{\nabla}\phi\right|}$$

Normalized convective (electroosmotic) mass transfer rate: $$\frac{\left|c_i\vec{u}\right|}{\left|c_i\vec{u}\right|+\left|D_i\vec{\nabla}c_i\right|+\left|z_i\mu_{m,i}Fc_i\vec{\nabla}\phi\right|}$$

Figure 5.6 illustrates the effects of the nanopore's radius and their angular orientation on the averaged ionic concentration through the nanopores. Tables 5.2 and 5.3 also show this information. From this figure, it is clear that increasing the nanopore radius will intensify the averaged ionic concentration through the nanopores. However, the angular orientation of the nanopores has less impact on the averaged ionic concentration.

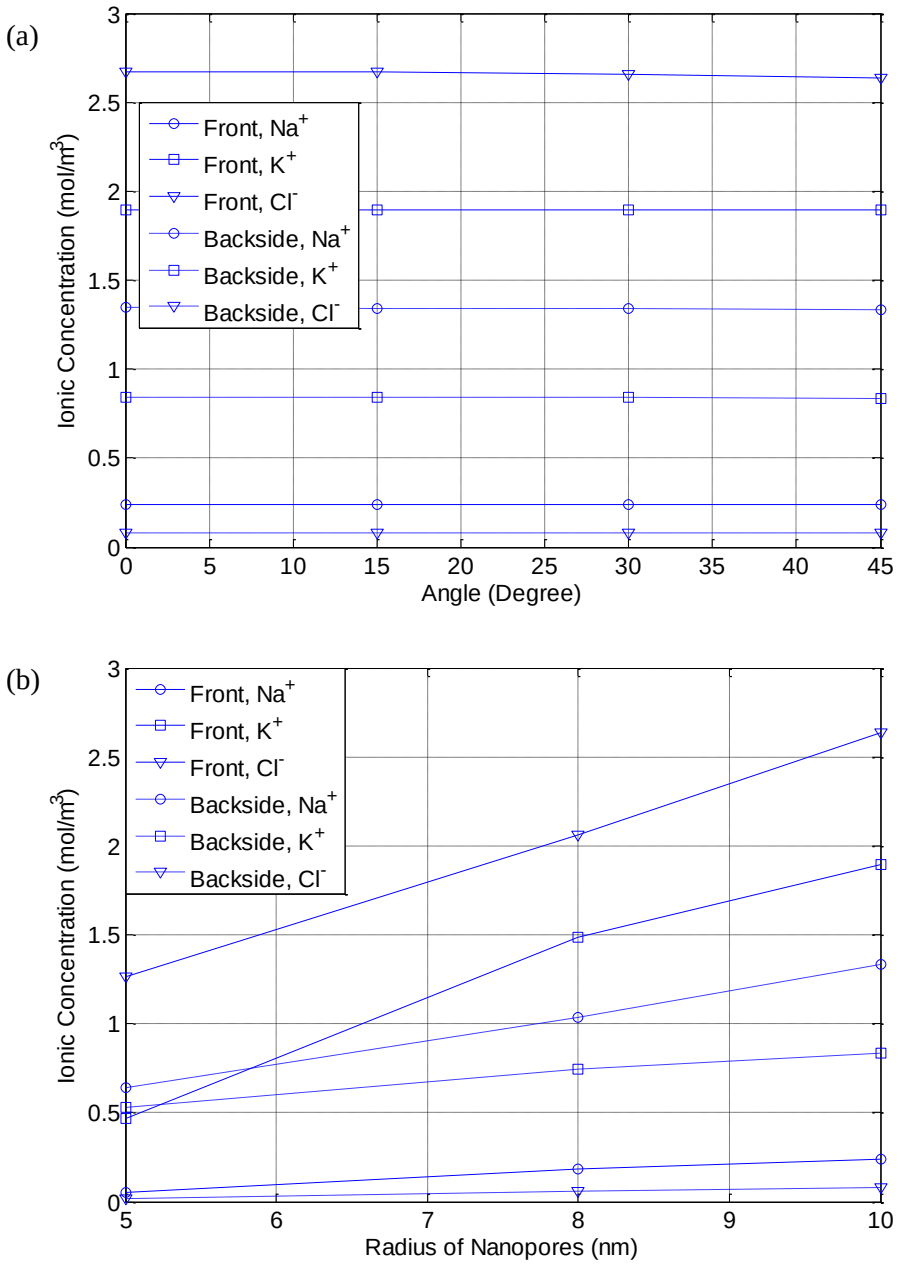

Figure 5-6 Averaged ionic concentrations at the cross section of the nanopores. In parts (a) and (b), radius and angle are 10 nm and 45°, respectively. Here, angle is defined as θ and (π-θ) in front and backside of the cell membrane, respectively. It is clear that on each side of the cell, angular orientation of the nanopores on cell membrane has negligible effects on the ionic concentration (5-6.a). Increasing the nanopore radius will result in increase in averaged ionic concentration (5-6.b).

For different values of the nanopore radius and angular position, Tables 5.4 and 5.5 present the convective (electroosmotic), the electrophoretic, and the diffusive mass transfer rates. Figure 5.7 also illustrates the normalized convective (electroosmotic), electrophoretic, and diffusive mass transfer rates. From this figure, one can conclude that: First, the effect of the diffusive ionic mass transfer rate is negligible in comparison with the electrokinetic based mass transfer rates. Second, increasing the size of the nanopores will intensify influence of the convection (electroosmosis) on the ionic mass transfer rates in comparison with the electrophoretic mass transfer rate. This can be explained by considering the fact that increasing the nanopores radius will increase the electroosmotic flow velocity through the nanopores. Finally, it is clear that the ionic mass transfer rates are different at the two sides of the cell membrane. However, on a given side of the cell membrane, the angular orientation of the nanopores has negligible effects on the mass transfer rates through the nanopores.

Table 5-4 Effects of nanopore radius on ionic mass transfer rates (IMTR) through the nanopores (Angle=45°)

	Radius (nm)	Diffusive IMTR (mol/s)			Electrophoretic IMTR (mol/s)			Convective IMTR (mol/s)		
		Na^+	K^+	Cl^-	Na^+	K^+	Cl^-	Na^+	K^+	Cl^-
Front	5	1.94E-11	3.08E-10	-6.55E-10	8.46E-10	7.37E-09	-2.74E-08	-1.86E-13	-2.26E-12	-4.48E-12
	8	1.15E-10	1.81E-09	-1.49E-09	3.29E-09	2.77E-08	-5.18E-08	-2.34E-10	-1.85E-09	-2.66E-09
	10	2.17E-10	3.01E-09	-3.23E-09	4.64E-09	3.73E-08	-6.91E-08	-6.66E-10	-5.05E-09	-7.31E-09
Back	5	-2.36E-10	-3.27E-10	8.98E-12	-9.97E-09	-8.37E-09	3.87E-10	6.88E-10	5.44E-10	1.94E-11
	8	-5.38E-10	-6.65E-10	5.31E-11	-1.88E-08	-1.39E-08	1.51E-09	6.04E-09	4.18E-09	3.51E-10
	10	-1.18E-09	-1.25E-09	1.00E-10	-2.52E-08	-1.62E-08	2.13E-09	1.68E-08	1.02E-08	1.00E-09

Table 5-5 Effects of nanopore angular orientation on ionic mass transfer rates through the nanopores. Angle is defined as θ and (π-θ) in front and backside of the cell membrane, respectively (R=10 nm).

	Angle (degree)	Diffusive IMTR (mol/s)			Electrophoretic IMTR (mol/s)			Convective IMTR (mol/s)		
		Na^+	K^+	Cl^-	Na^+	K^+	Cl^-	Na^+	K^+	Cl^-
Front	0	2.17E-10	3.01E-09	-3.28E-09	4.64E-09	3.73E-08	-7.02E-08	-6.30E-10	-4.79E-09	-7.02E-09
	15	2.17E-10	3.01E-09	-3.28E-09	4.64E-09	3.73E-08	-7.01E-08	-6.35E-10	-4.82E-09	-7.06E-09
	30	2.17E-10	3.01E-09	-3.26E-09	4.64E-09	3.73E-08	-6.98E-08	-6.47E-10	-4.91E-09	-7.17E-09
	45	2.17E-10	3.01E-09	-3.23E-09	4.64E-09	3.73E-08	-6.91E-08	-6.66E-10	-5.05E-09	-7.31E-09
Back	0	-1.19E-09	-1.26E-09	1.00E-10	-2.55E-08	-1.63E-08	2.13E-09	1.71E-08	1.03E-08	1.01E-09
	15	-1.19E-09	-1.26E-09	1.00E-10	-2.54E-08	-1.63E-08	2.13E-09	1.70E-08	1.03E-08	1.01E-09
	30	-1.19E-09	-1.26E-09	1.00E-10	-2.54E-08	-1.63E-08	2.13E-09	1.70E-08	1.03E-08	1.01E-09
	45	-1.18E-09	-1.25E-09	1.00E-10	-2.52E-08	-1.62E-08	2.13E-09	1.68E-08	1.02E-08	1.00E-09

(a)

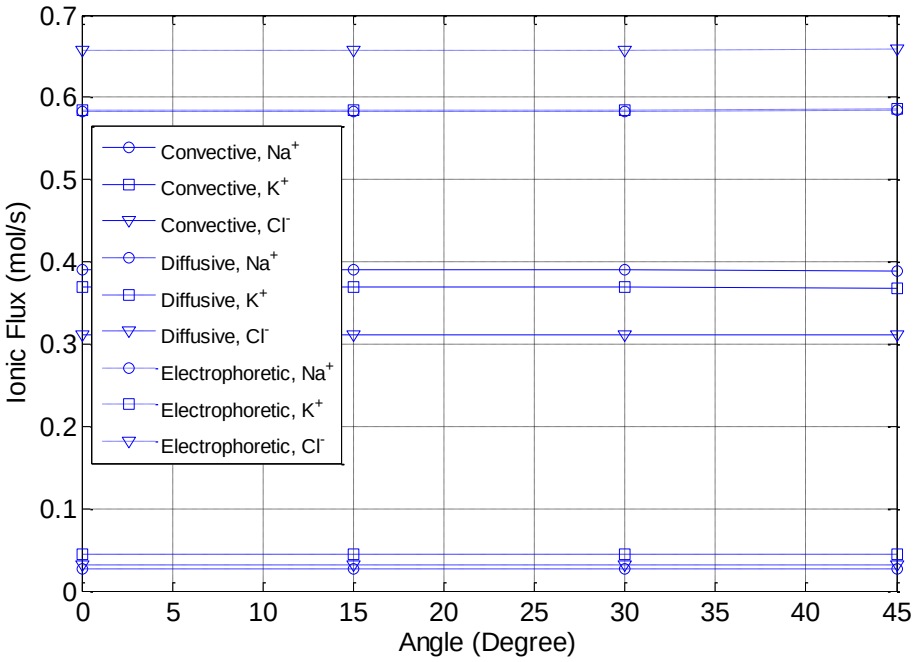

(b)

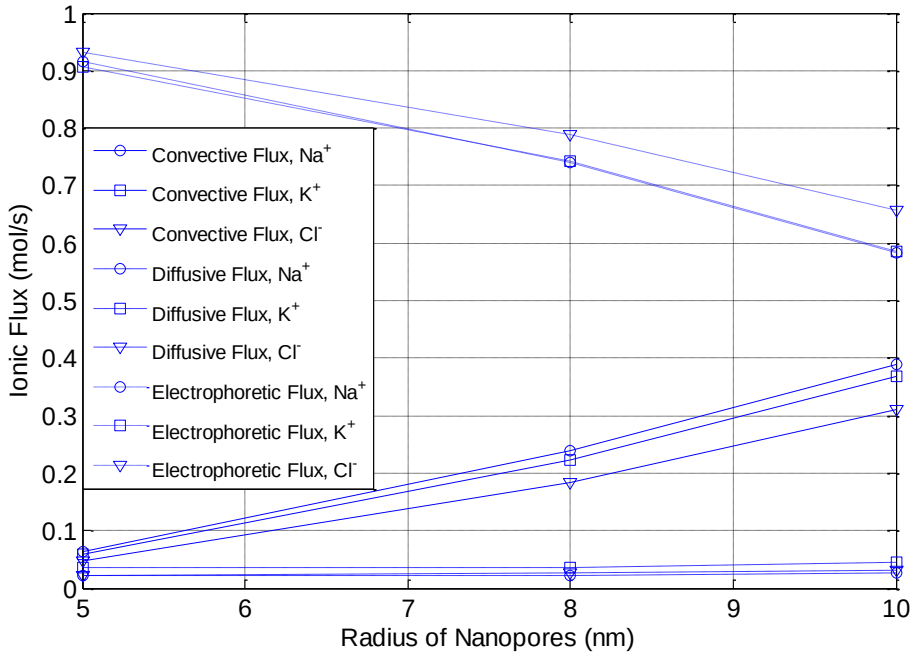

Figure 5-7 Effects of nanopore radius and its angular orientation on ionic mass transfer rates through the nanopores. The nanopores are located at the backside of the cell membrane. In parts (a) and (b), radius and angle are 10 nm and 45°, respectively. Angle is defined as θ and (π-θ) in front and backside of the cell membrane, respectively.

For different values of nanopore radii (5 nm and 10 nm), Figures 5.8 and 5.9 depict the ionic concentration of Na^+ and Cl^- at the cross-section surface midway of the nanopores. The surface electric charge is $\sigma_0 = -0.0001\, C/m^2$. These figures show that more positive ions are transported through the nanopores located at the back of the cell; more negative ions are transported through the nanopores at the front of the cell. Increasing the radius of the nanopores also intensifies ionic mass transfer.

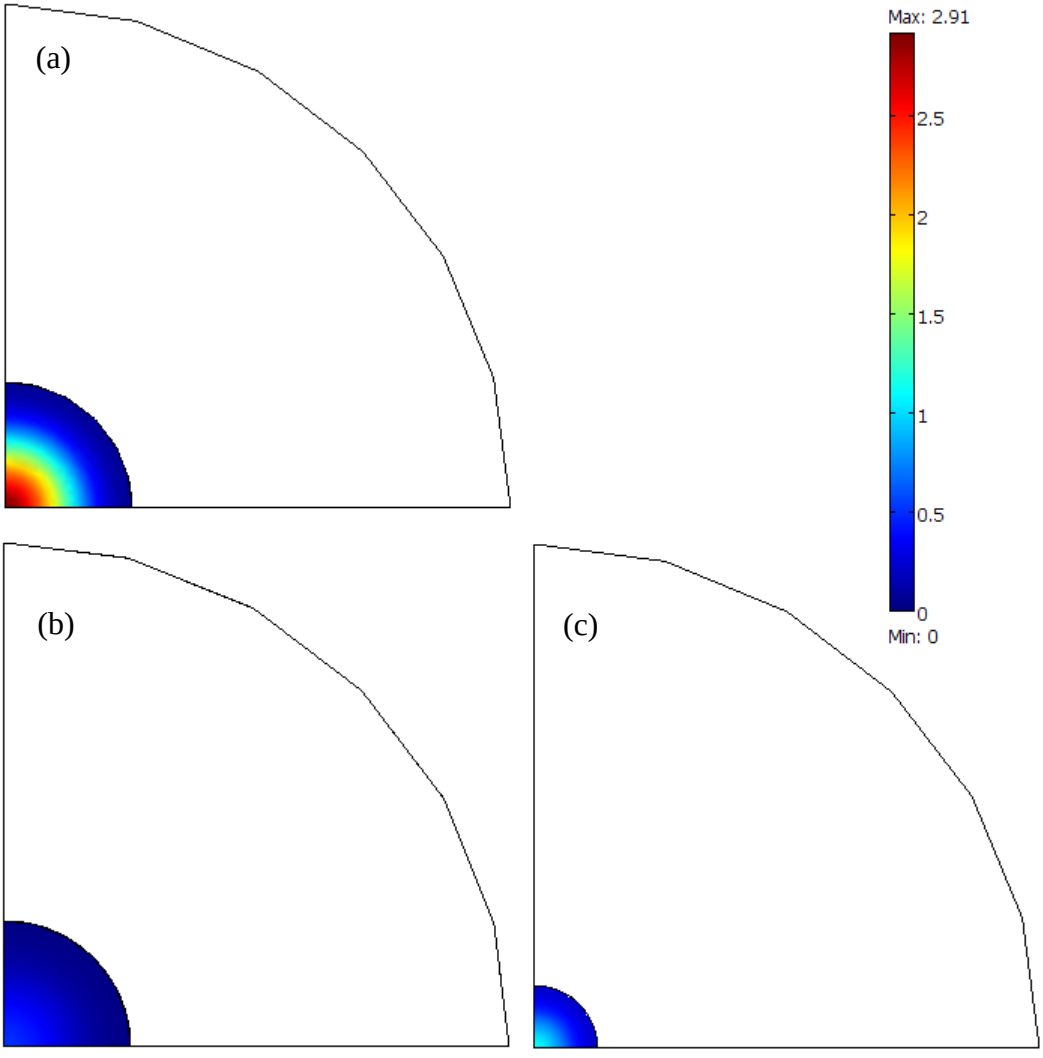

Figure 5-8 . Ionic concentration of the Na^+ ions at the cross-section midway of the nanopores. The surface electric charge is $\sigma_0 = -0.0001\, C/m^2$. (a) R=10 nm, back of the cell, (b) R=10 nm, front of the cell (c) R=5 nm, back of the cell.

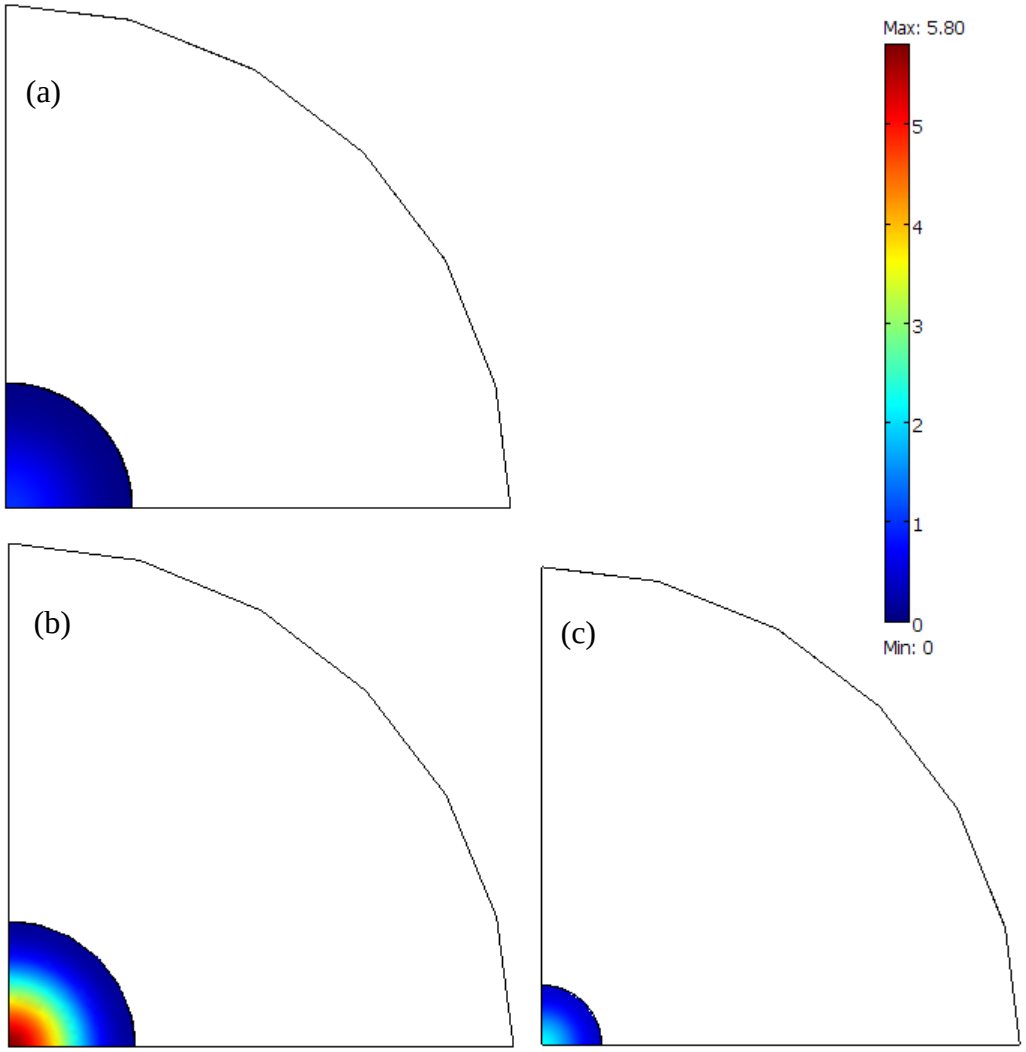

Figure 5-9 Ionic concentration of the Cl^- ions at the cross-section surface in the center of the nanopores. The surface electric charge is $\sigma_0 = -0.0001 C/m^2$. (a) R=10 nm, back of the cell, (b) R=10 nm, front of the cell (c) R=5 nm, front of the cell.

To finish the discussion part, I would like to qualitatively compare the findings of this study with the results of Pucihar and colleagues (Pucihar, et al., 2009). In that paper, the transport of PI dye into the Chinese hamster ovary cells was monitored during and after the electric pulse. Their results show that during the electric pulse, the ions are mainly electrophoretically transported; however, after removing the electric pulse, the transport becomes much slower and diffusion is the main means of the ionic transportation. In addition, during the electric pulse, the ionic transport becomes detectable

after 60 μs. Here, it should be mentioned that to perform the reversible electroporation and the cell transfection in the microfluidic based electroporative devices, the electric pulses usually last from few to tens of millisecond (for example see Table 2.3); thus, the lag between the start of applying electric pulse and the start of detectable transportation may not be significant compare with these millisecond pulses. In addition, the results of the current study reveal the importance of the electrokinetics (electrophoresis and electroosmosis) on the ionic transport during the cell electroporation. This may explain that how the electrophoretic based electroporation devices hasten transport of larger molecules into the cell. After applying the electric pulse, the presence of subcritical electric field near the cell can enhance delivery rate of the big molecules (Ionescu-Zanetti, et al., 2008). After removing the electric pulse, diffusive transport proceeds until resealing all the nanopores that takes from seconds to minutes. Although during the electric pulse diffusion might proceed at a thousand times lower rate than the electrophoresis and the electroosmosis, but it proceeds a thousand times longer. Thus, the effect of the diffusion may not be negligible on the cell transfection, though its effect is negligible during the few milliseconds of the electroporation while the electric pulse is present.

5.4.4 Conclusion

In this chapter, ionic mass transfer and fluid flow through the created nanopores in the cell membrane during the electroporation and in the presence of the electric pulse were studied. Previous studies only considered the effect of the diffusion on the cell transfection. Because of the transmembrane potential, the electrokinetic effects must consider on the ionic mass transfer through the nanopores. Because of the nanoscale dimensions of the created pores, the conventional electrokinetic theories such as the Poisson-Boltzmann distribution and the Helmholtz-Smoluchowski equation for the electroosmotic flow velocity could not be used. Therefore, in the present study, the Poisson-Nernst-Planck equations along with the modified Navier-Stokes equations were simulated directly in order to achieve the electric potential, the fluid flow, and the ionic concentration in the nanopores. The results of this paper involve some interesting findings. During the electroporation and in the presence of the electric pulse, the electrokinetic effects have great influences on the ionic mass transfer through the nanopores; the diffusive mass transfer rate has negligible effect on the ionic mass transfer compare with the electroosmosis and the electrophoresis ones. Increasing the nanopore radius also intensifies the effect of the convection (electroosmosis) on the ionic mass transfer rate. It is shown that increasing the radius of the nanopores will intensify the flow field and the ionic concentrations through the nanopores. The ionic concentrations, the flow field, and the electric potential are different

through the nanopores located at the front and backside of the cell membrane. However, for the nanopores located at each side of the cell membrane, the angular positions of the nanopores have insignificant influences on the flow field and the ionic mass transfers. Here, it should be pointed up that the electrophoretic and the electroosmotic transport only proceeds for as long as the electric pulse is present, which are the first milliseconds of the electroporation. After removing the electric pulse, ion diffusive transport proceeds until resealing all the nanopores that takes from seconds to minutes. Although during the electric pulse the ion transfer by diffusion is at a much lower rate than the ion transfer rate associated with the electrophoresis and the electroosmosis, the diffusion takes place over a much longer period of time, thus, the effect of diffusion on the cell transfection may not be negligible.

Chapter 6
Electrokinetic Motion of a Rectangular Nanoparticle in a Nanochannel*

6.1 Introduction

With the advancement of nano-fabrication technology, nano-fluidic devices involving nano-particles, such as for detecting aerosol nanoparticles and manipulating QDot and DNA, are highly desirable (Mijatovic, et al., 2005; Huh, et al., 2007; Bonthuis, et al., 2008; Tegenfeldt, et al., 2004; Reisner, et al., 2010; Li, et al., 2003; Yuan, et al., 2007). Another important application of transporting the nanoparticles in nanochannels is the electroporation where the nanoparticles (e.g., DNA and Qdots) are transported via nanopores of the cell membrane into the cell (Movahed, et al., 2011; Fox, et al., 2006; Lee, et al., 2009). Particle motion in microchannels under applied electric field has been studied extensively (Ye, et al., 2005; Ye, et al., 2002; Ye, et al., 2004; Ye, et al., 2004; Kang, et al., 2009; Xuan, et al., 2005; Daghighi, et al., 2010; Wu, et al., 2009; Wu, et al., 2009). However, the electrokinetic motion of the nano-particles in the nanochannels has not been well studied.

As it was explained in Chapter 4, by decreasing the size of the channels to the nanoscale, some conventional theories of the electrokinetics lose their applicability. This is because of the relatively thick electric double layers (EDL) that may overlap in the small nanochannels. In the microscale channels, EDL is usually much smaller than the channel's lateral dimension and hence are not overlapped in the channel. Therefore, the electric potential of the EDL is equal to zero in the center region of the channel; consequently, the bulk ionic concentrations of positive and negative ions are equal in the center region of the channel (outside EDL). These two statements (zero electric potential and zero net electric charge outside of EDL or in the center of the channels) are the underlying assumptions for the conventional electrokinetic theories and the governing equations of the electrokinetics, such as the Boltzmann distribution of the ions, the Poisson-Boltzmann equation for the electric potential at the cross section of microchannels, and the Helmholtz-Smoluchowski slip

* A version of this Chapter has been published in Journal of Colloid and Interface Science as: "Saeid Movahed, Dongqing Li, 'Electrokinetic motion of a rectangular nanoparticle in a nanochannel' Journal of Nanoparticle Research, Springer, 2012, Vol. 14, Issue 8, pp.: 1-15". The licence agreement of reprinting this article in the current dissertation has been presented in Permissions section (License Number: 3001441230540).

velocity for modelling the electroosmotic flow. In the small nanochannels (from a few nanometers to about 100 nanometers), the EDL thickness becomes larger or at least comparable with the channel lateral dimensions. Hence, the EDL from different channel walls may overlap, the electric potential is not zero at the center of the nanochannel, and the bulk ionic concentrations of co- and counter ions are not equal in the nanochannels.

There are a few papers reporting studies of the electrokinetic motion of the nanoparticles in nanopores and the nanochannels. Lee and colleagues studied diffusiophoretic motion of a charged spherical particle in the two-dimensional nanopore (Lee, et al., 2010). In that article, the walls of the nanopore are electrically neutral and the nanoparticle's motion is determined by the ionic concentration gradient in the nanopore. Ai and Qian conducted a two-dimensional numerical study on the translocation of a DNA-shaped nanoparticle through the nanopores (Ai, et al., 2011). They showed how externally applied electric field, the EDL thickness, and the initial orientation of the nanoparticle affects the movement of the nanoparticle through the nanopore. Their results show that thick EDL can trap the particle at the entrance of the nanopore. However, the nanoparticles will always pass the nanopore if the externally applied electric field is sufficiently high. Qian et al. studied the axial symmetric electrophoretic motion of the heterogeneous nanoparticle in the nanochannel (Qian, et al., 2008a; Qian, et al., 2008b). They examined the flow field and the ionic concentrations around the nanoparticle. However, they used an incorrect boundary condition $n\bullet\vec{N}_i=0$ for the non-permeating surface of the nanoparticle. The correct boundary condition for the non-permeating surface of the particle moving at a velocity $\vec{V}$ should be $n\bullet\vec{N}_i=n\bullet(c_i\vec{V})$ (Keh, et al., 1985). The right-hand side of this equation describes the convective mass transfer rate on the impermeable surface of the particle due to the particle movement. This difference in the boundary conditions can significantly influence the concentration field, the flow field, and the particle's velocity in the nanochannel, and will be discussed in the later section of this chapter.

Furthermore, the previous studies (Qian, et al., 2008a; Qian, et al., 2008b) considered effectively the infinite long nanochannel and did not consider the end effects. For any practical applications, the nanochannels have a finite length, comparable with the nanochannel diameter; and the two ends of the nanochannel must connect to reservoirs or microchannels. The ends of the nanochannels have major influences on the electrokinetic transport phenomena and processes. Because of the overlap of EDL in the small nanochannels, the co-ions and the counter ions do not have the same concentration in the nanochannel. Concentration polarization occurs at the entrance and the exit of the nanochannel

to the reservoirs (Zangle, et al., 2010). These affect the electric potential, the flow field, and the ionic concentration in the nanochannels, and consequently the electrophoretic and hydrodynamic forces exerting on the nanoparticle. Thus, in order to have an accurate analysis of the electrokinetic effects in the nanochannels, the effects of the reservoirs at the two ends of the nanochannel (for example, the microchannels connecting the nanochannel) should be considered in the model and simulation. The present research aims to investigate the three-dimensional electrokinetic motion of the nanoparticles in the nanochannels with the consideration of the end reservoir effect. The effects of channel dimension, nanoparticle dimension, bulk ionic concentration, and surface electric charge of the nanochannel walls on the particle motion will be examined. Because crystallized quantum dots usually have cubic shape (Chattopadhyay, et al., 2011; Oron, et al., 2009), and the nanopores in the cell membrane can be approximated as the nanochannels with a circular cross-section, the three-dimensional rectangular nanoparticle in the circular nanochannel will be considered in this study. In the following sections, a physical description and a mathematical modeling of the system in the current study will be provided first. After outlining the numerical method, the numerical simulation results are presented and discussed. Effects of the Brownian force, the surface electric charge of the nanochannel wall, and the cross sectional area of the nanochannel on the nanoparticle motion are described.

6.2 Modelling

6.2.1 Physical Modeling

Figure 6.1 illustrates the nanochannel system of this study. The nanochannel has a circular cross sectional area of radius R and length L and connects two reservoirs. The nanochannel and the reservoirs are filled with an aqueous solution (e.g., $NaCl$). The cubic nanoparticle ($a \times a \times a$) is considered at the center of the nanochannel. Application of electric potential at the two ends of the nanochannel causes liquid flow, ionic mass transfer, and motion of the nanoparticle through the nanochannel (the electrokinetic effects). The dash lines in Figure 5.1 outline the computational domain of the present study. The effects of the two reservoirs at the ends of the nanochannel should be considered in the simulations; therefore, two sections *ABKL* and *EFGH* are included in the computational domain. *CDIJ* and *MNPO* represent the nanochannel and the nanoparticle in the computational domain, respectively. The details of the governing equations and the boundary conditions will be explained in the following sections.

In the governing equations presented in the following sections, ϕ is the electric potential, $\vec{E}$ is the electric field, $\vec{D}$ is the electrical displacement, c_i, z_i, and $\vec{N}_i$ are the concentration, valance, and flux of ion species i, respectively. p, $\vec{u}$, and $\vec{V}_p$ are pressure, velocity vector, and translational velocity of the nanoparticle, correspondingly. m_p is mass of the nanoparticle. t represents time. σ_w and σ_p are the surface electric charge densities on the nanochannel wall and on the surface of the nanoparticle, respectively. The constants includes permittivity ($\varepsilon_0\varepsilon_r$), medium density ($\rho$), the Faraday number ($F$), fluid viscosity ($\eta$) and valance number ($z_i$), diffusion coefficient (D_i), and mobility (μ_i) of ion species i. The values of these constants and parameters are listed in Table 6.1.

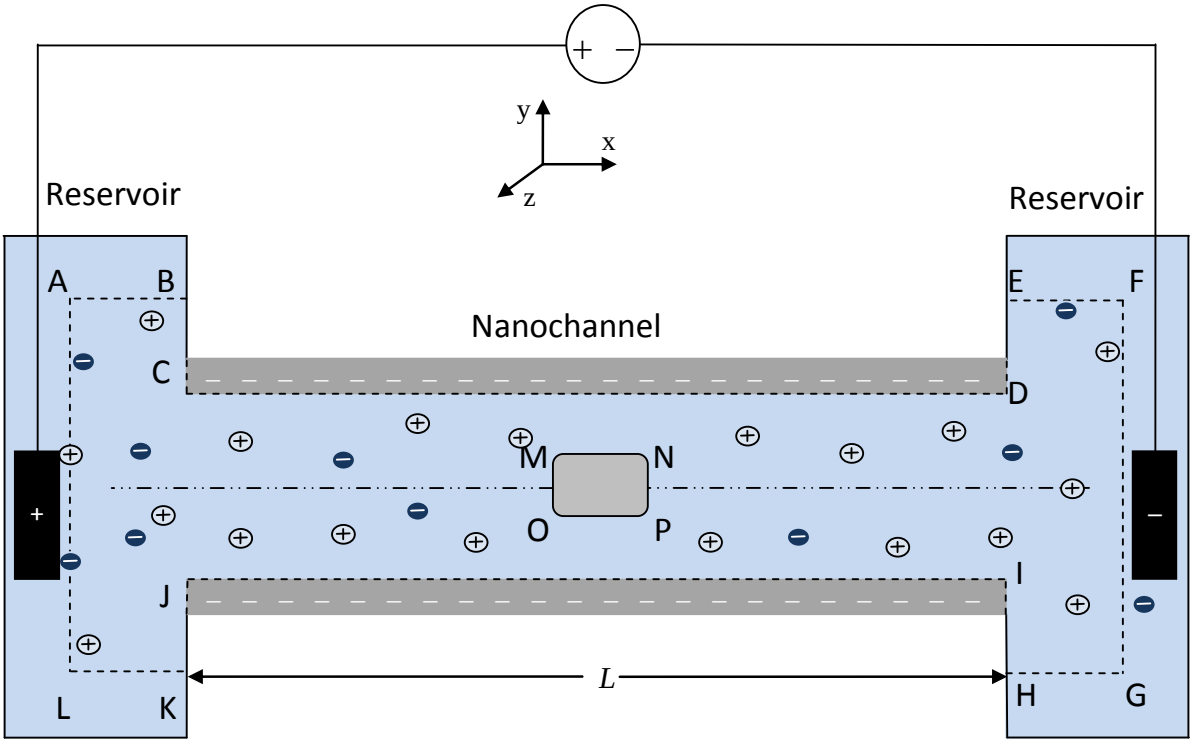

Figure 6-1 Schematic diagram of the nanochannel-nanoparticle system in this study. The dash line encloses the computational domain. Two reservoirs are connected to the circular nanochannel of length L and radius R. Two electrodes located in the reservoirs apply electric potential to the ends of the nanochannel. The nanochannel wall is negatively charged. A negatively charged cubic particle is initially positioned at the center of the nanochannel.

6.2.2 Mathematical Modeling

In order to model the electrokinetic motion of the nanoparticle in the nanochannel, it is necessary to find the forces exerted on the particle. The dominant forces acting on the nanoparticle are the electrophoretic and the hydrodynamic forces. Although the Brownian force can become important for such a nanoscale particle (Morgan, et al., 2002); it will be shown later in this article that the influence of this force is negligible in comparison with the electrophoretic force. After finding the forces, the Newton second law can be utilized to determine the velocity of the nanoparticle.

The continuum approach will be used in developing the model. Existing experimental studies show that the continuum assumption for aqueous solutions is valid up to 4 nm (Zheng, et al., 2003). It was explained in chapter 4 that the following set of highly coupled partial differential equations subjected to the proper boundary conditions are employed to describe the electric potential, the ionic concentration, and the flow field in the nanochannels (Movahed, et al., 2011):

$$-\nabla(\varepsilon_0 \varepsilon_r \nabla \phi) = F \sum_i z_i c_i \tag{6.1}$$

$$\vec{E} = -\nabla \phi \tag{6.2}$$

$$\frac{\partial c_i}{\partial t} + \nabla \bullet \vec{N}_i = 0 \tag{6.3}$$

$$\vec{N}_i = \vec{u} c_i - D_i \vec{\nabla} c_i - z_i \mu_i c_i \nabla \phi \tag{6.4}$$

$$\rho \frac{\partial \vec{u}}{\partial t} = -\nabla p + \mu \nabla^2 \vec{u} - (\sum_i z_i F c_i) \nabla \phi \tag{6.5}$$

$$\nabla \bullet \vec{u} = 0 \tag{6.6}$$

Eq. (6.1) is the Poisson equation. This equation should be solved in order to obtain the electric potential distribution in the computational domain. Term $F \sum_i z_i c_i$ on the right hand side of this equations shows that how the difference of co- and counter ions influence the electric potential inside the domain. The electric field is the gradient of the electric potential, as indicated by Eq. (6.2). Eq. (6.3) is the Nernst-Plank equation where the definition of ionic flux is given by Eq. (6.4). The first ($\vec{u} c_i$), second ($D_i \vec{\nabla} c_i$), and third ($z_i \mu_i c_i \nabla \phi$) terms at the right hand side of Eq. (6.4) represent how the flow field (the electroosmosis effect), diffusion, and electric field (the electrophoresis effect) contribute to the ionic mass transfer, respectively. The ionic concentration of each species can be found by solving these two equations. Eqns. (6.5) and (6.6) are the Navier-Stokes and the continuity

equations, respectively, which describe the velocity field and the pressure gradient in the computational domain. Proper boundary conditions for these equations are described as follows:

6.2.3 Electric potential:

Uniform surface electric charge is considered for the boundaries *BC*, *CD*, *DE*, *JK*, *IJ*, and *HI* that represent the walls of the channels (Eq. (6.8.a)), and the boundary *MNPO* that stands for the surface of the nanoparticle (Eq. (6.8.b)). Zero surface electric charge (Eq. (6.8.c)) is assumed at the boundaries *AB*, *KL*, *EF*, and *GH*. The applied electric potential at boundaries *LA* and *FG* are ϕ_1 (Eq. (6.9.a)) and ϕ_2 (Eq. (6.9.b)), respectively. In the following equations, $\vec{E}$ and $\vec{D}$ are the external electric field and electrical displacement, respectively. $\vec{n}$ is the normal vector directed from the surface to the fluid.

$$\vec{D} = \varepsilon\varepsilon_0\vec{E} \tag{6.7}$$

$$\vec{n}\bullet\vec{D}(r) = \sigma_w \tag{6.8.a}$$

$$\vec{n}\bullet\vec{D}(r) = \sigma_p \tag{6.8.b}$$

$$\vec{n}\bullet\vec{D}(r) = 0 \tag{6.8.c}$$

$$\phi_{LA} = \phi_1 \tag{6.9.a}$$

$$\phi_{FG} = \phi_2 \tag{6.9.b}$$

6.2.4 Mass transfer:

The walls of the solid nanochannels are impermeable for mass transfer (*BC*, *CD*, *DE*, *JK*, *IJ*, and *HI*). The symmetric boundary condition is assumed at the boundaries *AB*, *KL*, *EF*, and *GH*. Following mathematical equations represent these two kinds of boundary conditions (symmetric and impermeable). The following equations represent that the normal ionic flux must be zero at these boundaries:

$$\vec{n}\bullet\vec{N}_i = 0 \tag{6.10.a}$$

$$\vec{N}_i = -D_i\nabla c_i - z_i\mu_i c_i\nabla\phi + c_i\vec{u} \tag{6.10.b}$$

Constant bulk ionic concentration (c_0) is assumed at the boundaries *LA* and *FG* (two reservoirs):

$$c_i = c_0 \tag{6.11}$$

The surface of the nanoparticle (boundary *MNPO*) is also impermeable for mass transfer. The mathematical condition representing the impermeable surface of the nanoparticle is given by (Keh, et al., 1985):

$$\vec{n} \bullet \vec{N} = \vec{n} \bullet (c_i \vec{U}) \tag{6.12}$$

where $\vec{n}$ is a unit vector normal to the surface of the nanoparticle. This equation means no molecules can penetrate into the particle. In this equation, $\vec{U}$ is the velocity of the liquid-particle interface. When the relative velocity of the ions and the surface is zero, ions do not enter to or exit from this boundary. In this study, for simplicity, the nanoparticle is considered to have a translational velocity $\vec{V}_p$ only and no rotation. Therefore, Eq. (6.12) can be re-written as:

$$\vec{n} \bullet \vec{N} = \vec{n} \bullet (c_i \vec{V}_p) \tag{6.13}$$

The open boundary condition is assumed for the surfaces *LA* and *FG* (Eq. (6.14)); flow can both enter to and exit from the open boundary. For this type of boundary condition, it is assumed that there is not any applied pressure gradient and viscous stress at these boundaries. This boundary condition is employed to model the connection of the nanochannel with the reservoirs. No slip velocity (Eq. (6.15)) is applied at the walls of the nanochannel and the reservoirs, boundaries *BC*, *CD*, *DE*, *JK*, *IJ*, and *HI*. The computational domain boundaries *AB*, *KL*, *EF*, and *GH* are treated as the symmetric boundary condition (Eqns. (6.16) and (6.17)). In Eq. 6.17, I is the identity tensor.

$$(\mu(\nabla \vec{u} + (\nabla \vec{u})^T))\vec{n} = 0\,, \quad p = 0 \tag{6.14}$$

$$\vec{u} = 0 \tag{6.15}$$

$$n \bullet \vec{u} = 0 \tag{6.16}$$

$$\vec{t} \bullet [-pI + \mu(\nabla \vec{u} + (\nabla \vec{u})^T)] = 0 \tag{6.17}$$

No slip boundary condition is also assumed for the surface of the nanoparticle (boundary *MNOP*). At the solid-liquid interface of the nanoparticle translating at the velocity $\vec{V}_p$, the no slip velocity is defined as (Keh, et al., 1985):

$$\vec{u} = \vec{V}_p \tag{6.18}$$

Eq. (6.18) means that the relative velocity of the liquid to the solid particle must be zero.

6.2.5 Particle Motion

Because the surface of the nanoparticle is negatively charged, the externally applied electric field brings electrostatic force ($\vec{F}_{ep}$) on the nanoparticle (electrophoresis effect). Due to the particle motion and the electroosmotic flow of the liquid in the nanochannel, the frictional force (hydrodynamic force) is also exerted on the nanoparticle by the liquid flow ($\vec{F}_{hd}$). The total force acting on the particle is:

$$\vec{F}_t = \vec{F}_{ep} + \vec{F}_{hd} \tag{6.19}$$

The electrophoretic and the hydrodynamic forces can the calculated as follow:

$$\vec{F}_{ep} = \iint_s \vec{\vec{T}} \bullet d\vec{s} \tag{6.20.a}$$

$$T_{ij} = \varepsilon\varepsilon_0 (E_i E_j - \frac{1}{2}\delta_{ij} |E|^2) \tag{6.20.b}$$

$$\vec{F}_{hd} = \iint_s \vec{n} \bullet (-p\vec{I} + \mu\left[\nabla\vec{u} + (\nabla\vec{u})^T\right]) ds \tag{6.21}$$

In the above equations, $\vec{I}$ is the identity tensor and $\vec{\vec{T}}$ is the Maxwell stress tensor; T_{ij} is the representation of this tensor with Einstein notation.

At each time steps, the Newton second law can be utilized to find the velocity of the nanoparticle ($\vec{V}_p$):

$$\vec{F}_t = m_p \frac{d\vec{V}_p}{dt} \tag{6.22}$$

6.2.6 Brownian Force

It should be mentioned that the Brownian force is neglected in the above model. In the following, a simple two dimensional analysis is presented to compare the effects of the electrophoretic and the Brownian forces on a cylindrical nanoparticle (radius *a* and a unit length) moving in the nanochannels. The Brownian force can be modeled as (Kadaksham, et al., 2004; Liu, et al., 2005):

$$\vec{F}_B = \zeta \sqrt{\frac{12\pi a \mu k_B T}{\Delta t}} \tag{6.23}$$

In this equation, ς is the Gaussian random number with zero mean and unit variance; a is the radius of the particle, μ is viscosity, k_b is Boltzmann constant, T is temperature, and Δt is time step. To find a simple and two-dimensional approximate solution for the electrophoretic force (Eq. (6.20)), the applied electric potential is assumed to be linear in the computational domain. By considering the uniform surface electric charge on the cylindrical nanoparticle (radius *a* and a unit length), estimation for the electrophoretic force is given by:

$$\vec{F}_{ep} = E_z \sigma_p 2\pi a \tag{6.24}$$

The ratio of the Brownian to electrophoretic forces (α) can be found as:

$$\alpha = \frac{\vec{F}_B}{\vec{F}_{ep}} = \frac{C}{E_z \sqrt{a \times \Delta t}} \tag{6.25}$$

Where:

$$C = \varsigma \frac{\sqrt{12\pi\mu k_B T}}{2\pi\sigma_p} \tag{6.26}$$

In Eq. (6.25), *C* is constant that can be found by solving Eq. (6.26). Using the parameter values listed in Table 6.1, the maximum value of *C* becomes $\approx 1.99\times10^{-8}$. E_z, Δt, and a are determined by the characteristics of the system in this study. For example, $a = 5\times10^{-9}\ m$, Transient period of nanoparticle movement in the nanochannels is in the order of 10^{-15} second (It will be shown at the rest of this chapter); therefore, $\Delta t = 10^{-15}\ s$. In most practical applications, such as in electroporation (creating nanopores on cell membrane), even a small electric potential difference (e.g., the trans-membrane potential is about 1 Volt) over a very short length (e.g., the membrane thickness 5~10 nm) of the nanochannel (nanopore) will generate a very strong electric field in the nanochannels (~ $10^{5\sim6}$ V/m). Using these values, the maximum ratio of the Brownian force to the electrophoretic force, Eq. (6.25), is approximately $\approx 3\times10^{-3}$. Thus, neglecting the Brownian force in comparison with the electrophoretic force is a reasonable assumption for the present study. As it can be seen from Eq. (6.25), the large value of E_z in the nanochannel results in this conclusion. The numerical results of this study, as shown in the following sections, indicate that the electrophoretic and the hydrodynamic forces are of the same order of magnitude. Thus, without loss of generality, it can conclude that,

under the conditions of the present study, the effect of Brownian force is negligible in comparison with both electrophoretic and hydrodynamic ones.

6.3 Numerical Method

This study considers the three-dimensional nanochannel with a circular cross section connected to the two reservoirs at the ends. The nanoparticle is initially located at the center of the nanochannel. The Poisson-Nernst-Plank, the Navier-Stokes, and the continuity equations are solved simultaneously to calculate the electric potential, the ionic concentration, and the fluid flow in the computational domain. The numerical method of solving these equations has been explained in Chapter 4, Section 4.3. These governing equations are highly coupled; the results are affected by all these equations and the corresponding boundary conditions. The numerical simulation was conducted by using the COMSOL Multiphysics 3.5a. A mesh independent structure is employed to make sure that the results are unique and will not change if any other grid distribution is applied. In order to discretize the solution domain, the structured meshes are applied. The solution domain is broken into small meshes that fully cover the solution domain without overlapping. The reliable numerical results should be grid independent; therefore, in this study, the effect of different number of grids was examined; finally, the number of grids was found with which the numerical results would not change if further increase in grid number was applied.

At each time steps, by simulating the flow field, the ionic concentration, and the electric potential (Eqns. (6.1)-(6.6)), the total force exerted on the nanoparticle is computed (Eqns. (6.19)-(6.21)); consequently, the Newton second law is utilized to obtain the velocity of the nanoparticle (Eqn. (6.22)). The assumed tolerances for electric potential are $1x10^{-3}$ V and for the other parameters, $c\,(mol/m^3)$, $u\,(m/s)$, and $p\,(MPa)$, is $1x10^{-8}$. Here, it should mention that the smallest binary number in the COMSOL that can differentiate from 1 is "eps" = $2.2x10^{-16}$. To examine the correctness of the proposed numerical method, a simple case of the motion of the rectangular micro-particle in a rectangular microchannel was simulated and the result was compared with the steady state analytical results of Li et al. (Daghighi, et al., 2010). Figure 6.2 depicts this comparison. The key parameters used in this simulation are indicated in this figure. Good agreement in terms of the steady state velocities between both approaches supports the proposed theoretical model and the numerical method.

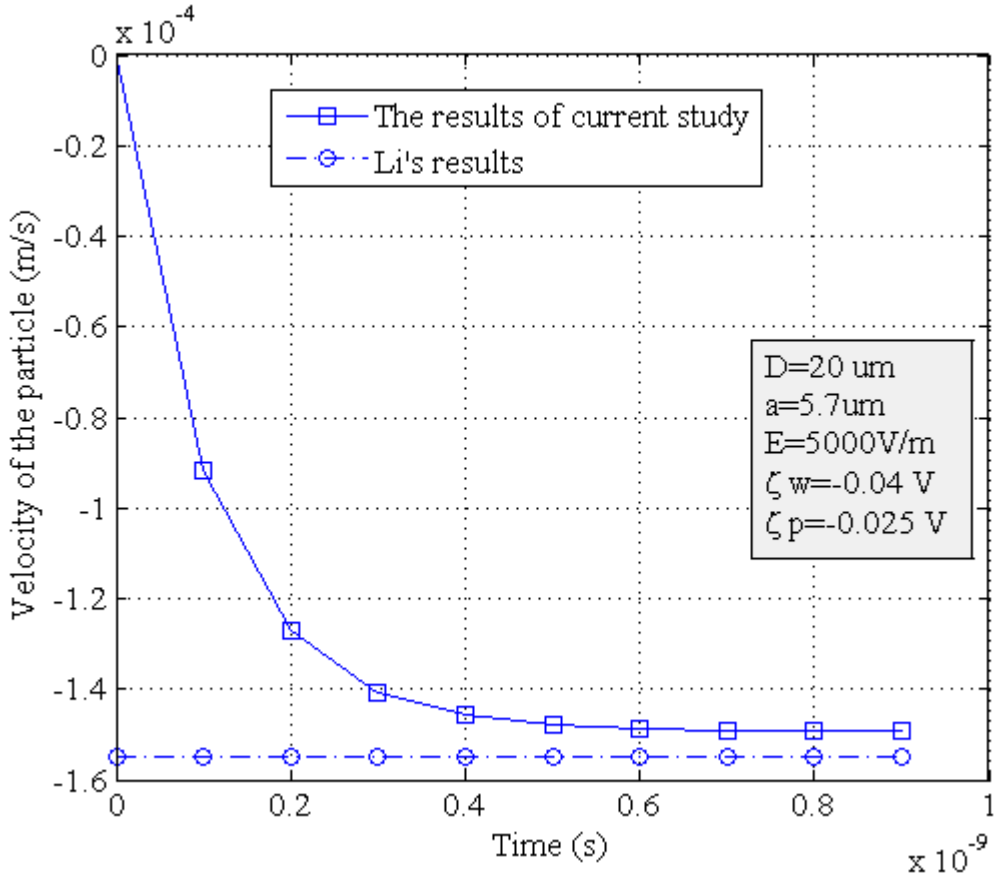

Figure 6-2 Application of the model and the numerical method to a case of electrokinetic motion of a rectangular micro-particle in a rectangular microchannel. The particle velocity at steady state is compared with an analytical solution.

6.4 Results and Discussion

In this study, a cubic nanoparticle is considered in the simulation to mimic the shape of the quantum dots. The electrical and geometrical parameters used in the simulations are summarized in Table 6.1. The radius of the nanochannel (R) is assumed to be 10 ~ 15 nm; the side of the nanoparticle (a) is 5 ~ 10 nm; the dimensions of the boundaries in Figure 6.1, *AB*, *EF*, *FG*, *GH*, *KL*, and *LA* are $100\ nm$. The surface electric charge density of the nanoparticle is $\sigma_p = -0.0001\, C/m^2$. The surface electric charge density of the walls of the nanochannel (σ_w) is –0.0001 ~ –0.0005 C/m^2; and the applied electric potential difference is $\Delta\phi = 1V$.

Table 6-1The values for constants and parameters used in the simulations

Parameter	value/range	Unit
ε_T *(relative permittivity)*	80	-
ε_0 *(absolute permittivity))*	8.85×10^{-12}	*F/m*
ρ *(liquid density)*	1000	Kg/m^3
σ_w *(surface electric charge on the walls of nanochannel)*	$-0.0001\sim-0.0005$	C/m^2
σ_p *(surface electric charge of nanoparticle)*	–0.0001	C/m^2
ϕ_1 *(electric potential on the left)*	0	*V*
ϕ_2 *(electric potential on the right)*	–1	*V*
μ *(dynamic viscosity)*	1×10^{-3}	*Pa·s*
F(Faraday constant)	96485.3415	$A\bullet s/mol$
k_B *(Boltzmann constant)*	1.381×10^{-23}	$J/.K$
Rg (universal gas constant)	8.314	$J/(mol\bullet.K)$
R (nanochannel radius)	$10\sim15$	*nm*
a (nanoparticle side dimension)	$5\sim10$	*nm*
L (nanochannel length)	120	*nm*
AB, EF, FG, GH, KL, LA (see Fig. 6.1)	100	*nm*
D_+ *(diffusion coefficient of positive ion)*	1.28×10^{-9}	m^2/s
D_- *(diffusion coefficient of negative ion)*	1.77×10^{-9}	m^2/s
μ_i *(mobility of ion species i)*	$D_i/(R_g\bullet T)$	-
C_0 *(bulk ionic concentration)*	$10^{-3}\sim0.3$	mol/m^3
T (temperature)	300	*.K*
ς *(Gaussian Random Number)*	1	-

6.4.1 Effects of the boundary conditions and the reservoirs

As mentioned in the introduction (Section 6.1), the correct boundary condition for the non-permeating surface of the particle moving at a velocity $\vec{V}$ should be $n\bullet\vec{N}_i = n\bullet(c_i\vec{V})$ (Keh, et al., 1985), i.e., Eq. (6.13), not $n\bullet\vec{N}_i = 0$. The right-hand side of Eq. (6.13) describes the convective flux on the impermeable surface of the particle due to the particle movement. This difference in the boundary conditions can significantly influence the concentration field, the flow field, and the particle's velocity in the nanochannel. As an example, let us consider one specific case: a *NaCl* aqueous solution, $C = 1\,mol/m^3$, the surface electric charge density on the walls of the nanochannel and the surface electric charge of the nanoparticle are $-0.0001 C/m^2$, the nanochannel radius is $R = 15\,nm$, the applied electric voltage between boundaries *LA* and *FG* is $1V$, and the nanoparticle dimension is $5\,nm \times 5\,nm \times 5\,nm$. As an example, Figure 6.3 shows the effects of using these two different boundary conditions on the ionic concentration of the counter-ion (Na^+). Figure 6.3(a) used the correct boundary condition ($n\bullet\vec{N}_i = n\bullet(c_i\vec{V})$) and Figure 6.3(b) used the incorrect boundary condition ($n\bullet\vec{N}_i = 0$) for the non-permeating walls of the moving particle. This figure clearly shows the significant differences in the ionic concentration and the velocity of the nanoparticle.

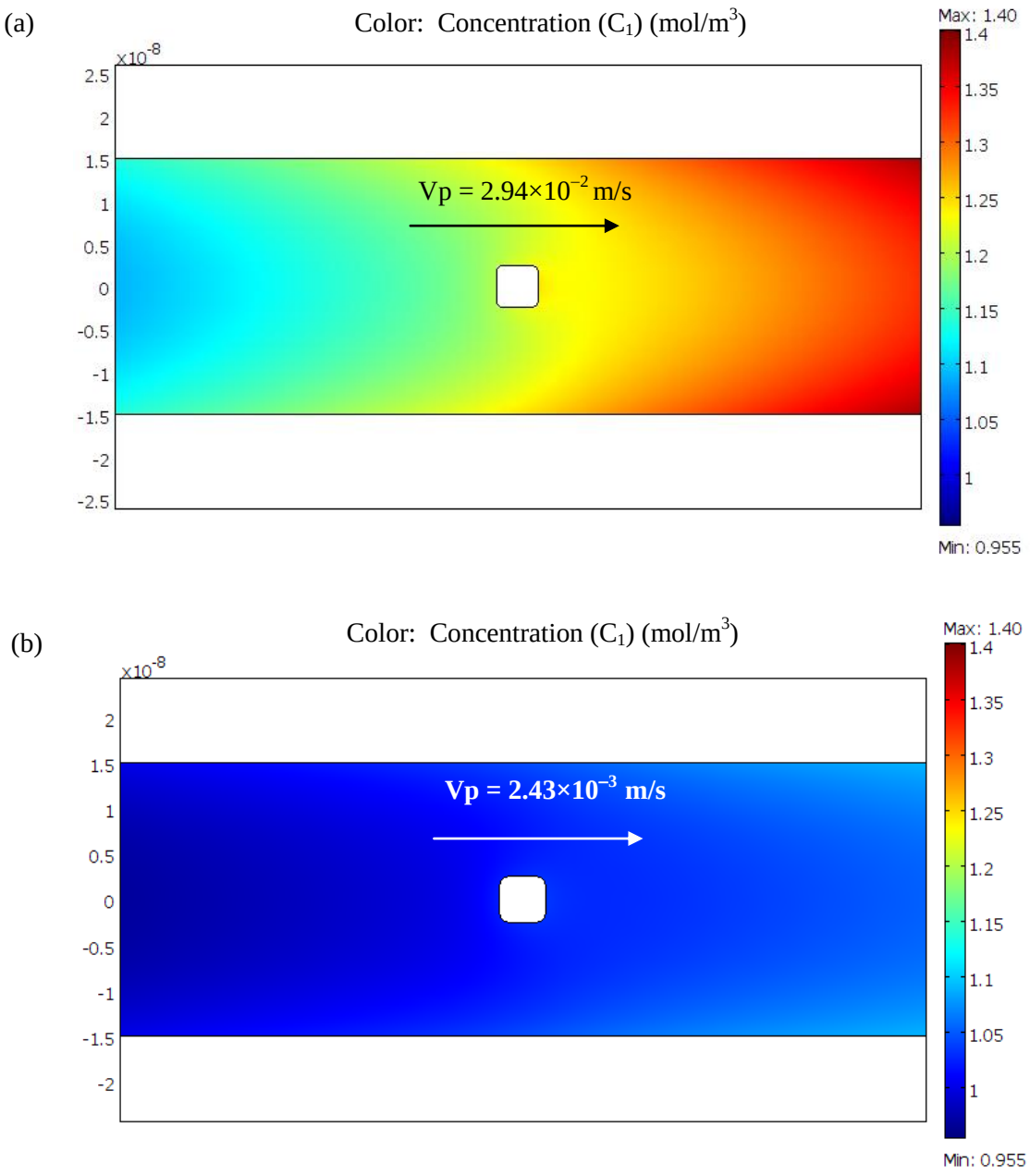

Figure 6-3 The effects of applying (a) the correct non-permeating boundary condition ($n\bullet\vec{N}_i = n\bullet(c_i\vec{V})$), and (b) the incorrect non-permeating boundary condition ($n\bullet\vec{N}_i = 0$) at the surface of a moving particle on the ionic concentration distribution and velocity of the nanoparticle. The color bar indicates the concentration of counter-ion (Na^+) along the channel at the surface across the center line of the channel (z = 0).

Figure 6.4 depicts the difference between the concentrations of the positive and the negative ions (counter-ions and co-ions) in the nanochannel region. In this figure, $C = 10^{-2}\ mol/m^3$, $\sigma_w = \sigma_p = -0.0001 C/m^2$, $R = 10\ nm$, $a = 5\ nm$, $\Delta\phi = 1V$. As indicated in Figure 6.1, the applied electric field and consequently the electroosmotic flow are from the left to the right. As it can be seen from this figure, at the exit of the nanochannel to the microchannel (section A-A), this concentration difference increases substantially. Such an accumulation of the counter-ions (here, the positive ions) at the exit of the nanochannel is usually referred as ion polarization effect (Zangle, et al., 2010). Without considering the end reservoir effects, i.e., the interface of the microchannel and the nanochannel, such ion polarization effect cannot be modeled and simulated, which will in turn affect the electroosmotic flow and electrophoresis inside the nanochannel.

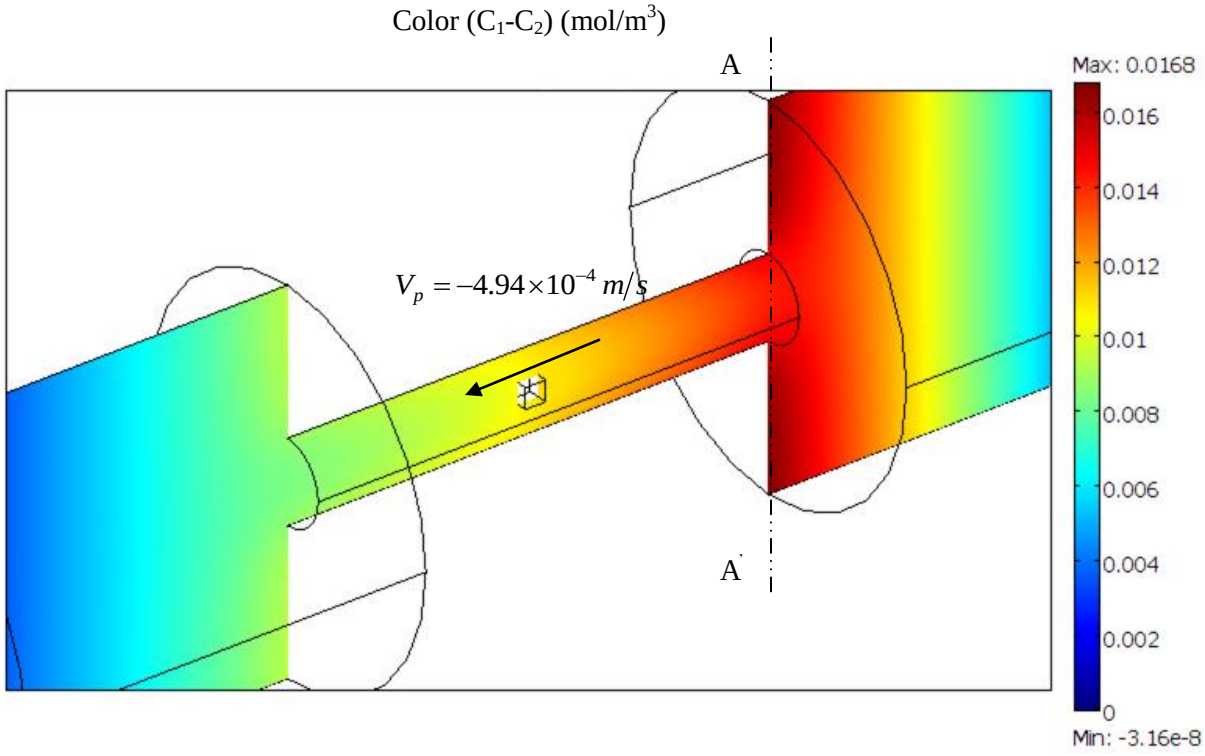

Figure 6-4 The concentration difference of the counter ions and the co-ions in the nanochannel ($C = 10^{-2}\ mol/m^3$, $\sigma_w = \sigma_p = -0.0001 C/m^2$, $R = 10\ nm$, $a = 5\ nm$, and $\Delta\phi = 1V$). The color bar indicates the ionic concentration difference in mol/m^3. The nanoparticle moves from the right to the left at a velocity $V_p = -4.94 \times 10^{-4}\ m/s$.

6.4.2 Effects of the nanoparticle size

As explained before, the electrophoretic and the hydrodynamic forces act on the nanoparticle. The electrophoretic force is a function of the externally applied electric field, the particle surface electric charge, and dimensions of the nanochannel (Eq. 6.20). The hydrodynamic force is dependent on the velocity field that is the function of the bulk ionic concentration, the applied electric field, the dimensions of the nanochannel and the nanoparticle, and the surface electric charge of both the channel and the particle. Figure 6.5 illustrates the induced pressure around the moving nanoparticle. An enlarged view of the flow field in vicinity of the nanoparticle for this specific case is shown in Figure 6.5b. Under the assumed parameters of this case, the nanoparticle moves from the right to the left, i.e., opposite to the electroosmotic flow. The electrophoretic movement of the nanoparticle through the nanochannel causes an induced pressure in the nanochannel.

For the same size nanochannels ($R = 15nm$), Figure 6.6 depicts the velocity field of the two different nanoparticles ($a = 5, 10nm$). The bulk ionic concentration, the surface electric charge and the applied electric field are kept constant ($C = 10^{-2}\ mol/m^3$, $\sigma_w = \sigma_p = -0.0001 C/m^2$, R = 15 nm, and $\Delta\Phi$ = 1V). In this case of study, the nanoparticle moves in the direction of the electrophoretic force. This figure shows that the bigger nanoparticle moves faster in the same size nanochannels. The same size nanochannels have the same EDL thickness; by increasing the size of the nanoparticles, the gap between the nanoparticle and the wall of nanochannel decreases, consequently, the local electric field in the smaller gap and hence the electrophoresis drive force to the particle increases. Thus, the nanoparticle should move faster.

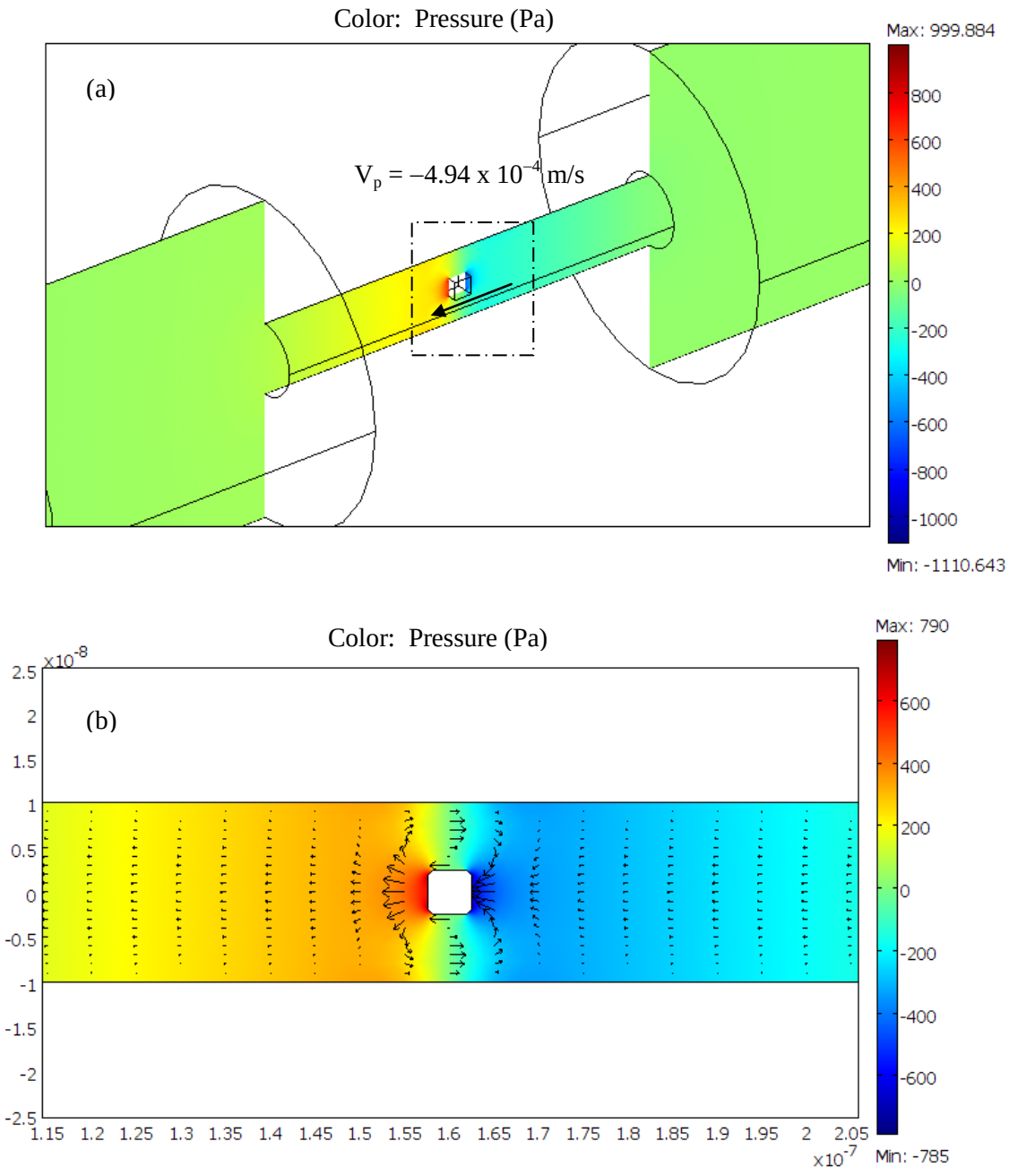

Figure 6-5 (a) The induced pressure field, and (b) the flow field around the moving cubic particle in the nanochannel. The color bar indicates the induced pressure in Pa. The nanoparticle moves from the right to the left at a velocity Vp = - 4.94 x 10-4 m/s. ΔΦ = 1V, $C = 10^{-2}\ mol/m^3$, $\sigma_w = \sigma_p = -0.0001 C/m^2$, $R = 10\,nm$, **and** $a = 5\,nm$.

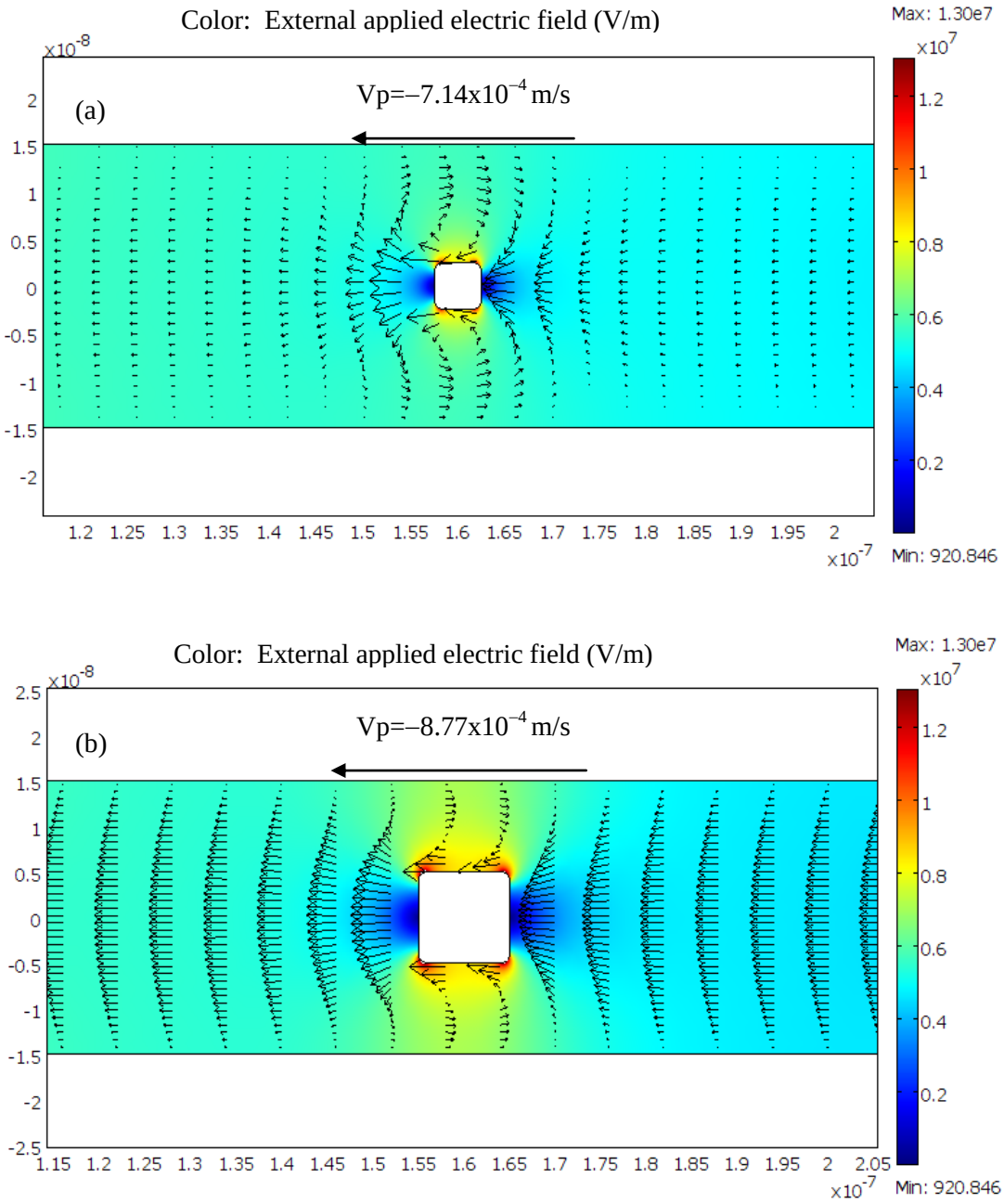

Figure 6-6 Applied external electric field and velocity vectors around moving cubic particle in nanochannel ($C=10^{-2}\ mol/m^3$, $\sigma_w=\sigma_p=-0.0001C/m^2$, $R=15\,nm$, **and** $\Delta\phi=1V$**). (a)** $a=5\,nm$**, (b)** $a=10\,nm$**. The color bar indicates the externally applied electric field.**

6.4.3 Effects of bulk ionic concentration

Generally, the ionic concentration of the liquid will affect the electric double layer fields of the nanochannel and the nanoparticle, and the applied electric field along the nanochannel. Consequently, the ionic concentration affects the velocity of the nanoparticle. Figure 6.7 illustrates the net velocity variation of the nanoparticle with time for four different values of the bulk ionic concentrations. The negative sign of the velocity of the nanoparticle means that the particle moves in the opposite direction of the x-axis, i.e., from the right to the left (see Figure 6.1). It should be realized that, because both the nanoparticle and the nanochannel are negatively charged, the electrophoresis tends to move the nanoparticle towards the left (the positive electrode in Figure 6.1); and the electroosmotic flow caused by the negatively charged channel wall tends to move towards the right (the negative electrode in Figure 6.1). In this simulation, the surface charge densities of the nanoparticle and the channel wall are the same, $-0.0001\ \mathrm{C/m^2}$. It should be pointed out that, the body force for the electroosmotic flow in the nanochannels is $\sum_i (z_i F c_i)\nabla\phi$, see Eq. (6.5). This force is function of the bulk ionic concentration c_i. When the bulk ionic concentration increases, the body force for the electroosmosis increases and therefore the EOF velocity increases. Thus, the motion of the nanoparticle towards the left will be reduced, and the particle velocity becomes smaller.

As explained above, by increasing the bulk ionic concentration, the electroosmotic flow increases, and hence, according to Eq. (6.21), the hydrodynamic force strengthens. Therefore, increasing the bulk ionic concentration can also change the direction of the nanoparticle movement. As an example, Figure 6.7 also shows that the velocity of the nanoparticle can change from negative to positive when the bulk ionic concentration changes from $0.001\,mol/m^3$ to $0.3\,mol/m^3$.

It should emphasize that for the low values of the bulk ionic concentration, the nanoparticle moves in the opposite direction of the flow field, due to the electrophoresis effect; increasing the bulk ionic concentration retards the nanoparticle motion. Further increase of the bulk ionic concentration can reverse the direction of the nanoparticle movement.

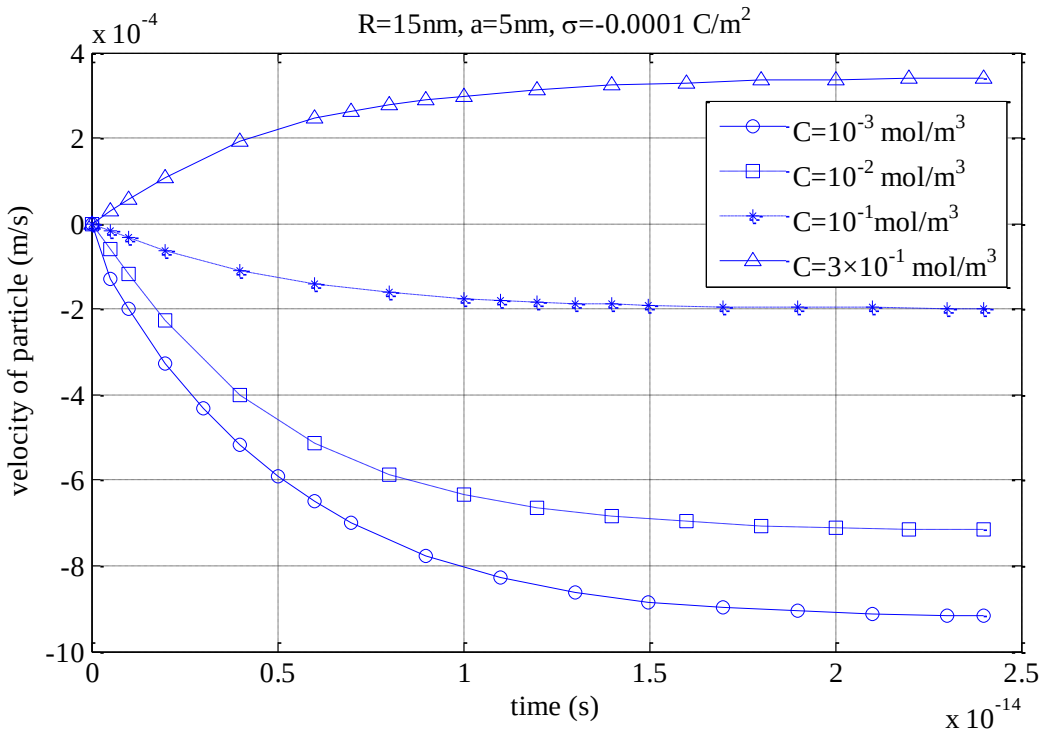

Figure 6-7 Effects of bulk ionic concentration on the velocity of the nanoparticle. The radius of the nanochannel is 15 nm and the particle size is 5 nm, respectively. Surface electric charge densities on the walls of the nanochannel and on the surface of the nanoparticle are $-0.0001 C/m^2$ **, and** $\Delta\phi = 1V$ **.**

6.4.4 Effects of surface electric charge of the nanochannel

As explained before, the two different forces (the electrophoretic and the hydrodynamic) determine the nanoparticle motion. Direction of the nanoparticle movement is determined by the net force of these two forces. Similar to the bulk ionic concentration, increase of the surface electric charge of the walls of the nanochannel intensifies the electroosmotic flow and hence the hydrodynamic force on the nanoparticle. Figure 6.8 shows the effects of the surface electric charge of the nanochannel on the velocity of the nanoparticle. In this simulation, the surface charge density of the nanoparticle is $-0.0001 C/m^2$. This figure shows that, for lower values of the surface electric charge on the walls, the nanoparticle moves in the negative direction of x-axis. This implies that the electrophoretic effect is dominant. Increasing the surface electric charge on the channel wall will increase the electroosmotic flow in the positive direction of the x-axis (from the left to the right as

shown in Figure 6.1). Over a certain value of the surface charge density, the electroosmotic flow is so strong that the associated hydrodynamic force (viscous frictional force on the particle by the moving liquid) will carry the particle to move with the flow (in the positive direction of the x-axis). Therefore, higher values of the surface electric charge can reverse the direction of nanoparticle motion.

In summary, it should be noted that for the case of low surface electric charge on the walls of the nanochannel (hence the weaker electroosmotic flow), the nanoparticle moves in the opposite direction of the flow field (dominant by the electrophoresis). Intensifying this surface electric charge of the channel wall slows down the nanoparticle; further increase of the surface electric charge can reverse the direction of the nanoparticle motion.

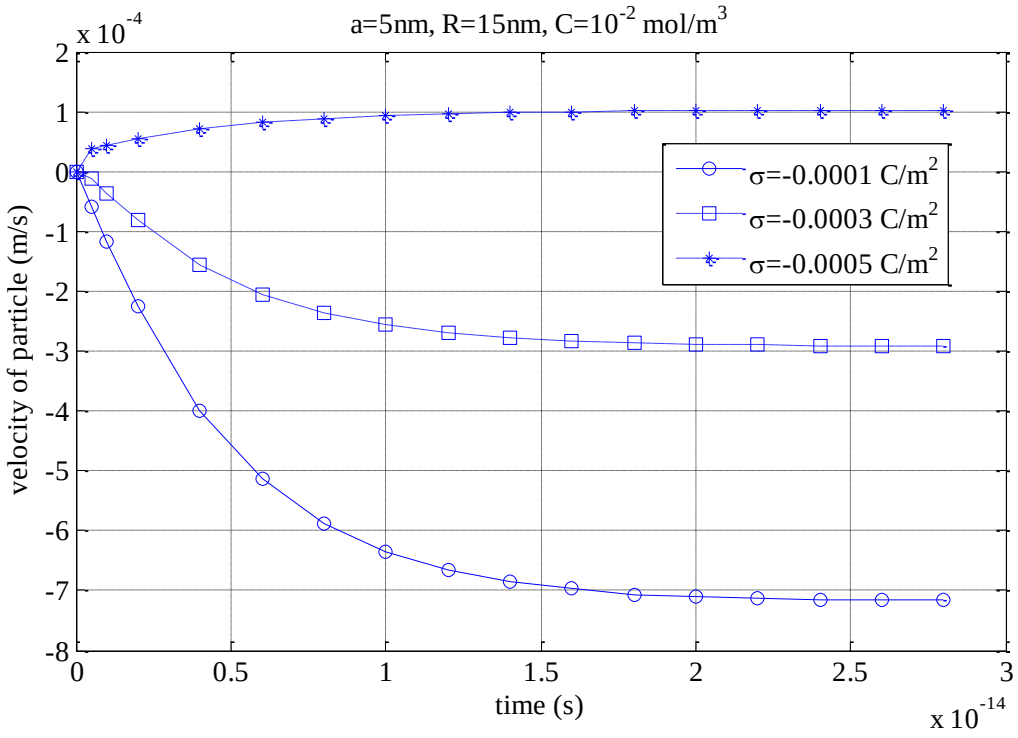

Figure 6-8 Effects of the surface electric charge density of the nanochannel on the velocity of the nanoparticle. The surface charge density of the nanoparticle is -0.0001C/m^2, and $\Delta\phi = 1V$.

6.4.5 Effects of the nanochannel cross-sectional area

The effects of the particle size and channel size on the electrophoretic motion of micro-particles in microchannels have been studied previously (Ye, et al., 2005; Xuan, et al., 2005; Daghighi, et al., 2010). For the case of thin EDL, a larger particle moves faster than a smaller particle in a microchannel with a fixed size. This is because the electrophoretic force on the particle or the local applied electric field near the particle is intensified by the smaller gap between the particle and wall of the microchannel. Furthermore, for the case of the thin EDL, changing the dimension of the microchannel has no effects on the electroosmotic flow (i.e., the EOF velocity is independent of the microchannel size) and consequently the hydrodynamic force on the particle. However, this story is different for the case of the microchannel with a thick EDL or the case of the small nanochannel where the EDL thickness is comparable with the channel's dimension. In these cases, the electroosmotic flow velocity field is not independent of the channel size. It has been shown that the particle moves slower in the smaller microchannel with the thick EDL (Shugai, et al., 1999). For the electrophoretic motion of the particles in the nanochannels, because the EDL thickness is similar to the size of the nanochannel, one should expect the behaviour similar to that in the microchannels with the thick EDL: The particle of a fixed size should move slower in the smaller nanochannels.

Figure 6.9 shows the influences of the nanochannel cross sectional area on the velocity of the nanoparticle of a fixed size, a = 5 nm. The negative value of particle velocity in this figure indicates that the nanoparticle moves in the negative direction of x-axis, i.e., the opposite direction of the electroosmotic flow. It shows that the velocity of the particle decreases as the nanochannel's diameter decreases. This may be understood as the following: When the size of the nanochannel is smaller, the EDL overlap increases, and the EDL field is stronger. Consequently the electroosmotic flow is stronger in a smaller nanochannel. Because the electroosmotic flow is in the opposite direction to the electrophoresis of the particle, the particle's motion from the right-to the left is therefore decreased. In brief, if the surface electric charge and the bulk ionic concentrations keep constant, the same size nanoparticles move faster in the bigger nanochannels.

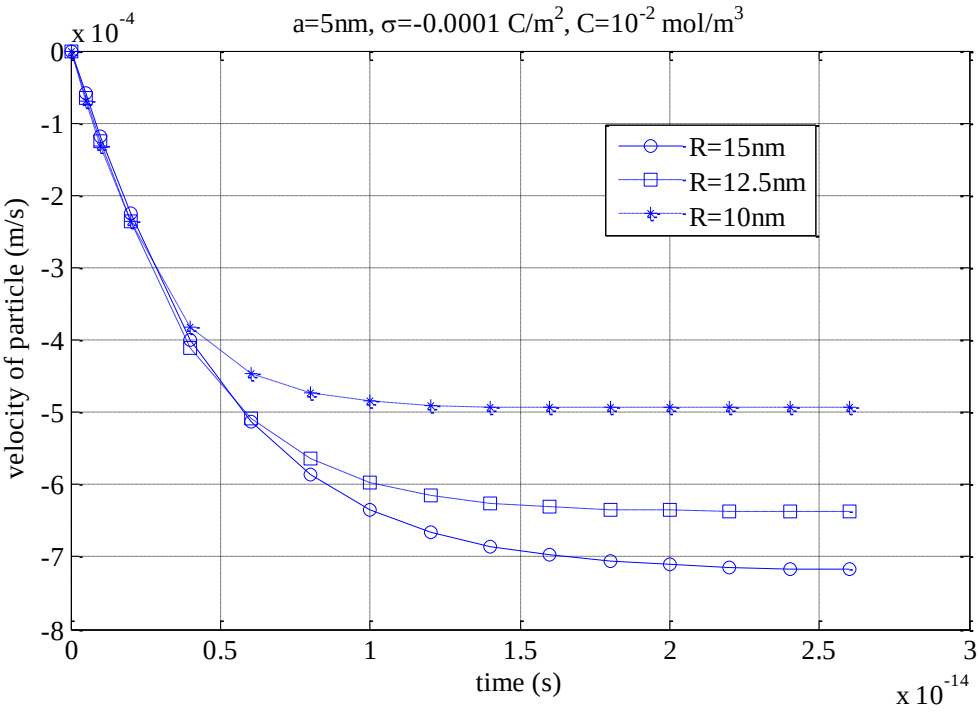

Figure 6-9 . Effects of nanochannel cross sectional area on the velocity of nanoparticle. The size of the nanoparticle is 5 nm. Surface electric charge densities on the walls of the nanochannel and the surface of the nanoparticle are the same $-0.0001\,C/m^2$ **,** $C = 0.01\,mol/m^3$ **, and** $\Delta\phi = 1V$ **.**

Figures 6.7, 6.8, and 6.9 show that the nanoparticle accelerates very fast in the nanochannels and its transient response is in the order of femtosecond. This is too fast to be detected by the current experimental methods. Thus, understanding of the characteristics at steady state will be sufficient for the appreciation of the electrokinetic motion of the nanoparticles in the nanochannels. Figure 6.10 shows how the bulk ionic concentration, surface electric charge, and size of the nanochannel impact the steady state velocity of the nanoparticle. This figure represents all the major conclusions of sections 6.4.2 to 6.4.5.

(a)

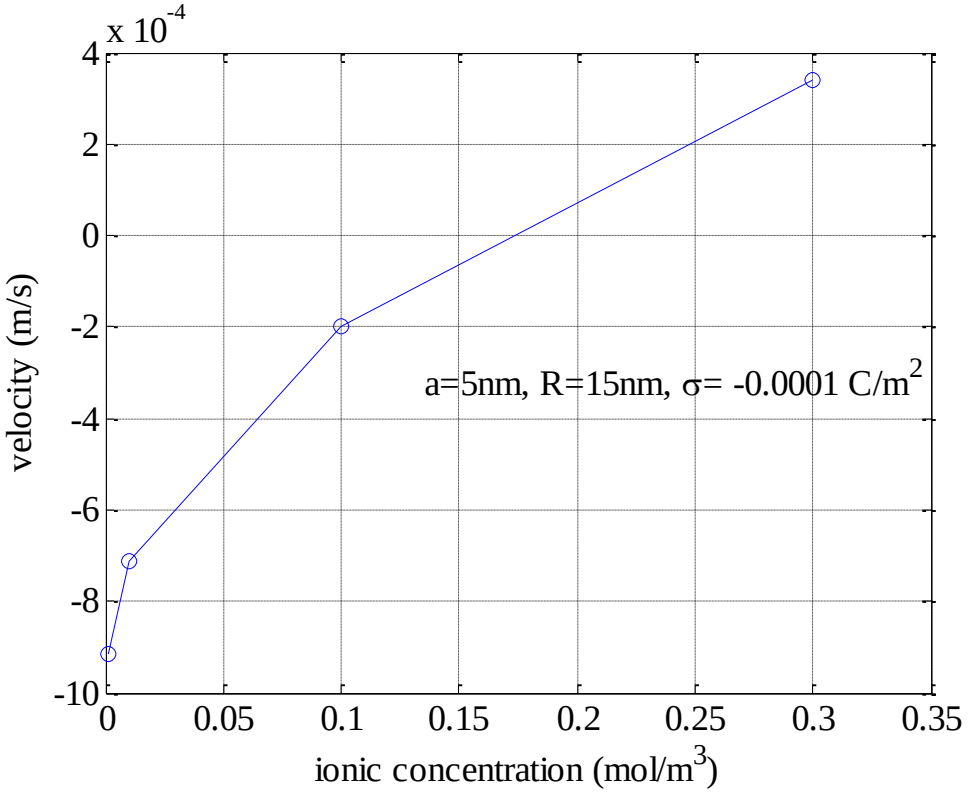
x 10^-4
4
2
0
-2
-4
-6
-8
-10
velocity (m/s)
a=5nm, R=15nm, σ= -0.0001 C/m^2
0
0.05
0.1
0.15
0.2
0.25
0.3
0.35
ionic concentration (mol/m^3)

(b)

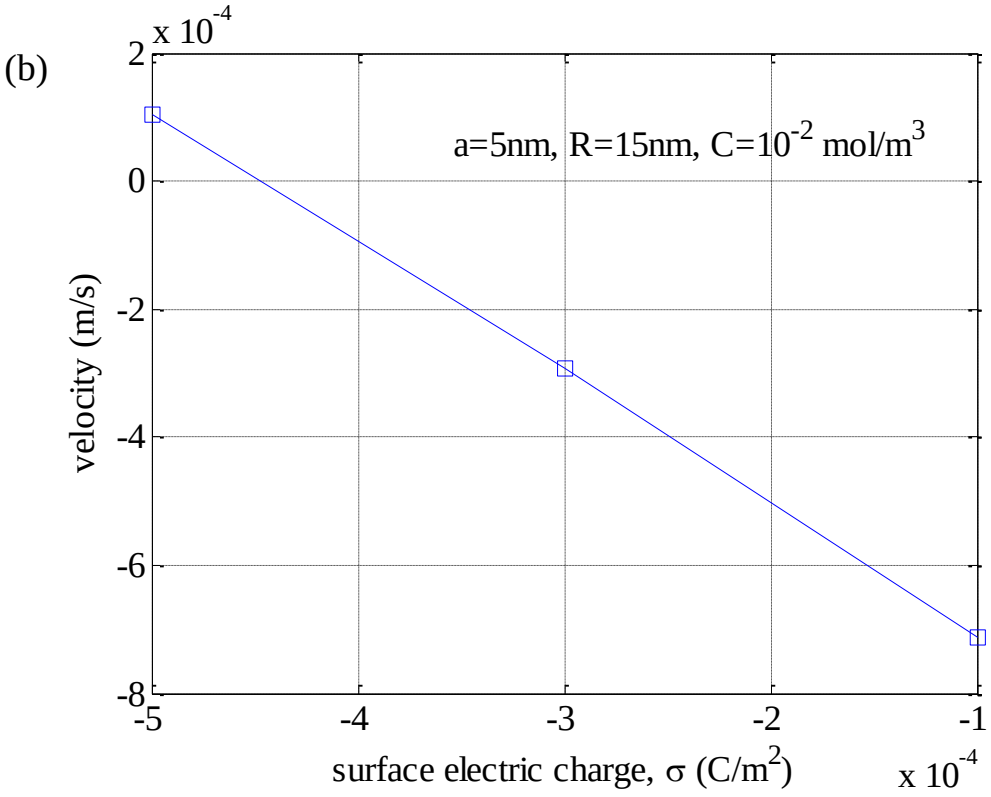
x 10^-4
2
0
-2
-4
-6
-8
velocity (m/s)
a=5nm, R=15nm, C=10^-2 mol/m^3
-5
-4
-3
-2
-1
surface electric charge, σ (C/m^2)
x 10^-4

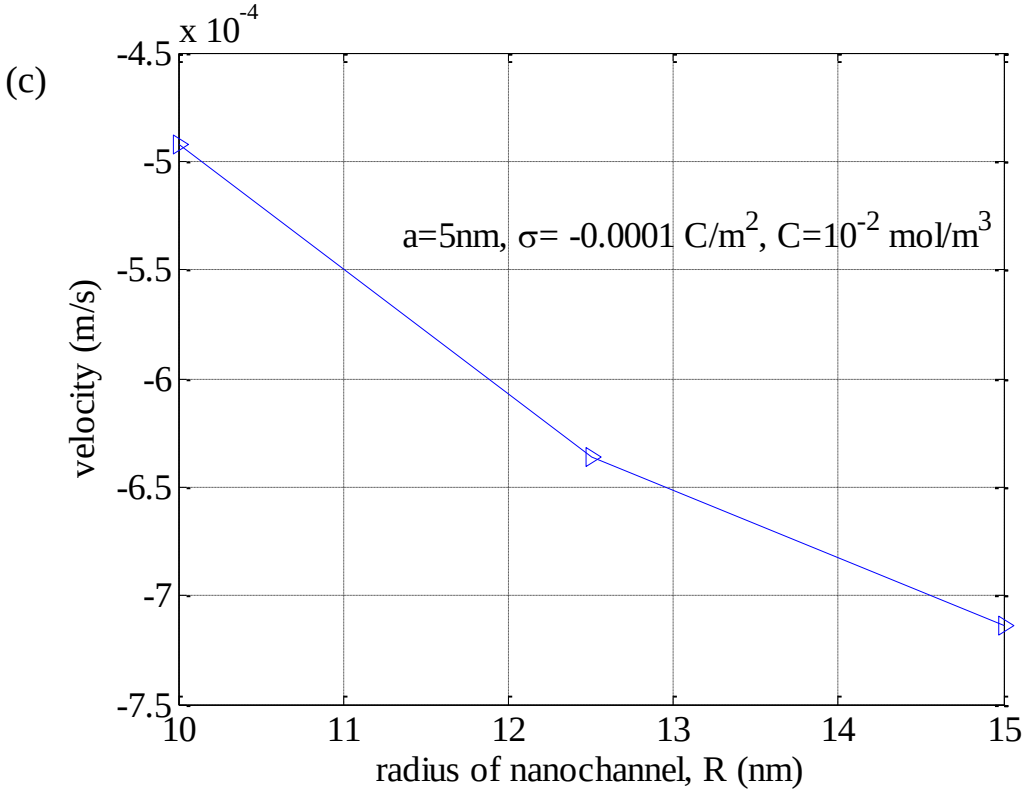

Figure 6-10 Effects of bulk ionic concentration (a), surface electric charge on the walls of the nanochannel (b), and the radius of the nanochannel (c) on the steady state velocity of the nanoparticle.

6.5 Concluding Remarks

The electrophoretic motion of a negatively charged cubic nanoparticle in the nanochannel with the circular cross-section was studied. The influences of the reservoirs at the ends of the nanochannel on the electric field, the ionic concentration field, the flow field were considered. Because of the very large electric field applied over the nanochannel, the Brownian motion of the nanoparticle is negligible in comparison with the electrokinetic effects. Increasing the bulk ionic concentration increases the electroosmotic flow and may change the particle's motion and carry the particle with the electroosmotic flow. Increasing the surface charge density of the nanochannel wall has the same effect. For a fixed nanochannel size, a larger nanoparticle will move faster than a smaller nanoparticle under the same conditions, because of the stronger local electric field in the smaller gap region between the larger particle and the channel wall. For the nanoparticles of the same size,

decreasing the nanochannel size will increase the electric double layer field and hence the electroosmotic flow in the nanochannel, consequently affect the particle's motion.

Chapter 7
Electrokinetic Transport of Nanoparticles to the Opening of Nanopores in Cell Membrane during Electroporation

7.1 Introduction

So far this thesis has studied different parameters affecting the membrane permeabilization and transfection during the electroporation of a single cell located in the microchannel. After performing a complete literature survey in Chapter 2, membrane permeabilization of the single cell located in a microchannel has been investigated in Chapter 3. The results of this chapter show that how the electric pulse induces the electric potential on the cell membrane (Transmembrane Potential, TMP) and what is the density and radius of the created nanopores on the cell membrane. Chapter 4 investigates an electrokinetic transport through the nanochannels. In Chapter 5, I have utilized the proposed model of Chapter 4 to investigate the electric potential, the flow field, and the ionic mass transfer through the created nanopores on the cell membrane during the electroporation. Chapter 6 examines the electrokinetic motion of the nanoparticle in the nanochannel. The results of this part may be exploited to mimic how the QDots move through the created nanopores on the cell membrane during the electroporation.

Until now, the results of this study explain many aspects of the single cell electroporation in the microchannel and the electrokinetics in nanofluidics. However, it has not clarified yet that how the nanoparticles (nanoscale biosamples such as QDots) will be transported to the opening of the nanopores and what forces influence the process. In this chapter, the aim is to study the nanoparticle transport to the opening of created nanopores on the cell membrane during the electroporation. It is explained what forces play an important role on the process and how the size and the surface electric charge of the nanoparticle influence the nanoparticle transport. The influence of an angular position of the created nanopores on the nanoparticle transport will also be investigated. In the following sections, first, an assumed physical model and computational domains of the current study will be explained. Next, the mathematical modeling and the governing equations will be reviewed. Then, the numerical simulation techniques will be introduced. After that, the results will be shown and discussed, and finally, the concluding remarks will be presented.

7.2 Model Description

Reversible electroporation can create nanopores in the cell membrane which serve as a pathway for biological samples, ions, and fluid transport. "Theory of cell membrane permeabilization" explains how the nanopores create on the cell membrane during electroporation (Neu, et al., 1999). The flow and the ion transfer in such a nanoscale channel can be analyzed by a combination of equations governing electrostatics, mass transfer, and momentum transfer (Movahed, et al., 2012). Once the flow field, the ionic mass transfer, and the electric potential are determined, the applied electroosmotic and electrophoretic forces on the nanoparticles can be calculated, and consequently the Newton second law will be utilized to find the velocity of the nanoparticle and trace it in the computational domain.

In the current study, first, we apply the required electric pulse around a spherical cell of radius a (diameter d_0) to electroporate it. The cell immersed an aqueous solution in a microchannel of height h_c (see Figure 7-1). The thickness of the cell membrane is assumed to be t_m. The electric pulse is applied to the cell via the two electrodes placed on the side walls of the microchannel. Once the radius and location of the nanopores and also the electric potential in the vicinity of the created nanopores are determined, a highly coupled system of partial differential equations will be solved to find the ionic mass transfer, fluid flow, and electric potential and consequently exerted electroosmotic and electrophoretic forces on the nanoparticle. The detail of the mathematical modeling and the governing equations will be explained in the next section.

The assumed computational domain of created nanopores has been depicted in Figure 7-2. The nanopore is assumed to have a circular cross-section, and the length of the nanopore is equal to the cell membrane thickness. "Inside" and "outside" domains, that represent the interior and the exterior of the cell, should be considered to have an accurate analysis on the electrokinetic transport through the generated nanopores.

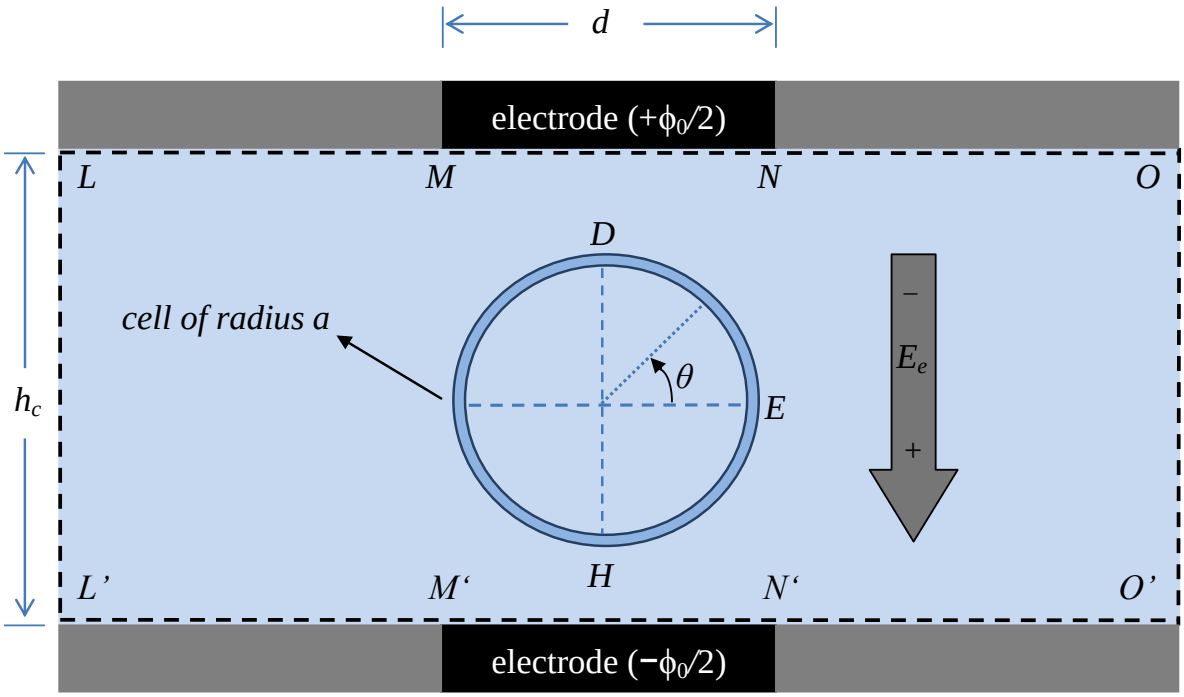

Figure 7-1 The schematic diagram of the assumed system of the current study. A cell of radius a is assumed in the microchannel of height h_c. The microchannel is filled with the conductive medium. The required voltage of the electroporation (ϕ_0) is applied via the two electrodes of length d located on the wall of the microchannel.

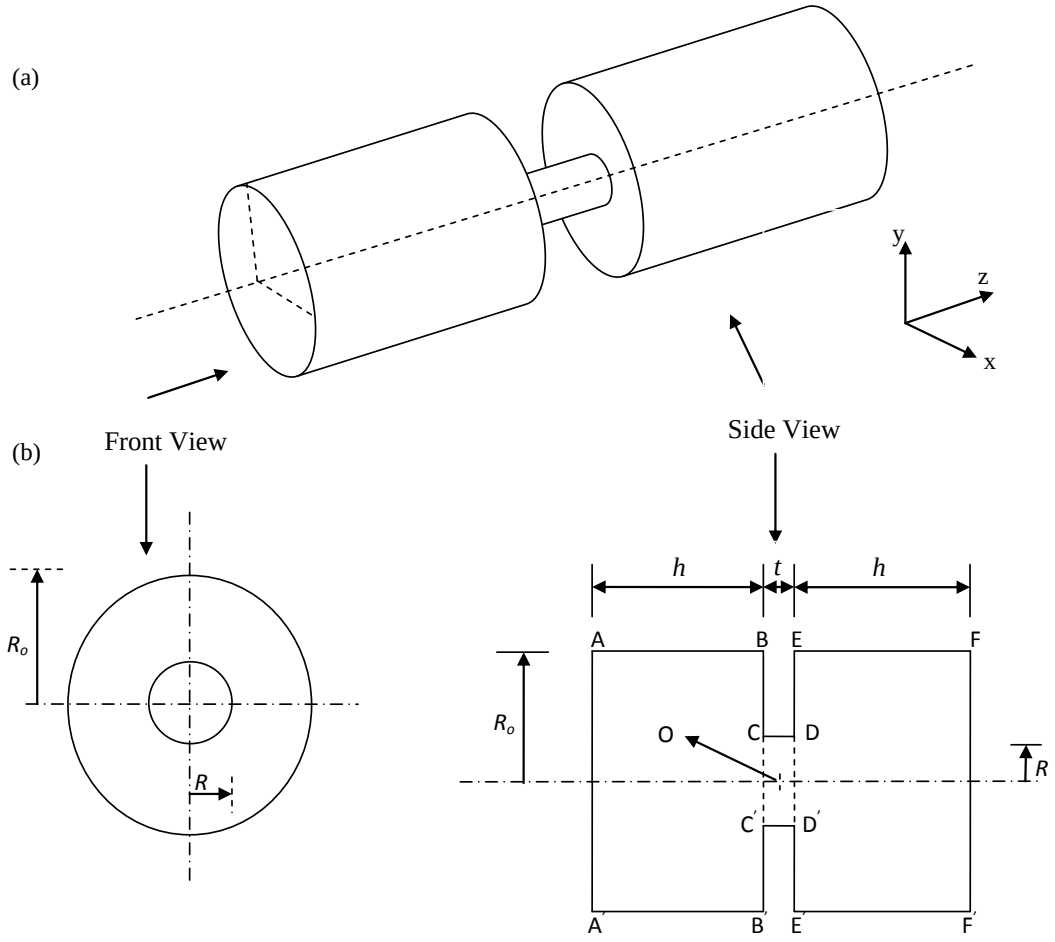

CDD′ C′: Nanopore ABB′A′: Outside of the cell EFF′E′: Inside of the cell

Figure 7-2 Schematic diagram of the computational domain. Parts (a) and (b) are 3-D and side-view illustrations of the computational domain. Arrows show the view of each figures of part (b). The pore is circular with a radius R. The length of the pore is equal to the cell membrane thickness (t_m). h is assumed to be ten times of the membrane thickness ($h = 10t_m$). In order to consider the effects of interior and exterior of the cell on the flow field, the ionic mass transfer, the electric potential, and the nanoparticle transport to the opening of the created nanopores, $ABB'A'$ and $EFF'E'$ sections are considered. The radius at these parts is R_o ($R_0 = 10R$).

7.3 Mathematical Modeling

In this section, the mathematical modeling of the current study is introduced. First, the governing equations of the membrane permeabilization will be reviewed. The equations should be solved to find the size, density, and location of the created nanopores on the cell membrane. In section 7.3.2, the coupled system of partial differential equations will be reviewed that should be solved to find the electrokinetic transport (electric potential, ionic mass transfer, and fluid flow) in the created nanopores. Consequently, the Newton second law should be utilized to trace the nanoparticle in the vicinity of the created nanopores.

7.3.1 Cell Membrane Permeabilization

7.3.1.1 Electric Field

The Laplace equation ($\nabla^2 \phi_{i,e} = 0$) should be solved to find the electric potential inside (ϕ_i) and outside (ϕ_e) the cell. The required voltage of the electroporation (ϕ_0) is applied via the embedded electrodes on the two sides of the cells. Thus, the electrical boundary condition on boundaries MN and M´N´ is assumed as:

$$\phi_{e,MN} = \phi_0/2 \tag{7.1.a}$$

$$\phi_{e,M'N'} = -\phi_0/2 \tag{7.1.b}$$

The walls of the microchannels are electrically insulated. There is also no current flow at the two ends of the microchannel. Therefore, the assumed electrical condition on boundaries *LM*, *NO*, *OO*', *O*'*N*', *M*'*L*', and *L*'*L* is:

$$\hat{n} \bullet \vec{J} = 0 \tag{7.2}$$

The electric current density should be continuous across the cell membrane (DeBruin, et al., 1999; DeBruin, et al., 1999):

$$-\hat{n} \bullet (s_i \nabla \phi_i) = -\hat{n} \bullet (s_e \nabla \phi_e) = c_m \frac{\partial V_m}{\partial t} + g_1 (V_m - V_{rest}) + I_p \tag{7.3}$$

In this equation $\hat{n}$ is the local outward unit vector normal to the surface of cell membrane, ∇ is the Nabla symbol, s_i and s_e are the intracellular and extracellular conductivities; V_m and V_{rest} are the transmembrane potential (TMP) and rest potential. g_1 and c_m are the surface conductance and

capacitance of the membrane, in that order. The transmembrane potential is defined as $V_m = \phi_i(t, a, \theta) - \phi_e(t, a, \theta)$.

The first and the second terms of the right hand-side of Eq. (7.3) represent the capacitive current ($c_m \partial V_m / \partial t$) and the current through the protein channels ($g_1(V_m - V_{rest})$), respectively. I_p represents the current through the created nanopores. If the cell membrane is discretized into k elements, the surface area of each segment can be found as $\Delta A = 2\pi a / k$. At each of these sections of membrane, I_p can be found as (Krassowska, et al., 2007):

$$I_p(t) = \frac{1}{\Delta A} \sum_{j=1}^{m} i_p(r_j, V_m) \tag{7.4}$$

Here, m is the number of the created nanopores at each segment; i_p is the current through each nanopore that can be computed by using the following equation (Krassowska, et al., 2007):

$$i_p(r, V_m) = \frac{V_m}{R_p + R_i} \tag{7.5}$$

where R_p is the Ohmic resistance of the cylindrical pores and R_i is the correcting resistance that is used to consider the effect of changing in transmembrane potential in vicinity of the pores. (Krassowska, et al., 2007):

$$R_p = \frac{t_m}{s\pi r^2} \tag{7.6}$$

$$R_i = \frac{1}{2sr} \tag{7.7}$$

In the above equations, t_m and s are the membrane thickness and the conductivity of the solution filling the nanopore, respectively.

7.3.1.2 Number of nanopores:

The rate of creation of the nanopores can be found as (Neu, et al., 1999):

$$\frac{dN(t)}{dt} = \alpha e^{(V_m / V_{ep})^2} \left(1 - \frac{N(t)}{N_{eq}(V_m)}\right) \tag{7.8}$$

where $N(t)$ is the density of pores define as:

$$N(t) = \int_{r_*}^{\infty} n(r,t)dr \tag{7.9}$$

N_{eq} is the equilibrium pore density for the given transmembrane voltage, V_m :

$$N_{eq}(V_m) = N_0 e^{q(V_m/V_{ep})^2} \tag{7.10}$$

In the above Equations, α , V_{ep} , q , and N_0 are the constants that can be found in Table 7-1.

7.3.1.3 Radius of nanopores:

Based on the theory of the membrane permeabilization, the nanopores are initially created with a radius of r^* (Neu, et al., 1999). By increasing the applied electric field, the nanopores start to develop in order to minimize the energy of the cell membrane. For the membrane with n nanopores, the rate of change of their radii, r_j , can be determined by the following set of equations (Neu, et al., 1999):

$$\frac{dr_j}{dt} = U(r_j, V_m, \sigma_{eff}), \quad j = 1,2,....,n \tag{7.11.a}$$

$$U(r,V_m,A_p) = \frac{D}{kT}\{4\beta(\frac{r_*}{r})^4 \frac{1}{r} - 2\pi\gamma + 2\pi\sigma_{eff} r + \frac{V_m{}^2 F_{\max}}{1+r_h/(r+r_t)}\}, \quad \text{in } r \geq r_* \tag{7.11.b}$$

The constants of the above equations have been defined in Table 7-1. σ_{eff} is the effective tension of the membrane. If A is the surface area of the cell membrane and A_p is the area of the created nanopores

($A_p = \sum_{i=1}^{n} \pi r_i^2$), σ_{eff} can be computed as (Krassowska, et al., 2007):

$$\sigma_{eff}(A_p) = 2\sigma' - \frac{2\sigma' - \sigma_0}{(1 - A_p/A)^2} \tag{7.12}$$

7.3.2 Electrokinetic Transport

Once the location and size of the created nanopores are determined, the Electrokinetic theory should be utilized to find the electric potential, the ionic transfer, the fluid flow, and the nanoparticle transport toward the opening of the nanopores. Because of comparable dimensions of the EDL thickness and the nanopore radius, the conventional Electrokinetics such as the Helmholtz-Smoluchowski velocity and the Poisson-Boltzmann equation may not be applicable anymore.

However, former experimental studies show that the continuum hypothesis is valid up to 4 nm for aqueous solutions (Zheng, et al., 2003). In this study, we have utilized a more generalized model to study the electrokinetic effects in the system (Movahed, et al., 2011) that will be briefly reviewed in the following sections. In the equations of this section, ϕ is the electrostatic potential and c_i is the concentration of ion species *i*; p and $\vec{u}$ are the pressure and the velocity vector, respectively. The constants include permittivity ($\varepsilon_0\varepsilon_r$), medium density ($\rho$), Faraday number ($F$), fluid viscosity ($\eta$), valance number ($z_i$), diffusion coefficient (D_i), and mobility (μ_i) of ion species *i*.

7.3.2.1 Electric potential in the nanopores:

In such a nanoscale dimensions, the Poisson equation ($\nabla\bullet(-\varepsilon_0\varepsilon_r\vec{\nabla}\phi) = F\sum_i z_i c_i$) must be solved in order to find the electric potential distribution in the nanopore. This equation is a function of the local ionic concentrations that can be found by the Nernst Plank equation. Electric field is the gradient of the electric potential ($\vec{E} = -\vec{\nabla}\phi$). The electric field through the nanopores is influenced by the nanopores dimension, the ionic concentrations, and the surface charged of the nanopores. Here, z_i and c_i are the valence and concentrations of ion type i, ϕ is the electric potential, $\vec{E}$ is the electric field, ε_0 and ε_r are the absolute and relative permeability, and F is the Faraday constant.

The electrical boundary conditions have been determined from the numerical results of section 7.3.1. Transmembrane potential (U_m) is the potential difference along the nanopore length direction. Inside the cell membrane, the electric potential is equal to rest potential ($\phi_{rest} = -80\ mV$); so, in the computational model the electric potential at boundaries ED, $E'D'$, BC, and $C'B'$ become:

$$\phi_{ED} \text{ and } \phi_{E'D'} = \phi_{rest} \tag{7.13.a}$$

$$\phi_{BC} \text{ and } \phi_{C'B'} = -TMP + \phi_{rest} \tag{7.13.b}$$

The wall of the nanopore has electrostatic charge. If the constant surface electric charge density (ρ_s) is considered at the walls of the nanopore, following relations can be used to set the electrical boundary conditions at the walls of the nanopores (boundaries *CD* and $C'D'$):

$$D = \varepsilon\varepsilon_0 E \tag{7.14.a}$$

$$n\bullet D = -\rho_s \tag{7.14.b}$$

Boundaries AA' and *FF'* are located on two sides of the membrane, outside and inside the cell domain. As it was indicated before, the Laplace equation should be solved to find the electric potential outside (ϕ_e) and inside (ϕ_i) the cell domain (see section 7.3.1). The proper electrical boundary conditions (ϕ_1 and ϕ_2), that are the solutions of the Laplace equation at these boundaries, should be applied at the boundaries AA' and *FF'* in order to consider the effects of external electric field (E_e) on the electrokinetic effects in the vicinity and through the nanopore:

$$\phi_{AA'} = \phi_1 \tag{7.15.a}$$

$$\phi_{FF'} = \phi_2 \tag{7.15.b}$$

There is no surface electric charge at boundaries *AB*, *EF*, $A'B'$ and $E'F'$:

$$n \bullet D = 0 \tag{7.16}$$

7.3.2.2 Ionic Concentration Field:

The Nernst-Planck equation (Eq. (7.17)) is used to describe the mass transfer in the computation domain.

$$\nabla \bullet (\vec{u} c_i) - \nabla \bullet (D_i \vec{\nabla} c_i) - \nabla \bullet (z_i \mu_i c_i \nabla \phi) = 0 \tag{7.17}$$

In this equation, the first term is the effect of electroosmosis (convection) on ionic mass transfer. The second and the third terms present the influences of diffusion and electrophoresis on ionic mass transfer, respectively.

At boundaries *AH* and *KB*, constant bulk ionic concentration c_0 is utilized (Eq. (7.18)). Here, subscripts *i* and *e* indicate the inside and the outside of the cell.

$$c = c_{0,i} \tag{7.18.a}$$

$$c = c_{0,e} \tag{7.18.b}$$

The walls of the nanopore (boundaries *CD* and $C'D'$) and the cell membrane surface (*BC*, DE, $B'C'$ and $D'E'$) are assumed to be impermeable for mass transfer.

$$n \bullet N_i = 0 \tag{7.19}$$

$$N_i = -D_i \nabla c_i - z_i \mu_i c_i \nabla \phi + c_i \vec{u} \tag{7.20}$$

7.3.2.3 The Flow Field:

Modified Navier-Stokes equations (Eq. (7.22)) along with the continuity equation (Eq. (7.21)) should be solved in order to find the flow field in the system. Boundaries AA' and FF' are assumed as the open boundary (Eq. (7.23)). This type of boundary condition is usually used when the boundaries are connected to a large reservoir (for example, comparing the volume of the nanopore with the interior of the cell). The flow can either enter or exit from these boundaries. At the wall of the nanopore (*CD* and $C'D'$) and the surface of the cell (*BC*, $B'C'$, *ED*, and $E'D'$), no-slip boundary condition is assumed (Eq. (7.24)). We also utilized the symmetric boundary condition (Eqns. (7.25) and (7.26)) for other boundaries (*AB*, *EF*, $A'B'$, and $E'F'$).

$$\nabla \bullet \vec{u} = 0 \tag{7.21}$$

$$\rho(\frac{\partial \vec{u}}{\partial t} + (\vec{u} \bullet \nabla)\vec{u}) = -\nabla p + \eta \nabla^2 \vec{u} - (\sum_i z_i F c_i)\nabla \phi \tag{7.22}$$

$$\nabla \vec{u} = 0\,, \quad p = 0 \tag{7.23}$$

$$\vec{u} = 0 \tag{7.24}$$

$$n \bullet \vec{u} = 0 \tag{7.25}$$

$$t \bullet [-pI + \eta(\nabla u + (\nabla u)^T)] = 0 \tag{7.26}$$

7.3.2.4 Electrokinetic Motion of the Nanoparticle:

Once the flow field, ionic concentration, and electric potential in the vicinity of the created nanopore are determined, the exerted electroosmotic (hydrodynamic, $\vec{F}_{hd}$) and electrophoretic ($\vec{F}_{ep}$) forces on the nanoparticle can be calculated to study the nanoparticle transport into the created nanopores. Because the surface of the nanoparticle is negatively charged, the electrophoretic and the electroosmotic effects are in the opposite directions. Unlike the electroosmotic effects, the electrophoretic force is in the opposite direction of the electric field. Because of the nanoscale of the particles, the Brownian force ($\vec{F}_B$) may also influence the particle motion.

The total force acting on the particle is:

$$\vec{F}_t = \vec{F}_{ep} + \vec{F}_{hd} + \vec{F}_B \tag{7.27}$$

The electrophoretic, the hydrodynamic and the Brownian forces can the calculated as follow (Hsu, et al., 2007; Kadaksham, et al., 2004; Liu, et al., 2005):

$$\vec{F}_{ep} = \iint_s \vec{\vec{T}} \bullet d\vec{s} \tag{7.28.a}$$

$$T_{ij} = \varepsilon\varepsilon_0 (E_i E_j - \frac{1}{2}\delta_{ij} |E|^2) \tag{7.28.b}$$

$$\vec{F}_{hd} = \iint_s \vec{n} \bullet (-p\vec{I} + \mu\left[\nabla\vec{u} + (\nabla\vec{u})^T\right]) ds \tag{7.29}$$

$$\vec{F}_B = \varsigma \sqrt{\frac{12\pi a \mu k_B T}{\Delta t}} \tag{7.30}$$

In the above equations, $\vec{I}$ is the identity tensor and $\vec{\vec{T}}$ is the Maxwell stress tensor; T_{ij} is the representation of this tensor with Einstein notation. In Eq. (7.30), ς is the Gaussian random number with zero mean and unit variance; a is the radius of the nanoparticle, μ is viscosity, k_b is Boltzmann constant, T is temperature, and Δt is time step.

At each time steps, the Newton second law can be utilized to find the velocity of the nanoparticle ($\vec{V}_p$):

$$\vec{F}_t = m_p \frac{d\vec{V}_p}{dt} \tag{7.31}$$

7.4 Numerical Simulation

The numerical simulation of the current study consists of two parts. In the first step, the explained equations of section 7.3.1 are solved in the computational domain of Figure 7-1 to find the size, density, and location of the created nanopores on the cell membrane. Then, the equations of section 7.3.2 are simulated in the computational domain of Figure 7-2 to find the ionic mass transfer, the fluid flow, and the nanoparticle transports near the created nanopores. In order to discretize the solution domain, the structured meshes are applied. We employ a mesh independent structure to make sure that the results are unique and will not change if any other grid distribution is applied. In order to find the reliable results, which are grid independent, we examine the effect of different number of grids. Finally, we find the number of grids with which the numerical results will not change if we further increase the number of grids.

We employ "Comsol 4.2a with Matlab" commercial package to simulate the equations. In the first step, the cell membrane of Figure 7-1 is discretized with the discretization steps of $\Delta\theta = \pi/60$. In order to discretize the solution domain, the un-structured meshes are applied. The solution domain is

broken into small meshes to allow that the meshes fully cover the solution domain without overlapping. Before applying the electric pulse, the transmembrane potential is equal to the rest potential ($V_m = V_{rest}$). At each time step, first the Laplace equation subjected to proper boundary conditions (Eqns. (7.1-7.5)) is solved by the Finite Element Method to find the electric potential in the domain. As the electric potential is determined, Eqns. (7.6-7.12) can then be solved to find the location, number, and radius of the created nanopores on the membrane. The Runge-Kutta method is utilized to solve ODE equations 7.8 and 7.11. This system of equations is solved with the time-step of $\tau_c/32$, in which τ_c is the time constant of the cellular polarization (Hibino, et al., 1993):

$$\tau_c = aC_m(\frac{1}{s_i} + \frac{1}{s_e}) = 2.4\mu s \tag{7.32}$$

In the next step, the highly-coupled equations of section 7.3.2 are solved simultaneously in the computational domain of Figure 7-2 to study the transport of the nanoparticle near the created nanopores. The solution domain is broken into small meshes to allow that the meshes fully cover the solution domain without overlapping.

7.5 Results and Discussion

Table 7-1 summarized the values of the parameters used in the current study. We assumed a mammalian cell of radius $a = 7.5\ \mu m$ (diameter $d_0 = 15\ \mu m$) suspended in the microchannel of height $h_c = 30\ \mu m$. The electric pulse with the intensity of $\phi_0 = 1.7\,V$ and the duration of $t_0 = 10\ \mu s$ is applied via the two embedded electrodes with a width $d = 20\ \mu m$. The microchannel is filled with the aqueous mixture of $NaCl$ and KCl. The assumed ionic concentrations of the filling aqueous solution were presented in Table 7-1. We consider typical intercellular ionic concentrations of the mammalian cells (Lodish, et al., 2003). The ionic characteristics of different ions Na^+, K^+, and Cl^- can be found elsewhere (Koneshan, et al., 1998).

The radius (R) and position (θ) of the created nanopores, the transmembrane potential (TMP), and the electric potential in vicinity of the created nanopores (ϕ_1 and ϕ_2) will be determined by simulating the simulating the ODE system of section 7.3.1.

Table 7-1 The values for constants and parameters used in the simulations

Parameter	value (unit)	Definition
$d_0 (= 2a)$	$15\,(\mu m)$	diameter of the cell
t_m	$5\,(nm)$	cell membrane thickness (Glaser, et al., 1988)
h_c	$30\,(\mu m)$	height of the microchannel
d	$20\,(\mu m)$	length of the electrode
ϕ_0	$1.7\,(V)$	electric pulse intensity
t_0	$10\,(\mu s)$	electric pulse duration
s_i	$0.455\,(S\,m^{-1})$	intracellular conductivity (Hibino, et al., 1993)
s_e	$5\,(S\,m^{-1})$	extracellular conductivity (Hibino, et al., 1993)
s	$2\,(S\,m^{-1})$	Conductivity of the solution filling the pore (Smith, et al., 2004)
c_m	$0.0095\,(F\,m^{-2})$	Specific membrane capacitance (Hibino, et al., 1993)
g_1	$2\,(S\,m^{-2})$	Surface conductance of the membrane (Hibino, et al., 1993)
V_{rest}	$-80\,(mV)$	rest potential (Chambers, et al., 1979)
α	$1\times10^{9}\ (m^{-2}s^{-1})$	Creation rate coefficient (DeBruin, et al., 1999)
V_{ep}	$0.258\,(V)$	Characteristic voltage of electroporation (DeBruin, et al., 1999)
N_0	$1\times10^{9}\ (m^{-2})$	Equilibrium pore density at $V_m = 0$ (DeBruin, et al., 1999)
r^*	$0.51\,(nm)$	Minimum radius of hydrophilic pores (Glaser, et al., 1988)
r_m	$0.8\,(nm)$	Minimum energy radius at $V_m = 0$ pores (Glaser, et al., 1988)
D	$5\times10^{-14}\ (m^2\,s^{-1})$	Diffusion coefficient for pore radius (Freeman, et al., 1994)
T	$300\,(.K)$	Temperature
β	$1.4\times10^{-19}(J)$	Steric repulsion energy (Neu, et al., 1999)
γ	$1.8\times10^{-11}(J\,m^{-1})$	Edge energy (Glaser, et al., 1988)
$F_{\max}$	$0.7\times10^{-9}(N\,V^{-2})$	Max electric force for $V_m = 1V$ (Neu, et al., 2003)
r_h	$0.97\times10^{-9}(m)$	Constant in Eq. (7.11.b) for advection velocity (Neu, et al., 2003)
r_t	$0.31\times10^{-9}(m)$	Constant in Eq. (7.11.b) for advection velocity (Neu, et al., 2003)
q	$(r_m/r^*)^2$	Constant in Eq. (7.10) for pore creation rate (DeBruin, et al., 1999)
σ'	$2\times10^{-2}(J\,m^{-2})$	Tension of hydrocarbon-water interface (Israelachvili, 1992)

σ_0	$1\times10^{-6}(J\ m^{-2})$	Tension of the bilayer without pores (Hénon, et al., 1999)
F	$96485.3415\,(A\,s\,mol^{-1})$	Faraday constant (Li, 2004)
ε_T	80	relative permittivity (Li, 2004)
ε_0	$8.85\times10^{-8}(F\ m^{-1})$	Vacuum permittivity (Li, 2004)
μ	$1\times10^{-3}\ (Pa\,s)$	Viscosity of medium (Li, 2004)
ρ	$1000(kg\ m^{-3})$	medium density (Li, 2004)
σ_s	$-0.0001(C\,m^{-2})$	surface electric charge of the nanochannel walls
σ_p	$-0.3\sim-0.6\,(C\,m^{-2})$	surface electric charge of nanoparticle
d_p	$10, 12$, and $15\,(nm)$	diameter of the nanoparticle
R_g	$8.314\,(J\ mol^{-1}\ .K^{-1})$	gas constant
$D(Na^+)$	$1.28\times10^{-9}\ (m^2s^{-1})$	diffusion coefficient of Na^+ (Koneshan, et al., 1998)
$D(K^+)$	$1.83\times10^{-9}\ (m^2s^{-1})$	diffusion coefficient of K^+ (Koneshan, et al., 1998)
$D(Cl^-)$	$1.77\times10^{-9}\ (m^2s^{-1})$	diffusion coefficient of Cl^- (Koneshan, et al., 1998)
μ_i	$D_i/(R_g \bullet T)$	mobility of ion species type i
$C_{0,i}(Na^+)$	$12\,(mM)$	Intercellular concentration of Na^+ (Lodish, et al., 2003)
$C_{0,i}(K^+)$	$139\,(mM)$	Intercellular concentration of K^+ (Lodish, et al., 2003)
$C_{0,i}(Cl^-)$	$4\,(mM)$	Intercellular concentration of Cl^- (Lodish, et al., 2003)
$C_{0,e}(Na^+)$	$50\,(mM)$	Extracellular concentration of Na^+
$C_{0,e}(K^+)$	$50\,(mM)$	Extracellular concentration of K^+
$C_{0,e}(Cl^-)$	$100\,(mM)$	Extracellular concentration of Cl^-
k_B	$1.38065\times10^{-23}\ (m^2\ kg\ s^{-2}\ K^{-1})$	Boltzmann Constant (Li, 2004)

In the following sections, first we investigate the membrane permeabilization of the cell suspended in the microchannel. Once the size, the location, and the electric potential near the cell membrane are determined, we utilize the electrokinetic model in section 7.3.2 to study the nanoparticle transport to the created nanopores. In this part, we examine what forces affect the nanoparticle transport and how close the nanoparticles will be to the opening of the nanochannel in order to get into the nanopores. Furthermore, the effects of size and surface electric charge of the nanoparticle on its transport to the opening of the nanopores will be investigated.

In this study, we assume the negatively charged nanoparticles. The results of this study show that the electrophoretic force is the dominant one in transporting the nanoparticle. The electrophoretic

force exerting on the negatively charged nanoparticle is in the opposite direction of the electric field. Thus, the negatively charged nanoparticle should be inserted to the cell from the back of the cell (the side that facing the negative electrode ($180 \le \theta \le 360$), see Figure 7-3) where the TMP is positive and the direction of the electrophoretic force is from outside to the inside of the cell membrane.

7.5.1 Membrane Permeabilization:

Figure 7-3 shows that how the presence of the electric pulse affects the TMP and creates the nanopores on the cell membrane. As indicated before, the radius of the cell and the height of the microchannel are $a = 7.5\ \mu m$ and $h_c = 30\ \mu m$, respectively. The electric pulse intensity and duration are $\phi_0 = 1.7\,V$ and $t_0 = 10\ \mu s$. The obtained results show that the nanopores' radius and density are symmetric along the equator (see Figure 7.1). The transmembrane potential has the same magnitude but with the opposite sign on the two sides of the cell membrane ($0^\circ \le \theta \le 180^\circ$ and $180^\circ \le \theta \le 360^\circ$). Thus, Figure 7-3 only shows the distribution of the radius of the created nanopores and the transmembrane potential for one side of the cell membrane ($180^\circ \le \theta \le 360^\circ$).

In the next section, the created nanopores at the two points of the cell membrane are selected ($\theta = 270°$ and $\theta = 288°$) to study the nanoparticle transport to the opening of the created nanopores. The radius and the transmembrane potential of these nanopores are determined by the numerical solution of the equations of section 7.3.1 (see Figure 7-3). The angular position $\theta = 270°$ represents the nearest point of the cell membrane to the negative electrode. The largest nanopores with the highest value of TMP are generated at this point (see Figure 7.3). At $\theta = 288°$, the radius of the created nanopores is around $15\ nm$ which is still large enough to insert the biological nanoparticles to the cell.

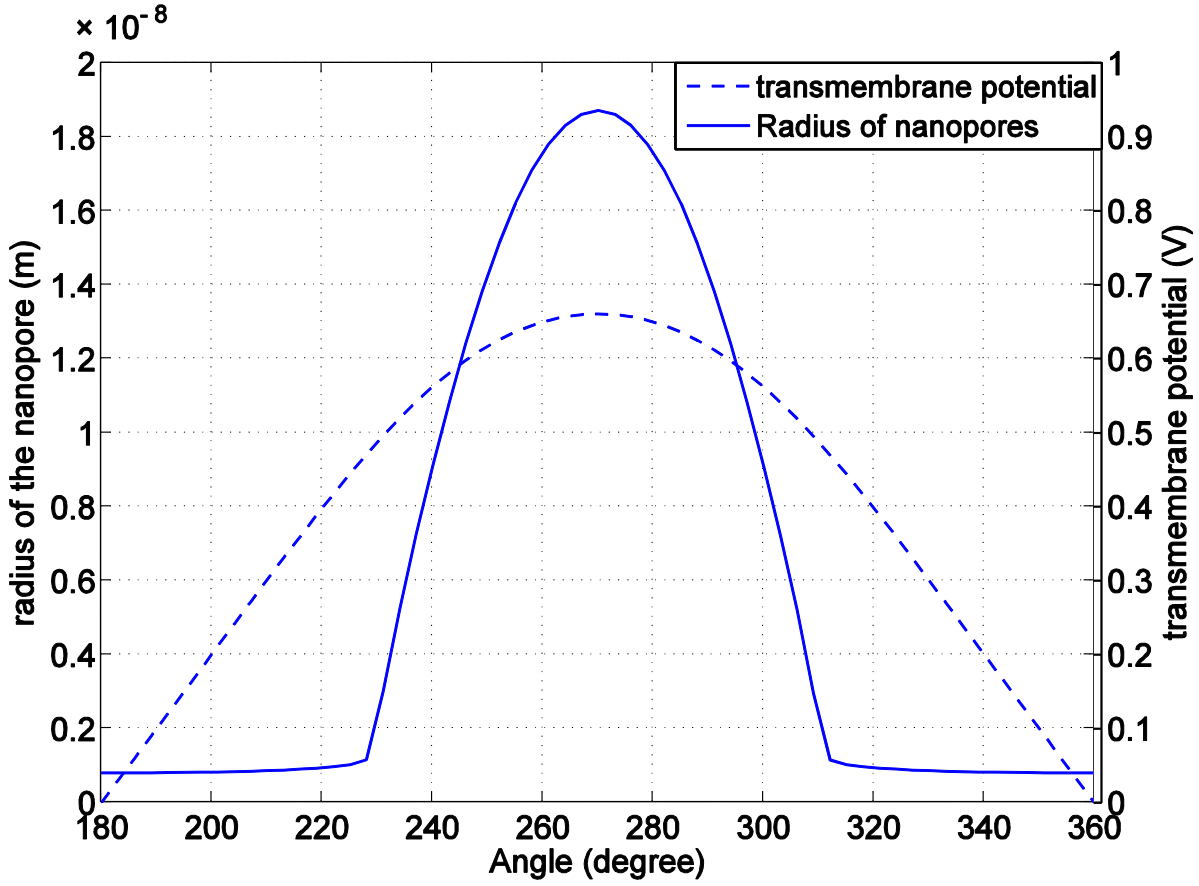

Figure 7-3 Distributions of the trans-membrane potential and the radius of the created nanopores on one side of the cell membrane ($180 \le \theta \le 360$). Here, $h_c = 30\ \mu m$, $a = 7.5\ \mu m$, $\phi_0 = 1.7V$, $t_0 = 10\ \mu s$, and $d = 20\ \mu m$. These distributions are symmetric around the equator of the cell (Figure 7-1).

7.5.2 Electrokinetic transport of the nanoparticles to the opening of the created nanopores:

As explained before, in this section we examine how the nanoscale particles move to the opening of the created nanopores of Figure 7-3. Figure 7-4 depicts the electric potential field and the velocity field in a nanopore located at $\theta = 270°$. The radius of this nanopore and the TMP are $R = 20\ nm$ and $V_m = -0.66\,V$, respectively. For this nanopore, the calculated electric potential at the boundaries AA' and FF' are $\phi_1 = -0.747\,V$ and $\phi_2 = -0.08\,V$, respectively (see Eqns. (7.15)). In a closer view, Figure

7-5 depicts the velocity vectors (a) and the electric field near the generated nanopores at $\theta = 270°$ (b). The surface of the cell membrane is negatively charged ($\sigma_s = -0.0001(C\,m^{-2})$) and the electric field is from outside to inside of the cell membrane. Thus, as it is clear from Figure 5(a), the electroosmotic effect and consequently flow field should be from inside to the outside of the cell membrane. In this study, it is assumed that the nanoparticle is negatively charged ($\sigma_p = -0.3 \sim -0.6\,(C\,m^{-2})$). The assumed diameters of the nanoparticles are $d_p = 10 \sim 15\,(nm)$. The exerted electrophoretic force on the negatively charged nanoparticles is in the direction of the electric field, that is from the outside to the inside of the nanopore at cell membrane. Thus, unlike the hydrodynamic effect (electroosmotic effect), the electrophoretic force tends to bring the nanoparticle into the opening of the nanopore.

Figure 7.5.b shows the direction of the electric field near the generated nanopore at $\theta = 270°$. In this figure, the color bar represents the norm of the electric field ($(|\vec{E}|)$) in logarithm scale ($\log(\sqrt{E_x^{\,2} + E_y^{\,2} + E_z^{\,2}})$). Suppose that q is the total electric charge of the nanoparticle ($q = \int \sigma_p dA$). Then, the magnitude of the exerted electrophoretic force on the nanoparticle can be estimated as $|\vec{F}_{ep}| = q|\vec{E}|$. The direction of this exerted force on the negatively charge nanoparticle is in the direction of the electric field. Therefore, the magnitude of the electrophoretic force is proportional to the norm of electric field ($|\vec{F}_{ep}| \propto |\vec{E}|$).

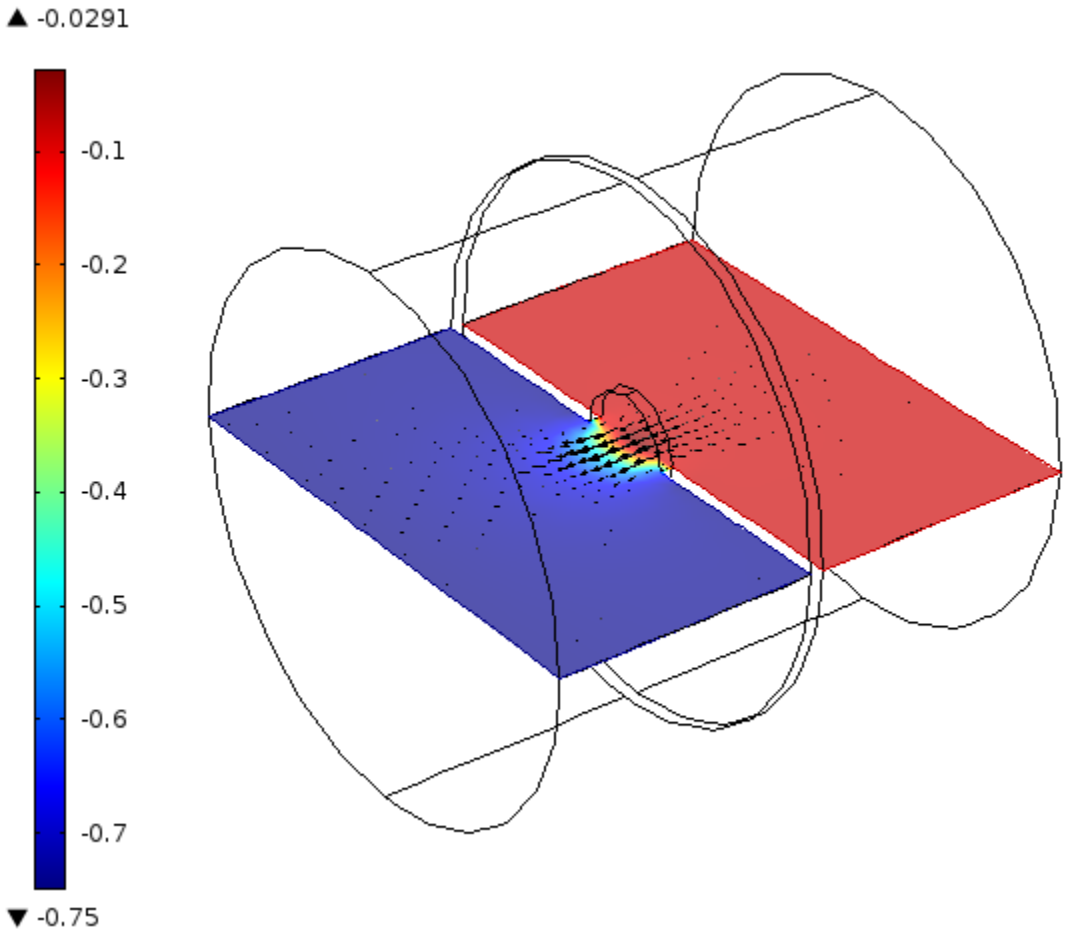

Figure 7-4 This figure shows the electric potential and generated flow field through the created nanopore at $\theta = 270°$. The radius of the created nanopore and the transmembrane potential is $R \approx 20\,nm$ and $TMP = -0.66\,V$, respectively. The color bar is for electric potential.

(a)

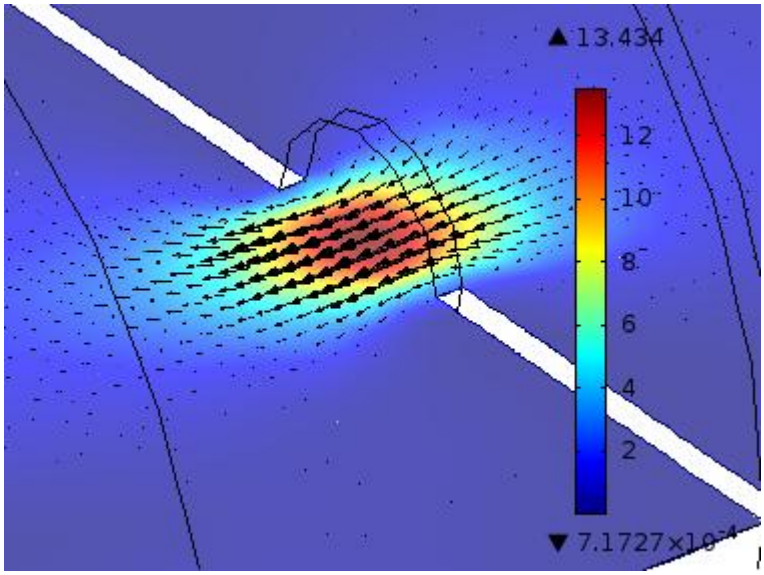

(b)

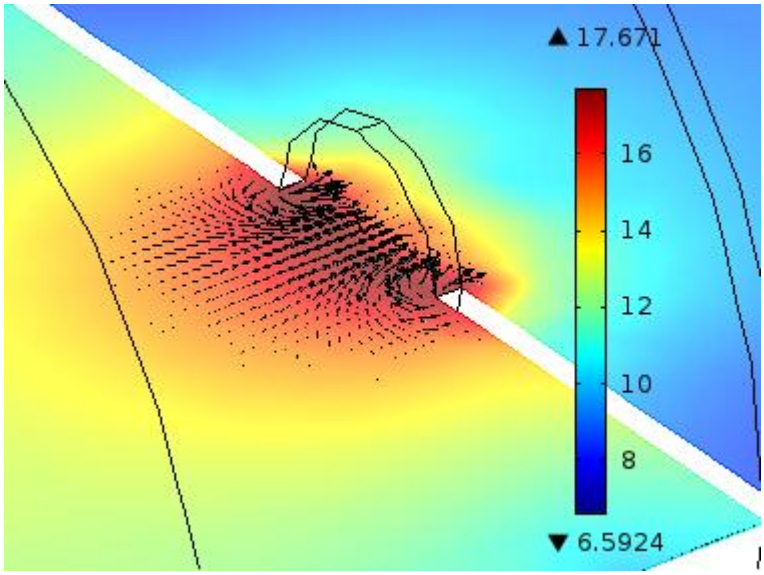

Figure 7-5 (a) The velocity field (m/s) and (b) the external electric field (V/m) in vicinity of the generated nanopores at $\theta = 270°$. The color bar in Figure 7.5 (a) indicates the magnitude of the velocity field. In Figure 5 (b), the color bar represents the norm of electric field in logarithmic scale ($\log(\sqrt{E_x^2 + E_y^2 + E_z^2})$).

Now, the question is how close the nanoparticle should be from the nanopore in order to be trapped and transported to the opening of the nanopore. Based on the force balance, as long as the electrophoretic force is stronger than the hydrodynamics resistance, the nanopore should move towards the opening of the nanopore. As an example, consider Figure 7-6. This figure illustrates the trajectory of the nanoparticle near the opening of the nanopore of Figure 7.4. The diameter and the surface electric charge of the nanoparticle are $\sigma_p = -0.45\, C/m^2$ and $d = 10\, nm$. When the nanoparticle releases from a point $(-55\, nm, -50\, nm, 0\, nm)$, the nanoparticle passes the opening of the nanopore and does not come to the nanopore. However, when the nanoparticle is released close enough to the nanopore from a point $(-50\, nm, -50\, nm, 0\, nm)$, it turns towards the opening of the nanopore. To explain this, let's compare the exerted electrophoretic and hydrodynamic forces on the nanoparticle. In Figure 7.6(a), when the particle releases from a point $(-55\, nm, -50\, nm, 0\, nm)$, the value of exerted electrophoretic and hydrodynamic resistance on the nanoparticle are $|F_{hd}| = 0.06\, nN$ and $|F_{ep}| = 0.04\, nN$, respectively. The nanoparticle move towards the nanopore until the electrophoretic force is dominated by the hydrodynamic resistance. For example, at the point $(-45.7\, nm, -3.7\, nm, 11\, nm)$ where the magnitude of the hydrodynamic resistance and electrophoretic forces are $|F_{hd}| = 0.2261\, nN$ and $|F_{ep}| = 0.2204\, nN$. At this point, the stronger hydrodynamic resistance changes the direction of the nanoparticle and repels it from the nanopore.

When the nanoparticle is closed enough to the nanopore, the electric field and consequently electrophoretic force is strong enough to dominate the hydrodynamic resistance and move the nanoparticle toward the nanopore. For example, consider Figure 7-6 (b) where the nanoparticle releases from $(-50\, nm, -50\, nm, 0\, nm)$. At this point, the magnitude of the electrophoretic force and the hydrodynamic resistance are $|F_{ep}| = 0.0567\, nN$ and $|F_{hd}| = 0.0317\, nN$, respectively. The stronger electrophoretic force moves the nanoparticle towards the nanopore. When the nanoparticle approaches the nanopore, both the electrophoretic and hydrodynamic forces increase. However, the electrophoretic force is still strong enough to suppress the hydrodynamic resistance. At the point $(-37.3\, nm, -0.41\, nm, 8.6\, nm)$, the electrophoretic force ($|F_{ep}| = 1.1\, nN$) overpowers the hydrodynamic resistance ($|F_{ep}| = 0.7\, nN$) and turns the nanoparticle toward the opening of nanopore.

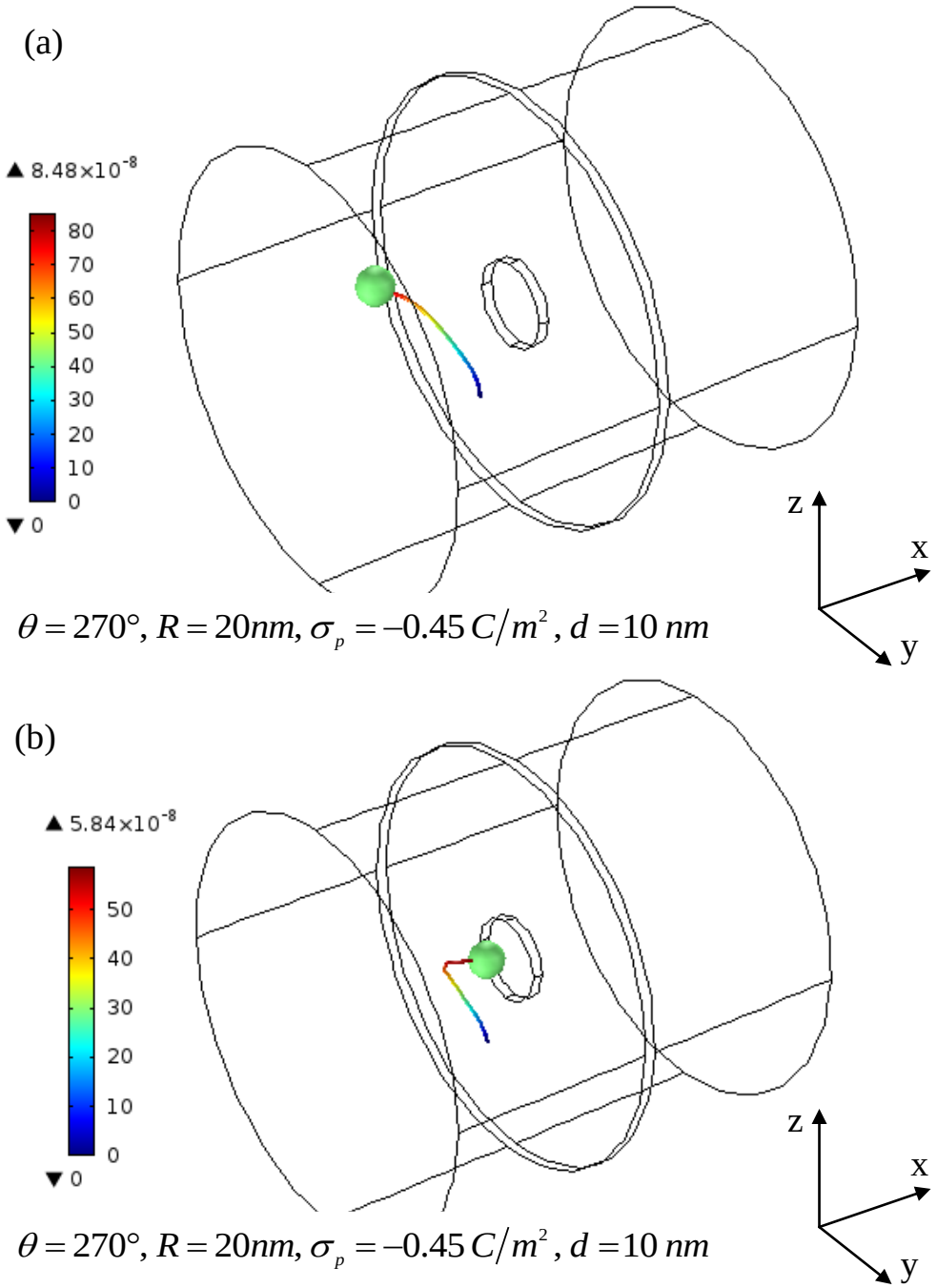

Figure 7-6 This figure shows how the nanoparticles will be close to the opening of the nanopore in order to get into it. The origin of the coordinate system is located on the center of the nanopore (point *O*, see figure 2). The initial position of the nanoparticle (x_0, y_0, z_0) **is (a)** $(-55\ nm, -50\ nm, 0)$ **and (b)** $(-50\ nm, -50\ nm, 0)$**, respectively. The color bar is for time.**

Here, it should be pointed out that the magnitude of the exerted Brownian force (Eq. 7.30) on the nanoparticle is in the order of $10^{-11} N$ which is two orders of magnitude smaller that the electrophoretic and hydrodynamic forces that are in the order of $nN\ (10^{-9} N)$. Thus, the Brownian force has less effect on the nanoparticle transport compare with the hydrodynamic and electrophoretic forces.

Figure 7-4 explains that unlike the electroosmotic (hydrodynamic) effect, the electrophoresis tends to move the negatively charged nanoparticle towards the opening of the nanopores. Therefore, by intensifying the electrophoretic force on the nanoparticle, the nanoparticle transport to the opening of the nanopore will be improved. This force is affected by the external electric field, the surface electric charge, and the size of the nanoparticle. During the electroporation, the electric field around the cell membrane is controlled by the external applied electric field (ϕ_0) via the electrodes. If this applied electric field is low, the nanopores may be not created on the cell membrane. As the nanopores are created, further increase of this applied electric field may ruin the membrane structure and kill the cell. Thus, this applied electric field should be kept around the specific value that the nanopores are created and the cell is still live. Further explanations are presented in Chapter 3. However, the size and the surface electric charge of the nanoparticle may be modified in order to strengthen the electrophoretic effect and consequently nanoparticle transport to the opening of the nanopores. The effects of these parameters are studied in Figures 7.7 and 7.8.

Figure 7-7 demonstrates that how increasing the surface electric charge of the nanoparticle improves the its transport to the opening of the nanopore. The nanoparticle is initially released from $(-50nm, 0, -25nm)$. The assumed radiuses of the nanoparticle and the created nanopores are $5nm$ and $20nm$, respectively. By increasing the surface electric charge of the nanoparticle from $\sigma_p = -0.3\,C/m^2$ to $\sigma_p = -0.6\,C/m^2$, the nanoparticle turn towards the nanopore and get into its opening. Here, increasing the surface electric charge make the electrophoretic force stronger. However, because the nanoparticle size is kept constant, the hydrodynamic resistance against its motion is not changed dramatically and consequently the nanoparticle transport to the opening of the nanopore improves.

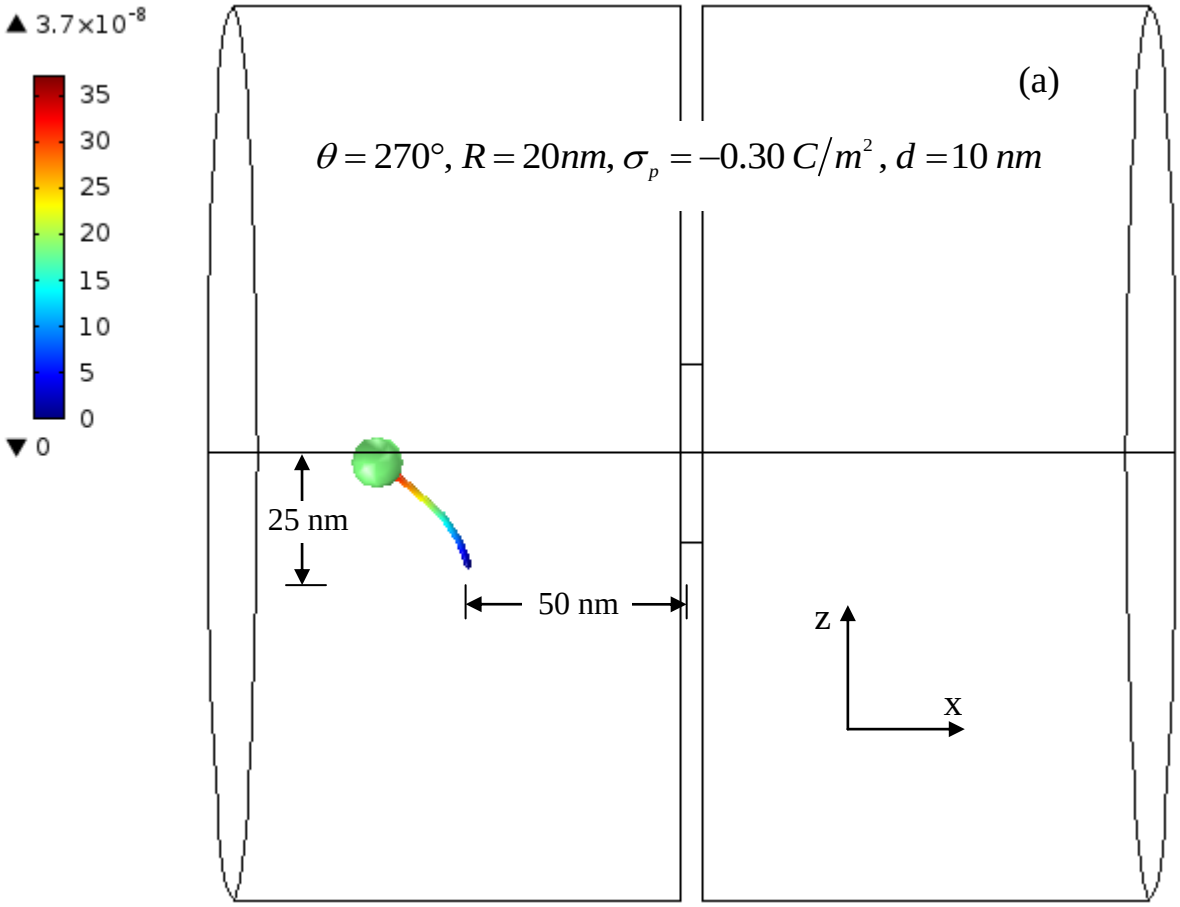
▲ 3.7×10^-8
35
30
25
20
15
10
5
0
▼ 0
(a)
θ = 270°, R = 20nm, σ_p = –0.30 C/m², d = 10 nm
25 nm
50 nm
z
x

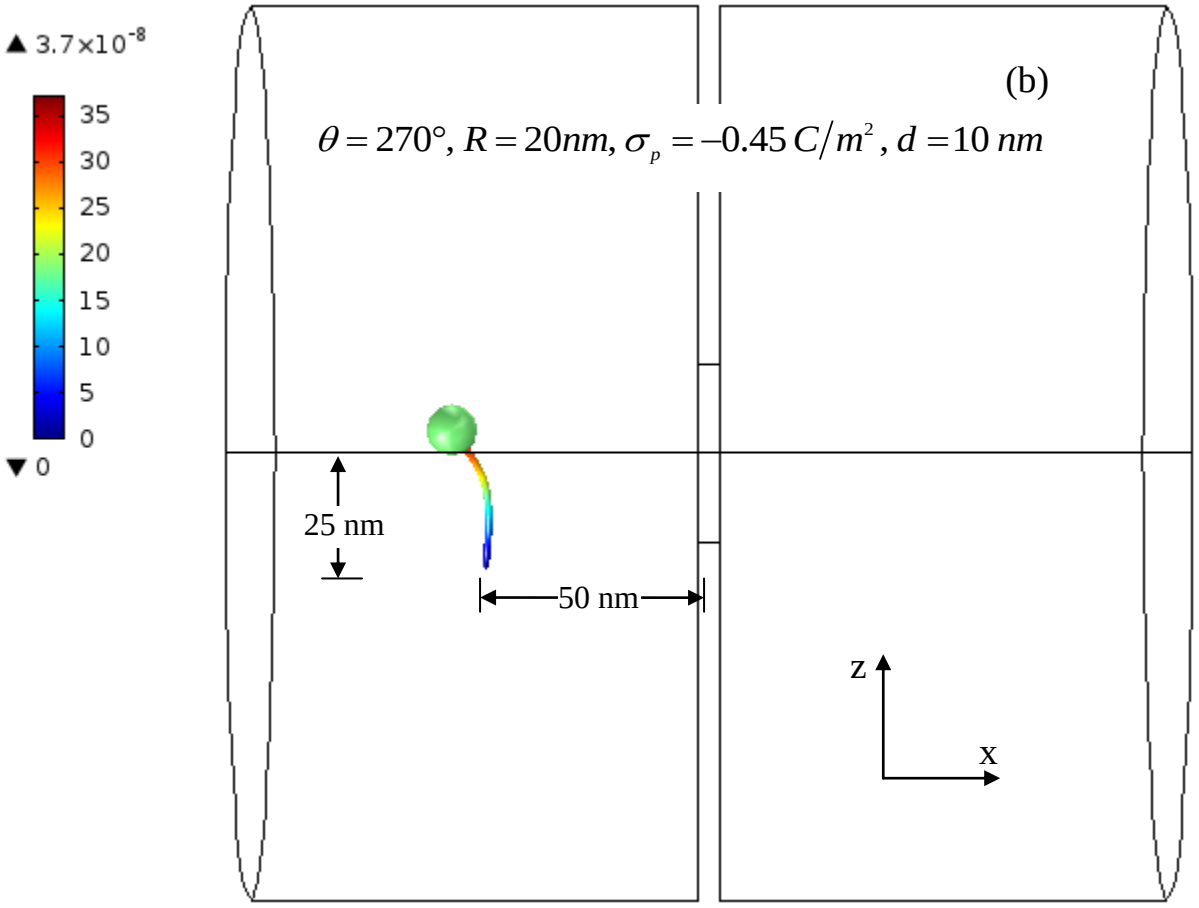
▲ 3.7×10^-8
35
30
25
20
15
10
5
0
▼ 0
(b)
θ = 270°, R = 20nm, σ_p = –0.45 C/m², d = 10 nm
25 nm
50 nm
z
x

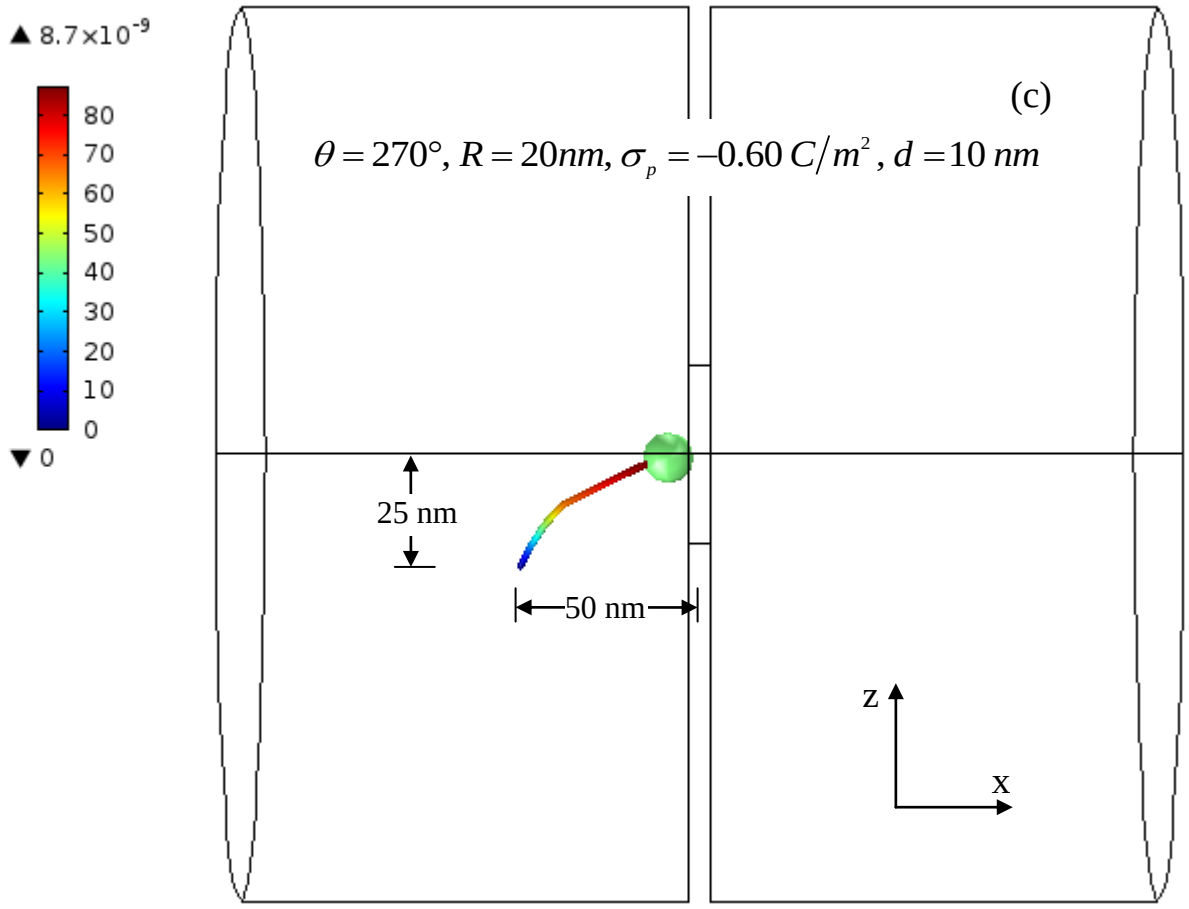

Figure 7-7 This figure shows the effect of surface electric charge of the nanoparticle on the nanoparticle transport to the opening of the nanopore. (a) $\sigma_p = -0.30\, C/m^2$ **, (b)** $\sigma_p = -0.45\, C/m^2$ **, and (c)** $\sigma_p = -0.60\, C/m^2$ **. In this figure** $\theta = 270°, R = 20nm, d = 10\ nm$ **. The nanoparticle is initially located at** $(-50\ nm, -25\ nm, 0\ nm)$ **. The origin of the coordinate system is located on the center of the nanopore (point *O*, see figure 2).**

For one specific case of study ($\theta = 270°, R = 20nm, \sigma_p = -0.45\, C/m^2$), Figure 7-8 shows that by increasing the nanoparticle size, its transport to the opening of the nanoparticle becomes more difficult. Further increase of the nanoparticle size may also change the direction of the nanoparticle motion. In fact, by increasing the size of the nanoparticle, the hydrodynamic resistance increases. It should be mentioned that because the surface electric charge kept constant, increasing the size of the nanoparticle causes intensifying the electric charge of the nanoparticle and consequently the electrophoretic forces. However, it seems that by increasing the size of the nanoparticle, the hydrodynamic resistance strengthens more dramatically rather than the electrophoretic force and consequently the nanoparticle transport to the opening of the nanopores becomes more difficult.

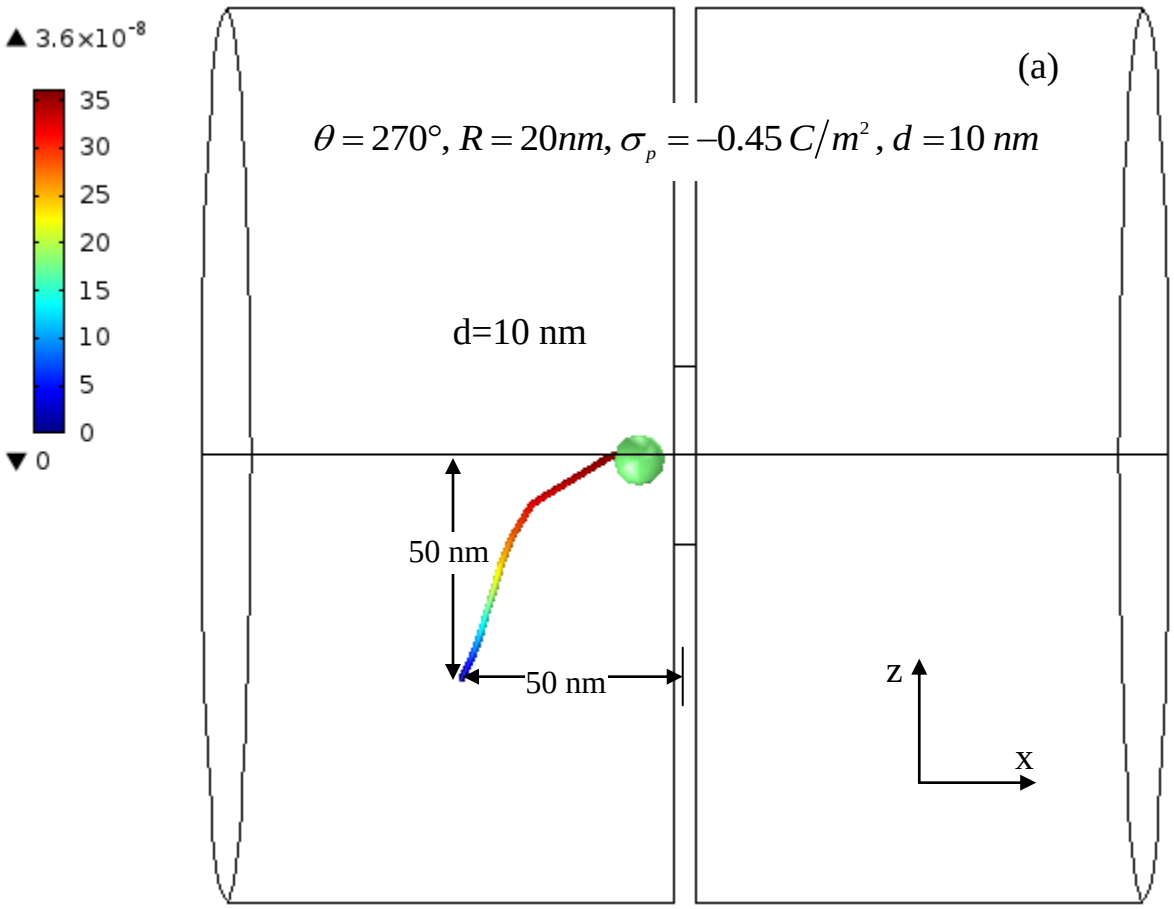

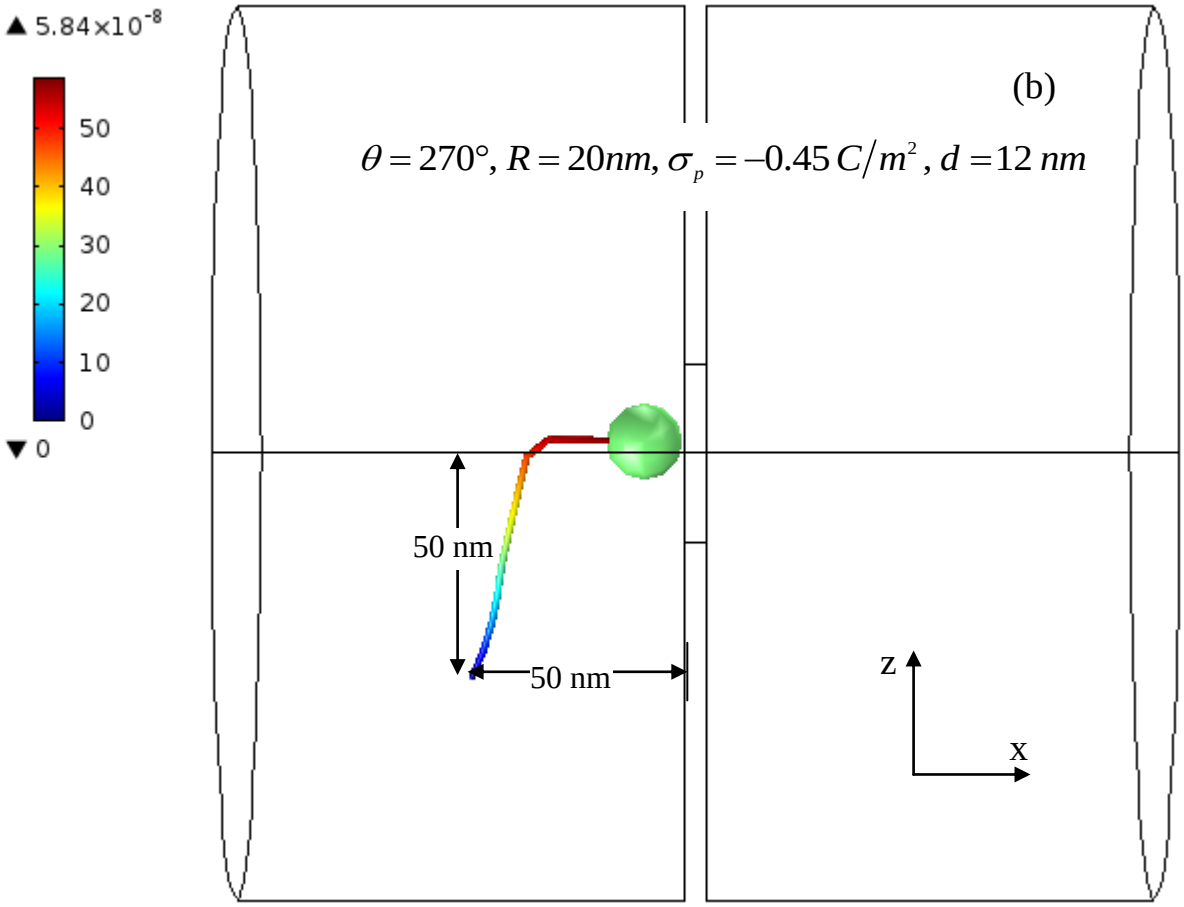
▲ 5.84×10^-8
50
40
30
20
10
0
▼ 0
(b)
θ = 270°, R = 20nm, σ_p = –0.45 C/m², d = 12 nm
50 nm
50 nm
z
x

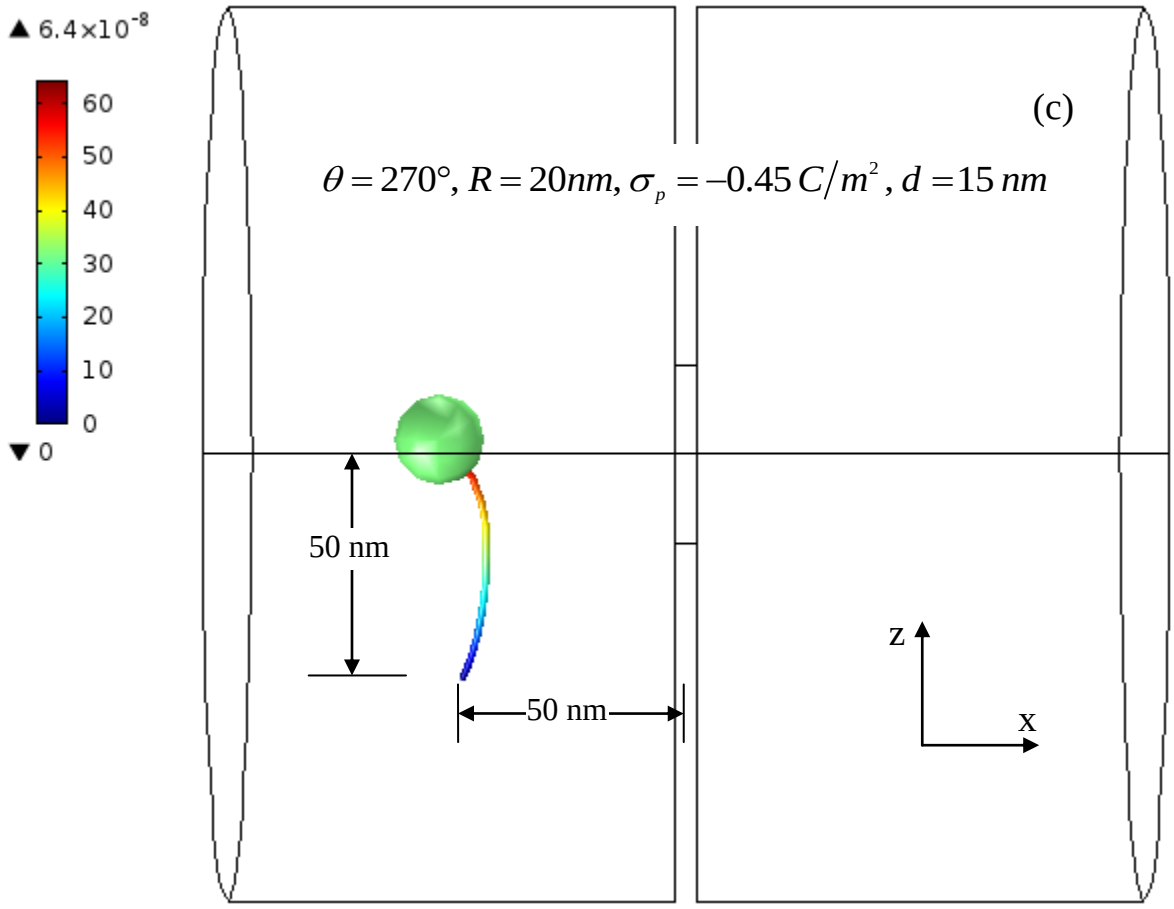

Figure 7-8 This figure shows the effect of the nanoparticle size on its transport to the opening of the nanopore. (a) $d = 10\ nm$**, (b)** $d = 12\ nm$**, and (c)** $d = 15\ nm$**. In this figure** $\sigma_p = -0.45\ C/m^2$**,** $\theta = 270°$, and $R = 20nm$**. The nanoparticle is initially located at** $(-50\ nm, -50\ nm, 0\ nm)$**. The origin of the coordinate system is located on the center of the nanopore (point *O*, see figure 7.2).**

The results of this study also demonstrates that for the closer nanopores to the poles of the cell ($\theta = 270°$), the nanoparticles transports to the opening become easier and faster. It can be explained by considering these facts that by getting closer to the poles, the TMP becomes stronger and the created nanopores become bigger. For example, we compare the nanoparticle transport to the opening of the nanopores created at $\theta = 270°$ and $\theta = 288°$. The radius of the created nanopores and the TMP at points $\theta = 270°$ and $\theta = 288°$ are: $TMP_{\theta=270} = 0.66\,V$, $TMP_{\theta=288} = 0.6V$, $R_{\theta=270} \approx 20\ nm$,

and $R_{\theta=288} \approx 15\,nm$. The nanoparticle release from $(-40\,nm, -40\,nm, 0\,nm)$. It takes about $18.7\,ns$ and $46.2\,ns$ to transport the nanoparticle to the opening of the nanopores created at $\theta = 270°$ and $\theta = 288°$, respectively.

7.6 Concluding remarks

In this chapter, I have studied the nanoparticle transport to the opening of the created nanopores on the cell membrane during the electroporation. First, the permeabilization of the cell studied. While the radius and the TMP of the created nanopores were established, the transport of the nanoparticles to these created nanopores was investigated. It was shown that unlike the electroosmotic effect, the electrophoretic force tends to move the nanoparticle to the opening of the nanopores. The effect of Brownian force is negligible compare with electroosmosis and electrophoresis. More highly charge and smaller nanoparticles transport easier to the opening of the nanopores. As the nanopores get closer to the poles of the cell ($\theta = 270°$), the transport of the nanoparticles to their openings becomes easier.

Chapter 8
Conclusions and Future Works

8.1 Conclusions and Contributions of this Thesis

This thesis dealt with the underlying concepts of the microfluidic cell electroporation. The contributions of this work include investigating the electrokinetic effects in nanoscale dimensions, electrokinetic motion of nanoparticles in nanochannels, the membrane permeabilization of the cell in the microchannel, and mechanism of cell transfection during the electroporation. Key contributions may be summarized as follows:

1. Investigating the membrane permeabilization of the cells located in the microchannels is one of the contributions of the current study. This part is presented in Chapter 3. The findings of this part shows that:

    - By keeping the electric pulse constant, increasing the microchannel height reduces the number and the radius of the biggest nanopores, as well as the electroporated area of the cell membrane.

    - If the width of the electrodes is bigger than the cell diameter, the transmembrane potential will be centralized and have a sinusoidal distribution around the cell if nanopores are not generated.

    - As the width of the electrode decreases and becomes smaller than the cell diameter, the local transmembrane potential decreases; in the non-electroporative area, the transmembrane potential distribution deviates from the sinusoidal behavior; the induced transmembrane potential also concentrates around the poles of the cell membrane (the nearest points of the cell membrane to the electrodes).

    - During cell membrane permeabilization, the biggest nanopores are initially created at the poles and then the nanopore population expands toward the equator.

    - The number of the created nanopores reaches its maximal value within a few microseconds; further presence of the electric pulse may not influence the number and location of the created nanopores anymore but will develop the generated nanopores.

- Strengthening the electric pulse intensifies the size and number of the created nanopores as well as the electroporated area on the cell membrane.

2. A comprehensive study of the electrokinetic transport through the nanochannels is one of the main contributions of the current study. The details of this part have been explained in Chapter 4. The results of chapters reveal that:

   - Unlike the microchannels, the electric potential field, ionic concentration field, and velocity field are strongly size-dependent in the nanochannels.
   - The electric potential gradient along the nanochannel also depends on the surface electric charge of the nanochannel.
   - More counter ions than the co-ions are transported through the nanochannel.
   - The ionic concentration enrichment at the entrance and the exit of the nanochannel is completely evident from the simulation results.
   - The study also shows that the flow velocity in the nanochannel is higher when the surface electric charge is stronger or the radius of the nanochannel is larger.

3. In Chapter 5, ionic mass transfer and fluid flow through the generated hydrophilic nanopores of the cell membrane during the electroporation are examined. The results show that:

   - The electric potential, velocity field, and ionic concentration vary with the size of the nanopores and are different through the nanopores located at the front and backside of the cell membrane.
   - On a given side of the cell membrane, angular position of nanopores has fewer influences on liquid flow and ionic transfer.
   - By increasing the radius of the nanopores, the averaged velocity and the ionic concentration through the nanopores are increased.
   - It is also shown that, in the presence of electric pulse, the electrokinetic effects (electroosmosis and electrophoresis) have significant influences on ionic mass transfer through the nanopores, while the effect of diffusion on ionic mass flux is negligible in comparison with electrokinetics.

- Increasing the radius of the nanopores intensifies the effect of convection (electroosmosis) in comparison with electrophoresis on ionic mass transfer.

4. Electrokinetic motion of the nanoparticles through the nanochannels is another contribution of the present study. Chapter 6 gives details of this part of the study:

    - Because of the large applied electric field over the nanochannel, the impact of the Brownian force is negligible in comparison with the electrophoretic and the hydrodynamic forces.
    - Increasing the bulk ionic concentration or the surface charge of the nanochannel will increase the electroosmotic flow, and hence affect the particle's motion.
    - Unlike microchannels with thin EDL, the change in nanochannel size will change the EDL field and the ionic concentration field in the nanochannel, affecting the particle's motion.
    - If the nanochannel size is fixed, a larger particle will move faster than a smaller particle under the same conditions.

5. Nanoparticle transport to the opening of the created nanopores on the cell membrane during the electroporation is the last contribution of the current study. The results of this part have been presented in chapter 7:

    - It was found that the negatively charged nanoparticles preferably move into the nanopores from the side of the cell membrane that faces the negative electrode.
    - Opposite to the electroosmotic flow effect, the electrophoretic force tends to draw the negatively charged nanoparticles into the opening of the nanopores.
    - The effect of the Brownian force is negligible in comparison with the electroosmosis and the electrophoresis.
    - Smaller nanoparticles with stronger surface charge transport more easily to the opening of the nanopores.
    - Positively charged nanoparticles preferably enter the nanopores from the side of the cell membrane that faces the positive electrode. On this side, both the electrophoretic and electroosmotic forces are in the same directions and contribute to bring the positively charged particles into the nanopores.

8.2 Future Works

Many aspects of this study can be extended for the future studies. Some of them are discussed below:

- Experimental studies should be performed and a simple lab-on-a-chip design should be purposed for microfluidic cell electroporation. In these future studies, the results of the current dissertation can be utilized as a guideline to find the optimum parameters and values of different geometrical and electrical parameters. As an example, the optimal microchannel height and electrode size may be set by considering the results of this study. This study also explains how the electric pulse intensity and duration should be manipulation in order to create reversible nanopores on the cell membrane and to not kill the cell during the electroporation. The optimum electrical and geometrical characteristics of nanoparticles can be found from the results of this study. These results explain that how the size and surface electric charge of the nanoparticle influence the nanoparticle transport toward the opening of the nanopores. The results also show that how the angular position of the generated nanopores affects the transportation of negatively and positively charged nanoparticles into the cell. It shows that how the biological nanoparticle should be pre-concentrated in order to enhance transfection rate.

- Previous experimental studies showed that the cells start to growth in the presence of external electric field (Wang, et al., 2006-b). There is not any theory that explains the exact mechanism behind the swelling of the cell in the applied electric field. Having the accurate theory to predict the kinetics of the electroporation can also allow us to design the control system which is not case dependent.

- Theory of membrane permeabilization should be modified to consider cell deformations during the electroporation. The current model has some underlying assumptions that must be considered carefully. As an example, first, cells are considered to be spherical. However, many previous studies show that the cells are elliptical and have a deformed shape under the applied electric field or pressure. Furthermore, the effect of cell expansion and rotation during the electroporation were not considered. More sophisticated models are needed to investigate the effects of electro-deformations such as swelling and rotation.

- Experimental studies showed that feedback control improves the electroporation efficiency of single cells (Cukjati, et al., 2007; Khine, et al., 2007). The feedback control can be utilized to

monitor the radii of the pores and the time duration for which the pores remain open, and hence ensure the safe and accurate transfection during the reversible electroporation. Although a few experimental studies have been reported on the feedback control of the single cell electroporation, more analytical studies for dynamic response of cell membrane to the external electric field must be performed to develop better feedback control of cell electroporation. Because of nonlinear behavior of the cell electroporation, many conventional controllers cannot be used. Other user-friendly control techniques (for example fuzzy logic) may be utilized to control the electroporation process.

Appendix A

Papers from the results of this thesis

Journal Papers:

1. Saeid Movahed, Dongqing Li, '**A Theoretical Study of Single Cell Electroporation in a Microchannel'**, Journal of Membrane Biology, Published online: 6 November, 2012.

2. Saeid Movahed, Dongqing Li, '**Electrokinetic motion of nanoparticles through the nanochannels',** Journal of Nanoparticle Research, Springer, 2012, Vol. 14, No. 8: 1032.

3. Saeid Movahed, Dongqing Li, '**Electrokinetic Transport through the Nanopores in Cell Membrane during Electroporation'** Journal of Colloid and Interface Sciences, Elsevier, 2012, Vol. 369, Issue 1, pp.: 442-452.

4. Saeid Movahed, Dongqing Li **'Electrokinetic Transport Through Nanochannels'**, Electrophoresis Journal, Wiley, 2011, Vol. 32, No. 11, pp.: 1259-1267.

5. Saeid Movahed, Dongqing Li **'Microfluidics Cell Electroporation '**, Microfluidics and Nanofluidics Journal, Springer, 2011, Vol. 10, No. 4, pp. : 703-734.

Submitted Journal Papers:

6. Saeid Movahed, Dongqing Li, **'Electrokinetic Transport of Nanoparticles to the Opening of Nanopores in Cell Membrane during Electroporation'.**

Appendix B
Approximate Solution of the Electrokinetic Effects in Slit Nanochannels

In this section, the aim is to find an analytical and approximate method to compare the effects of electroosmosis and electrophoresis on ion mass transfer through the nanochannels. To simplify the analysis, we will consider a one-dimensional slit nanochannel of height *h*, as shown in Figure B-1. At the cross section of the slit nanochannel, the electroosmotic and electrophoretic ionic fluxes will be estimated and compared. Generally, Nernst-Planck equation can be used to find the ionic flux:

$$\vec{N} = c_i\vec{u} - D_i\vec{\nabla}c_i - z_i\mu_{m,i}Fc_i\vec{\nabla}\phi \tag{B.1}$$

In this equation, the first, second and third terms represent the influences of convection (electroosmosis), the diffusion, and the electrophoresis on ion flux of type *i*, respectively. Thus, the ration of the electroosmosis flux ($\vec{N}_{EO}$) to the electrophoresis flux ($\vec{N}_{EP}$) of ion types *i* can be written as:

$$\frac{\vec{N}_{EO}}{\vec{N}_{EP}} = \frac{c_i\vec{u}}{z_i\mu_{m,i}Fc_i\vec{\nabla}\phi} \tag{B.2}$$

In the above equation, $\vec{u}$ and $\vec{\nabla}\phi$ are unknown. Finding exact analytical expressions for these parameters seems to be impossible; therefore, we will look for an approximate solution for them.

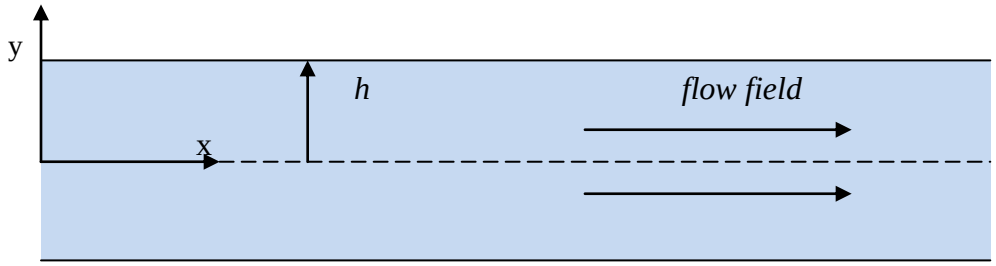

Figure B-1 Schematic diagram of slit nanochannel

It is assumed that there is an unidirectional and fully developed flow field through the slit nanochannel; following equation with proper boundary conditions should be solved to find the velocity:

$$\eta \frac{\partial^2 u}{\partial x^2} = -FE_x z_i c_i \tag{B.3}$$

$$\left.\frac{\partial u}{\partial x}\right|_{y=0} = 0 \tag{B.4}$$

$$u\big|_{y=\pm h} = 0 \tag{B.5}$$

By integrating Eq. (B.3) over the nanochannel cross section we have:

$$\int_0^y \eta \frac{\partial^2 u}{\partial x^2} dr = \int_0^y -FE_x z_i c_i dr \;\Rightarrow \left.\frac{\partial u}{\partial x}\right|_y - \left.\frac{\partial u}{\partial x}\right|_0 = \int_0^y -FE_x z_i c_i dr$$

$$\Rightarrow \left.\frac{\partial u}{\partial x}\right|_y = \int_0^y -FE_x z_i c_i dr \tag{B.6}$$

Eq. (B.6) can be integrated in order to find the velocity in the nanochannel:

$$\Rightarrow \int_0^y \frac{\partial u}{\partial x} ds = \int_0^y \int_0^y -FE_x z_i c_i dr ds$$

$$\Rightarrow u\big|_y - u\big|_0 = \int_0^y \int_0^y -FE_x z_i c_i dr ds \tag{B.7}$$

If we integrate Eq. (B.7) from 0 to *h*, the velocity at the center of the nanochannel (U_{EO}) can be found as:

$$\Rightarrow u\big|_h - u\big|_0 = \int_0^h \int_0^h -FE_x z_i c_i dr ds$$

$$\Rightarrow U_{EO} = \int_0^h \int_0^h FE_x z_i c_i dr ds \tag{B.8}$$

Eq. (B.8) can be calculated approximately by the average value of integral $\overline{FE_x z_i c_i}$ multiple by h^2:

$$\Rightarrow U_{EO} = h^2 \overline{FE_x z_i c_i} \tag{B.9}$$

Permissions

License Agreement for Chapter 2:

This is a License Agreement between Saeid Movahed ("You") and Springer ("Springer") provided by Copyright Clearance Center ("CCC"). The license consists of your order details, the terms and conditions provided by Springer, and the payment terms and conditions.

License Number	3001440592254
License date	Oct 03, 2012
Licensed content publisher	Springer
Licensed content publication	Microfluids and Nanofluids
Licensed content title	Microfluidics cell electroporation
Licensed content author	Saeid Movahed
Licensed content date	Jan 1, 2010
Volume number	10
Issue number	4
Type of Use	Thesis/Dissertation
Portion	Full text
Number of copies	1
Author of this Springer article	Yes and you are the sole author of the new work
Title of your thesis / dissertation	Electrokinetic Transport Process in Nanopores Generated on Cell Membrane during Electroporation
Expected completion date	Dec 2012
Estimated size (pages)	200
Total	0.00 USD

License Agreement for Chapter 3:

This is a License Agreement between Saeid Movahed ("You") and Springer ("Springer") provided by Copyright Clearance Center ("CCC"). The license consists of your order details, the terms and conditions provided by Springer, and the payment terms and conditions.

License Number	3033881359908
License date	Nov 21, 2012
Licensed content publisher	Springer
Licensed content publication	Journal of Membrane Biology
Licensed content title	A Theoretical Study of Single-Cell Electroporation in a Microchannel
Licensed content author	Saeid Movahed
Licensed content date	Jan 1, 2010
Type of Use	Thesis/Dissertation
Portion	Full text
Number of copies	1
Author of this Springer article	Yes and you are the sole author of the new work
Title of your thesis / dissertation	Electrokinetic Transport Process in Nanopores Generated on Cell Membrane during Electroporation
Expected completion date	Dec 2012
Estimated size (pages)	200
Total	0.00 USD

License Agreement for Chapter 4:

This is a License Agreement between Saeid Movahed ("You") and John Wiley and Sons ("John Wiley and Sons") provided by Copyright Clearance Center ("CCC"). The license consists of your order details, the terms and conditions provided by John Wiley and Sons, and the payment terms and conditions.

License Number	2936541284804
License date	Jun 26, 2012
Licensed content publisher	John Wiley and Sons
Licensed content publication	Electrophoresis
Licensed content title	Electrokinetic transport through nanochannels
Licensed content author	Saeid Movahed, Dongqing Li
Licensed content date	May 3, 2011
Start page	1259
End page	1267
Type of Use	Thesis/Dissertation
Requestor type	Author of this Wiley article
Format	Print and electronic
Portion	Full article
Will you be translating?	No
Order reference number	
Total	0.00 USD

License Agreement for Chapter 5:

This is a License Agreement between Saeid Movahed ("You") and Springer ("Springer") provided by Copyright Clearance Center ("CCC"). The license consists of your order details, the terms and conditions provided by Springer, and the payment terms and conditions.

License Number	3001440988704
License date	Oct 03, 2012
Licensed content publisher	Elsevier
Licensed content publication	Journal of Colloid and Interface Science
Licensed content title	Electrokinetic transport through the nanopores in cell membrane during electroporation
Licensed content author	Saeid Movahed, Dongqing Li
Licensed content date	1 March 2012
Licensed content volume number	369
Licensed content issue number	1
Number of pages	11
Type of Use	reuse in a thesis/dissertation
Portion	full article
Format	both print and electronic
Are you the author of this Elsevier article?	Yes
Will you be translating?	No
Order reference number	None
Title of your thesis / dissertation	Electrokinetic Transport Process in Nanopores Generated on Cell Membrane during Electroporation
Expected completion date	Dec 2012
Estimated size (pages)	200
Elsevier VAT number	GB 494 6272 12
Permissions price	0.00 USD
VAT/Local Sales Tax	0.0 USD / 0.0 GBP
Total	0.00 USD

License Agreement for Chapter 6:

This is a License Agreement between Saeid Movahed ("You") and Elsevier ("Elsevier") provided by Copyright Clearance Center ("CCC"). The license consists of your order details, the terms and conditions provided by Elsevier, and the payment terms and conditions.

License Number	3001441230540
License date	Oct 03, 2012
Licensed content publisher	Springer
Licensed content publication	Journal of Nanoparticle Research
Licensed content title	Electrokinetic motion of a rectangular nanoparticle in a nanochannel
Licensed content author	Saeid Movahed
Licensed content date	Jan 1, 2012
Volume number	14
Issue number	8
Type of Use	Thesis/Dissertation
Portion	Full text
Number of copies	1
Author of this Springer article	Yes and you are the sole author of the new work
Title of your thesis / dissertation	Electrokinetic Transport Process in Nanopores Generated on Cell Membrane during Electroporation
Expected completion date	Dec 2012
Estimated size (pages)	200
Total	0.00 USD

Bibliography

Agarwal Aparna [et al.] Control of the Release of Freely Diffusing Molecules in Single-Cell Electroporation [Journal] // Anal. Chem.. - 2009. - Vol. 81. - pp. 8001–8008. - 10.1021/ac9010292.

Ai Ye and Qian Shizhi Electrokinetic particle translocation through a nanopore [Journal] // Phys. Chem. Chem. Phys.. - 2011. - Vol. 13. - pp. 4060-4071. - DOI: 10.1039/c0cp02267e.

Algar W. Russ and Krull Ulrich J. Multiplexed Interfacial Transduction of Nucleic Acid Hybridization Using a Single Color of Immobilized Quantum Dot Donor and Two Acceptors in Fluorescence Resonance Energy Transfer [Journal] // Analytical chemistry. - 2010 : [s.n.]. - Vol. 82. - pp. 400-405.

Algar W. Russ and Krull Ulrich J. Toward A Multiplexed Solid-Phase Nucleic Acid Hybridization Assay Using Quantum Dots as Donors in Fluorescence Resonance Energy Transfer [Journal] // analytical chemistry. - 2009. - Vol. 81. - pp. 4113–4120.

Baldessari Fabio Electrokinetics in nanochannels Part I. Electric double layer overlap and channel-to-well equilibrium [Journal] // Journal of Colloid and Interface Science. - 2008. - Vol. 325. - pp. 526–538.

Baldessari Fabio Electrokinetics in nanochannels Part II. Mobility dependence on ion density and ionic current measurements [Journal] // Journal of Colloid and Interface Science. - 2008. - Vol. 325. - pp. 539–546.

Bao Ning [et al.] Microfluidic electroporation of tumor and blood cells: observation of nucleus expansion and implications on selective analysis and purging of circulating tumor cells [Journal] // Integr. Biol.. - 2010.

Bao Ning, Wang Jun and Lu Chang Microfluidic electroporation for selective release of intracellular molecules at the single-cell level [Journal] // Electrophoresis. - 2008. - Vol. 29. - pp. 2939–2944.

Behrens Sven Holger and Borkovec Michal Electrostatic Interaction of Colloidal Surfaces with Variable Charge [Journal] // J. Phys. Chem. B. - 1999. - Vol. 103. - pp. 2918-2928.

Bilska Anna O, DeBruin Katherine A and Krassowska Wanda Theoretical modeling of the effects of shock duration, frequency, and strength on the degree of electroporation [Journal] // Bioelectrochemistry. - 2000. - Vol. 51. - pp. 133–143.

Bonthuis Douwe Jan [et al.] Conformation and Dynamics of DNA Confined in Slitlike Nanofluidic Channels [Journal] // Physical Review Letters. - 2008. - Vol. 101. - p. 108303.

Brennan Desmond [et al.] Emerging optofluidic technologies for point-of-care genetic analysis systems: a review [Journal] // Anal Bioanal Chem. - 2009. - Vol. 395. - pp. 621-636. - DOI 10.1007/s00216-009-2826-5.

Brouzes Eric [et al.] Droplet microfluidic technology for single-cell high-throughput screening [Journal] // PNAS. - 2009. - 34 : Vol. 106. - pp. 14195–14200.

Cao Yi [et al.] Study of high-throughput cell electrofusion in a microelectrode-array chip [Journal] // Microfluid Nanofluid. - 2008. - Vol. 5. - pp. 669–675.

Catacuzzeno Luigi, Fioretti Bernard and Franciolini Fabio Modeling Study of the Effects of Membrane Surface Charge on Calcium Microdomains and Neurotransmitter Release [Journal] // Biophysical Journal. - 2008. - Vol. 95. - pp. 2160–2171.

Chambers E.L. and Armendi J. de Membranepotential, actionpotential and activationpotential of eggs of the seaurchin, Lytechinus variegatus [Journal] // Experimental Cell Research. - 1979. - 1 : Vol. 122. - pp. 203–218.

Chattopadhyay Saikat [et al.] Lattice expansion in ZnSe quantum dots [Journal] // Materials Letters. - 2011. - Vol. 65. - pp. 1625–1627.

Cheng Li-Jing Ion and molecule transport in nanochannels [Report] : PhD thesis / Electrical Engineering and Computer Science ; University of Michigan. - 2008.

Cheng Wei [et al.] Microfluidic cell arrays for metabolic monitoring of stimulated cardiomyocytes [Journal] // Electrophoresis. - 2010. - Vol. 31. - pp. 1405–1413.

Cho Y.H. [et al.] Fabrication of high-aspect-ratio polymer nanochannels using a novel Si nanoimprint mold and solvent-assisted sealing [Journal] // Microfluid Nanofluid. - 2010. - Vol. 9. - pp. 163-170. - DOI 10.1007/s10404-009-0509-3.

Choi Yong Seok and Kim Sung Jin Electrokinetic flow-induced currents in silica nanofluidic channels [Journal] // Journal of Colloid and Interface Science. - 2009. - 2 : Vol. 333. - pp. 672-678. - doi:10.1016/j.jcis.2009.01.061.

Cukjati David [et al.] Real time electroporation control for accurate and safe in vivo non-viral gene therapy [Journal] // Bioelectrochemistry. - 2007. - Vol. 70. - pp. 501–507.

Daghighi Yasaman and Li Dongqing Eccentric electrophoretic motion of a rectangular particle in a rectangular microchannel [Journal] // Journal of Colloid and Interface Science. - 2010. - Vol. 342. - pp. 638–642.

DeBruin Katherine A and Krassowska Wanda Modeling Electroporation in a Single Cell. I. Effects of Field Strength and Rest Potential [Journal] // Biophysical Journal. - 1999. - Vol. 77. - pp. 1213–1224.

DeBruin Katherine A and Krassowska Wanda Modeling Electroporation in a Single Cell. II. Effects of Ionic Concentrations [Journal] // Biophysical Journal. - 1999. - Vol. 77. - pp. 1225–1233.

Escoffre J.M. [et al.] Membrane perturbation by an external electric field: a mechanism to permit molecular uptake [Journal] // Eur Biophys J. - 2007. - Vol. 36. - pp. 973–983.

Escoffre Jean-Michel [et al.] What is (Still not) Known of the Mechanism by Which Electroporation Mediates Gene Transfer and Expression in Cells and Tissues [Journal] // Mol Biotechnol. - 2009. - Vol. 41. - pp. 286–295.

Fei Zhengzheng [et al.] Gene Transfection of Mammalian Cells Using Membrane Sandwich Electroporation [Journal] // Anal. Chem.. - 2007. - 15 : Vol. 79. - pp. 5719-5722.

Fei Zhengzheng [et al.] Micronozzle Array Enhanced Sandwich Electroporation of Embryonic Stem Cells [Journal] // Anal. Chem.. - 2010. - Vol. 82. - pp. 353-358.

Fox M.B. [et al.] Electroporation of cells in microfluidic devices: a review [Journal] // Anal Bioanal Chem. - 2006. - Vol. 385. - pp. 474–485.

Fox M.B. [et al.] Inactivation of L. plantarum in a PEF microreactor The effect of pulse width and temperature on the inactivation [Journal] // Innovative Food Science and Emerging Technologies. - [s.l.] : Elsevier, 2008. - Vol. 9. - pp. 101-108.

Freeman S.A., Wang M.A. and Weaver J.C. Theory of electroporation of planar bilayer membranes: predictions of the aqueous area, change in capacitance, and pore-pore separation [Journal]. - 1994. - 1 : Vol. 67. - pp. 42–56.

Freund J.B. Atomistic simulation of electro-osmosis in a nanometer-scale channel [Conference] // Proceedings of the Summer Program. - [s.l.] : Center for Turbulence Research, 2000. - pp. 21-29.

Garcia Anthony L [et al.] Electrokinetic molecular separation in nanoscale fluidic channels [Journal] // Lab on a Chip. - 2005. - Vol. 5. - pp. 1271–1276. - DOI: 10.1039/b503914b.

Geng Tao [et al.] Flow-through electroporation based on constant voltage for large-volume transfection of cells [Journal] // Journal of Controlled Release. - 2010. - doi:10.1016/j.jconrel.2010.01.030.

Gimsa Jan A comprehensive approach to electro-orientation, electrodeformation, dielectrophoresis, and electrorotation of ellipsoidal particles and biological cells [Journal] // Bioelectrochemistry. - 2001. - Vol. 54. - pp. 23-31.

Glaser Ralf W [et al.] Reversibleelectricalbreakdown of lipid bilayers: formation and evolution of pores [Journal] // Biochimica et Biophysica Acta (BBA) - Biomembranes. - 1988. - 2 : Vol. 940. - pp. 275–287.

Gothelf Anita, Mir Lluis M and Gehl Julie Electrochemotherapy: results of cancer treatment using enhanced delivery of bleomycin by electroporation [Journal] // Cancer Treatment Reviews. - 2003. - 5 : Vol. 23. - pp. 371–387.

Granot Yair and Rubinsky Boris Mass transfer model for drug delivery in tissue cells with reversible electroporation [Journal] // International Journal of Heat and Mass Transfer. - 2008. - Vol. 51. - pp. 5610–5616.

Gross David, Loew Leslie M. and Webb Watt W. Optical imaging of cell membrane potential changes induced by applied electric fields [Journal] // BIOPHYS Journal. - 1986. - Vol. 50. - pp. 339-348.

Grosse Constantino and Schwan Herman P Cellular membrane potentials induced by alternating fields [Journal] // Biophysical Journal. - 1992. - 6 : Vol. 63. - pp. 1632-1642.

Hénon S [et al.] A new determination of the shear modulus of the human erythrocyte membrane using optical tweezers [Journal] // Biophys J.. - 1999. - 2 : Vol. 76. - pp. 1145–1151.

Herwadkar Anushree and Banga Ajay K Peptide and protein transdermaldrugdelivery [Journal] // Drug Discovery Today: Technologies. - In Press, Corrected Proof.

Hibino M [et al.] Membrane conductance of an electroporated cell analyzed by submicrosecond imaging of transmembrane potential [Journal] // Biophysical Journal. - 1991. - 1 : Vol. 59. - pp. 209-220.

Hibino M, Itoh H and Kinosita Jr K Time courses of cell electroporation as revealed by submicrosecond imaging of transmembrane potential [Journal] // Biophysical Journal. - 1993. - 6 : Vol. 64. - pp. 1789-1800.

Hibino Masahiro, Itoh Hiroyasu and Kinosita Kazuhiko Time courses of cell electroporation as revealed by submicrosecond imaging of transmembrane potential [Journal] // Biophysical Journal. - 1993. - 6 : Vol. 64. - pp. 1789–1800.

Ho Yi-Ping and Leong Kam W. Quantum dot-based theranostics [Journal] // Nanoscale. - 2010. - Vol. 2. - pp. 60-68.

Hsu Jyh-Ping, Yeh Li-Hsien and Ku Ming-Hong Evaluation of the electric force in electrophoresis [Journal] // Journal of Colloid and Interface Science. - 2007. - Vol. 305. - pp. 324–329.

Huang Yong and Rubinsky Boris Flow-through micro-electroporation chip for high efficiency single-cell genetic manipulation [Journal] // Sensors and Actuators A. - 2003. - Vol. 104. - pp. 205–212.

Huang Yong and Rubinsky Boris Micro-electroporation: improving the efficiency and understanding of electrical permeabilization of cells [Journal] // Biomed. Microdev.. - 2000. - Vol. 3. - pp. 145-150.

Huang Yong and Rubinsky Boris Microfabricated electroporation chip for single cell membrane permeabilization [Journal] // Sensors and Actuators A. - 2001. - Vol. 89. - pp. 242-249.

Huh Dongeun [et al.] Tuneable elastomeric nanochannels for nanofluidic manipulation [Journal] // nature materials. - 2007. - Vol. 6. - pp. 424-428.

Ikeda Norifumi [et al.] On-Chip Single-Cell Lysis for Extracting Intracellular Material [Journal] // Japanese Journal of Applied Physics. - 2007. - 9B : Vol. 46. - pp. 6410–6414.

Ionescu-Zanetti Cristian, Blatz Andrew and Khine Michelle Electrophoresis-assisted single-cell electroporation for efficient intracellular delivery [Journal] // Biomed Microdevices. - 2008. - Vol. 10. - pp. 113–116.

Israelachvili Jacob N. Intermolecular and Surface Forces [Book]. - London : Academic Press, 1992. - Vol. 2 nd. .

Janina Schaper, Richard Bohnenkamp Hermann and Thomas Noll New Electrofusion Devices for the Improved Generation of Dendritic Cell-tumour Cell Hybrids [Book Section] // Cell Technology for Cell Products / book auth. Smith Rodney. - [s.l.] : Springer, 2007.

Joseph Sony and Aluru N.R. Hierarchical Multiscale Simulation of Electrokinetic Transport in Silica Nanochannels at the Point of Zero Charge [Journal] // Langmuir. - 2006. - Vol. 22. - pp. 9041-9051.

Kadaksham A.T.J., Singh P and Aubry N Dielectrophoresis of nanoparticles [Journal] // Electrophoresis. - 2004. - Vol. 25. - pp. 3625–3632.

Kakorin S, Liese T and Neumann E Membrane curvature and high-yield electroporation of lipid bilayer vesicles. [Journal] // J. Phys. Chem. B.. - 2003. - Vol. 107. - pp. 10243-10251.

Kang Yuejun and Li Dongqing Electrokinetic motion of particles and cells in microchannels [Journal] // Microfluid Nanofluid (2009) 6:. - 2009. - Vol. 6. - pp. 431–460. - DOI 10.1007/s10404-009-0408-7.

Keh H. J. and Anderson J. L. Boundary effects on electrophoretic motion of colloidal spheres [Journal] // J . Fluid Mech.. - 1985. - Vol. 153. - pp. 417-439.

Khine Michelle [et al.] A single cell electroporation chip [Journal] // Lab on a Chip. - 2005. - Vol. 5. - pp. 38-43.

Khine Michelle [et al.] Single-cell electroporation arrays with real-time monitoring and feedback control [Journal] // Lab on a Chip. - 2007. - Vol. 7. - pp. 457–462.

Kim Sang Kyung [et al.] Continuous Low-Voltage dc Electroporation on a Microfluidic Chip with Polyelectrolytic Salt Bridges [Journal] // Anal. Chem.. - 2007. - Vol. 79. - pp. 7761-7766.

Kim Sung Jae [et al.] Concentration Polarization and Nonlinear Electrokinetic Flow near a Nanofluidic Channel [Journal] // Physical Review Letters. - 2007. - 4 : Vol. 99. - p. 044501(4).

Koneshan S [et al.] Solvent Structure, Dynamics, and Ion Mobility in Aqueous Solutions at 25 °C [Journal] // J. Phys. Chem. B 1998. - 1998. - Vol. 102. - pp. 4193-4204.

Kotnik T, Slivnik T and Miklavcic D Time course of transmembrane voltage induced by time-varying electric fields: a method for theoretical analysis and its application [Journal] // Bioelectrochem. Bioenerg.. - 1998. - Vol. 45. - pp. 3-16.

Kotnik Tadej and Miklavčič Damijan Analytical Description of Transmembrane Voltage Induced by Electric Fields on Spheroidal Cells [Journal] // Biophysical Journal. - 2000. - 2 : Vol. 79. - pp. 670-679.

Kotnik Tadej, Bobanović Feda and Miklavc Damijian Sensitivity of transmembrane voltage induced by applied electric fields—A theoretical analysis [Journal] // Bioelectrochemistry and Bioenergetics. - 1997. - 2 : Vol. 43. - pp. 285-291.

Krassowska Wanda and Filev Petar D Modeling Electroporation in a Single Cell [Journal] // Biophysical Journal. - 2007. - Vol. 92. - pp. 404–417.

Krassowska Wanda and Neu John C Theory of Electroporation [Book Section] // Cardiac Bioelectric Therapy / book auth. Igor R. Efimov Mark W. Kroll and Patrick J. Tchou. - [s.l.] : Springer US, 2009.

Lee Eunice S [et al.] Microfluidic electroporation of robust 10-µm vesicles for manipulation of picoliter volumes [Journal] // Bioelectrochemistry. - 2006. - Vol. 69. - pp. 117–125.

Lee Sang Yoon [et al.] Diffusiophoretic Motion of a Charged Spherical Particle in a Nanopore [Journal] // J. Phys. Chem. B. - 2010. - Vol. 114. - pp. 6437–6446. - 10.1021/jp9114207.

Lee Won Gu, Demirci Utkan and Khademhosseini Ali Microscale electroporation: challenges and perspectives for clinical applications [Journal] // Integrative Biology. - 2009. - Vol. 1. - pp. 242–251.

Li Dongqing Electrokinetics in Microfluidics [Book]. - [s.l.] : Elsevier, 2004.

Li Dongqing Encyclopedia of Microfluidics and Nanofluidics [Book]. - [s.l.] : Springer, 2008.

Li Jianbo and Lin Hao Numerical simulation of molecular uptake via electroporation [Journal] // Bioelectrochemistry. - 2011. - doi:10.1016/j.bioelechem.2011.04.006.

Li Shulin Electroporation Protocols: Preclinical and Clinical Gene Medicine [Book]. - [s.l.] : Springer, 2008-b.

Li Wanli [et al.] Sacrificial polymers for nanofluidic channels in biological applications [Journal] // Nanotechnology. - 2003. - PaulA Kohl, Jeff Krotine, James C Sturm : Vol. 14. - pp. 578–583.

Lim Jit Kang, Zhou Hao and Tilton Robert D Liposome rupture and contents release over coplanar microelectrode arrays [Journal] // Journal of Colloid and Interface Science. - 2009. - Vol. 332. - pp. 113-121.

Lin Yen-Heng and Lee Gwo-Bin An optically induced cell lysis device using dielectrophoresis [Journal] // Applied Physics Letters. - 2009. - 3 : Vol. 94. - p. 033901.

Liu D, Maxey MR and Karniadakis GE Simulations of dynamic self-assembly of paramagnetic microspheres in confined microgeometries [Journal] // J. Micromech. Microeng.. - 2005. - Vol. 15. - pp. 2298–2308.

Lodish Harvey [et al.] Molecular Cell Biology, Fifth Edition [Book]. - [s.l.] : W. H. Freeman, 2003. - ISBN: 0716743663.

Lu Hang, Schmidt Martin A and Jensen Klavs F A microfluidic electroporation device for cell lysis [Journal] // Lab on a Chip. - [s.l.] : The Royal Society of Chemistry, 2005. - Vol. 5. - pp. 23-29.

Luo Chunxiong [et al.] Picoliter-volume aqueous droplets in oil: Electrochemical detection and yeast cell electroporation [Journal] // Electrophoresis. - 2006. - Vol. 27. - pp. 1977-1983.

Marszalek P, Liu D.S. and Tsong T.Y. Schwan equation and transmembrane potential induced by alternating electric field [Journal] // Biophysical Journal. - 1990. - 4 : Vol. 58. - pp. 1053-1058.

Mijatovic D, Eijkel J. C. T and Berg A van den Technologies for nanofluidic systems: top-down vs. bottom-up—a review [Journal] // Lab Chip. - 2005. - Vol. 5. - pp. 492–500.

Miklavcic Damijan and Towhidi Leila Numerical study of the electroporation pulse shape effect on molecular uptake of biological cells [Journal] // Radiol Oncol. - 2010. - 1 : Vol. 44. - pp. 34-41.

Morgan Hywel and Green Nicolas G AC Electrokinetic: Colloids and Nanoparticles [Book]. - Baldock : RESEARCH STUDIES PRESS LTD., 2002.

Mossop Brian J [et al.] Electric Fields around and within Single Cells during Electroporation—A Model Study [Journal] // Annals of Biomedical Engineering. - 2007. - 7 : Vol. 35. - pp. 1264–1275.

Movahed S and Li D Numerical studies of continuous nutrient delivery for tumour spheroid culture in a microchannel by electrokinetically-induced pressure-driven flow [Journal] // Biomedical Microdevices. - [s.l.] : Springer, 2010. - 6 : Vol. 12. - pp. 1061-1072.

Movahed Saeid and Li Dongqing Electrokinetic transport through the nanopores in cell membrane during electroporation [Journal] // Journal of Colloid and Interface Science. - 2012. - 1 : Vol. 369. - pp. 442-452.

Movahed Saeid and Li Dongqing Electrokinetic Transports through Nanochannels [Journal] // Electrophoresis Journal. - [s.l.] : Wiely, 2011 . - Vol. 32. - pp. 1259–1267.

Movahed Saeid and Li Dongqing Microfluidics cell electroporation [Journal] // Microfluid Nanofluid. - 2011. - 4 : Vol. 10. - pp. 703-734. - In press. - DOI 10.1007/s10404-010-0716-y.

Neu John C and Krassowska Wanda Asymptotic model of electroporation [Journal] // Phys Rev E. - 1999. - Vol. 59. - pp. 3471–3482.

Neu John C, Smith Kyle C and Krassowsk Wanda Electrical energy required to form large conducting pores [Journal] // Bioelectrochemistry. - 2003. - 1–2 : Vol. 60. - pp. 107–114.

Neu Wanda Krassowska and Neu John C. Theory of Electroporation [Book Section] // Cardiac Bioelectric Therapy / book auth. Efimov Igor R., Kroll Mark W. and Tchou Patrick. - [s.l.] : Springer, 2009.

Neumann E [et al.] Gene transfer into mouse lyoma cells by electroporation in high electric fields [Journal] // EMBO J. . - 1982. - 7 : Vol. 1. - pp. 841–845.

Neumann Eberhard and Rosenheck Kurt Permeability changes induced by electric impulses in vesicular membranes [Journal] // JOURNAL OF MEMBRANE BIOLOGY. - 1972. - 1 : Vol. 10 . - pp. 279-290. - DOI: 10.1007/BF01867861.

Oron Dan [et al.] Universal Role of Discrete Acoustic Phonons in the Low-Temperature Optical Emission of Colloidal Quantum Dots [Journal] // Physical Review Letters. - 2009. - Vol. 102. - p. 177402.

Park Sangyun, Chung Taek Dong and Kim Hee Chan Ion bridges in microfluidic systems [Journal] // Microfluid Nanofluid. - 2009. - Vol. 6. - pp. 315-331. - DOI 10.1007/s10404-008-0391-4.

Pauly H, Schwan, HP Über die Impedanz einer Suspension von kugelförmigen Teilchen mit einer Schale [Journal] // Z Naturforschung . - 1959. - Vol. 14b. - pp. 125-131.

Pennathur Sumita and Santiago Juan G Electrokinetic Transport in Nanochannels. 1. Theory [Journal] // Analytical Chemistry. - 2005. - 21 : Vol. 77. - pp. 6772-6781.

Pennathur Sumita and Santiago Juan G. Electrokinetic Transport in Nanochannels. 2. Experiments [Journal] // Anal. Chem.. - 2005. - Vol. 77. - pp. 6782-6789.

Petsev Dimiter N and Lopez Gabriel P Electrostatic potential and electroosmotic flow in a cylindrical capillary filled with symmetric electrolyte: Analytic solutions in thin double layer approximation [Journal] // Journal of Colloid and Interface Science. - 2006. - Vol. 294. - pp. 492–498.

Pucihar G, Miklavcic D and Kotnik T A Time-Dependent Numerical Model of Transmembrane Voltage Inducement and Electroporation of Irregularly Shaped Cells [Journal]. - 2009. - 5 : Vol. 56. - pp. 1491 - 1501.

Qian Shizhi [et al.] Electrophoretic Motion of a Spherical Particle with a Symmetric Nonuniform Surface Charge Distribution in a Nanotube [Journal] // Langmuir. - 2008b. - Vol. 24. - pp. 5332-5340.

Qian Shizhi and Joo Sang W Analysis of Self-Electrophoretic Motion of a Spherical Particle in a Nanotube: Effect of Nonuniform Surface Charge Density [Journal] // Langmuir. - 2008a. - Vol. 24. - pp. 4778-4784.

Qiao R. and Aluru N. R. Ion concentrations and velocity profiles in nanochannel electroosmotic flows [Journal] // JOURNAL OF CHEMICAL PHYSICS VOLUME 118, NUMBER 10 8 MARCH 2003. - 2003. - 10 : Vol. 118. - pp. 4692-4701. - DOI: 10.1063/1.1543140.

Qiao R. and Aluru N. R. Surface-charge-induced asymmetric electrokinetic transport in confined silicon nanochannels [Journal] // APPLIED PHYSICS LETTERS. - 2005. - Vol. 86. - p. 143105.

Qiao R. and Aluru N. R. Transient Analysis of Electroosmotic Flow in Nano-diameter Channels [Journal] // Modeling and Simulation of Microsystems. - 2002. - pp. 28-31.

Reisner Walter [et al.] Single-molecule denaturation mapping of DNA in nanofluidic channels [Journal] // PNAS. - 2010. - 30 : Vol. 107. - pp. 13294–13299.

Rice C.L. and Whitehead R Electrokinetic Flow in a Narrow Cylindrical Capillary [Journal] // The Journal of Physical Chemistry. - 1965. - 11 : Vol. 69.

Schaper Janina, Bohnenkamp Hermann Richard and Noll Thomas New Electrofusion Devices for the Improved Generation of Dendritic Cell-tumour Cell Hybrids [Book Section] // Cell Technology for Cell Products / book auth. Smith R.. - [s.l.] : Springer, 2007.

Sedgwick H [et al.] Lab-on-a-chip technologies for proteomic analysis from isolated cells [Journal] // J. R. Soc. Interface. - 2008. - and J. M. Cooper : Vol. 5. - pp. S123–S130.

Shil Pratip, Bidaye Salil and Vidyasagar Pandit B Analysing the effects of surface distribution of pores in cell electroporation for a cell membrane containing cholesterol [Journal] // Journal of physics D: Applied physics. - 2008. - Vol. 41. - p. 055502 (7pp).

Shin Young Shik [et al.] Electrotransfection of Mammalian Cells Using Microchannel-Type Electroporation Chip [Journal] // Anal. Chem.. - 2004. - Vol. 76. - pp. 7045-7052.

Shugai Alexander A and Carnie Steven L Electrophoretic Motion of a Spherical Particle with a Thick Double Layer in Bounded Flows [Journal] // Journal of Colloid and Interface Science. - 1999. - Vol. 213. - pp. 298–315.

Smith Kyle C, Neu ohn C and Krassowska Wanda Model of Creation and Evolution of Stable Electropores for DNA Delivery [Journal] // Biophys J.. - 2004. - 5 : Vol. 86. - pp. 2813–2826.

Sott Kristin [et al.] Optical systems for single cell study [Journal] // Expert Opin. Drug Discov.. - 2008. - 11 : Vol. 3.

Suzuki Takaaki [et al.] High throughput cell electroporation array fabricated by single-mask inclined UV lithography exposure and oxygen plasma etching [Conference] // The 14th International Conference on Solid-State Sensors, Actuators and Microsystems, June 10-14, 2007. - Lyon, France : IEEE, 2007. - pp. 687-690.

Taheri-Araghi Sattar Membrane-Disrupting Activity of Antimicrobial Peptides and the Electrostatic Bending of Membranes [Report]. - [s.l.] : PhD thesis, University of waterloo, 2010.

Talele Sadhana [et al.] Modelling single cell electroporation with bipolar pulse parameters and dynamic pore radii [Journal] // Journal of Electrostatics. - 2010. - pp. 1-14.

Tegenfeldt Jonas O [et al.] Micro- and nanofluidics for DNA analysis [Journal] // Anal Bioanal Chem. - 2004. - Vol. 378. - pp. 1678–1692.

Teissie J [et al.] Recent biotechnological developments of electropulsation. A prospective review [Journal] // Bioelectrochemistry. - 2002. - Vol. 55. - pp. 107-112.

Teissie J and Rols M.P. An experimental evaluation of the critical potential difference inducing cell membrane electropermeabilization. [Journal] // Biophys. J.. - 1993. - Vol. 65. - pp. 409-413.

Towhidi L [et al.] Variability of the minimal transmembrane voltage resulting in detectable electroporation. [Journal] // Electromag. Biol. Med.. - 2008. - Vol. 27. - pp. 372-385.

Valero A [et al.] Gene transfer and protein dynamics in stem cells using single cell electroporation in a microfluidic device [Journal] // Lab on a Chip. - 2008. - Vol. 8. - pp. 62-67. - DOI: 10.1039/b713420g.

Valley Justin K [et al.] Parallel single-cell light-induced electroporation and dielectrophoretic manipulation [Journal] // Lab on a Chip. - 2009-b. - Vol. 9. - pp. 1714–1720. - DOI: 10.1039/b821678a.

Valley Justin K. [et al.] Assessment of single cell viability following light induced electroporation through use of on-chip microfluidics [Conference] / ed. IEEE. - 2009-a. - 978-1-4244-2978-3.

Vassanelli S [et al.] Space and time-resolved gene expression experiments on cultured mammalian cells by a single-cell electroporation microarray [Journal] // New Biotechnology. - 2008. - 1 : Vol. 25.

Vlassiouk Ivan, Smirnov Sergei and Siwy Zuzanna Ionic Selectivity of Single Nanochannels [Journal] // Nano Letters. - 2008. - 7 : Vol. 8. - pp. 1978-1985.

Wan Qian-Hong Effect of Electrical Double-Layer Overlap on the Electroosmotic Flow in Packed-Capillary Columns [Journal] // Anal. Chem.. - 1997. - Vol. 69. - pp. 361-363.

Wang Hsiang-Yu and Lu Chang Electroporation of Mammalian Cells in a Microfluidic Channel with Geometric Variation [Journal] // Anal. Chem.. - [s.l.] : Wiley Periodicals, Inc., 2006-a. - Vol. 78. - pp. 5158-5164.

Wang Hsiang-Yu and Lu Chang High-Throughput and Real-Time Study of Single Cell Electroporation Using Microfluidics: Effects of Medium Osmolarity [Journal] // Biotechnology and Bioengineering. - [s.l.] : Wiley Periodicals, Inc., 2006-b. - 6 : Vol. 95. - pp. 1116-1125.

Wang Hsiang-Yu and Lu Chang Microfluidic Electroporation for Delivery of Small Molecules and Genes Into Cells Using a Common DC Power Supply [Journal] // Biotechnology and Bioengineering. - [s.l.] : Wiley Periodicals, Inc., 2008. - 3 : Vol. 100. - pp. 579-586. - DOI 10.1002/bit.21784.

Wang Hsiang-Yu, Bhunia Arun K and Lu Chang A microfluidic flow-through device for high throughput electrical lysis of bacterial cells based on continuous dc voltage [Journal] // Biosensors and Bioelectronics. - 2006. - Vol. 22. - pp. 582–588.

Wang Jun [et al.] Detection of Kinase Translocation Using Microfluidic Electroporative Flow Cytometry [Journal] // Anal. Chem.. - 2008. - 4 : Vol. 80. - pp. 1087-1093.

Wang Jun, Stine M. Jane and Lu Chang Microfluidic Cell Electroporation Using a Mechanical Valve [Journal] // Anal. Chem.. - 2007. - Vol. 79. - pp. 9584-9587.

Wang Manyan [et al.] Single-cell electroporation [Journal] // Anal Bioanal Chem. - [s.l.] : Springer, 2010. - Vol. 397. - pp. 3235–3248.

Wang Shengnian [et al.] Semicontinuous Flow Electroporation Chip for High-Throughput Transfection on Mammalian Cells [Journal] // Anal. Chem.. - 2009. - Vol. 81. - pp. 4414–4421.

Wang Xiayan [et al.] Electroosmotic pumps and their applications in microfluidic systems [Journal] // Microfluid Nanofluid. - 2009. - Vol. 6. - pp. 145-162. - DOI 10.1007/s10404-008-0399-9.

Weaver James C and Chizmadzhev Yu.A. Theory of electroporation: A review [Journal] // Bioelectrochemistry and Bioenergetics. - 1996. - Vol. 41. - pp. 135-160.

Weaver James C. Electroporation Theory Concepts and Mechanisms [Book Section] // Plant Cell Electroporation and Electrofusion Protocols / book auth. Nickoloff Jac A.. - 1995. - Vol. 55. - DOI: 10.1385/0896033287.

Wei Zewen [et al.] Laminar Flow Electroporation System for Efficient DNA and siRNA Delivery [Journal] // analytical chemistry. - [s.l.] : American Chemical Society, 2011. - 15 : Vol. 83. - pp. 5881–5887. - dx.doi.org/10.1021/ac200625b.

Wong PakKin, Tan Winny and Ho Chih-Ming Cell relaxation after electrodeformation: effect of latrunculin A on cytoskeletal actin [Journal] // Journal of Biomechanics. - 2005. - Vol. 38. - pp. 529–535.

Wu Z and Li D Induced-charge electrophoretic motion of ideally polarizable particles [Journal] // Electrochimica Acta. - 2009. - Vol. 54. - pp. 3960–3967.Z.

Wu Z, Gao Y and Li D Electrophoretic motion of ideally polarized particles in microchannels [Journal] // Electrophoresis. - 2009. - Vol. 30. - pp. 773 – 781.

Xuan X, Ye C and Li D Near-wall electrophoretic motion of spherical particles in cylindrical capillaries [Journal] // J. Colloid Interface Sci. - 2005. - Vol. 289. - pp. 286-290.

Ye C and Li D 3-D Transient Electrophoretic Motion of a Spherical Particle in a T-shaped Rectangular Microchannel [Journal] // J. Colloid Interface Sci.. - 2004. - Vol. 272. - pp. 480-488.

Ye C and Li D Eccentric Electrophoretic Motion of a Spherical Particle in a Circular Cylindrical Microchannel [Journal] // Microfluidics & Nanofluidics. - 2005. - Vol. 1. - pp. 234 – 241.

Ye C and Li D Electrophoretic Motion of Spherical Particle in a Microchannel under Gravitational Field [Journal] // J. Colloid and Interface Sci.. - 2002. - Vol. 251. - pp. 331-338.

Ye C and Li D Electrophoretic motion of two particles in a rectangular microchannel [Journal] // Microfluidics and Nanofluidics. - 2004. - Vol. 1. - pp. 52–61.

Yen-Heng Lin and Gwo-Bin Leea an optically induced cell lysis device using dielectrophoresis [Journal] // APPLIED PHYSICS LETTERS. - 2009. - Vol. 94.

Yuan Zhen [et al.] Electrokinetic transport and separations in fluidic nanochannels [Journal] // Electrophoresis. - 2007. - Vol. 28. - pp. 595–610.

Zaharoff David A [et al.] Mechanistic Analysis of Electroporation-Induced Cellular Uptake of Macromolecules [Journal]. - 2008. - pp. 94-105. - 10.3181/0704-RM-113.

Zangle Thomas A., Mani Ali and Santiago Juan G. Theory and experiments of concentration polarization and ion focusing at microchannel and nanochannel interfaces [Journal] // Chemical Society Reviews. - 2010. - Vol. 39. - pp. 1014-1035. - DOI: 10.1039/B902074H.

Zhan Yihong [et al.] Electroporation of Cells in Microfluidic Droplets [Journal] // Anal. Chem.. - 2009. - Vol. 81. - pp. 2027–2031.

Zhao Xiaopeng, Zhang Mingjun and Yang Ruoting Control of pore radius regulation for electroporation-based drug delivery [Journal] // Commun Nonlinear Sci Numer Simulat. - 2010. - Vol. 15. - pp. 1400-1407.

Zheng Zhi, Hansford Derek J and Conlisk Albert T Effect of multivalent ions on electroosmotic flow in micro- and nanochannels [Journal] // Electrophoresis. - 2003. - Vol. 24. - pp. 3006–3017. - DOI 10.1002/elps.200305561.

Zhu Tao [et al.] Electroporation based on hydrodynamic focusing of microfluidics with low dc voltage [Journal] // Biomed Microdevices. - 2010. - Vol. 12. - pp. 35-40. - DOI 10.1007/s10544-009-9355-z.

Ziaie Babak [et al.] Hard and soft micromachining for BioMEMS: review of techniques and examples of applications in microfluidics and drug delivery [Journal] // Advanced Drug Delivery Reviews. - 2004. - 3 : Vol. 56. - pp. 145-172 .